Rock-slope failures in Innerdalen and Innfjorddalen, western Norway:

rock-slope instabilities and rock avalanches in a changing landscape following the melt down of the Scandinavian ice sheet

---

Hangversagen von Festgesteinen in Innerdalen und Innfjorddalen, Westnorwegen:

Hanginstabilitäten und Sturzströme in einem sich verändernden Landschaftsraum in Folge des Abschmelzens des Skandinavischen Eisschildes

Der Naturwissenschaftlichen Fakultät

der Friedrich-Alexander-Universität

Erlangen-Nürnberg

zur

Erlangung des Doktorgrades Dr. rer. nat.

vorgelegt von

Markus T. Schleier

aus Schweinfurt

Als Dissertation genehmigt
von der Naturwissenschaftlichen Fakultät
der Friedrich-Alexander-Universität Erlangen-Nürnberg
Tag der mündlichen Prüfung: 29.01.2016

Vorsitzender des Promotionsorgans: Prof. Dr. Jörn Wilms
Gutachter: Prof. Dr. Joachim Rohn
Prof. Dr. Reginald L. Hermanns

Statement of candidate

I certify that this doctoral thesis entitled

"Rock-slope failures in Innerdalen and Innfjorddalen, western Norway: rock-slope instabilities and rock avalanches in a changing landscape following the melt down of the Scandinavian ice sheet"

is an original piece of research and has been written by myself.

I profess that all literature and sources of information used are indicated in this thesis, and that any help and assistance received for the research work and the preparation of this thesis have been acknowledged. I declare that this thesis has previously not been submitted for any degree to Friedrich-Alexander-University or any other university or institution, neither by me nor, as far as I know, by anybody else. I am aware that violations of the principles of independence are considered deception and that incorrectness of this statement results in the grade "unsatisfactory".

Erlangen, 25.07.2015

Markus T. Schleier
http://www.researcherid.com/rid/I-2357-2013

GeoZentrum Nordbayern
Department für Geographie und Geowissenschaften
Naturwissenschaftliche Fakultät
Friedrich-Alexander-Universität Erlangen-Nürnberg

Abstract

Large rock-slope failures that fail catastrophically as rock avalanches have within glacial cycles a first-order control on landscape evolution in steep mountain environments, and pose a high threat to communities. However, the identification and interpretation of complex deposits and geomorphological features caused by rock-slope failures are often difficult, and misinterpretations are not uncommon because of complex interactions between rock-slope failures and other geological processes, namely glaciation and isostasy. Such a complex geological environment can be found in the glacially overprinted mountains of western Norway.

The primary aim of this study is to understand the large rock-slope failures and associated phenomena in the valleys of Innerdalen and Innfjorddalen, western Norway. The main objectives are (I) to understand the complex deposits and geomorphological features formed by multiple rock avalanches to derive their paleodynamics (i.e., runout behavior) with respect to the Scandinavian Quaternary geology following glacial melt down after the Last Glacial Maximum (LGM), and (II) to understand the geomorphological features, geological constraints and displacements of an actively moving rock-slope instability to derive its failure kinematics, deformation rate and mechanisms.

The integrative approach applied in this study consists of (1) intensive field mapping including granulometric sampling, trenching, ground penetrating radar and geoelectric resistivity tomography, (2) GIS-based digital elevation model and orthophoto analyses, (3) geomechanical investigations including structural analyses by field measurements and terrestrial laser scanning (LiDAR) and kinematic feasibility tests, (4) differential global navigation satellite system displacement measurements, (5) terrestrial cosmogenic nuclide surface-exposure dating (^{10}Be), and (6) numerical dynamic runout modeling (DAN3D).

The results on spatial distribution and characteristics of surface deposits and geomorphological landforms imply hypotheses for the paleodynamics of the rock avalanches. The interpretations are confirmed by ^{10}Be dating and DAN3D modeling. The results on geomorphological features, geomechanical analyses and displacement measurements suggest complex kinematics and active deformation for the rock-slope instability.

For the Innerdalen Valley, the results reveal that two large rock avalanches occurred from the same source area since the Late Pleistocene. Both events show similar failure kinematics of strongly jointed gneissic source rock but different paleodynamics. One rock avalanche propagated onto the Late Pleistocene valley glacier and was deposited as a supraglacial debris cover. The remnants of this event and its interaction with the glacier are complex rock-boulder deposits distributed over a variety of landforms such as terminal and lateral moraines, kame mounds and large patches along the slope with no connection to any source area. Later in the Holocene, another rock avalanche propagated into the then ice-free valley and is preserved as a continuous, typical lobate rock-boulder deposit damming the valley and causing a lake.

The results for the Innfjorddalen Valley reveal that at least three rock avalanches occurred from the same source area composed of strongly jointed gneissic rock since the Late Pleistocene. Although of similar failure kinematics, the events again show different paleodynamics. One rock avalanche propagated into the Innfjord and was deposited below the former water level in the Late Pleistocene. Today the deposits are exposed on the valley bottom due to post-glacial isostatic rebound. Another rock avalanche in the Holocene and one of historic times propagated over rock-boulder deposits of the previous events. All of these events are preserved in deposits that are distributed over the valley bottom in a variety of landforms such as isolated hills of rock-boulder deposits, deformed and undeformed valley-fill sediments, and a stratified succession of continuous rock-boulder deposits forming natural dams.

The results of the investigations of the large rock-slope instability in the upper Innfjorddalen Valley reveal complex kinematics and active deformation that is controlled by preexisting geological structures in the gneissic source rock. The feasible kinematics for failure is a large wedge failure formed by a fault plane and the foliation with an intersection lying below the valley bottom. Therefore, the deformation changes along the slope, including wedge sliding and creep-like deformation. This complex deformation is represented in the field by the distribution of various geomorphological features such as coherent slide blocks, fractured block-fields, large counterscarps and a bulging slope. These diagnostic characteristics account for the definition of a deep seated gravitational slope deformation. As lateral limit of the rock-slope instability, a distinct km-long linear geomorphological lineament has developed in the form of a topographic step that runs oblique to the slope. It has previously been interpreted as a Holocene reverse fault indicating the first example of neotectonic activity in southern Norway. However, the newly obtained results exhibit the existence of an inherited normal fault, parallel to the post-Caledonian collapse with regional extension that is a major geological constraint on rock-slope instability. Therefore, the geomorphological step marks a gravitational reactivation of a slope scale of the regional tectonic fault.

The findings obtained from this thesis contribute to the understanding of Quaternary geology in Innerdalen and Innfjorddalen Valley, western Norway, with special regard on paleodynamics and kinematics of large rock-slope failures. The findings further improve identification and interpretation of complex rock-boulder deposits and geomorphological features associated with large rock-slope failures for other steep and glaciated mountain areas.

Kurzfassung

Großvolumige Hangversagen von Festgesteinen, die sich als katastrophale Sturzströme ereignen, stellen im zeitlichen Rahmen von glazialen Zyklen einen bedeutenden Kontrollfaktor der Landschaftsentwicklung in steilen Gebirgsregionen dar. Zusätzlich sind sie eine große Gefährdung für die Gesellschaft. Die Identifikation und Interpretation komplexer Ablagerungen und geomorphologischer Merkmale, die durch Hangversagen verursacht wurden, sind häufig schwierig. Fehlinterpretationen sind aufgrund der ineinandergreifenden Interaktionen zwischen Hangversagen und anderen schnellen geologischen Prozessen, wie Vergletscherung und Isostasie, nicht ungewöhnlich. Ein solch vielfältiges geologisches Umfeld findet sich im glazial überprägten Gebirge von Westnorwegen.

Die primäre Zielsetzung dieser Arbeit ist das Verständnis der großvolumigen Hangversagen von Festgesteinen und der damit verbundenen Phänomene in den Tälern von Innerdalen und Innfjorddalen in Westnorwegen. Die Hauptziele sind dabei wie folgt: (I) Das Verständnis der komplexen Ablagerungen und geomorphologischen Merkmale die von mehrfachen Sturzströmen geformt wurden, um daraus deren Paläodynamik (d. h. Auslaufverhalten) unter Berücksichtigung der Quartärgeologie Skandinaviens in Folge des glazialen Abschmelzens nach dem letzten glazialen Maximum (LGM) abzuleiten. (II) Das Verständnis der geomorphologischen Merkmale, der geologischen Randbedingungen und der Verschiebungsbeträge einer sich aktiv bewegenden Hanginstabilität, um daraus deren Kinematik des Hangversagens und die Deformationsmechanismen abzuleiten.

Das in dieser Arbeit angewandte integrative Vorgehen umfasst: (1) Intensive Geländekartierung einschließlich Stichprobenprüfung der Granulometrie, Erstellung von Schürfen, Bodenradar und Geoelektrik; (2) GIS-basierte Auswertung von digitalen Geländemodellen und Orthophotos; (3) geomechanische Untersuchung einschließlich Strukturanalyse mittels Geländemessung und terrestrischem Laserscanning (LiDAR) und Prüfung der kinematischen Möglichkeiten des Hangversagens; (4) Bewegungsmessung mittels differentiellem globalem Satellitennavigationssystem (dGNSS); (5) Datierung des Oberflächenexpositionsalters mittels terrestrischen kosmogenen Nukliden (^{10}Be); (6) numerische dynamische Auslaufmodellierung (DAN3D).

Aus den Ergebnissen der räumlichen Verteilung von oberflächlichen Ablagerungen und der geomorphologischen Formen lassen sich Hypothesen zur Paläodynamik der Sturzströme ableiten. Die Interpretationen werden durch die ^{10}Be Datierung und die DAN3D Modellierung bestätigt. Die Resultate der geomorphologischen Merkmale, geomechanischen Untersuchungen und Bewegungsmessungen lassen eine komplexe Kinematik und aktive Deformation der Hanginstabilität erkennen.

Für Innerdalen zeigen die Untersuchungsergebnisse, dass sich seit dem Oberpleistozän zwei großvolumige Sturzströme aus dem gleichen Herkunftsgebiet ereignet haben. Die beiden Ereignisse weisen eine ähnliche Kinematik des Hangversagens im stark zerklüfteten Gneis der steilen Felswand auf, jedoch eine unterschiedliche Paläodynamik. Ein Sturzstrom

breitete sich im Oberpleistozän auf den damaligen Talgletscher aus und wurde auf diesem als supraglaziale Schuttbedeckung abgelagert. Die Überreste dieses Ereignisses und dessen Interaktion mit dem Gletscher sind komplexe Ablagerungen von Felsblöcken, die sich über unterschiedliche Landformen verteilen, wie End- und Randmoränen, Kame-Hügel und große Areale entlang der Talhänge die keine Verbindung zu möglichen Herkunftsgebieten haben. Im Holozän breitete sich ein weiterer Sturzstrom in das nunmehr eisfreie Tal aus. Dieser ist als zusammenhängende, typisch lobenartige Ablagerung von Felsblöcken erhalten, welche das Tal abriegelte und einen See aufstaute.

Die Ergebnisse für Innfjorddalen zeigen, dass sich seit dem Oberpleistozän mindestens drei Sturzströme aus dem gleichen, von stark zerklüftetem Gneis aufgebauten Herkunftsgebiet ereignet haben. Obwohl die drei Ereignisse eine ähnliche Kinematik des Hangversagens aufweisen, zeigen diese wiederum eine unterschiedliche Paläodynamik. Ein Sturzstrom breitete sich im Oberpleistozän in den Innfjord aus und wurde unterhalb des damaligen Wasserspiegels abgelagert. Durch die postglaziale isostatische Landhebung sind dessen Ablagerungen in heutiger Zeit auf dem Talboden freigelegt. Im Holozän und in historischer Zeit breitete sich jeweils ein Sturzstrom über die von den vorangegangenen Ereignissen gebildeten Ablagerungen von Felsblöcken aus. All diese Sturzströme sind als Ablagerungen erhalten, die in unterschiedlichen Landformen entlang des Talbodens verteilt sind. Es sind die von Felsblöcken aufgebauten isolierten Hügel, die deformierten und nicht deformierten Talfüllungssedimente und die schichtenweise Abfolge von zusammenhängenden Ablagerungen aus Felsblöcken, welche hier natürliche Dämme bilden.

Für die große Hanginstabilität im oberen Teil von Innfjorddalen zeigen die Untersuchungsergebnisse eine komplexe Kinematik und aktive Deformation, die von den gegebenen geologischen Strukturen der Gneise am Felshang gesteuert werden. Die wahrscheinliche Kinematik des Hangversagens ist ein großer Gleitkeil, der durch eine Störungs- und eine Schieferungsfläche gebildet wird, wobei sich das Verschnittlinear unterhalb des Talbodens befindet. Dies bewirkt eine Veränderung des Deformationsmechanismus entlang des Hanges, was Keilgleiten und kriechähnliche Deformation einschließt. Im Gelände wird diese komplexe Deformation durch die Verteilung der unterschiedlichen geomorphologischen Merkmale dargestellt, wie zusammenhängende Gleitblöcke, zerbrochene Blockfelder, große hangaufwärts zeigende Steilstufen und einen sich ausbeulenden Hang. Aufgrund der diagnostischen Merkmale ist die Instabilität als tiefgreifende gravitative Hangdeformation (DSGSD) einzuordnen. Ein deutliches, kilometerlanges geomorphologisches Lineament, welches sich in Form einer schräg zum Hang verlaufenden topographischen Stufe ausgebildet hat, stellt eine seitliche Begrenzung der Hanginstabilität dar. Dieses Lineament wurde bisher als Holozäne Aufschiebung interpretiert und als erstes Beispiel für neotektonische Aktivität in Südnorwegen beschrieben. Die neu erzielten Ergebnisse zeigen jedoch die Existenz einer alten, parallel zum Kaledonischen Kollaps verlaufenden Abschiebung mit regionaler Ausdehnung, die eine bedeutende geologische Einschränkung für die Hanginstabilität darstellt. Demzufolge markiert die geomorphologische Stufe eine in Größenordnung des Hanges auftretende gravitative Reaktivierung der regionalen tektonischen Störung.

Die durch diese Doktorarbeit erlangten Erkenntnisse tragen zum Verständnis der Quartärgeologie von Innerdalen und Innfjorddalen in Westnorwegen bei, besonders hinsichtlich der Paläodynamik und Kinematik großvolumigen Hangversagens von Festgesteinen. Die Ergebnisse verbessern ferner die Identifikation und Interpretation komplexer Ablagerungen von Felsblöcken und geomorphologischer Merkmale, die im Zusammenhang mit großvolumigen Hangversagen stehen, auch für andere steile und vergletscherte Gebirgsregionen.

Acknowledgments

I express my sincere gratitude to Prof. Dr. Joachim Rohn and Prof. Dr. Reginald L. Hermanns for supervising me and for the great opportunity to make this doctoral thesis. Thank you very much for your guidance, patience and support during the last years. Furthermore, thank you for being members of my thesis committee.

At this point I also thank Prof. Dr. Roman Koch and Prof. Dr. Michael Moser for being members of my oral examination committee.

This doctoral study would not have been possible without the additional financial and scientific support by the Geological Survey of Norway (NGU) and the project “Landslide mapping in Møre og Romsdal County”.

I want to thank my colleagues and friends Manuela Bail, Trond Eiken, Dr. Luzia Fischer, Philipp Geigenberger, Prof. Dr. John, C. Gosse, Ingvar Krieger, Dr. Thierry Oppikofer, Jan Steinar Rønning, Günther Schleier, Jan Fredrik Tønnesen, Guang Yang and Dr. Freddy Xavier Yugsi Molina Dr. Susan R. Zimmerman who participated actively in this study, either in field, lab or at office. Thank you for all your contributions, help and advices, and the wonderful times in the Norwegian mountains.

I thank the staff of Renndølsetra and Innerdal Turisthytte for their hospitality and support during long field-work periods in Innerdalen.

I wish to acknowledge Prof. Dr. Oldrich Hungr for kindly providing me the software DAN3D.

I thank Tina Deans for spending her spare time for proof reading of this thesis.

I would also like to thank the staff of GeoZentrum Nordbayern for the comfortable working atmosphere during my whole studies. Special thanks to my friends and office colleagues Dr. Muhammad Basharat, Dr. Renneng Bi, Christian Dumperth, Dr. Ji-wei Jiang, Dr. Jin Luo and Johannes Wiedenmann for all the great moments and collaborations within various research projects.

I deeply acknowledge my family and friends who accompanied and supported me during my studies. I am especially grateful to my parents Gertrud and Günther, my brothers Hermann and Michael, and my girlfriend Manuela who always believe in me. Thank you for all your encouragement, patience and moral support that helped me to finish this thesis.

Table of Contents

List of Figures

List of Tables

List of Abbreviations

2D, 3D	two-dimensional, three-dimensional
^{10}Be	Beryllium 10
AD	Anno Domini
ALS	Aerial Laser Scanning
a.s.l.	above sea level
COM	Center of Mass
DAN3D	the software “Dynamic Analysis of Landslide Motion in Three Dimensions”
DEM	Digital Elevation Model
dGNSS	differential Global Navigation Satellite System
DInSAR	Differential InSAR
DSGSD	Deep Seated Gravitational Slope Deformation
ELA	Equilibrium Line Altitude
Fig.	Figure
FoS	Factor of Safety
GIS	Geographical Information System
GPR	Ground Penetrating Radar
GPS	Global Positioning System
HRDEM	High Resolution DEM
InSAR	Interferometric Synthetic Aperture Radar
ka	1000 years
LGM	Last Glacial Maximum
LiDAR	Light Detection and Ranging
NGU	Norges Geologiske Undersøkelse (Geological Survey of Norway)
SPH	Smoothed Particle Hydrodynamics
TCN	Terrestrial Cosmogenic Nuclide
TLS	Terrestrial Laser Scanning
UTM	Universal Transverse Mercator
WGR	Western Gneiss Region
YD	Younger Dryas

1 Introduction

1.1 Scientific background of rock-slope failures

1.1.1 Hazards due to rock-slope failures

Massive rock-slope deformation can result in catastrophic landslides that are a widespread hazardous phenomena in steep mountain areas around the world (Evans et al., 2006a). Typical post-failure processes are rock avalanches, sometimes referred to as “Sturzstroms” that are defined as large volumes of fragmented rock mass propagating as highly mobile flows (Heim, 1932; Hutchinson, 1988; Hungr et al., 2001). These are among the most destructive types of landslides because of the high release of energy, the excessive runout length and cascading effects that are common and obviously enlarge the affected area such as displacement waves, valley damming with dam breach and associated up- and downriver flooding (Heim, 1932; Hewitt, 1998; Crosta et al., 2004; Hermanns et al., 2004; Evans et al., 2006b; Evans et al., 2009a; Evans et al., 2009b; Evans et al., 2011; Hermanns et al., 2011c; Hermanns & Longva, 2012). In glacially oversteepened regions close to the sea level, such as in western Norway, large rock-slope failures are widespread processes that pose a high hazard potential, and especially the hazard of subsequent displacement waves generates significant risk for the populated fjords (Blikra et al., 2002; Braathen et al., 2004; Blikra et al., 2005; Blikra et al., 2006; Longva et al., 2009; Böhme et al., 2011; Saintot et al., 2012; Hermanns et al., 2014c). Therefore, systematic mapping activities are carried out (Hermanns et al., 2011a; Hermanns et al., 2012a; Oppikofer et al., 2013) to determine the spatial and temporal variability in rates, recurrence intervals, and style of rock avalanches and factors that control them to establish a hazard and risk classification system (Hermanns et al., 2012b; Hermanns et al., 2013b). Reliable hazard assessment requires detailed understanding of complex processes of rock-slope failures and associated landslides. That can be obtained by detailed studies of past events (e.g., rock avalanches) and currently active slope deformations (e.g., rock-slope instabilities).

1.1.2 Geomorphological impact of rock-slope failures

Rock-slope failures and associated rock avalanches have on an interglacial time scale first-order controls on landscape evolution in fluvial and alpine glacier environments in steep mountain areas (Hewitt et al., 2008; Hewitt, 2009a; Hewitt et al., 2011). Rock avalanches generate a significant fraction of the sediment delivered through the stream system in steeply

sloped, actively incising orogens (Burbank et al., 1996; Antinao & Gosse, 2009; Korup et al., 2010; Penna et al., 2015). They control valley evolution by creating rockslide dams, which impound lakes that reduce stream incision and increase sediment storage (Hewitt, 1998; Evans et al., 2011; Hermanns et al., 2011c), and in cases of supraglacial deposition, they alter the mass balance and dynamics of glaciers (Hewitt et al., 2008; Hewitt, 2009a; Hewitt et al., 2011; Shugar et al., 2012). Furthermore, large rock-slope failures significantly contribute to glacial trough widening (Jarman, 2009) in glacially formed and oversteepened valleys. The complex interaction of the different land forming processes can cause complex deposits and landforms that are difficult to interpret. This often impedes the understanding of the spatial and temporal distribution of rock-slope failures. However, knowledge of previous events provides implications that are important for a reliable hazard assessment of a specific region.

The identification and interpretation of complex deposits associated with rock-slope failures (e.g., rock avalanches) is an issue to overcome, especially in glacial and paraglacial alpine environments. The dynamic interaction between rock avalanches and glaciers is remarkable and causes distinct geomorphological and sedimentological characteristics and landforms. Supraglacial processes modify the sedimentology of rock-avalanche deposits that fell onto the glacier (Hewitt, 2009b; Shulmeister et al., 2009; Shugar & Clague, 2011), subsequent glacial overrunning deforms previous rock-avalanche deposits (Cook et al., 2013), and glacial advance induced by the supraglacial debris of rock avalanches influences the moraine formation (Deline, 2009; Reznichenko et al., 2011). Hence, the deposits complexity that is caused by common diamiction of glacial and rock-avalanche deposits, makes it difficult to distinguish between the different processes, particularly if the rock avalanche fell onto the glacier (Evenson et al., 2009) or runs over it and continues into ice-free terrain and entrains moraine material (Gosse & Evenson, 1994; Hermanns et al., 2014b). In alpine environments this has led to misinterpretations of landforms as moraine deposits that are indeed associated to rock-slope failures (Hewitt et al., 2011; Ostermann et al., 2012).

1.1.3 Dynamics and geomorphology of rock avalanches

As stated above, rock avalanches are typical catastrophic landslides from massive rock-slope failures (Evans et al., 2006b) and describe their post-failure stage. They are characterized by relatively large process volumes and flow type dynamics (Heim, 1932; Hutchinson, 1988; Hungr et al., 2001) and show high mobility with high velocities and long runout distances (Erismann & Abele, 2001; Legros, 2002; Pudasaini & Miller, 2013). The high mobility of rock avalanches and the corresponding large runout extent state difficulties for realistic hazard assessment of future events. The runout dynamics is highly dependent on the process volume, the topography of the runout area and the substrate along the travel path. Besides, various processes are discussed to explain the increased mobility and long runout distances of rock avalanches. These concern either the propagating rock mass or its interaction with the substrate along the travel path, including for instance, dynamic fragmentation, acoustic and mechanical fluidization, frictional heating, material entrainment, and lubrication by air or water (Abele, 1974; Abele, 1991; Erismann & Abele, 2001; Legros, 2002; Hungr & Evans, 2004; Geertsema et al., 2006; Hungr, 2006; McSaveney & Davies,

2006; Crosta et al., 2007; Hewitt et al., 2008; Crosta et al., 2009; Davies & McSaveney, 2009; Bowman et al., 2012; Pudasaini & Miller, 2013). Furthermore, with special regard to the substrate along the travel path, rock-avalanche mobility is increased by propagation over low frictional and water rich substrates such as glacial-ice bodies (Pirulli, 2009; Sosio et al., 2012; De Blasio, 2014; Delaney & Evans, 2014) or highly water saturated alluvial sediments (Abele, 1974; Erismann & Abele, 2001; Poschinger, 2002; Poschinger et al., 2006).

In general, rock-avalanche deposits show typical characteristics such as a carapace composed of large rock boulders with high angularity and meter to several tens of meters in diameter (Hewitt, 2009a) and geomorphological structures which indicate the high mobility, such as frontal rims, lateral levees, parallel ridges, or even a runup on the opposite slope (Evans et al., 1989; Erismann & Abele, 2001; Poschinger, 2002; Dufresne & Davies, 2009). However, the distribution of deposits and the geomorphological structures depend on the runout dynamics that include the interaction of propagating rock mass with landforms and substrates, and the complex emplacement histories. As described previously, these interactions can form complex deposits that could be complicated to identify and interpret to be of rock-avalanche origin. Such complex deposits can be formed, for instance, by rock-avalanche propagation onto a glacier with associated supraglacial modification, re-transportation and re-sedimentation of the material (Hewitt, 2009b; Shulmeister et al., 2009; Shugar & Clague, 2011). The propagation onto water saturated sediments can cause extended runout due to the effects of undrained loading or triggered secondary debris flows (Abele, 1991; Poschinger, 2002; Poschinger & Kippel, 2009). The direct impact into water bodies causes large displacement waves (Blikra et al., 2002; Blikra et al., 2005) and probably can induce surfing of the propagating mass (Mazzanti & De Blasio, 2011; Mazzanti & De Blasio, 2013). However, the final deposition below the water level hinders direct investigation of deposits and limits knowledge to bathymetric and seismic data. Nevertheless, although of complexities, it is necessary to study the deposits of previous events in order to understand post failure dynamics of rock-slope failures (Strom, 2006). Especially such complex deposits could show distinct characteristics and geomorphological structures that will improve their identification and the interpretation of their origin.

1.1.4 Kinematics and geomorphology of rock-slope instabilities

In general, besides the topography, the tectonics and the geology strongly control the spatial distribution and the type of mass movements (Hutchinson, 1988). Especially the kinematics and deformation mechanisms of large rock-slope failures are often linked to and show significant dependence on preexisting and inherited geological structures and discontinuities of various origin as, for instance, bedding, joint sets, foliation, exfoliation, and tectonic faults and folds (Dramis & Sorriso-Valvo, 1994; Bovis & Evans, 1996; Agliardi et al., 2001; Braathen et al., 2004; Saintot et al., 2011b; Agliardi et al., 2013; Bianchi Fasani et al., 2014). Rock-slope failures exhibit various types of deformation mechanisms during their pre-failure and failure stage (i.e., rock-slope instability), ranging from rather simple to more complex deformations. These are mainly based or composed of one or more of the basic kinematic types of failure such as planar sliding, wedge sliding, and direct and flexural toppling (Turner

& Schuster, 1996; Erismann & Abele, 2001; Wyllie & Mah, 2004). Thereby, typical structural features that delimit a failure block and that are necessary to cause a rock-slope failure are a distinct back-fracture, transfer faults (i.e., lateral release surfaces), and a basal sliding or shear plane (Henderson & Saintot, 2011). Moreover, especially the so called deep seated gravitational slope deformations (DSGSD) that are defined as large mass movements with small displacements, irrespective of the presence of a major sliding plane, often exhibit more complex kinematics and deformation mechanisms (Dramis & Sorriso-Valvo, 1994; Agliardi et al., 2001; Agliardi et al., 2009b; Agliardi et al., 2012; Chigira et al., 2013; Crosta et al., 2013). However, the definition is based on surface observations of geomorphological features, and various terms have been used to describe the phenomena of those large rock-slope instabilities including rockslides, rock slumps, lateral spreads, rock creep, rock flow and “Sackung” (sagging) (Radbruch-Hall et al., 1976; Varnes, 1978; Hutchinson, 1988) (Zischinsky, 1969a; Zischinsky, 1969b; Hungr et al., 2014). The term “Sackung” also includes the special types of “Talzuschub” and “Bergzerreißung” (Ampferer, 1939; Stini, 1941; Zischinsky, 1969a). As a general definition, a DSGSD is summarized as a large, non-catastrophic, long-lasting mass movement that can be identified by various characteristics and diagnostic surface deformation features (Dramis & Sorriso-Valvo, 1994; Agliardi et al., 2001; Agliardi et al., 2012).

These large slope deformations are common in high mountain ranges throughout the world. They further show distinct characteristic geomorphological features such as a back scarp, double ridges, coherent slide blocks, tension cracks, counterscarps (uphill-facing scarp), grabens, collapsed block fields, slope bulging and irregular slope topography (Zischinsky, 1969b; Bovis & Evans, 1996; Gutiérrez-Santolalla et al., 2005; Agliardi et al., 2009a; Reitner & Linner, 2009; Crosta et al., 2013; Jomard et al., 2014). These characteristics are linked to the deformation mechanisms and enable the interpretation of subsurface processes. However, linear morphostructures along slopes in high mountain terrain that form km-long linear features or swarms of smaller linear features, such as uphill or downhill-facing scarps, are often not clearly understood. These structures are often discussed to be caused by either tectonic faulting or gravitational slope deformation and sometimes need reinterpretation because of newly obtained data (Thompson et al., 1997; Hippolyte et al., 2006; Agliardi et al., 2009b; Li et al., 2010). Therefore, detailed geomorphological analyses are the main key to understand the complex processes and evolution of a DSGSD and its morpho-tectonic control.

1.1.5 Spatial and temporal distribution of rock-slope failures

The spatial and temporal distribution of rock-slope failures are often linked to more regional and even global effects such as tectonic activity (e.g., earthquakes), meteoric events (e.g., intense precipitation), climatic events (e.g., glaciations), and the complex history of quaternary landscape evolution. Spatial cluster of rock-slope failures can be observed along major tectonic features (Hermanns & Strecker, 1999; Ambrosi & Crosta, 2006; Agliardi et al., 2009a). Tectonic activity can cause fault structures and damaged zones that state distinct regional weakness zones in the bedrock (Brideau et al., 2009). Catastrophic seismic events

such as large earthquakes and associated ground motion can trigger large rock-slope failures (Jibson et al., 2006; Dunning et al., 2007). Especially the neotectonic activity (Hermanns et al., 2001; Blikra et al., 2002; Galadini, 2006; Hermanns et al., 2006b; Penna et al., 2011) and active tectonic deformations (Osmundsen et al., 2009; Gori et al., 2014) are proposed to condition rock-slope failures and therefore to cause not only spatial but also temporal clusters.

The regional landscape evolution, often showing a complex history including orogenesis, valley incision and glaciation, favor the distribution of rock-slope failures. The inherited stresses and the stress release might weaken the bedrock, and erosion can form steep valley slopes that increase susceptibility for rock-slope failures. Progressive failure within the rock slope and fatigue of rock bridges through time are proposed to be the main deformation and failure mechanism (Bjerrum, 1967; Eberhardt et al., 2004; Hermanns et al., 2012b). Accelerated decompression of the rock slope due to previous rock-slope failures increases the probability for future failure (Hermanns et al., 2006a). Moreover, clusters of rock avalanches in high mountain areas can often be linked to paraglacial environments and the processes of glacial debuttressing (Evans & Clague, 1994; Holm et al., 2004; Jarman, 2006; Cossart et al., 2008; Agliardi et al., 2009a; Crosta et al., 2013) and the decay of the permafrost within the steep rock slopes (Fischer et al., 2006; Fischer et al., 2012; Krautblatter et al., 2013; Lebrouc et al., 2013; Blikra & Christiansen, 2014). Therefore, the distribution of rock-slope failures in steep mountain terrain is dependent on various processes that could be linked by complex interaction.

1.1.6 Integrative investigations of rock-slope failures

Detailed understanding of the complex processes of rock-slope failures and associated catastrophic landslides, at least from pre-failure to post-failure stage, are required for a reliable hazard assessment. This includes the kinematics, the deformation pattern and the stability of the rock-slope instability, the trigger, the recurrence times, the runout dynamics and the impact of the catastrophic landslide (e.g., rock avalanche). This specific knowledge can be increased by detailed studies following an integrative attempt by using various techniques including, for instance, field methods, remote sensing, surface dating and numerical modeling. Studies might focus either on currently active processes (e.g., rock-slope instabilities) and their geological and geomorphological characteristics, kinematics, slope stability and slope deformation (Willenberg et al., 2008a; Blikra, 2012; Böhme et al., 2013; Booth et al., 2014), or on past events (e.g., rock avalanches) and their geomorphological characteristics, (paleo)dynamics and spatial and temporal distribution (Hermanns et al., 2006a; Welkner et al., 2010). Especially the geomorphological investigation of past rock avalanches is important to understand the post-failure behavior (Strom, 2006) and the spatial and temporal pattern (Blikra et al., 2006) of which both provide important implications for hazard assessment. Integrative studies combine field investigations such as geomorphological and geomechanical mapping with more advanced investigation and monitoring techniques.

Remote sensing data (airborne and terrestrial laser scanning, photogrammetry and differential global navigation satellite system) and the thereby derived digital elevation models can be used to support and improve geomorphological and geomechanical mapping in order to characterize the kinematics and to monitor the deformations of rock-slope failures (Oppikofer et al., 2009; Oppikofer et al., 2011; Oppikofer et al., 2012b; Yugsi Molina et al., 2012; Booth et al., 2013; Wolter et al., 2014). Especially laser scanning using the light detection and ranging (LiDAR) technique is well applied for landslide investigation (Jaboyedoff et al., 2012; Abellán et al., 2014) and a powerful tool to study inaccessible slopes such as high and steep rock cliffs in remote areas.

Numerical two- and three-dimensional modeling can be applied to study all failure stages of rock-slope failures (i.e., from pre- to post-failure). Different principles and theories for numerical models are applied accordingly such as, for instance, finite element, finite difference, discrete element, and particle flow dynamics. These methods can be used to study either the kinematics, stability and deformation of current rock-slope instabilities such as a DSGSD (Stead et al., 2001; Crosta et al., 2003; Eberhardt et al., 2003; Eberhardt et al., 2004; Hürlimann et al., 2006; Stead et al., 2006; Bachmann et al., 2009; Gischig et al., 2011), or the post-failure runout dynamics of the failed rock mass such as a rock avalanche (Hungr & Evans, 1996; McDougall & Hungr, 2004; Hungr, 2006; Poisel et al., 2008; Sosio et al., 2008; Crosta et al., 2009; Pedrazzini et al., 2012; Sosio et al., 2012; Delaney & Evans, 2014).

Surface-exposure dating techniques can be applied to rock-avalanche deposits in order to determine the age of deposition, which usually (i.e., non-disturbed sedimentation) represents the age of rock-avalanche occurrence. The derived temporal distribution of rock-slope failures enables to correlate the events with regional triggers such as climatic changes and to assess recurrence times. These ages further can be used to distinguish different deposits and processes, and to support the interpretation of the valley development. Relative ages can be determined, for instance, by using Schmidt-hammer tests by correlating the compressive strength of a rock surface with the surface weathering during the exposure time (Shakesby et al., 2004; Aa et al., 2007; Shakesby et al., 2011). More advanced techniques such as terrestrial in situ-produced cosmogenic nuclide (TCN) surface-exposure dating enable to determine absolute ages, and are widely used in Quaternary science for dating mass wasting deposits (Gosse & Phillips, 2001). It is usually applied in landslide research to determine the age of deposits and hence the past failures (Ballantyne et al., 1998; Hermanns et al., 2001; Hermanns et al., 2004; El Bedoui et al., 2009; Hippolyte et al., 2009; Ivy-Ochs et al., 2009; Blais-Stevens et al., 2011; Ballantyne et al., 2014; Sturzenegger et al., 2014). More recently, this technique is also applied to determine the exposure ages along sliding surfaces (Hermanns et al., 2012c; Hermanns et al., 2013c) in order to assess the long term deformations and the slip rates of large rock-slope failures.

1.2 Study area

The research work presented in this thesis focuses on large rock-slope failures in two valleys in Norway. The study areas of both, the Innerdalen Valley and Innfjorddalen Valley, are located in Møre og Romsdal County in western Norway (Fig. 1.1). The topography of this county is generally characterized by an alpine relief. Strong elevation differences occur within short distances, ranging from sea level at the coast and in the fjord areas up to around 2 400 m a.s.l. at the highest summits. Close to both study areas, the highest elevations reach around 1 900 m a.s.l. Typical geomorphological forms of this area are U-type shaped valleys with oversteepened slopes and deep fjords. Chapter 2 of this thesis focuses on the multiple rock-slope failures in the valley of Innerdalen (i.e., preserved rock-avalanche deposits), and Chapter 3 and 4 focus on those within Innfjorddalen Valley (i.e., either the preserved rock-avalanche deposits, or an active rock-slope instability).

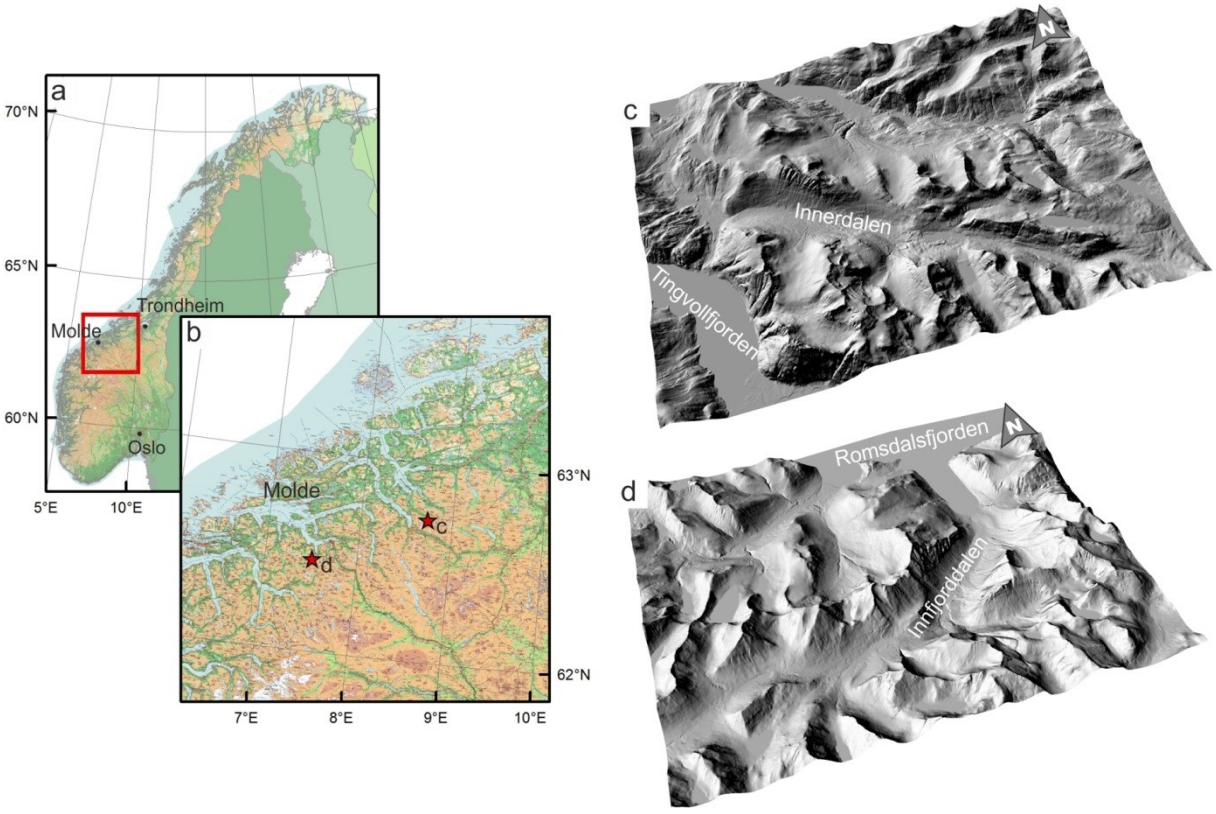

Fig. 1.1: Geographic overview of Norway and the study areas. (a) Topographic overview map of Norway, red rectangle marks inset of (b). (b) Map of western Norway showing the location of the study areas (red stars). Additionally shown are oblique 3D views of the hillshaded digital elevation models for (c) Innerdalen and (d) Innfjorddalen with adjacent areas representing the local topography. The area shown in (c) is around 20 km long and 17 km wide, and elevations range from sea level to 1 780 m a.s.l. For (d) it is around 27 km long and 20 km wide, with elevations ranging between sea level and 1 875 m a.s.l.

1.3 Geology of Norway

1.3.1 Basement geology and tectonics

1.3.1.1 Regional overview

The geology of Norway spans a very long history. The basement shows a large variety of mainly Precambrian and lower Paleozoic rocks, and the today's topography has chiefly developed during Quaternary times (Ramberg et al., 2008). The bedrock in Norway can be distinguished and described by several simplified geological units as marked in Fig. 1.2. The oldest rocks are autochthonous rocks in the Precambrian basement and can be found in northern and southern Norway. In northeast Norway (A') these are igneous and supracrustal rocks of Archaen (3 200–2 500 Ma) and Proterozoic age (2 500–1 950 Ma, Svecokarelian), whereas in southern Norway (A) these are slightly younger Proterozoic igneous and supracrustal rocks (1 700–900 Ma, Gothian and Sveconorwegian). The central and western part of Norway, stretching from southwest to northeast along the entire country, is mainly characterized by igneous and metamorphic Precambrian and lower Paleozoic rocks affected by the Caledonian orogeny (Table 1.1). These are several allochthonous Caledonian nappes (C1, C2 and C3), and the basement windows (B) of Proterozoic igneous and supracrustal rocks (1 700–900 Ma, Gothian and Sveconorwegian) that are varyingly affected by the Caledonian deformation. Some sedimentary rocks of a Late Silurian to Devonian sediment basin (D) that are not associated with the Caledonian Orogen can also be found in western Norway. Additionally, Permian-Carboniferous volcanic and plutonic rocks of the Oslo Rift (E) are exposed in southeast Norway. Besides the basement rocks of the continental landmass, the Norwegian shelf is mainly composed of sedimentary rocks such as sandstone, mudstone, limestone, and carboniferous rocks of Mesozoic (F) and Cenozoic (G) age. (Solli & Nordgulen, 2006; Fossen et al., 2008b; Nordgulen & Andresen, 2008)

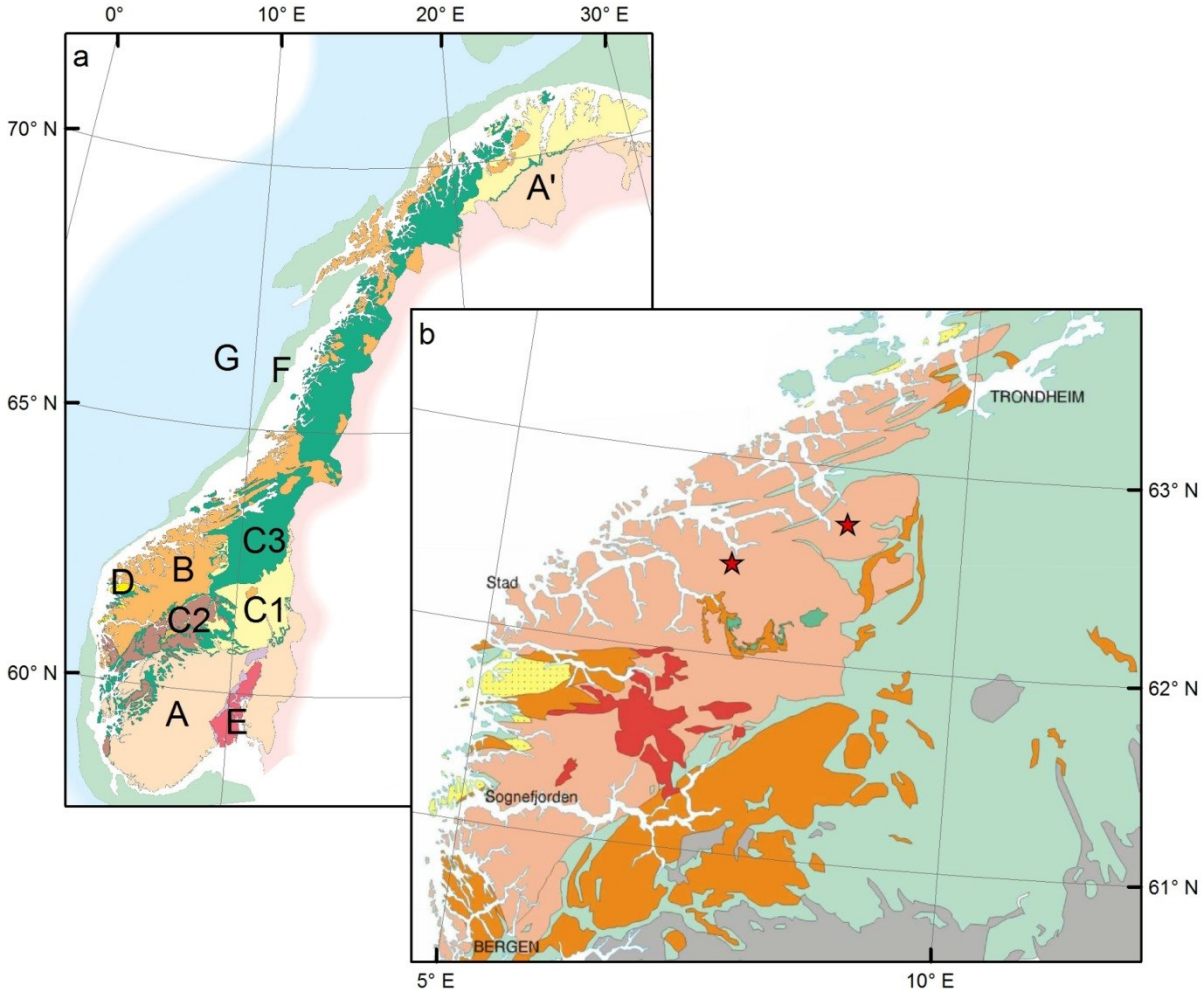

Fig. 1.2: Geological overview of Norway and the Western Gneiss Region (WGR). (a) Map of whole Norway, showing the main geological units, labeled A to G as described in the text and Table 1.1 (modified according to NGU, 2011). (b) Map of the WGR, showing general distribution of the gneisses (apricot) and the granites (red) of the Precambrian basement, the various Caledonian nappes (green and orange), and the Devonian rocks (yellow) (modified according to Nordgulen & Andresen, 2008). The study areas of Innderdalen and Innfjorddalen are indicated by red stars.

Table 1.1: Simplified tectonostratigraphy of the Norwegian Caledonides (combined by data from Solli & Nordgulen, 2006 and Fossen et al., 2008b). For spatial extent of the units, refer to Fig. 1.2.

	Unit	Origin	Age
Caledonian rocks	Uppermost allochthon	Granites, schists and volcanic rocks of exotic origin	Neoproterozoic–Ordovician
	Upper allochthon (C3)	Greenstones, gabbros and mica schists from the Iapetus ocean	Neoproterozoic–Silurian
	Middle allochthon (C2)	Basement nappes of Baltic origin	Mesoproterozoic–Cambrian
	Lower allochthon (C1)	Sandstones, phyllites and mica schists from the periphery of the Baltic basement	Mesoproterozoic–Palaeozoic
	Parautochthon (B)	Basement (igneous and supracrustal rocks) variably affected by the orogeny	Proterozoic (1700–900 Ma)
	Autochthon (A)	Basement (igneous and supracrustal rocks) mainly unaffected by the orogeny	Proterozoic (2500–900 Ma) Archaen (3200–2500 Ma)

1.3.1.2 Western Gneiss Region

The study areas are located in western Norway (Fig. 1.2), in the so-called Western Gneiss Region (WGR). This region is mainly composed of Precambrian and Lower Paleozoic metamorphic rocks, partly overlain by continental and oceanic allochthons that have been strongly affected and intensely reworked (i.e., deformed, metamorphosed and juxtaposed) by the Caledonian orogeny. The most important processes occurred during the so called Scandian orogeny, which is the main phase of the Caledonian orogeny (mainly Silurian to Early Devonian). The former Iapetus Ocean was closed and the allochthons were emplaced onto Baltica. The collision between Baltica and Laurentia causes the westward subduction of the Baltican basement and parts of the allochthons into ultrahigh pressure depth, and a bulk crustal shortening with general NW – SE orientation. The basement was exhumed to shallow crustal levels. The ascertained thrust transportation (ductile to brittle-ductile domain) of pre-Caledonian rocks toward SE onto the Precambrian basement of Baltica formed the Caledonian nappes (Fig. 1.2). The Precambrian basement rocks of western Baltica underwent high-grade metamorphism because of downward force into great depth during the orogeny. The tectonostratigraphy of the Norwegian Caledonides is summarized in Table 1.1. (Roberts & Gee, 1985; Roberts, 2003; Fossen et al., 2008b; Nordgulen & Andresen, 2008; Hacker et al., 2010; Corfu et al., 2014)

The Late- to Post-Caledonian extension or a transtensional system, the so-called Caledonian collapse (Devonian), led to a significant exhumation of the WGR and to the development of basement windows of the metamorphosed Precambrian (i.e., Proterozoic igneous and supracrustal) rocks. (Fossen, 2000; Roberts, 2003; Fossen et al., 2008a)

Besides metamorphism, the bedrock of western Norway was also significantly affected by tectonic stresses during several tectonic events. These are the ductile tectonics during the Caledonian orogeny, semi-ductile tectonics during the syn- or post-orogenic collapse, and additional intense brittle tectonics such as the Permo-Triassic and the Jurassic rifting phases and the opening of the North Atlantic Ocean. (Fossen, 2000; Mosar et al., 2002; Valle et al., 2002; Mosar, 2003; Ramberg et al., 2008; Saintot et al., 2011b)

Therefore, a large number of various tectonic structures with high density, such as folds and faults, have developed in the basement of the WGR that are associated to these different tectonic phases. The tectonized rocks were brought to the surface by the intense uplift of the Norwegian landmass. However, the tectonic phases show lack of stratigraphic record onshore western Norway and the major faults associated with the brittle tectonics are still not identified accurately. (Gabrielsen et al., 2002; Saintot et al., 2011b)

Since the Caledonian orogeny the Norwegian landmass (i.e., the Caledonian mountain chain) generally was generally only prone to erosional processes. No sedimentary basins developed except the rather small Devonian basin in the western part of the WGR. During the Cretaceous, the Norwegian landmass was a relatively flat lowland or even a peneplain. However, today's topography shows a long mountain chain (the so-called Scandes) with a high relief and deep valleys. This landscape development is mainly correlated to an intense uplift of the Norwegian landmass that is still ongoing and erosional processes during the Quaternary. The Norwegian mainland is proposed to have begun to rise during the Paleogene and that several uplift periods occurred during the Cenozoic. This significant uplift is correlated with the opening of the North Atlantic Ocean, including the Late Jurassic-Tertiary rifting phases and Tertiary sea floor spreading and the production of new oceanic crust. However, this interpretation is still in debate. Anyway, the present-day landscape was shaped by the same drainage river system that was already established in the Cenozoic. Today's current uplift of Norwegian mainland is mainly associated to the isostatic crustal response following the Last Pleistocene glaciation (i.e., post-glacial isostatic rebound). (Martinsen & Nøttvedt, 2008; Ramberg et al., 2008)

As stated above, the origin and causes of the Scandes mountain chain are still debated because of its location in far distance from any plate boundary. Therefore, various models have been proposed including, for instance, rift shoulder uplift, opening of the NE Atlantic, small-scale mantle convection, asthenospheric diapirism, isostatic response to glacial erosion, intraplate stresses, and modification of the Caledonian topography (isostasy-climate-erosion hypothesis). (Pascal & Olesen, 2009)

Concerning the exposed rocks in western Norway, in general, three main geological units can be distinguished in the WGR (Fig. 1.2). These are the Precambrian basement, the Caledonian nappes, and the Devonian sediments. These units show a variety of lithologies and various tectonic lineaments (i.e., faults) as shown in Fig. 1.3 and summarized in Tables 1.2 and 1.3. (Tveten et al., 1998; Gabrielsen et al., 2002; Solli & Nordgulen, 2006; NGU, 2014)

However, the major part of this region is represented by a basement window composed of the parautochthon rocks in the Precambrian basement. These are Proterozoic igneous and supracrustal rocks (1 700–900 Ma, Gothian and Sveconorwegian) that were variably affected by the Caledonian orogeny. This is also the geological unit in which both study areas are located.

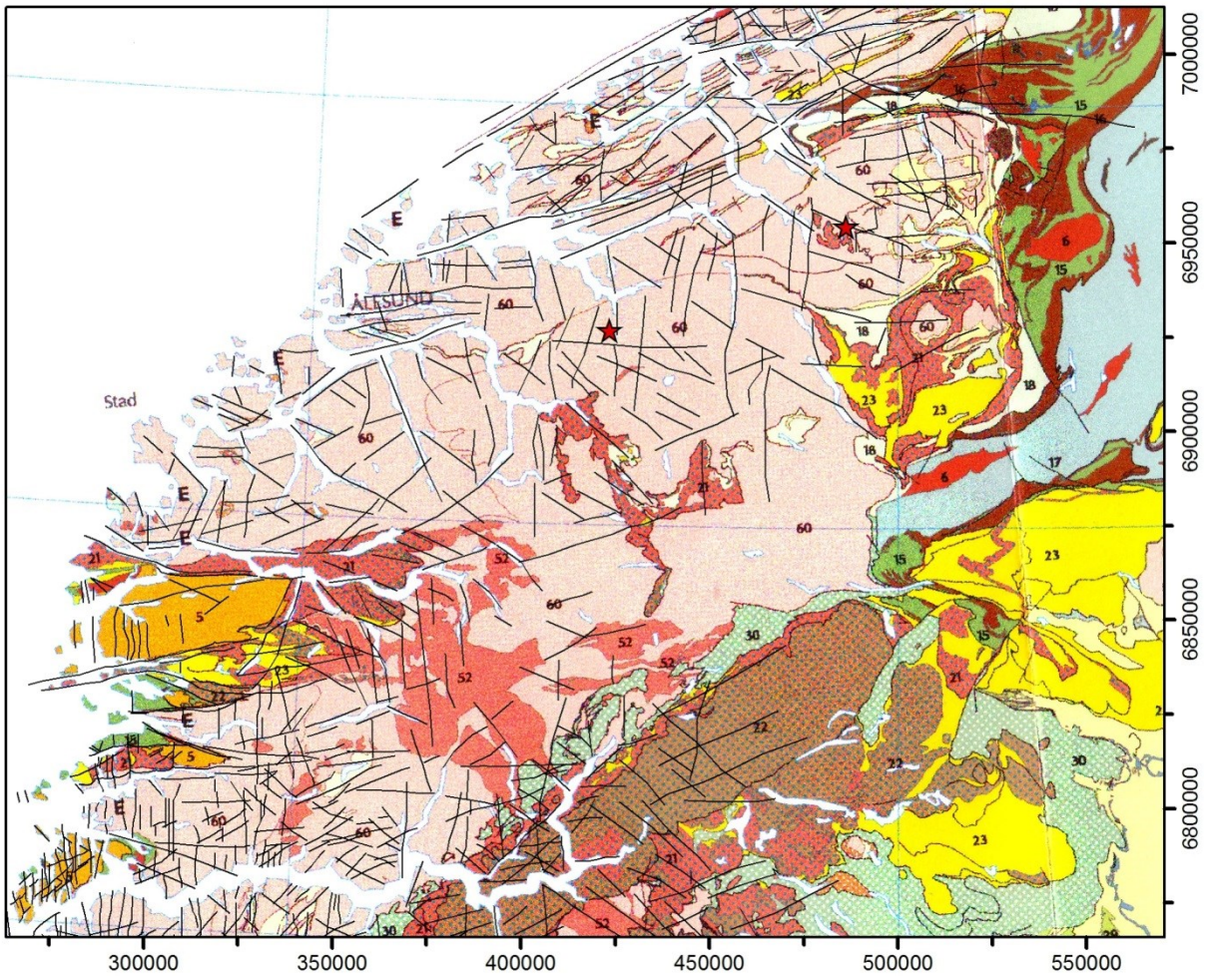

Fig. 1.3: Geological map of the Western Gneiss Region (WGR). The main lithologies are labeled by numbers as presented in Table 1.2 (based on Solli & Nordgulen, 2006). The major tectonic lineaments are shown by black lines and summarized in Table 1.3 (based on Tveten et al., 1998 and Gabrielsen et al., 2002). The study areas are indicated by red stars. (Coordinate system: WGS1984, UTM Zone 32N)

Table 1.2: The main lithologies exposed in the Western Gneiss Region (WGR) as shown and labeled in Fig. 1.3 (based on Solli & Nordgulen, 2006).

Map number	Lithology	Age/Nappe	Unit/rock type
5	Sandstone and conglomerate	Late Silurian to Devonian	Sedimentary rocks (D)
6	Granite, granodiorite, tonalite, monzonite	500–425 Ma	Plutonic rocks
15	Mica shist and phyllite	Köli Nappes	Upper allochthon (C3)
16	Greenstone	Köli Nappes	
17	Mica schist, amphibolite, phyllite	Gula Nappe	
18	Mica schist	Seve Nappes	
21	Granite and augen gneiss	Meso- and Neoproterozoic	Middle allochthon (C2)
22	Gabbro diorite, anorthosite	Meso- and Neoproterozoic	
23	Sandstone, shist, quartzite and amphibolite	Neoproterozoic	
30	Mica schist and phyllite	Neoproterozoic to Ordovician	Lower allochthon (C1)
52	Granites and granodiorites	1 000–920 Ma	Parautochthon (B)
60	Granitic to dioritic gneiss, in places migmatitic rocks	1 800–1 500 Ma	

Table 1.3: The major tectonic lineaments in the WGR as shown in Fig. 1.3, and their mean orientations and associations to the different fault complexes (based on Tveten et al., 1998 and Gabrielsen et al., 2002).

Fault complex	Mean orientation
Møre–Trøndelag (MTFC)	ENE – WSW NE – SW NW – SE
Mandal–Ustaoset	N – S
Western Norway	N – S NNE – SSW NNW – SSE
Southern Norway	NE – SW ENE – WSW EENE – WWSW NW – SE WNW – ESE
Oslo Rift	N – S NNE – SSW
Other	E – W

1.3.2 Quaternary glaciations and neotectonics

1.3.2.1 Glaciations

The Quaternary geology of Norway is mainly characterized by several glacial episodes that affected entire Fennoscandia and strongly contributed to landform development. The typical topography of western Norway shows a high mountain relief with coastal islands, deep fjords, lakes and long U-shaped valleys with over-deepened slopes and steep rock faces. (Vorren & Mangerud, 2008; Fredin et al., 2013; Olsen et al., 2013b)

The last glaciation, that is, the Late Weichselian, in the Late Pleistocene, was the most prominent for Fennoscandia. During its maximum around 20 ka ago, which is often referred to as the Last Glacial Maximum (LGM), the ice extent reached the outer part of the continental shelf (Fig. 1.4). However, extent and impact of penultimate and earlier Quaternary glaciations in Fennoscandia is not yet well defined, because the Late Weichselian ice sheet has removed most of the sediments from previous periods. (Sollid & Sørbel, 1979; Andersen & Mangerud, 1989; Olsen et al., 2013c)

After the LGM, western Norway was affected by a deglaciation phase (mainly Bølling-Allerød interstadial), but the innermost fjords were not completely ice free. The glaciers re-advanced and reached extents close to the coast (Fig. 1.4) during the cooling event of the Younger Dryas stadial (YD) around 12.8 to 11.5 ka ago. However, in western and southern Norway, some areas have still been ice free since the LGM. During the YD, valley glaciers developed at the margin of the main ice cap that showed ice thicknesses of around 500 m in western Norway. The glaciers that reached the fjords, which are up to 500 m deep show ice margins at around 800 m a.s.l. However, it is proposed that elevations above around 1 000–1 500 m a.s.l. had been ice free in western Norway during this period and afterwards. (Mangerud et al., 1979; Sollid & Sørbel, 1979; Nesje & Dahl, 1993; Andersen et al., 1995; Olsen et al., 2013c)

The YD was a very short-lived (~1.3×10^3 yr) cooling event compared to the long-lasting (< 1×10^4 yr) LGM glaciation and was preceded and followed by a rapid warming (Andersen & Mangerud, 1989; Wanner et al., 2008; Shakun & Carlson, 2010).

This rapid warming and the concomitant rapid rise of the sea level triggered an accelerated glacial decay and permafrost thawing that caused a rapid change of the ice volume. This effect caused faster rates of lithospheric unloading and a post-glacial isostatic rebound. The fjords and valleys became ice free around 10 ka ago at least. However, many cirque glaciers and one large plateau glacier, the Jostedalsbreen, still exist in western Norway, which retreated since the Little Ice Age (LIA) maximum at around AD 1750. (Nesje & Dahl, 1993; Nesje, 2009; Olsen et al., 2013b; Olsen et al., 2013c)

The today's average regional equilibrium line altitude (ELA) for southern and western Norway is around 1 500 m a.s.l. Glacial deposits indicate a regional trend for an average paleo-ELA showing elevations that were around 1 000 m lower than today during the LGM, around 500 m during the YD, and around 150 m during the LIA, respectively. (Dahl & Nesje, 1992; Lie et al., 2003; Bakke et al., 2005a; Bakke et al., 2005b)

The above mentioned isostatic rebound associated with the glaciations further affected the relative sea level and landscape evolution. Present day distribution of marine sediments at elevations up to 220 m a.s.l. indicate that the landmass in western Norway, formerly located near the shoreline, has risen up several hundred meters since the LGM. The marine limit, which is defined as the highest relative sea level stand following the Pleistocene glaciation, is proposed at a today's elevation of around 120 m a.s.l. for the region of the study areas based on regional modeling. (Hansen et al., 2012; Hansen et al., 2014; NGU, 2015)

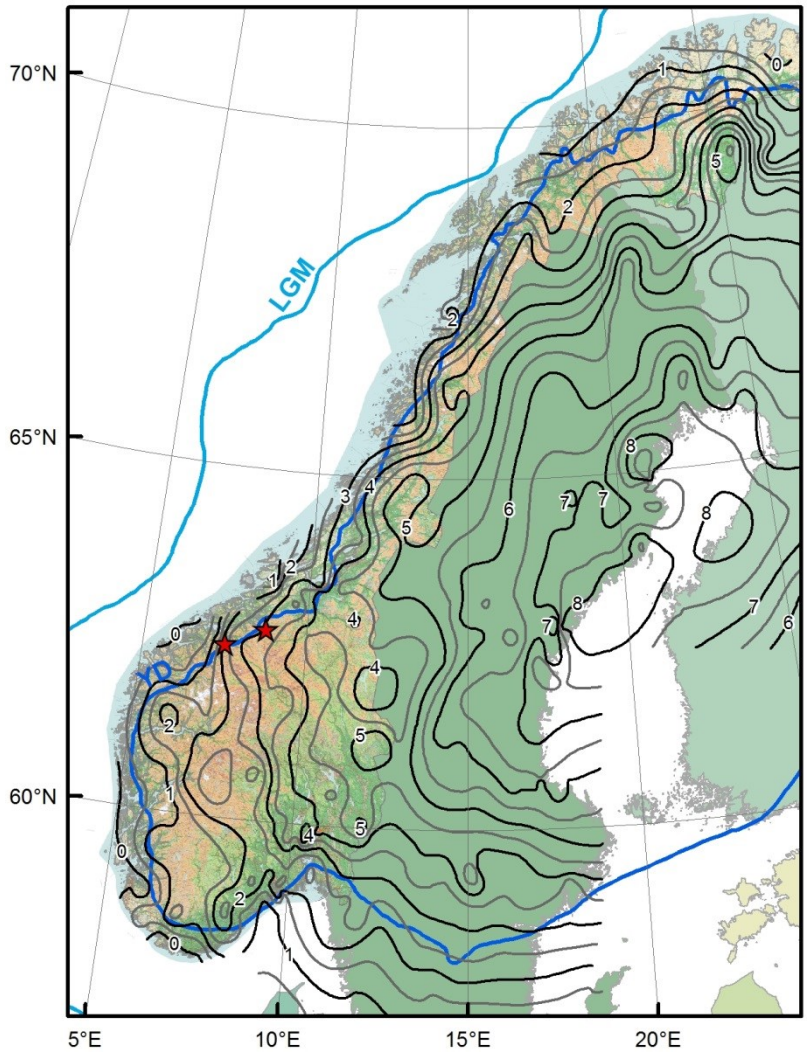

Fig. 1.4: Quaternary overview map of Norway. The ice margins of the Last Glacial Maximum (LGM) and Younger Dryas (YD) glaciations are marked by blue lines (adopted from Olsen et al., 2013c). Additionally, the current apparent uplift rates of Fennoscandia (in mm/yr) are marked by black contours (following Dehls et al., 2000). The study areas are indicated by red stars.

1.3.2.2 Neotectonics

Norway was affected by significant glacial and post-glacial tectonic (i.e., neotectonic) activity. The melting of the ice cap with associated ice volume changes and crustal unloading generated regional post-glacial isostatic rebound of Fennoscandia and triggered various neotectonic activities including large-magnitude earthquakes that occurred directly after the deglaciation and regional and local faulting. (Fjeldskaar et al., 2000; Olesen et al., 2000; Olesen et al., 2004; Olesen et al., 2013)

The dome-like uplift of Fennoscandia is a still ongoing process and shows current apparent uplift rates of up to 8 mm/yr in the Gulf of Bothnia, and up to 5 mm/yr within Norway. With focus on the study areas, the uplift is up to 3 mm/yr (Fig. 1.4). However, during the Holocene, the rebound rate was not constant. It was much higher shortly after the deglaciation showing a maximum of 50–500 mm/yr around 10 ka ago. Besides the post-glacial rebound, also other geodynamic effects are in debate that might contribute to these current uplift rates and to the neotectonic activity of Norway. (Mörner, 1979; Dehls et al., 2000; Fjeldskaar et al., 2000; Olesen et al., 2004; Pascal & Olesen, 2009; Bungum et al., 2010)

Today, the seismic intensity of Norway is low to intermediate and shows a concentration of earthquake activity west of the coast of western Norway. This activity and distribution is in concordance with the location at a rifted passive continental margin. (Bungum et al., 2000; Dehls et al., 2000; Fjeldskaar et al., 2000)

1.4 Rock-slope failures in Norway

Large rock-slope failures are a widespread phenomenon in the steep mountain terrain in Norway and pose a severe natural hazard, especially if the failure occurs as highly destructive rock avalanches. Not only the direct impact but also secondary effects, such as natural damming by landslides and associated flooding, or displacement waves triggered by the impact into water bodies, are high risk scenarios. Because of the topography of Norway, many very steep and high rock slopes that are susceptible for rock-slope failures exist directly above the fjords or large lakes. Several large rock-slope failures and related tsunami waves are recorded in Norway during the last century that caused severe damage and casualties because these waves could propagate over long distances (e.g., tens of kilometers with up to tens of meters high runup waves) and most cities, settlements, industries and infrastructure (i.e., elements at risk) are located close to the shoreline along the fjords (Bjerrum & Jørstad, 1968; Blikra et al., 2005; Furseth, 2006; Hermanns et al., 2014c). Examples include, for instance, the disasters of Loen in AD 1905 and 1936 where several displacement waves triggered by rockslides into a lake killed in total 135 people and Tafjord in AD 1934 where a displacement wave triggered by a rockslide into the fjord killed 40 people and destroyed cities and infrastructure. There are still many large rock-slope instabilities that are actively moving and that pose similar future hazard for the Norwegian fjordlands.

This high hazard potential of rock-slope failures led to increased mapping and research activities conducted mainly by the Geological Survey of Norway (NGU). It is further in the responsibility of the NGU to carry out the hazard and risk assessments for the identified unstable rock slopes (Hermanns et al., 2012b).

1.4.1 Characteristics of rock-slope failures

The large rock-slope failures in the relatively hard gneissic rocks of western Norway are mainly controlled by pre-existing geological structures, that is, discontinuity sets such as foliation, exfoliation, joints and faults. Most of the rock-slope failures generally show relatively simple kinematics of planar or wedge sliding. Further, these pre-existing structures in the hard gneissic rocks are often reactivated by gravitational deformation. (Braathen et al., 2004; Henderson et al., 2006; Oppikofer, 2009; Oppikofer et al., 2011; Saintot et al., 2011b; Saintot et al., 2012)

Typical structural characteristics for rock-slope failures that are necessary to cause failure are a back fracture, transfer faults or lateral release surfaces, and a basal sliding/shear plane (Henderson & Saintot, 2011). Especially the generally well-developed foliation of the gneisses is often involved in rock-slope failures as a basal sliding surface or another main delimiting structure (Saintot et al., 2011b). However, limiting structures such as the basal sliding surface are often complex and composed of several different surfaces that form a rather stepped morphology (Oppikofer et al., 2011). Several simplified basic types which are typical for rock-slope failures in Norway are summarized as (1) rock fall (horizontal lengthening), (2) rock slide (surface parallel lengthening), and (3) complex failure, with either planar or listric fault geometry (both, slope oblique lengthening), following Braathen et al. (2004).

Western Norway shows an increased susceptibility for rock-slope failures due to its geology with the fractured and tectonized bedrock and the topography with its steep alpine relief (Böhme, 2014). The geological history with its various tectonic events formed and exposed the well foliated and heavily fractured bedrock. The Quaternary glaciations with glaciation and deglaciation phases show a strong influence on the landscape development and the topography. Both strongly affect the stability of the rock slopes.

Therefore, important factors that might cause destabilization of rock slopes and favor or even trigger rock-slope failures in western Norway are summarized as follows (non-exhaustive list without importance ranking): (1) Geological history that formed high concentration of pre-existing geological structures; (2) glacial erosion that formed long U-type shaped valleys with oversteepened slopes; (3) glacial isostatic rebound that caused large-magnitude earthquakes after deglaciation and other tectonic activity that might have triggered rock-slope failures; (4) glacial debuttressing that changed internal rock stresses after the sudden unloading; (5) decay of permafrost that lowered the permafrost limit, increased water discharge and increased water pressure in fractures; (6) frost wedging into pre-existing fractures that causes additional stresses, for instance, during a glacial re-advance such as the YD; (7) neotectonic activity such as faulting due to ongoing uplift of Fennoscandia or

various reasons; (8) current climatic conditions including seasonal heavy precipitation, and long frost periods with intense snow melting in spring that cause intensive seasonal freeze-and-thaw cycles and associated frost wedging. (Blikra et al., 2002; Blikra et al., 2006; Saintot et al., 2011b; Böhme, 2014)

1.4.2 Research activity about rock-slope failures

Mapping of rock-slope failures and unstable rock slopes in Norway started in the last decade of the 20th century (Braathen et al., 2004; Blikra et al., 2006). Because of the high susceptibility for large rock-slope failures and the high hazard associated with their catastrophic failure, more systematic mapping and research activity has been carried out by the Geological Survey of Norway (NGU) since then (Hermanns et al., 2011a; Hermanns et al., 2012a). The major aim is to identify and assess all unstable rock slopes that could fail catastrophically in future. The hazard and risk assessments for the identified unstable rock slopes are conducted in the framework of the national mapping project as standard investigations following the working approach presented in Hermanns et al. (2012b) Hermanns et al. (2013b) and Hermanns et al. (2014a).

Up to now, the main focus is drawn on the areas that show the highest density of rock-slope failures in form of either post-glacial slope failures such as rock avalanches or active rock-slope instabilities. These areas are the counties of Møre og Romsdal and Sogn og Fjordane in western Norway, and Troms in northern Norway. Mapping and research activity on large rock-slope failures in Norway is mainly related to the framework of hazard and risk assessment. However, a wide variety of topics are addressed. Generally, the studies can be classified as either regional analyses or more site specific investigations and summarized as follows. (Note that many of the studies presented in the following summary are integrative researches and might cover several topics and methods but are named only once to prevent repetition. The list is not exhaustive and only limited to large rock-slope failures and no other types of mass movements)

Regional studies focus on the mapping of rock-slope failures (past events and unstable rock slopes) to determine spatial and temporal distribution in order to gain implications for susceptibility and hazard assessment. Investigations focus either on western Norway (Bjerrum & Jørstad, 1968; Blikra et al., 2006; Furseth, 2006; Henderson et al., 2006; Henderson & Saintot, 2007; Saintot et al., 2008; Longva et al., 2009; Hermanns et al., 2011b; Saintot et al., 2012; Oppikofer et al., 2013; Böhme, 2014) or northern Norway (Bunkholt et al., 2011; Bunkholt et al., 2012; Bunkholt et al., 2013). Other regional studies show additional focus on the influence of bedrock geology and inherited tectonic structures (Böhme et al., 2011; Henderson & Saintot, 2011; Saintot et al., 2011b) and also neotectonic activity (Blikra et al., 2002) on the spatial distribution of rock-slope failures.

The more local or site specific studies mainly draw attention to large unstable rock slopes with active deformation. Some of the more recent works, focus on hazard assessment and early warning of catastrophic rock-slope failures (Hermanns et al., 2012b; Blikra et al., 2013; Hermanns et al., 2013b; Oppikofer et al., 2014). Others also deal with associated secondary

effects such as natural dams (Hermanns et al., 2013a) or displacement waves in the fjords or lakes (Blikra et al., 2005; Romstad et al., 2009; Eidsvig et al., 2011; Harbitz et al., 2014; Hermanns et al., 2014c). Many of the site specific studies deal with the description and understanding of large unstable rock slopes including the analysis of the failure mechanism (e.g., structural control and kinematics) and the assessment of the displacement rates (i.e., monitoring). These studies often follow an integrative approach using a variety of techniques such as field mapping, remote sensing (LiDAR, dGNSS, InSAR), surface-exposure dating, and numerical modeling (Derron et al., 2005; Hermanns et al., 2006a; Ganerød et al., 2008; Jaboyedoff et al., 2011; Oppikofer et al., 2011; Blikra, 2012; Böhme et al., 2012; Böhme et al., 2013; Booth et al., 2014). However, some other investigations show a more focused attempt. These apply satellite and ground based InSAR (Lauknes, 2010; Lauknes et al., 2010; Henderson et al., 2011; Dehls et al., 2012; Kristensen et al., 2013) and LiDAR (Oppikofer, 2009; Oppikofer et al., 2009; Oppikofer et al., 2012b) for mapping and characterization of rock-slope failures and displacement monitoring. Others focus on a new attempt to use surface-exposure dating with cosmogenic nuclides to assess long term velocities of deformation (Hermanns et al., 2012c; Hermanns et al., 2013c). Some authors deal with numerical modeling and stability analysis (Bhasin & Kaynia, 2004; Kveldsvik, 2008; Kveldsvik et al., 2009; Grøneng, 2010). Others apply additional investigations on subsurface conditions using drill core logging (Saintot et al., 2011a; Oppikofer et al., 2012a; Ganerød, 2013a,2013b). Some focus on the causes and pattern of displacements, for instance, in correlation to seasonal climatic pattern (Nordvik et al., 2010) and permafrost activity (Blikra & Christiansen, 2014). Others emphasize more on the interaction of rock-slope failures and inherited and also active tectonic fault structures (Anda et al., 2002; Osmundsen et al., 2009; Redfield & Osmundsen, 2009; Krieger et al., 2013).

However, although many studies deal with rock-slope failures in Norway, most of them focused on hazard and risk assessment. Few draw attention to pre-historic rock-slope failures that failed catastrophically such as rock avalanches. These studies use mapping and dating of the associated deposits (Blikra et al., 2002; Bøe et al., 2004; Aa et al., 2007; Longva et al., 2009; Fenton et al., 2011; Schleier et al., 2013b) to examine the geomorphological impact and to correlate them with the paleoenvironmental conditions, or apply additional numerical runout modeling to investigate the paleodynamics of rock avalanches (Schleier et al., 2015) in detail.

1.5 Aims and scope of the research study

The research study presented in this doctoral thesis was carried out within the framework of a scientific collaboration between the Geological Survey of Norway (Norges Geologiske Undersøkelse, NGU) and the GeoZentrum Nordbayern (GZN). The project gained great amount of scientific and financial support by the NGU, especially the landslide research group (skred) and the project “Landslide mapping in Møre og Romsdal County” (Project number 309 900).

1.5.1 Thesis objectives

Large rock-slope failures that fail catastrophically such as rock avalanches have first-order controls on landscape evolution and pose high hazard potential in steep mountain environments. However, the identification and interpretation of complex deposits and geomorphological features formed by rock-slope failures are often difficult. Complex interactions with various landscape-forming and geological processes such as erosion, glaciation, isostasy and tectonics affect the dynamics and kinematics of rock-slope failures. The glacially overprinted mountains of western Norway are very prone to large rock-slope failures and enable the study of these processes in such a complex geological setting.

The primary aim of this study is to understand large rock-slope failures and associated phenomena in western Norway, with special regard to the Scandinavian Quaternary geology following the glacial melt-down after the LGM, and to derive implications that can be useful for investigations in other glaciated mountain areas. Therefore, the multiple rock-slope failures in the valleys of Innerdalen and Innfjorddalen were chosen to study their interaction with both, glaciation and isostasy. The focus of the study was drawn to understand the complex processes and not to carry out a detailed hazard assessment. From a more specific point of view, the main objectives of the study are as follows.

(I) Rock-avalanche deposits generally show typical geomorphological features but the deposits can be rather complex dependent on the dynamics and paleoenvironmental conditions. Therefore, deposits are often of uncertain origin. The main objective is to understand the complex deposits and the geomorphological features formed by the multiple rock avalanches in Innerdalen and Innfjorddalen (Chapters 2 and 3) in order to derive the paleodynamics, that is, the runout behavior, of these events and the origin of the deposits.

(II) Rock-slope instabilities show a variety of geomorphological features dependent on their kinematics and deformation mechanisms. However, especially long linear features are often of uncertain origin. The main objective is to understand the geomorphological features, the geological constraints and the deformation pattern of a actively moving large rock-slope instability in Innfjorddalen (Chapter 4) in order to conclude failure kinematics and the origin of such linear features.

To address the above mentioned objectives, the multiple rock-slope failures in the glacial affected valleys of Innerdalen and Innfjorddalen, western Norway, were investigated by an integrative approach using various techniques: (1) Detailed field investigations including geomorphological mapping, granulometric sampling and trenching to determine spatial distribution and characteristics of surface deposits and geomorphological features; (2) remote sensing analyses using orthophotos and digital elevation models derived by airborne and terrestrial laser scanning (LiDAR) to support field mapping by improved identification of large scale geomorphological features; (3) geophysical investigations including geoelectric resistivity tomography and ground penetrating radar (GPR) to support field investigations by subsurface data; (4) geomechanical analyses including structural analyses and kinematic feasibility tests to obtain orientations and characteristics of discontinuity sets and derive probable failure kinematics; (5) periodic differential global navigation satellite system (dGNSS) monitoring to determine mean displacement orientations and velocities; (6) surface-exposure dating using the in-situ terrestrial cosmogenic nuclide Beryllium-10 (TCN with ^{10}Be) to determine the temporal distribution of rock-slope failures and to correlate the events with the Quaternary valley evolution; (7) numerical dynamic runout modeling (backward analyses) using the smoothed particle hydrodynamics (SPH) based code DAN3D to test hypothesis and to confirm interpretations for the paleodynamics of rock avalanches and to derive model configurations useful for future forward analyses.

From a local perspective, this integrative study contributes to the understanding of rock-slope failures in the valleys of Innerdalen and Innfjorddalen, western Norway. It correlates these processes and associated phenomena with the local Quaternary geology, enabling to derive implications for the local landscape evolution. Furthermore, it provides new datasets for spatial and temporal distribution and numerical runout modeling of multiple rock-slope failures in western Norway. These can be useful input data for future studies concerning hazard and risk assessment in this area carried out by the NGU. From a more global perspective, the findings of the study will improve the identification and the interpretation of complex deposits and geomorphological features correlated with large rock-slope failures in other steep mountain ranges throughout the world.

1.5.2 Thesis outline

This doctoral thesis is divided into five main chapters. The chapters two to five contain material and are based on several manuscripts of scientific articles that have been published (Krieger et al., 2013; Schleier et al., 2013a; Schleier et al., 2013b; Schleier et al., 2015), submitted (Schleier et al., 2015, submitted) or are in preparation (Schleier et al., in preparation) for publication. Furthermore, Chapter 4 also contains some findings included in the master thesis of Krieger (2013) that was prepared based on the conducted field investigations and that was co-supervised as part of this doctoral thesis. The detailed references are outlined at the beginning of each single chapter.

Chapter 1 comprises this general introduction, including short summaries of: (1) The scientific background according to the investigation of large rock-slope failures; (2) the location of the study area and the geological background of Norway; (3) the research activities on large rock-slope failures in Norway.

Chapter 2 focuses on the multiple rock-slope failures (i.e., rock avalanches) in Innerdalen Valley and its implications for the paleodynamics. This includes: (1) The spatial and temporal distribution, and characteristics of multiple rock-avalanche deposits; (2) the geological characteristics and kinematics of the associated rock-slope failures; (3) the runout analyses of rock avalanches under different conditions such as propagation onto a valley glacier or into an ice-free valley.

Chapter 3 focuses on multiple rock-slope failures (i.e., rock avalanches) in Innfjorddalen Valley and its implications for the paleodynamics. This includes: (1) The spatial and temporal distribution, and characteristics of multiple rock-avalanche deposits; (2) the geological characteristics and kinematics of the associated rock-slope failures; (3) the runout analyses of rock avalanches under different conditions such as propagation into the water body of the fjord or onto previous rock-avalanche deposits.

Chapter 4 focuses on the rock-slope failure (i.e., rock-slope instability) of Middagstinden Mountain in Innfjorddalen Valley and its implications for the kinematics and deformation mechanisms. This includes: (1) The geological characteristics and geomorphological features along the slope; (2) the displacements and kinematics of the slope deformation including the influence of pre-existing geological structures on the deformation mechanisms; (3) the origin of the linear geomorphological features that might be either tectonic or gravitational.

Chapter 5 presents a summary of the general conclusions in addition to the specific conclusions that are included within the individual chapters.

Finally, this doctoral thesis is completed by a complemented list of references.

2 Paleodynamics of multiple rock avalanches in Innerdalen: supraglacial rock avalanching onto a Late Pleistocene ice body

This chapter is based on the manuscripts Schleier et al. (2013b) and Schleier et al. (2015).

Schleier, M., Hermanns, R.L. & Rohn, J. (2013b). Spatial distribution of rockslide deposits and their morphological features suggest timing and palaeo-environmental conditions for rock slope failures in Innerdalen and Innfjorddalen, Møre og Romsdal county, western Norway. *In:* R. Genevois & A. Prestininzi (Eds.), International Conference on Vajont – 1963-2013 – Thoughts and analyses after 50 years since the catastrophic landslide, Padua, Italy, 8-10. October 2013. *Italian Journal of Engineering Geology and Environment*, Book Series (6): 493-505.

Schleier, M., Hermanns, R.L., Rohn, J. & Gosse, J. (2015). Diagnostic characteristics and paleodynamics of supraglacial rock avalanches, Innerdalen, Western Norway. *Geomorphology*, 245: 23-39.

2.1 Abstract

Misinterpretation of rock-avalanche deposits in mountain environments is not uncommon because of the complex interactions between rock avalanches and glaciers. This study for the first time presents a detailed description of suspicious rock-boulder deposits, which are remnants of a rock avalanche onto a Late Pleistocene glacier. The boulder deposits cover around 1.1 km^2 and are distributed over an area of around 7.5 km^2 and a variety of landforms: three closely nested distinct terminal moraines (0.45 km^2) and dislocated terminal moraines (0.34 km^2) entirely built up of large boulders, lateral moraines that decrease in elevation over a short distance and connect to the terminal moraines, small patches (0.02 km^2) of boulders that occur in islands on a peat-dominated valley floor, and large patches of boulder fields (0.25 km^2 in size) hanging 350 m above the valley floor. The latter are disconnected from any potential source area. ^{10}Be cosmogenic nuclide ages of the three terminal moraines give an indistinguishable Late Pleistocene age of 13.6 ± 1.4 ka, whereas the largest boulder field that is located on the opposite side of the valley from the failed mountain yield a ^{10}Be age of 14.1 ± 0.4 ka which is slightly older but indistinguishable from the moraine deposits within uncertainty margins. All boulder deposits add up to a volume of 31 × 10^6 m^3. The interpretation of a single rock-avalanche source for those landforms is further confirmed by numerical runout modeling using DAN3D. A failure of the entire volume

from Skarfjellet Mountain would result in a runout pattern that is identical to that of the distributed boulder fields when considering that the valley was filled with a glacier around 350 m thick. The rock avalanche would not reach the position of the terminal moraines, however, a glacial re-advance could have transported the boulders to that position. The Late Pleistocene rock avalanche was followed by a Holocene rock avalanche with a volume of 23×10^6 m^3 and a typical lobate deposit damming the Innerdalen Valley and creating a lake. ^{10}Be ages indicate that this event occurred 7.97 ± 0.94 ka ago. Structural measurements performed on high-resolution LiDAR scans show a strongly jointed source rock with three joint sets with dip/dip direction 81°/034° ± 12°, 86°/331° ± 10°, and 77°/354° ± 11° and a foliation with 22°/003° ± 15°. The kinematic of the failures can thus be a combination of small-scale wedge failures and planar sliding on shallow dipping foliation. Our detailed description can enable a better identification and interpretation of similar deposits in other mountain areas.

2.2 Introduction

Rock avalanches, that is, large volumes of fragmented rock mass propagating as highly mobile flows (Heim, 1932; Hutchinson, 1988; Hungr et al., 2001), have on an interglacial time scale first-order controls on landscape evolution in fluvial and alpine glacier environments. They are among the most destructive types of landslides because of the high release of energy, an excessive runout length, and secondary effects such as displacement waves and damming (Heim, 1932; Crosta et al., 2004; Evans et al., 2006b; Evans et al., 2009a; Evans et al., 2009b; Evans et al., 2011; Hermanns & Longva, 2012). In steeply sloped, actively incising orogens, rock avalanches may generate a significant fraction of the sediment delivered through the stream system (Burbank et al., 1996; Antinao & Gosse, 2009; Korup et al., 2010). Rock avalanches control valley evolution by creating dammed lakes that reduce stream incision and increase sediment storage, and in the common case of supraglacial deposition, they alter the mass balance and dynamics of glaciers (Hewitt et al., 2008; Hewitt, 2009a; Hewitt et al., 2011).

In high-latitude glacially oversteepened regions such as western Norway, such rock failures and subsequent displacement waves are widespread hazardous processes that generate significant risk in populated fjords (Braathen et al., 2004; Blikra et al., 2005; Blikra et al., 2006; Longva et al., 2009; Böhme et al., 2011). Recent improvement in our understanding of the complex relations between melting glaciers or thawing permafrost and rock-slope failure (Cossart et al., 2008; Fischer et al., 2013; Krautblatter et al., 2013; Lebrouc et al., 2013; Ballantyne et al., 2014; Blikra & Christiansen, 2014) has further illustrated the difficulties in assessing future risk associated with rock avalanches. This has led to increased systematic mapping activities in Norway (Hermanns et al., 2011a; Hermanns et al., 2012a) to establish the spatial and temporal variability in rates, recurrence intervals, style of rock avalanches and factors that control them.

However, the recognition of the co-influence of glaciers and slope failures in the Quaternary and Holocene geological record is complicated. Rock-avalanche dynamics is increased by

propagation over low friction glacial surfaces (Pirulli, 2009; Sosio et al., 2012; De Blasio, 2014; Delaney & Evans, 2014). Glacial dynamics is affected by rock-avalanche debris cover because it reduces melting and induces glacial advance (Deline, 2009; Reznichenko et al., 2011). Glacial and landslide deposits are often diamictons, which makes them difficult to distinguish in many alpine environments, particularly if a landslide fell onto a glacier (Evenson et al., 2009). This has led to misinterpretations of landforms associated with rock-slope failures as moraine deposits (Hewitt et al., 2011; Ostermann et al., 2012). It is even more difficult when a rock avalanche runs over a glacier but continues into an ice-free terrain and entrains moraine material (Gosse & Evenson, 1994; Hermanns et al., 2014b). The sedimentology of rock avalanches can be modified during the winnowing of fine sediment by supraglacial meltwater, leading to avalanches with coarser grainsize distributions and boulder lags (Hewitt, 2009b; Shulmeister et al., 2009; Shugar & Clague, 2011). Glacial deformation of rock-avalanche sediment can cause not only geometric disturbance but also sediment compaction, mixing with glacigenic sediment, or mixing of previous rock-avalanche deposits, which is potentially increasing the uncertainty on volume estimates and rates (e.g., Cook et al., 2013). Such a complex situation was found in the Innerdalen Valley, western Norway (Schleier et al., 2013b).

This chapter presents a detailed description of the landforms in Innerdalen Valley, together with cosmogenic ^{10}Be exposure ages of the deposits. Runout modeling was conducted for two rock avalanches from the same source area, one that fell onto ice and another that ran into an ice-free valley. The study contributes a new dataset of surface-exposure ages of multiple rock avalanches in western Norway and provides insights for assessing landslide risk from rock-avalanche deposits associated with deglaciation.

2.3 Regional setting

The Innerdalen Valley (62.72° N, 8.73° E) is located in Sunndal Commune, Møre og Romsdal County, western Norway (Fig. 2.1 a). Geographically, it is part of the Trollheimen mountain area, with a relief extending from hundreds of meters below modern sea level to mountain peaks over 1 600 m a.s.l. It is situated in the cold temperate (boreal) climate zone. Like most of Fennoscandia, the regional geomorphology was affected strongly by multiple Quaternary glaciations. This is expressed by oversteepened valleys, rock slopes, and fjords up to 1 000 m deep. The extent of penultimate and earlier Quaternary glaciations is not yet well defined, in contrast to our growing knowledge of the dynamics, chronology, and extent of glaciations in Norway during the Last Glacial Maximum (LGM) and the Younger Dryas (YD) (Sollid & Sørbel, 1979; Olsen et al., 2013c) (Fig. 2.1).

The LGM and YD events left strong evidence for the impact of glaciation on landscape evolution and sediment storage (Blikra et al., 2006). In contrast to the long-lasting ($< 1 \times 10^4$ yr) LGM glaciation, the YD was a very short-lived (~12.8 to 11.5 kyr ago) cooling event preceded and followed by rapid warming (Andersen & Mangerud, 1989; Wanner et al., 2008; Shakun & Carlson, 2010). In western Norway, the YD chron is characterized by a cooler and drier climate. Most glaciers rapidly re-advanced, because conditions deteriorated

toward the full ice-age climate of the LGM in less than a century. Then, rapid warming and concomitant rapid rise in sea level following the YD triggered an accelerated decay of the glaciers and the accompanying thawing of permafrost. This rapid change in ice volume contributed to faster rates of lithospheric unloading and post-glacial isostatic uplift (Nesje & Dahl, 1993; Olsen et al., 2013b).

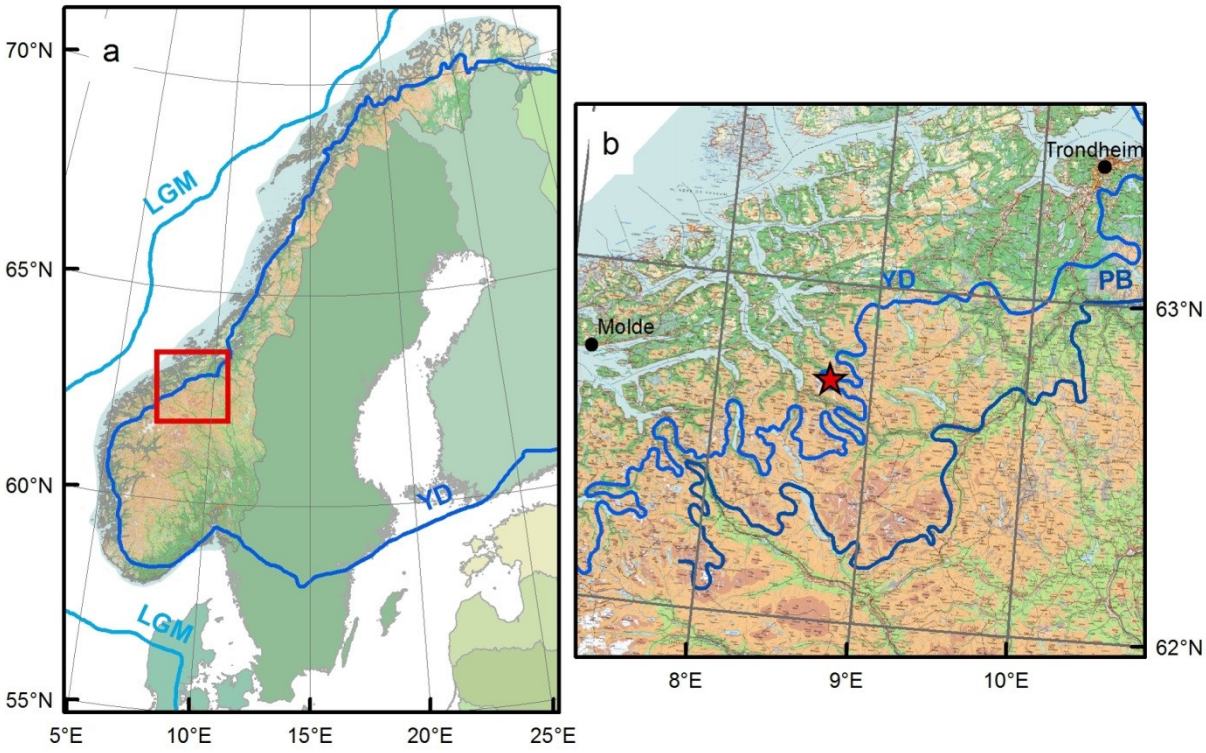

Fig. 2.1: Map of Last Glacial Maximum (LGM) and Younger Dryas (YD) glaciations in Fennoscandia. (a) Overview map of Norway, showing ice margins adopted from Olsen et al. (2013c). The red rectangle delimits area of (b). (b) Area around Innerdalen (red star), showing the local glacial-ice extent of YD and Preboreal (PB) times, following Sollid & Sørbel (1979). (Schleier et al., 2015)

The LGM and YD glacial geology and oversteepened valley walls are particularly evident in the valley of Innerdalen. Prominent terminal-moraine ridges are well preserved and interpreted to define the YD ice extent. Although the valley was completely covered by glacial ice during the LGM, the YD limit was farther upstream (Sollid & Sørbel, 1979; Wasrud, 2010). Today the study area shows high topographic relief and stretches between elevations of 200 m a.s.l. in the NW part and 1 770 m a.s.l. at the highest peak of Skarfjellet Mountain at the southern border (Fig. 2.2). A landslide-dammed lake, the Innerdalsvatna (spanning around 557×10^3 m^2) is located in the center of the valley with a mean water level of 396 m a.s.l.

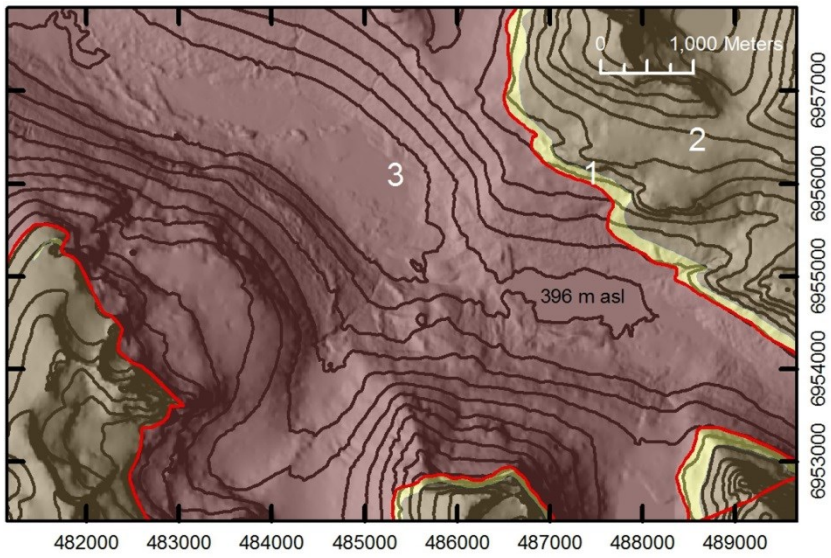

Fig. 2.2: Geological map of Innerdalen. The topography is represented by the hillshade and 100 m contour lines. The three lithological units are indicated by polygons: (1, yellow) meta-arkose and quartzite; (2, brown) granitic-to-dioritic gneiss; (3, red brown) coarse grained granitic gneiss and augengneiss. The tectonic faults are indicated by red line. The geology is based on Tveten et al. (1998). (modified after Schleier et al., 2015; Coordinate system: WGS1984, UTM Zone 32N)

Geologically, the study area is located in the so-called Western Gneiss Region of Norway. According to Hacker et al. (2010) these metamorphic rocks are composed of Proterozoic gneisses, chiefly orthogneisses, and partly also overlying oceanic and continental sediments which have been influenced by the Caledonian orogeny. The exposed rocks in the study area are the typical erosion-resistant gneisses with a low fracture density that are common to this region. Three lithological units are exposed (Fig. 2.2): (1) Meta-arkose and quartzite; (2) biotite containing coarse-to-fine grained granitic-to-dioritic gneiss, and (3) coarse grained granitic gneiss, augengneiss, and gneissic granite (Tveten et al., 1998). The principal tectonic structures controlling foliation, jointing, and fracture orientations include a regionally-extensive thrust fault dipping slightly SE along which the lithological units (1) and (2) are thrusted over unit (3), and some local, steeply dipping, mainly WNW striking minor faults. Furthermore, these gneisses generally have a well-developed foliation that is often involved as main delimiting structures in rock-slope failures (Henderson & Saintot, 2011; Saintot et al., 2011b).

2.4 Materials and methods

2.4.1 Field investigations and orthophoto and DEM analyses

An intensive field mapping was carried out in an area of around 16 km^2 in Innerdalen Valley to determine the spatial distribution and the morphological characteristics of surface deposits. Special regard was given to deposits of multiple rock avalanches in order to distinguish between different events and to interpret their origin (Schleier et al., 2013b). This included geomorphological mapping and sampling for granulometric analysis in order to determine the boulder size and the roundness distribution. Boulder size and roundness were recorded in the field at 75 sampling locations throughout the deposits by analysis of 100 randomly connected boulders (at least >0.1 m diameter) for each location. The boulder diameter was estimated in meter (0.5 m classes). Additionally, the average maximum boulder size of the whole sampling location was estimated and recorded directly in the field. The boulder roundness was recorded following the classification of Pettijohn & Doornkamp (1973) using six roundness classes (very angular, angular, sub-angular, sub-rounded, rounded and well rounded) and two sphericity classes (low and high). Based on these dataset and the mapping results, nine units of similar deposits were classified and mean values have been determined.

Furthermore, Schmidt Hammer (Typ N) rebound tests were also carried out at these 75 locations (in total around 100 blows at several boulders for each location) to determine the surface compressive strength of the boulders (represented by Schmidt Hammer R-value). Following the idea that this strength is reduced by degree of weathering the rebound value might be an indication for relative ages between deposits of the same rock type due to different exposure time (Shakesby et al., 2004; Aa et al., 2007; Shakesby et al., 2011). However, unfortunately these measurements show no significant results due to instrumental errors during field campaign and too many irregularities in sampled rock surfaces, for instance, different lithology, tested minerals and orientation of foliation. Therefore, the values cannot be used to obtain reliable chronology of the deposits.

The field mapping and deposit geometric analysis was supported by orthophotos and topographical analysis performed by using a digital elevation model (DEM) and its derivatives, for example, hillshade (i.e., shaded relief), slope angle, slope aspect and slope curvature (Fig 2.3, with reference to the Geological Survey of Norway database). The DEM has a 10 m × 10 m spatial resolution (grid size) and is based on the interpolation of 20 m contour lines from 1 : 50 000 topographic maps. The mean bulk volumes of the deposits were calculated by multiplying the field-estimated mean thicknesses and the mapped deposit areas (spatial extent). Thereby the deposit thickness is a rough subjective estimate that is mainly based on field observations of main valley topography, local deposit geomorphology and boulder size, and supported by three-dimensional inspections of the DEM. The data analyses were carried out by using the Geographical Information System software ArcGIS 10.x (Esri Inc.).

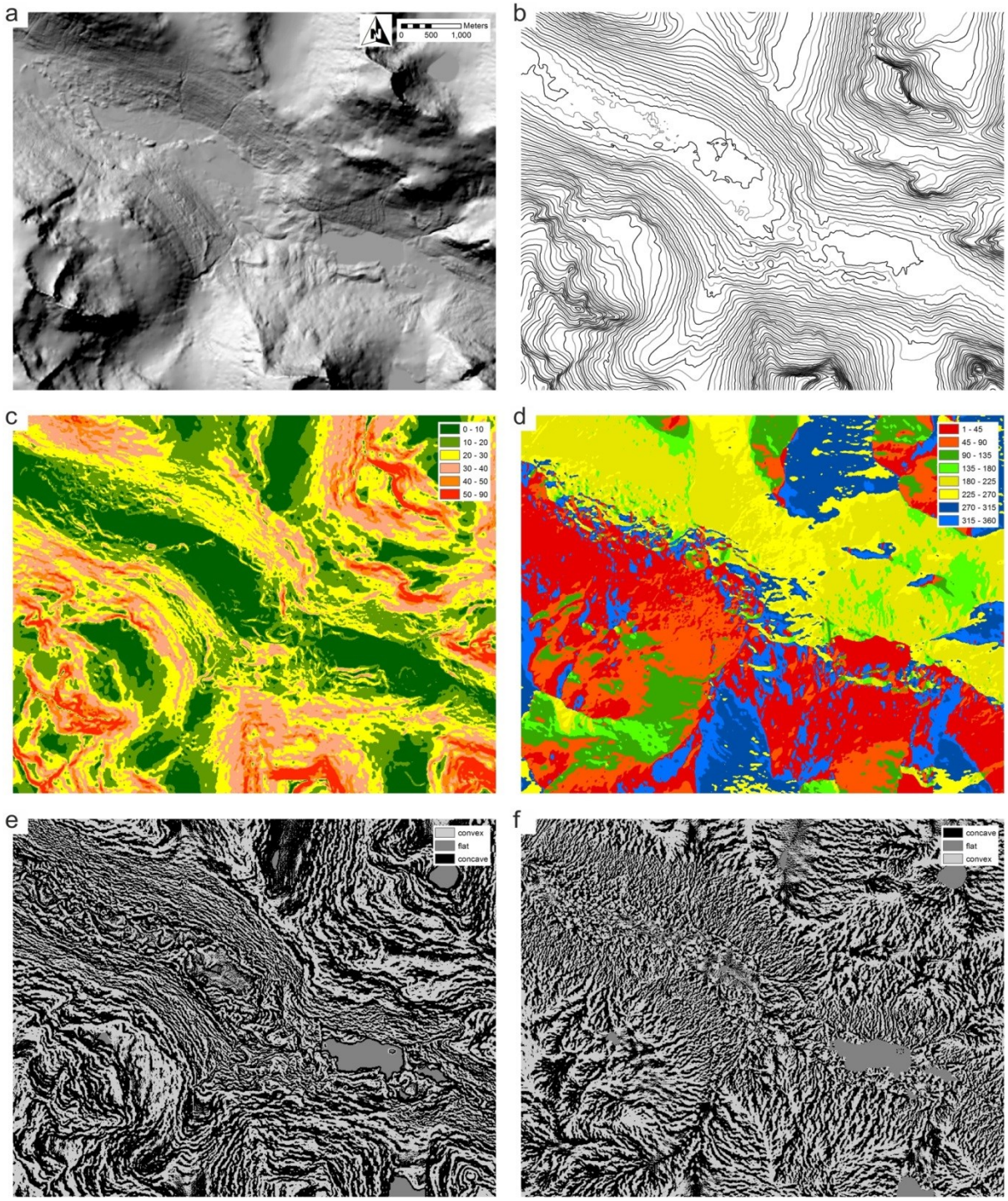

Fig. 2.3: Topographic characteristics of Innerdalen, represented by the DEM derivatives (10 m grid size). (a) hillshade, (b) 25 m contour lines, (c) slope angle in degree, (d) slope aspect in degree, clockwise from north, (e) profile slope curvature, and (f) planar slope curvature.

2.4.2 Surface-exposure dating

Terrestrial *in situ*-produced cosmogenic nuclide (TCN) exposure dating (Gosse & Phillips, 2001) has been used widely to date mass wasting deposits. Its application to landslide research (Ballantyne et al., 1998; Hermanns et al., 2001; Hermanns et al., 2004; Ivy-Ochs et al., 2009; Sturzenegger et al., 2014) is useful for landform interpretation and to determine temporal distribution of landslide events, correlate their occurrence with climatic changes (Ballantyne et al., 2014), assess realistic frequencies for similar events and conditions (Blais-Stevens et al., 2011), and determine long-term slide velocities of slow-moving rockslides (Hermanns et al., 2012c).

To determine the absolute ages of the landslide deposits and to improve the interpretation of the regional geological history, cosmogenic ^{10}Be was measured in quartz in boulders on the surface of the deposits. ^{10}Be is produced when secondary cosmic-rays (primarily fast neutrons and muons) interact with exposed nuclei of Si and O in the quartz.

A total of 15 samples were collected from large boulders on five different deposits which are either rock-avalanche deposits or deposits that appear to have been formed by rock avalanching on glacier ice (Fig. 2.5). For each sample, approximately 100 g of more or less pure quartzite (mainly out of quartz veins) were obtained with a hammer and chisel. Approximately 2 cm of rock were removed from the center of flat-topped-boulder surfaces. Large boulders were chosen to minimize the effect of influencing factors on TCN production and age calculations, such as snow cover, vegetation, post-depositional movement, and exhumation of a boulder through a moraine by erosion of a till or heaving of the boulder. Additional measurements were taken to adjust for other factors, such as topographic shielding of the cosmic-ray flux and geometric effects, for example, surface dip and proximity to the boulder edge (Blais-Stevens et al., 2011; Hermanns et al., 2012c). The positions (latitude and longitude) of the sampling sites were determined in the form of UTM coordinates (Zone 32) with a handheld GPS-device (global positioning system, accuracy 5-10 m) and converted to decimal degrees. Their elevations were determined with barometric altimeter and 1 : 50 000 topographic maps. The dip direction and the dip of each sampled boulder surface were directly measured by using a Clar-type geological compass. Additionally, the thickness of each rock sample was recorded. Topographic shielding was determined by measuring the trend and plunge of the skyline with a compass and clinometer in 30° steps clockwise starting from north. Only boulders with apparently stable surfaces were sampled (i.e., they exhibited no evidence of recent erosion on the basis of lichen cover, staining, or grus at the base of the boulder). Although it is unlikely that small differences in erosion rates or shielding on the boulders would contribute uncertainties greater than a millennia (e.g., for erosion rates of ~1 mm/ka), it is possible that boulders in the same deposit may yield substantially different ages if they have different amounts of inheritance (i.e., non-zero initial ^{10}Be concentrations) at the time of deposition. Thus, samples from three different boulders were collected for each deposit to obtain a mean age and to test for age variability due to inheritance (Blais-Stevens et al., 2011).

Mineral separation and ^{10}Be target chemistry was completed at Dalhousie Geochronology Centre (by G. Yang with partial support by NSERC-MRS-342052 grant to JCG). The mineral

separation included differential leaching with dilute hydrofluoric or hexafluorosilicic acid, froth flotation, and magnetic separation until the quartz concentrate had an Al concentration of <100 ppm (an indication of the success of feldspar removal). Before dissolution of 20.0 or 15.0 g of pure quartz, 220 mg of ^{9}Be was added as carrier (produced from an Ural Mountain phenacite, Carrier Be31 has 282 ug/mL Be, and ^{10}Be/^{9}Be is below 1×10^{-16}) at Lawrence Livermore National Laboratory, Livermore (USA), where the accelerator mass spectrometry (AMS) was conducted (by S. Zimmerman at CAMS-LLNL). Process blank subtraction (2.48×10^{4} atoms) was less than 2.5% of all samples. Precision of the AMS measurements averaged 3.0%. One sample with excessive Al yielded low initial currents and was not measured (IND-14). Ages were computed (by J.C. Gosse at Dalhousie Geochronology Centre) by using the CRONUS calculator at the KU server, version 1.0 (Borchers et al., 2015), by using ^{10}Be production systematics according to Sato, as described in Lifton et al. (2014). The internal error reflects the AMS error, 2% contribution to the error in chemistry and the Be concentration of the carrier, and the error contributed by the uncertainty in the process blank ^{10}Be/^{9}Be. The external error in age reflects systematic and random errors contributed by, for instance, uncertainty in the production rates at each sample and the decay constant of ^{10}Be.

2.4.3 Structural and kinematic analyses

According to Schleier et al. (2013b) the source area for the investigated rock-slope failures is located at the same slope and characterized by a 460 m high and 80° steep rock face. This source area has been confirmed for the continuous rock avalanche but is assumed for the discontinuous deposits of uncertain genesis farther down the valley. Because of its location and because of the present rock-fall hazard, the face is inaccessible for geomechanical field investigations. In order to obtain structural data, mainly orientations of discontinuity sets, the analysis of a high-resolution digital elevation model (HRDEM) was carried out.

A terrestrial laser scanning (TLS) survey was performed in the year 2013 from two locations focusing on the rock face by using an Optech ILRIS-LR LiDAR-device (Optech Inc.) and time-of-flight technique. Technical specifications of the scanner device are summarized in Optech (2014). The rock face itself and the connected slope were scanned with a mean distance of 1.8 km and with an average x-y spot spacing of 150 mm, and such of 1.6 km and 125 mm, respectively. Postprocessing of the scan data (raw point clouds) was carried out by using Polyworks software package (InnovMetric Software Inc.). With the Polyworks IMAlign software the point clouds were aligned at first by three manually chosen common points using the “Point Pair Alignment” method, and in a second step, the point clouds were automatically aligned by an Iterative closest point (ICP) algorithm by using the “Best-fit Alignment & Comparison” to minimize distances between the nearest neighbors. Final georeferencing of the whole point cloud was conducted by the two scanner positions and two manually added reference points in the scan. For details about LiDAR technique and data treatment, refer to Oppikofer et al. (2008), Oppikofer (2009) and the review papers by Jaboyedoff et al. (2012) and Abellán et al. (2014).

The structural analysis of the TLS-derived HRDEM data, that is, determination of main discontinuity sets and its orientations, was carried out by manual selection of the plane normals representing the orientation of discontinuities by using the Coltop3D software (terr@num Inc., Jaboyedoff et al., 2007; Jaboyedoff et al., 2009). The obtained structural data, that is, dip and dip direction of discontinuity sets (a total of 85 496 pole vector entries), were plotted in Schmidt net, lower hemisphere, equal area. Cluster analyses were performed to determine the mean orientation of the main discontinuity sets and kinematic analyses (Wyllie & Mah, 2004) for rock-slope failure were carried out by using the software Dips 6.0 (Rocscience Inc.).

Additionally, rough stability estimations, that is, deterministic factor of safety (FoS) calculations and sensitivity analyses (e.g., water pressure), were carried out with simple geometries and mechanical parameters by using the software Swedge 5.0 and RocPlane 2.0 (Rocscience Inc.) in order to support the kinematic analyses.

2.4.4 Dynamic analyses

To assess the runout of landslides, numerical methods are applied. The two dimensional code DAN was established especially to model the dynamic propagation of fast moving landslides of the flow type, for example, rock avalanches (Hungr, 1995; Hungr & Evans, 1996). With the more advanced code DAN3D it is possible to model such landslide propagation also over a complex three-dimensional terrain (McDougall & Hungr, 2004; Hungr & McDougall, 2009), and to take into account effects such as material entrainment (McDougall & Hungr, 2005) or different types of substrate along the travel path, for example, glacial ice (Sosio et al., 2008; Sosio et al., 2012; Delaney & Evans, 2014). Dynamic runout analyses of the rock avalanches were applied using numerical modeling and the continuum mechanics numerical code DAN3D. This code applies a depth-averaged meshless smoothed particle hydrodynamics (SPH) principle, using a two-dimensional Lagrangian solution to solve equations for shallow open channel fluid flow, describing the mechanics of a continuum based on mass and momentum conservation laws (McDougall & Hungr, 2004). For calculation and to consider different flow types and model conditions, it uses digital terrain models which characterize path topography and initial failure volume, and user assigned rheologies and material parameters which describe mechanical properties, especially concerning the basal friction, that is, the boundary between topography and flowing mass which is defined by the basal rheology. The code has an open kernel to assign different rheologies such as Frictional, Bingham, or Voellmy type, whereas the latter combines frictional and turbulent behavior. Rheology can also change along the runout path as materials change, for instance, when propagating over rock and ice (McDougall & Hungr, 2004,2005; McDougall, 2006; Hungr & McDougall, 2009). The code models the propagation of the mass represented by single particles and can output for instance, particle location, velocity, thickness, erosion, etc. for defined time steps.

Besides initial process volume and path topography, the internal friction of the material (e.g., for dry broken rock represented by friction angle) and the basal resistance, which is

described by the assigned rheology are the most limiting factors for modeling flow propagation. The most common rheologies used for modeling rock-avalanche runout with the best results are the frictional and Voellmy rheologies (Hungr & Evans, 1996; McDougall, 2006; McKinnon et al., 2008). The main equations characterizing the basal resistance according to McDougall et al. (2006) are as follows. For frictional rheology, it is $\tau = \sigma_z \tan \varphi_b$, where τ is the basal shear stress, σ_z is the bed normal stress and φ_b is the bulk friction angle (Hungr, 1995). For Voellmy rheology, it is $\tau = \sigma_z f + \rho g \, v^2/\xi$, where f is the friction coefficient (analogous to *tan* φ_b), ρ is the material density, g is the gravitational acceleration, v is the depth averaged flow velocity, and ξ is the so-called turbulence parameter. Thereby, the first term accounts for the frictional component, and the second term on the right side of the equation accounts for all possible velocity-dependent influences on resistance (turbulent component). The latter term was introduced by Voellmy (1955) for the propagation of snow avalanches.

In this study, numerical runout modeling (performed by using the code DAN3D) was carried out for the rock-slope failures to describe rock-avalanche propagation and to test the reliability of landform interpretation. Two main models were used according to our hypotheses for deposit genesis (Schleier et al., 2013b): (1) model of a rock avalanche into an ice-free portion of the valley, and (2) model of a rock avalanche onto glacier ice.

Backward modeling was applied in order to approximate the best-fit model. Therefore, the models were run iteratively with different settings (e.g., mechanical properties) and the results were evaluated with field-mapping data (e.g., spatial distribution of deposits). To obtain the pre-failure topographies, modifications of the digital terrain models were carried out by manually modifying the 25 m contour lines of the DEM according to field estimates and morphological interpretation. The topography of travel paths and source volumes were modified by, for instance, removing the deposits or adding paleolandforms at the rock slope. The input data of rheology and mechanical parameters for both models were changed manually after applying the initial model parameters according to similar examples described in the literature (e.g., Hungr & Evans, 1996; Sosio et al., 2012). The model parameters that show the best results are summarized in Table 2.1.

According to Hungr & Evans (1996) and McDougall (2006), Voellmy rheology with f = 0.1 and ξ = 500 is recommended for a simple rock avalanche and hence a rock avalanche into an ice-free valley. The conducted parameters are very similar. For a rock avalanche onto a glacier, two different rheologies were applied to take into account different materials along the path. For the natural slope above the glacier, the same rheology as that for the rock avalanche into an ice-free valley was applied. A wide range of parameters is addressed for modeling the runout behavior of rock avalanches onto a glacier by Hungr & Evans (1996) and Sosio et al. (2012). The latter contribution summarizes a range of 0.03–0.1 for f and 1 000–2 000 m/s² for ξ for such events. Best-fit DAN3D models of the well-investigated Mount Munday case (rock avalanche on glacier) show f = 0.07 and ξ = 1 000 m/s² (Sosio et al., 2012) and f = 0.08 and ξ = 1 050 m/s² (Delaney & Evans, 2014). The parameters used to model the propagation along the low friction surface of the glacial-ice body are similar to those of these examples.

Table 2.1: Rheology settings for materials used in the DAN3D models for Innerdalen, that is, rock avalanching in an ice-free valley and rock avalanching on a glacier. (Schleier et al., 2015)

	Rock avalanche	Rock avalanche on glacier	
Material	Natural slope	Natural slope	Glacier surface
Rheology	Voellmy	Voellmy	Voellmy
Unit weight (kN/m^3)	28	28	28
Friction coefficient	0.15	0.15	0.06
Turbulence coefficient (m/s^2)	500	500	1 000
Internal friction angle (°)	35	35	35

In addition to dynamic modeling, for one well preserved rock avalanche, it was possible to perform approximate analytical velocity estimation by using the preserved runup height on the opposite slope. By following Crandell & Fahnestock (1965) and Evans et al. (1989), this estimation is based on simple energy balance of potential and kinetic energy ($mgh = 1/2\ mv^2$) and can be expressed by the equation $v = \sqrt{2gh}$, where v is the velocity, *g* is the gravitational acceleration (9.81 m/s^2), and *h* is the maximum vertical runup height.

Furthermore, the Fahrböschung parameter values (Heim, 1932) were determined for the mapped and modeled rock-avalanche deposits if possible. This parameter is defined by the angle between the horizontal line and the line connecting the scarp's upper limit with the most distal deposits and represents the apparent friction angle (Heim, 1932). It can be further determined by the fall height (*h*) and the horizontal travel length (*l*) and is sometimes referred to as angle of reach. It can be calculated by using the equation $\alpha = \tan^{-1}(h/l)$, where *α* is the Fahrböschung, *h* is the vertical height difference, and *l* is the horizontal distance between the main scarp's upper limit and the most distal deposit (Fig. 2.4). The travel angle was also calculated within the DAN3D model. Analogous to Fahrböschung, it is the angle between the horizontal line and the line connecting the initial center of mass (COM) with the final COM of the modeled material volume.

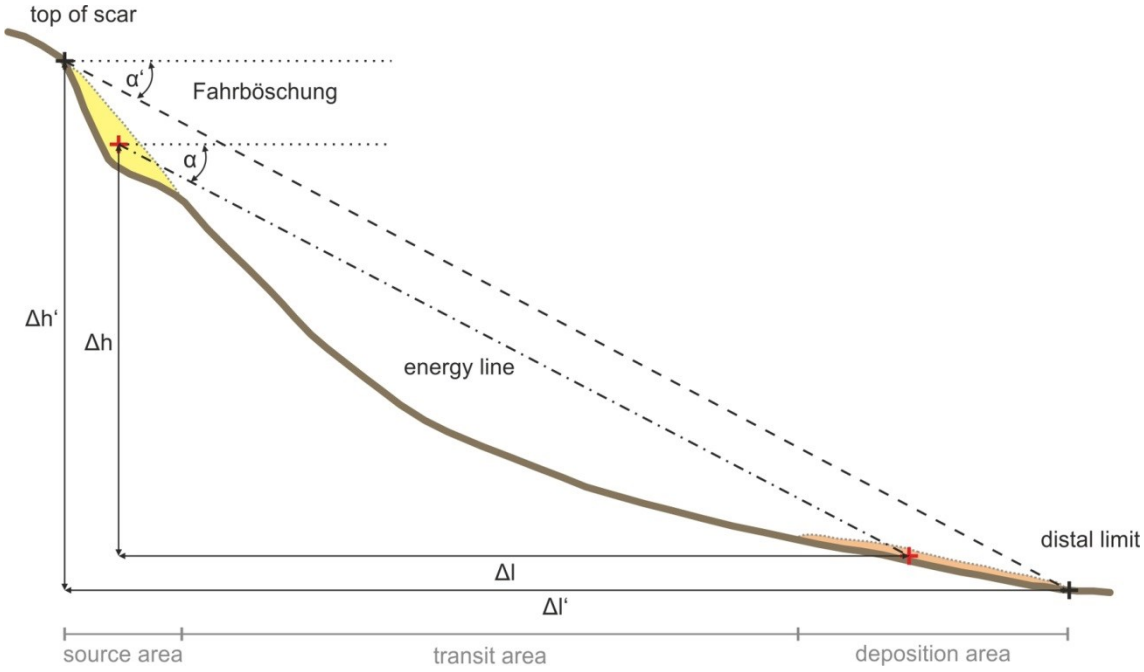

Fig. 2.4: Schematic model of Fahrböschung and travel angle (modified based on Poschinger, 2002). Δh' is the vertical height difference between the uppermost limit of the scarp and the most distal limit of the deposit, and Δh is this between the initial and final center of mass (COM, red cross), respectively. Δl' is the horizontal distance between the main scarp's upper limit and the most distal deposit, and Δl this between the initial and final COM. The angles between the connecting lines and the horizontal line (dotted black line) are defined as the Fahrböschung (α‘) and the travel angle (α), represented by the energy line.

2.5 Results

2.5.1 Spatial distribution and characteristics of rock-avalanche deposits

Preliminary results of the research have already been published (Schleier et al., 2013b). However, improvements in the data have resulted from improved mapping and data analyses, mainly for the areas and volumes of deposits and granulometric characteristics. The spatial distribution of deposits in Innerdalen Valley, for example, talus and till material, as well as bedrock outcrops and deposits of multiple rock avalanches, are shown in Fig. 2.5. These rock-avalanche deposits are composed of rock boulders several meters to tens of meters in diameter, showing distinct morphological characteristics and forming various geomorphological units depending on paleoenvironments. They cover an area of around 2.9 km^2 and exhibit an estimated volume of 54 × 10^6 m^3. According to Schleier et al. (2013b) two main groups of deposits are determined: (1) a continuous rock-avalanche deposit and (2) complex discontinuous boulder deposits that are separated from each other by several kilometers.

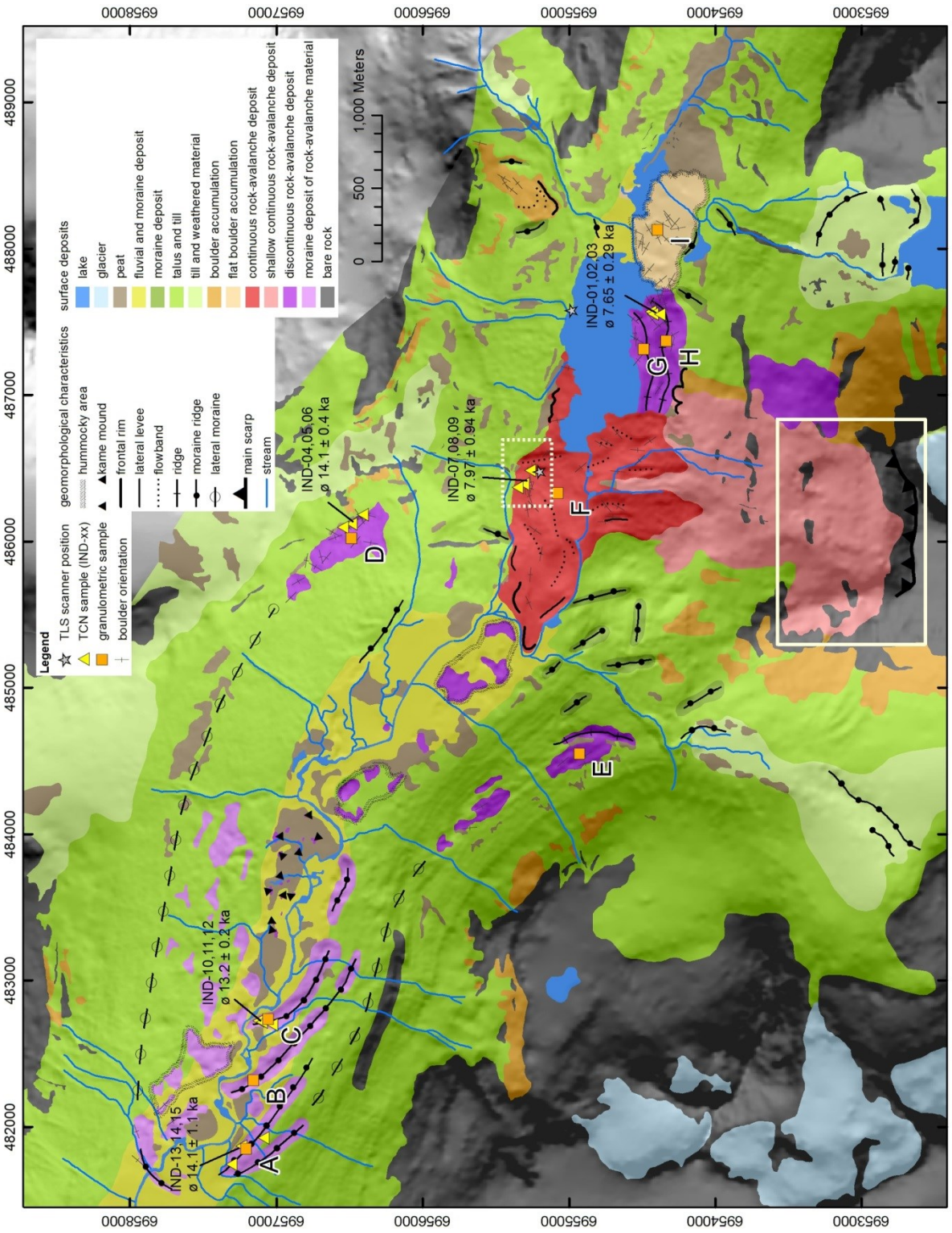

Fig. 2.5: Map of rock-avalanche deposits and surface sediments in Innerdalen, showing the spatial distribution of deposits, the geomorphological characteristics, the different sampling locations, and the surface-exposure ages. Areas for granulometric description are labeled (A to I). The rock-avalanche source area located at Skarfjellet Mountain is outlined by the solid white rectangle, and the runup area is outlined by the dotted white rectangle. (Schleier et al., 2015; Coordinate system: WGS1984, UTM Zone 32N)

The main geomorphological units as described in the following text are marked in Fig. 2.6 and might contain several of the nine units for granulometric description (A to I) as defined in Fig. 2.5. They can be named as follows: terminal-moraine ridges (A, B and C), kame-like mounds or isolated boulder patches (D and E), two valley-parallel ridges (G and H), a flat boulder patch (I), a boulder patch high above the lake, and a large continuous rock-avalanche deposit (F).

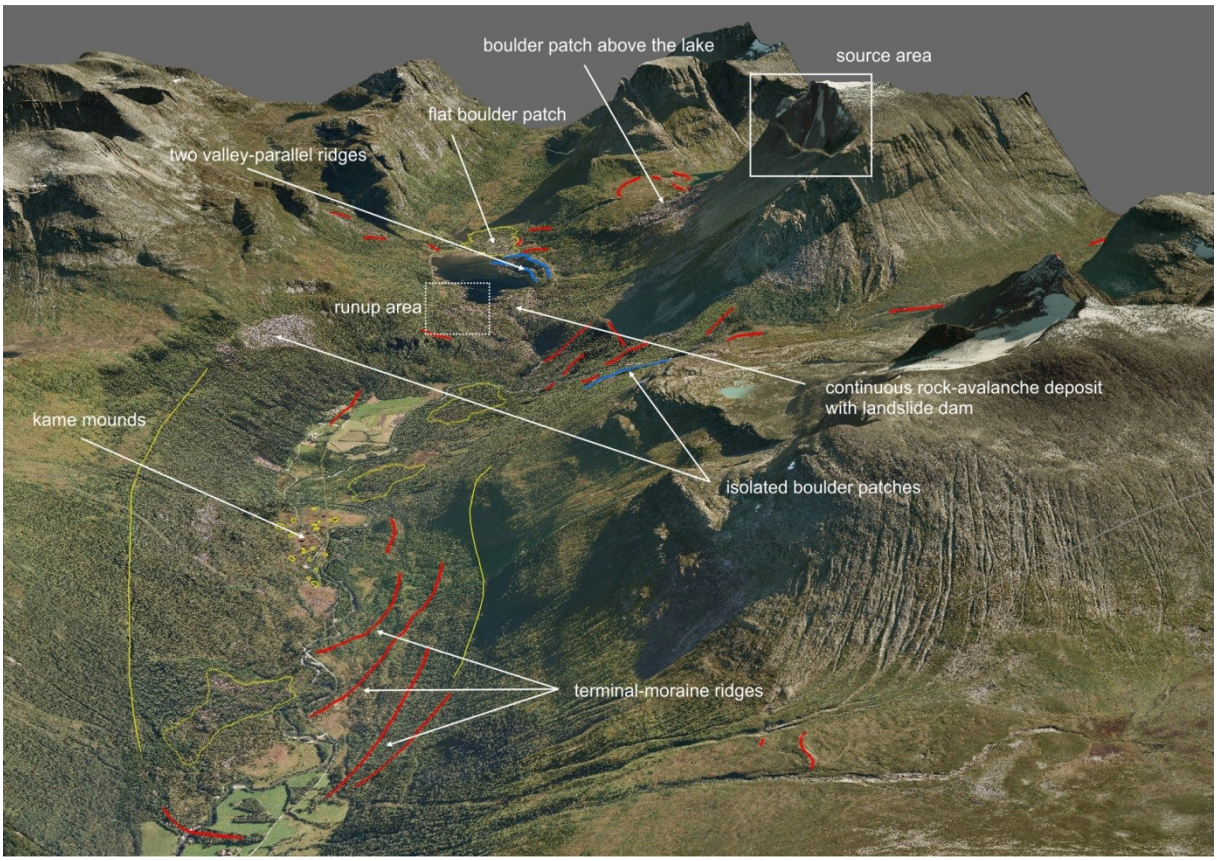

Fig. 2.6: Oblique three-dimensional view of Innerdalen (view direction toward WSW). The main geomorphological units are labeled (see text for detailed description). The geomorphological structures are outlined with line signature (blue, distinct morphological sediment ridge; red, moraine ridge; yellow, lateral moraine; dashed yellow, hummocky surface; yellow circle, kame mounds). The rock-avalanche source area is marked by a solid white rectangle, and the runup area is marked by a dotted white rectangle. For scale, refer to Fig. 2.2 and Fig. 2.5. (Schleier et al., 2015, modified after Schleier et al., 2013b)

According to their material, all sampled deposits show more or less similar characteristics. They are composed of unsorted boulders several meters to tens of meters in diameter with only some small variations. The basic findings are already described in detail in Schleier et al. (2013b), but the improved data on selected characteristics are presented here for completion. The granulometric characteristics of all landslide deposits, that is, the boulder size distribution and the boulder roundness and sphericity, are summarized in Table 2.2, and Figs. 2.7 and 2.8. According to the boulder size, the largest amount of boulders is generally smaller than 2 m in diameter (69–90%) and the mean field-estimated average maximum size

is around 5 m diameter. However, some deposits show slight differences in distribution and in recorded maximum boulder sizes. Concerning the roundness and sphericity, the distribution shows a concentration of angular (24–46%) and sub-angular (43–76%) boulders. Only in some cases very angular or sub-rounded boulders are found, but no rounded or well-rounded boulders were recognized. Generally the frequency of boulders with low sphericity is slightly higher than those showing a high sphericity. Additionally, the deposit volumes derived by mapped spatial extent and field-estimated thicknesses are shown in Table 2.3.

Table 2.2: Boulder size statistics for the sampled deposits (A to I) in Innerdalen. The size values are in meters. Additionally included is the field-estimated average maximum boulder size (av.max.). For location, refer to Fig. 2.4. (according to Schleier et al., 2015)

	A	B	C	D	E	F	G	H	I
Mean	1.1	1.1	1	1.7	1.6	1.7	2	1.8	1.4
Std. deviation	1.1	0.9	0.9	1.8	1.7	1.7	1.9	1.9	1.4
Minimum	0.1	0.1	0.1	0.1	0.3	0.2	0.2	0.2	0.1
Maximum	10	5	5	12	15	18	25	15	15
Av. max.	4	3	4	10	7	6	5	7	4

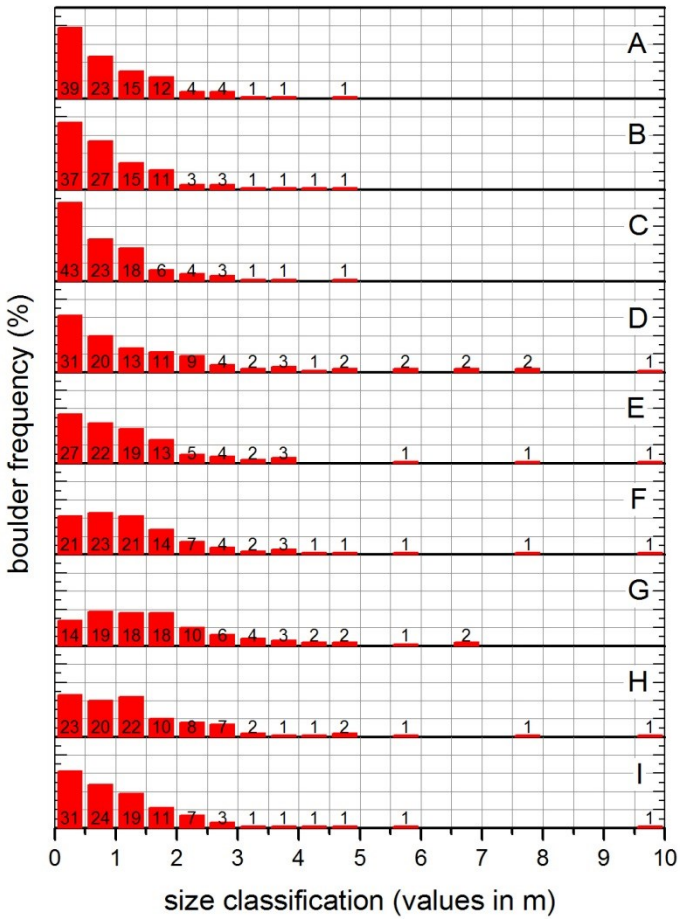

Fig. 2.7: Boulder size distribution for the sampled deposits (A to I) in Innerdalen. The horizontal grid lines mark 10% intervals. For location, refer to Fig. 2.5. (Schleier et al., 2015)

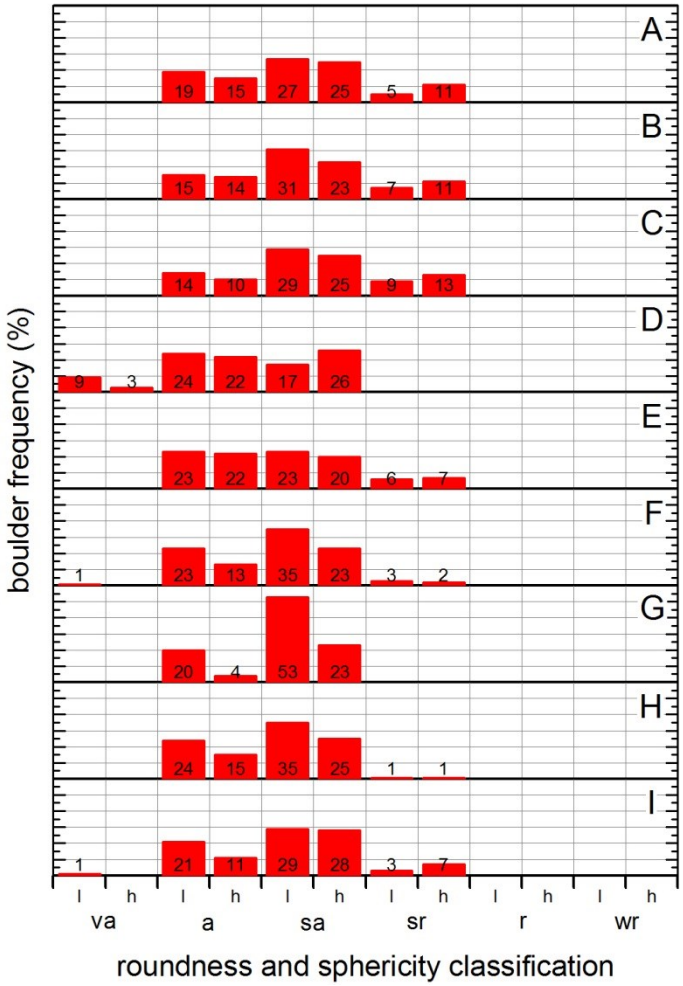

Fig. 2.8: Boulder roundness and sphericity distribution for the sampled deposits (A to I) in Innerdalen. The abbreviations are: va, very angular; a, angular; sa, sub-angular; sr, sub-rounded; r, rounded; wr, well rounded; l, low sphericity; h, high sphericity. The horizontal grid lines mark 10% intervals. For location, refer to Fig. 2.5. (Schleier et al., 2015)

Table 2.3: Field-estimated thickness, mapped spatial extent and calculated volume of deposits in Innerdalen. For location, refer to Figs. 2.4 and 2.5. (according to Schleier et al., 2015)

Deposit	Abbreviation	Field-estimated mean thickness (m)	Mapped spatial extent (10^3 m^2)	Volume, bulked (10^6 m^3)
Terminal-moraine ridge	A	20	148	3.0
Terminal-moraine ridge	B	20	141	2.8
Terminal-moraine ridge	C	15	164	2.5
Isolated boulder patch	D	15	151	2.3
Isolated boulder patch	E	15	95	1.4
Continuous rock-avalanche deposit	F	20	1 121	22.4

Valley-parallel ridge	G	40	86	3.4
Valley-parallel ridge	H	50	156	7.8
Flat boulder patch	I	10	259	2.6
Hummocky surface (dislocated moraine)	-	10	343	3.4
Boulder patch above the lake	-	10	233	2.3

2.5.1.1 Terminal-moraine ridges (A, B and C)

Three prominent closely nested moraine ridges are preserved on the southern side of the lower valley at around 200 m a.s.l. (Figs. 2.5 and 2.6). These ridges are ca. 1 km long, have an average elevation of 15 m above the valley floor and have been dissected by post-glacial incision. The ridges are composed of boulders similar to those of the other deposits. Near the surface the moraines are clast-supported with lack of fines. However, in fluvial cuts, the internal structure is exposed, showing a carapace of large boulders on a massive matrix supported diamicton with sandy matrix and angular-to-rounded clasts with a wide range of sizes (Fig. 2.9 d). These deposits show the highest frequency of small boulders (62–66% smaller than 1 m and 77–84% smaller 1.5 m) with a mean size of 1 m (Fig. 2.7).There is no significant amount of boulders larger 5 m and the average maximum is 4 m, but also some larger ones might occur and the maximum recorded size is 10 m. It is peculiar that these deposits show the highest frequency of sub-rounded boulders (around 16–22%) (Fig. 2.8). Both, the outermost (A) and the middle (B) moraine ridge show a field-estimated mean thickness of 20 m and therefore a volume of 3.0×10^6 m^3 (A) and 2.8×10^6 m^3 (B), respectively. The innermost moraine ridge (C) has an average thickness of 15 m and shows a volume of 2.5×10^6 m^3 (Table 2.3). The abundance of quartzitic boulders in the moraines decreases in the up-ice direction. Whereas the terminal moraines are prominent ridges on the southern side of the valley, they do not appear to have been preserved on the northern side. Instead, on the northern side, the deposits of similar boulder material are developed as patches, showing irregular and partly hummocky surfaces (Figs. 2.5 and 2.6).

2.5.1.2 Kame-like mounds

Between the continuous rock-avalanche deposit (F) and the innermost terminal moraine (C), distinct concentric mounds of similar rock-boulder material are found isolated and randomly distributed in the fluvial affected glacial and glaciofluvial valley-fill sediments (Figs. 2.5 and 2.6). These deposits have an average height of around 2.5 m and show characteristics similar to those of the described terminal-moraine ridges, with carapace of large rock boulders situated onto fine grained sandy matrix (Fig. 2.9 e).

Fig. 2.9: Photographs of geomorphological units in Innerdalen. The extents of the units are outlined by dotted lines, and linear structures are outlined by dashed lines. Abbreviations are summarized in the legend. (a) Skarfjellet Mountain (view direction toward SW) showing the source area (main scarp marked by solid line) and transit area of rock avalanches, as well as the valley-parallel ridges along the lake (dashed line). The dashed-dotted line marks the estimated trace of the main thrust fault. The horizontal distance from the viewpoint to the top of the scarp is around 3 000 m, and it is around 550 m to the opposite waterside. The inset is showing the two morphological ridges from another viewpoint looking toward SSE. (b) Closer view of the scarp area at the N-facing steep rock slope of Skarfjellet Mountain (view direction toward WSW). The trace of the foliation is outlined by the dashed line. The average slope angle of the rock face is around 85°, whereas that of the lower slope is less steep, around 40°. (c) Continuous rock-avalanche deposit, showing a natural dam and runup on the opposite slope (view direction toward NW). The maximum runup height is estimated to be 80 m. The isolated boulder patch is part of the discontinuous rock-avalanche deposits and is located around 300 m above the valley floor. (d) Terminal-moraine ridge composed of rock-avalanche material, around 12 m high.

The inset displays a 4 m high fluvial cut, showing a carapace of rock boulders with fine grained sandy matrix in subsurface (modified after Schleier et al., 2013b). (e) Kame mounds composed of rock-avalanche material, around 2.5 m high. The inset displays a fluvial cut, showing characteristics similar to those of the terminal moraines. (Schleier et al., 2015)

2.5.1.3 Isolated boulder patches (D and E)

Two main isolated boulder patches, several 100 m^2 large, occur on both sides of the valley (Figs. 2.5 and 2.6). These boulder patches are separated from each other and are located on the slope around 300 m high above the valley floor. They show no continuous connection with other boulder deposits or direct affiliation to any source area. One is located on the northern, that is SW-facing, slope of the valley (D) (Fig. 2.9 c), whereas the other one is located on the opposite side on the NE-facing slope (E). Deposit of patch (D) shows a higher frequency of boulders larger 5 m, but both show a mean boulder size of 2 m, maximum boulders of 15 m and an average maximum of 8 m (Fig. 2.7). These deposits show the highest frequency of angular boulders, whereas angular and sub-angular forms are equally distributed (both around 45%). Furthermore, patch (D) is the only deposit showing a significant amount of very angular boulders (12%), whereas, in contrast, patch (E) shows no very angular, but also sub-rounded boulders (13%) (Fig. 2.8). Both deposits have a field-estimated thickness of 15 m but due to spatial extent the volumes are 2.3×10^6 m^3 (D) and around 1.4×10^6 m^3 (E), respectively (Table 2.3). The long axes of elongated boulders show a trend of running parallel to the valley toward NNE. Furthermore, it is conspicuous that the boulder patch (D) mostly contains quartzite boulders.

2.5.1.4 Valley-parallel ridges (G and H)

There are two prominent ridges located along the southern shore of the lake at the N-facing slope of Skarfjellet Mountain with their crests running parallel to the main valley in the E – W direction (Figs. 2.5, 2.6 and 2.9 a). These ridges are 800–1 000 m long. It is peculiar that these deposits are limited to the southern side of the lake. Besides the morphology with relatively steep ridges with a mean height of 30 m above water level, they show some conspicuous granulometric characteristics. The deposits show a higher frequency of boulders between 2–5 m diameter and the largest maximum boulders with 25 m diameter, the average maximum size is 6 m (Fig. 2.7). Further, they show a very high frequency of sub-angular boulders (60–76%) and no sub-rounded or very angular ones (Fig. 2.8). The first ridge (G) shows a field-estimated thickness of 40 m and a volume of 3.4×10^6 m^3, the second ridge (H) 50 m and 7.8×10^6 m^3, respectively (Table 2.3). At the western border, these deposits are partly covered by the continuous rock-avalanche deposit (F) that forms a stratigraphically higher deposit and includes slightly fewer very large boulders. The orientations of elongated boulders show trends to run parallel to the valley toward WNW and ENE.

2.5.1.5 Flat boulder patch (I)

Another boulder deposit is located at the SW shore of the lake in continuation to the valley-parallel ridges (G) and (H) (Figs. 2.5 and 2.6). From its granulometric characteristics this deposit is similar to the others. It shows a mean boulder size of 1.5 m diameter, a maximum of 15 m and an average maximum of 4 m, and chiefly angular and sub-angular forms (Figs. 2.7 and 2.8). The main difference to other deposits is its morphology. It shows a relatively flat patch with a partly hummocky surface. The field-estimated thickness is around 10 m and therefore the deposit has a volume of around 2.6×10^6 m^3 (Table 2.3). The deposit shows some interactions with moraine ridges and is surrounded by such deposits. The boulder orientations show no distinct direction or pattern, however, two main trends toward NW and ENE can be estimated.

2.5.1.6 Boulder patch above the lake

East of the rock-avalanche transit area is a boulder deposit at 350 m above the lake (Figs. 2.5, 2.6 and 2.9 a). The boulder patch is composed of material similar to that of the other deposits, but it has a relatively flat surface. Its thickness is estimated by field evidence with 10 m and its volume is around 2.3×10^6 m^3 (Table 2.3). The deposits upper boundary is marked by the steep rock slope of the mountain, which shows evidence for current rock-fall activity. Downslope, it shows a sharp boundary at a morphological edge along a bare rock outcrop and no continuous connection with other boulder deposits, including the valley-parallel ridges (G) and (H) located down the slope.

2.5.1.7 Continuous rock-avalanche deposit (F)

In the middle of the valley, a continuous rock-avalanche deposit has developed north of the Skarfjellet Mountain in front of the main lake (Figs. 2.5 and 2.6). This boulder deposit covers the entire valley width and shows typical lobate shapes with frontal rims and lateral levees. Internal flowbands are also visible. The deposit further indicates a runup on the opposite slope of around 80 m in height, creates a natural landslide dam (Fig. 2.9 a, c) and partly covers moraine deposits. The mean boulder size is 2 m diameter, the maximum sampled size is 18 m and the field-estimated average maximum is 6 m (Fig. 2.7). The deposit shows chiefly angular and sub-angular boulder forms (Fig. 2.8). The mean thickness is roughly estimated by field evidence with 20 m. The deposit covers an area of 1.1×10^6 m^2 and therefore has a volume of around 22.4×10^6 m^3 (Table 2.3). At its eastern limit, it is visibly evident that the deposit also covers other boulder deposits, namely, the valley-parallel ridges. The orientations of the longitudinal boulders are in accordance with other flow structures and show a valley-perpendicular trend (NNE) in the proximal areas following a shift to valley-parallel orientations (W and WSW) due to a 90° shift of the rock avalanche during propagation.

2.5.2 ^{10}Be chronology of rock-avalanche deposits

The ^{10}Be exposure dating of boulders on the deposits (Table 2.4) generally supports the relative chronology based on morphology, spatial distribution, and interaction between deposits of multiple rock avalanches and such of other genesis. Ages were calculated by assuming no erosion and by assuming 1 mm/ka steady surface erosion (generally <1% effect). To provide a more thorough adjustment for environmental conditions, we assume (1) an average erosion rate of 1 mm/ka, (2) a 20 cm thick snow cover for 4 months of the year throughout the exposure history—adjustment with a 0.9% decrease in production rates with snow density 0.2 g/cm^3 because most sampled boulder surfaces were above the mean winter snowfall for the past decade, and (3) a long-term average moss and mineral density of 0.2 g/cm^3—adjustment for shielding by moss and grus cover with a 0–1.2% decrease in production rate based on observed moss thicknesses in the field.

Although there is an uncertainty in the long term average of each of these factors, there was improvement in the variation about the mean age of four out of the five deposits; therefore, the fully adjusted boulder ages were used to determine the final ages of the deposits. The inherited ^{10}Be concentration from exposure prior to final deposition of the boulder, if any, is unknown and therefore not considered. Any production that occurred during the supraglacial transport of boulders are ignored because it is likely a relatively short transportation time. Also, the boulders may currently not be in the same orientation anymore. The fully adjusted boulder ^{10}Be exposure ages range from 7.35 ± 0.64 ka to 9.05 ± 0.87 ka for the rock-avalanche deposits and from 13.0 ± 1.3 ka to 14.9 ± 1.5 ka for the terminal-moraine ridges. The large (~10%) 1σ uncertainties are dominated by the uncertainty in the production rate which varies with the magnetic-field intensity over time.

The non-weighted mean exposure ages (n = 3 except for the outermost terminal moraine with n = 2) for the deposits of the described morphological units have coefficients of variation (CV) that are similar to their AMS measurement precisions, ranging from 1.5–3.7%. The outermost terminal moraine has higher CV but lower n values. The highest CV value, 11.8%, is caused by one apparently old exposure age (IND-09). This sample might be a statistical outlier due to ^{10}Be inheritance (1σ uncertainties do not overlap with the other samples from the same deposit). The mean age of the outermost moraine at location (A) (Fig. 2.5) is 14.1 ± 1.1 ka. An isolated boulder patch in a stratigraphically equivalent position on the opposite side of the valley has a mean age of 14.1 ± 0.4 ka. The recessional moraine near location (C), inside the outer moraine ridge, has a younger mean age of 13.2 ± 0.2 ka. The rock-avalanche deposits are younger. The large continuous rock-avalanche deposit at location (F) has a mean age of 7.97 ± 0.94 ka. If sample IND-09 is considered a statistical outlier because of ^{10}Be inheritance and is disregarded, the mean age of the deposit at location F is 7.43 ± 0.11 ka. The age of the valley-parallel ridge within the discontinuous rock avalanche is 7.65 ± 0.29 ka. Nevertheless, the ages are statistically indistinguishable at 1σ confidence.

Table 2.4: ^{10}Be exposure ages for samples in Innerdalen, including mean ages for the different deposits. ε is the erosion rate, σ is the standard deviation, and CV is the coefficient of variation. For sample location, refer to Fig. 2.4. (according to Schleier et al., 2015)

Sample	Description	Location (UTM 32V)		Elev.	^{10}Be age ε=0 mm/ka	Ext. Unc	^{10}Be age ε=1 mm/ka	Ext. Unc	^{10}Be age ε=1 mm/ka, snow, moss	Ext. Unc	Deposit Mean Age		
		x (m)	y (m)	(m a.s.l.)	(ka)	(1σ ka)	(ka)	(1σ ka)	(ka)	(1σ ka)	(ka)	(CV)	(1σ ka)
IND-01	Valley-parallel ridge	487 569	6 954 441	420	7.53	0.69	7.57	0.68	7.64	0.74			
IND-02		487 555	6 954 424	420	7.26	0.60	7.31	0.63	7.37	0.64	7.65	3.7%	0.29
IND-03		487 551	6 954 380	430	7.81	0.78	7.87	0.77	7.94	0.83			
IND-04	Isolated boulder patch	486 182	6 956 410	615	13.4	1.3	13.5	1.3	13.6	1.3			
IND-05		486 122	6 956 486	625	14.1	1.4	14.2	1.3	14.4	1.4	14.1	3.1%	0.4
IND-06		486 097	6 956 546	630	14.0	1.4	14.2	1.4	14.3	1.4			
IND-07	Rock-avalanche deposit	486 485	6 955 264	455	7.22	0.62	7.26	0.58	7.35	0.64			
IND-08		486 393	6 955 311	450	7.39	0.70	7.43	0.67	7.51	0.64	7.97	11.8%	0.94
IND-09		486 371	6 955 351	445	8.90	0.93	8.96	0.83	9.05	0.87			
IND-10	Innermost terminal moraine	482 722	6 957 125	225	12.6	1.3	12.8	1.3	13	1.3			
IND-11		482 720	6 957 098	220	12.8	1.3	12.9	1.2	13.2	1.2	13.2	1.5%	0.2
IND-12		482 704	6 957 025	225	13.0	1.3	13.2	1.4	13.4	1.4			
IND-13	Outermost terminal moraine	481 867	6 957 238	230	14.4	1.3	14.6	1.4	14.9	1.5			
IND-14		481 925	6 957 088	240	-	-	-	-	-	-	14.1	8.0%	1.1
IND-15		481 740	6 957 305	220	12.8	1.3	13.0	1.4	13.3	1.4			

2.5.3 Kinematics of rock-slope failures

According to Schleier et al. (2013b) the rock-avalanche source area and its main scarp are situated at the N-facing rock slope of Skarfjellet Mountain south of the lake (Figs. 2.5, 2.6, 2.9 a, b and 2.10). Because the source areas are located on the same rock slope, similar kinematics are assumed for the different rock-slope failures. On the basis of the structural analysis of the LiDAR-derived HRDEM, the main discontinuity sets were determined as they are developed today. Similar conditions are also assumed for the past events.

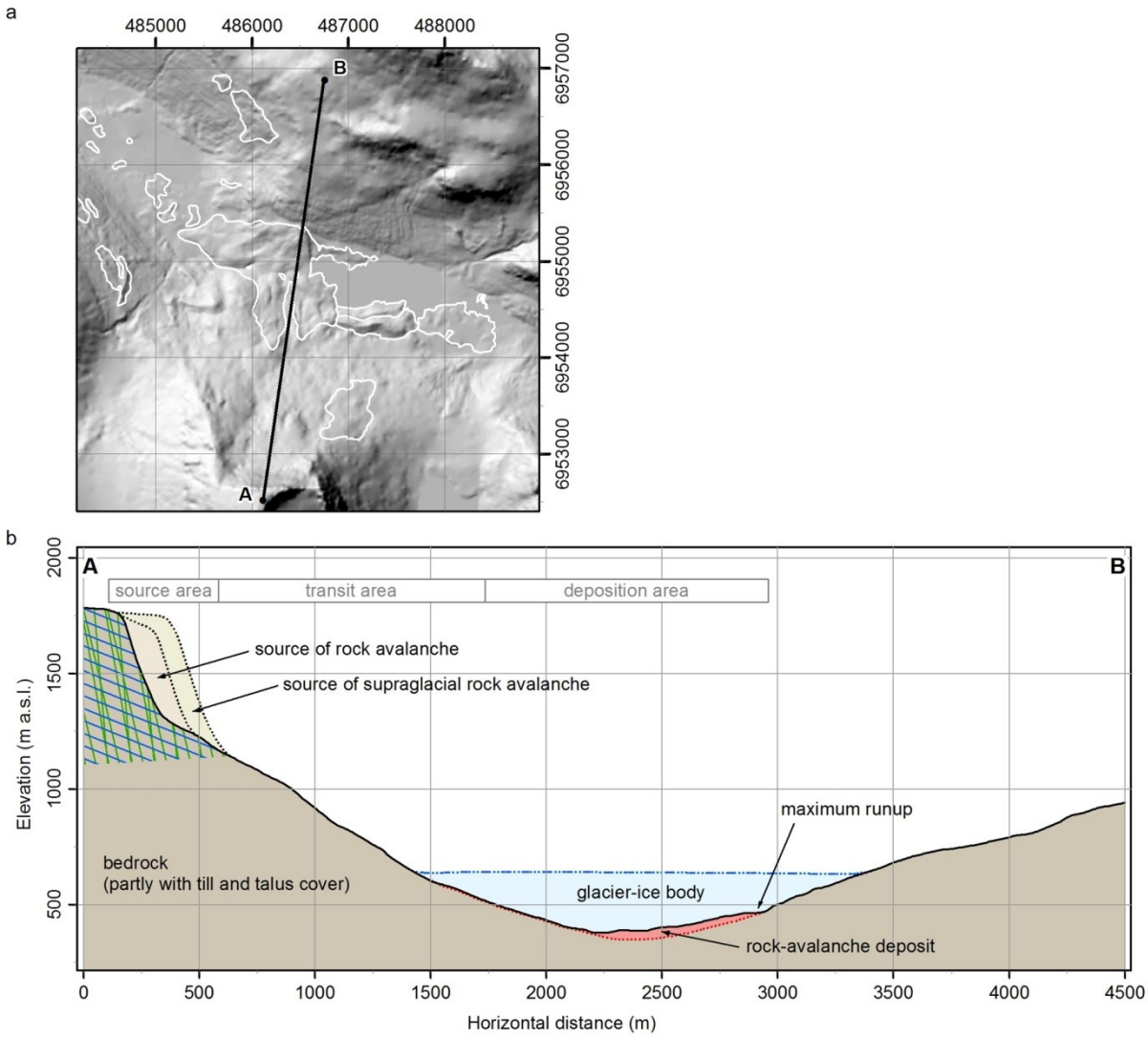

Fig. 2.10: Schematic profile across the valley of Innerdalen. (a) The trace of the profile. (b) The profile line A–B, showing the today's topography and the extent of the rock-avalanche deposit (red). Additionally shown are the apparent dip of the main discontinuity sets, including the foliation (solid blue line) and the joint sets (solid green line), and the modeled pre-failure topographies of the source areas (dotted black line), the glacier surface (dash-dotted blue line), and the pre-failure valley topography (dotted red line).

The main discontinuity sets are composed of three main joint sets with dip/dip direction of 81°/034° ± 12° (J1), 86°/331° ± 10° (J2), and 77°/354° ± 11° (J3), and foliation with 22°/003° ± 15° (f) (Table. 2.5). The latter is too shallow to be detected with TLS, and therefore, the mean orientation was derived by geological mapping. Intersections between mean surfaces of main discontinuity sets are summarized in Table 2.6.

Table 2.5: Mean orientation of main discontinuity sets in Innerdalen. Mean surfaces are derived by Dips 6.0 cluster analysis of the 85496 pole vector selections made in Coltop3D based on the TLS-derived HRDEM.

Name	Type	Dip (°)	Dip direction (°)	1σ variability (°)
J1	Joint	81	034	12
J2	Joint	86	331	10
J3	Joint	77	354	11
f	Foliation	22	003	15

Table 2.6: Orientation of intersections between the mean surfaces of the main discontinuities in Innerdalen (Table. 2.5).

Intersection	Trend (°)	Plunge (°)
J1#J2	034	80
J1#J3	346	76
J2#J3	051	66
f#J1	306	12
f#J2	060	12
f#J3	082	03

The mean orientations of the discontinuity sets and failure envelopes of possible failure kinematics are plotted in a Schmidt net (Fig. 2.11). The mean slope orientation was set to 85°/005°, and a medium friction angle of 25° was chosen for the kinematic analyses for conservative results.

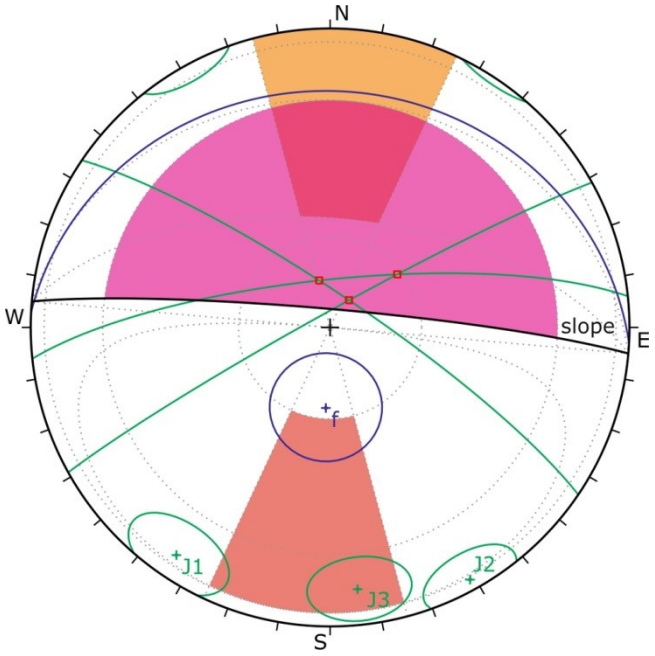

Fig. 2.11: Schmidt net plot of main discontinuity sets in Innerdalen (equal area, lower hemisphere). The discontinuities are the foliation, f, and the three main joint sets, J1, J2 and J3 (see Table 2.5). The circles display the 1σ variability of the mean orientations. The results of the kinematic analyses are outlined by the failure envelopes for planar (red), wedge (purple) and toppling (orange) failure. (Schleier et al., 2015)

The results show that only the discontinuity set J3 is critical for planar sliding with the applied friction angle. However, foliation (f) might become critical with lower friction angle or steeper dip angles. There are three critical intersections for wedge sliding between the mean joint sets showing trend/plunge of 034°/80° (intersection J1#J2), 346°/76° (intersection J1#J3), and 051°/66° (intersection J2#J3). The intersections between the joint sets and the foliation are not critical. The joint set J3 and the foliation (f) are also critical discontinuities for direct toppling.

Results from the stability and sensitivity tests performed by using simple geometries are summarized in Table 2.7. The FoS indicate that the steep intersecting wedge failures will probably fail under all conditions, even if totally dry. Planar failure along J3 also probably can occur, whereas planar sliding along the foliation (f) will probably not occur under the modeled dry conditions. However, with increasing water pressure in the fissures, FoS will decrease (<1 at around 35% water filling) showing an increased probability of failure during wet conditions. Furthermore, an increase in foliation dip angle will also raise the probability of failure. The joint sets, in general, show a low-to-medium persistence, whereas the foliation (f) is a highly persisting undulating structure. Therefore, the analyses also suggest that the possibility of planar failure along the foliation is an alternative.

Table 2.7: Factor of safety (FoS) for sensitivity analyses of deterministic stability in Innerdalen, performed by using simple column and wedge geometries. (according to Schleier et al., 2015)

Kinematics	Friction angle	Water filling in fissures				
		0%	25%	50%	75%	100%
Planar sliding along foliation	25°	1.15	1.07	0.87	0.65	0.47
	30°	1.43	1.33	1.08	0.81	0.58
	35°	1.73	1.61	1.31	0.98	0.70
Planar sliding along J3	25°	0.11	0.07	0.00	0.00	0.00
	30°	0.13	0.08	0.00	0.00	0.00
	35°	0.16	0.10	0.00	0.00	0.00
Wedge sliding along intersection J1xJ2	25°	0.07	0.05	0.00	0.00	0.00
	30°	0.09	0.06	0.00	0.00	0.00
	35°	0.11	0.08	0.00	0.00	0.00
Wedge sliding along intersection J1xJ3	25°	0.11	0.10	0.03	0.00	0.00
	30°	0.13	0.12	0.03	0.00	0.00
	35°	0.16	0.15	0.04	0.00	0.00
Wedge sliding along intersection J2xJ3	25°	0.88	0.87	0.77	0.51	0.33
	30°	1.09	1.07	0.95	0.63	0.41
	35°	1.32	1.30	1.16	0.76	0.50

2.5.4 Dynamics of rock-slope failures

2.5.4.1 Rock avalanche into an ice-free valley

The continuous rock-avalanche deposit has an estimated total volume of 22.4 × 10^6 m^3. This value was used as a reference to model the initial failure volume based on topographical constraints. It is likely that this deposit fell into an ice-free part of the valley, on the basis of the morphology and dominance of local monolithological clasts. An initial volume of 23.5 × 10^6 m^3 was assigned for modeling the rock-avalanche propagation by using DAN3D (Fig. 2.10), consistent with the erosion of the rock-avalanche deposit. The modeling results are shown as particle distributions at selected time steps in Fig. 2.12, and the runout dynamics (i.e., maximum particle velocities and average thicknesses) are summarized in Table 2.8. The associated model parameters are shown in Table 2.1.

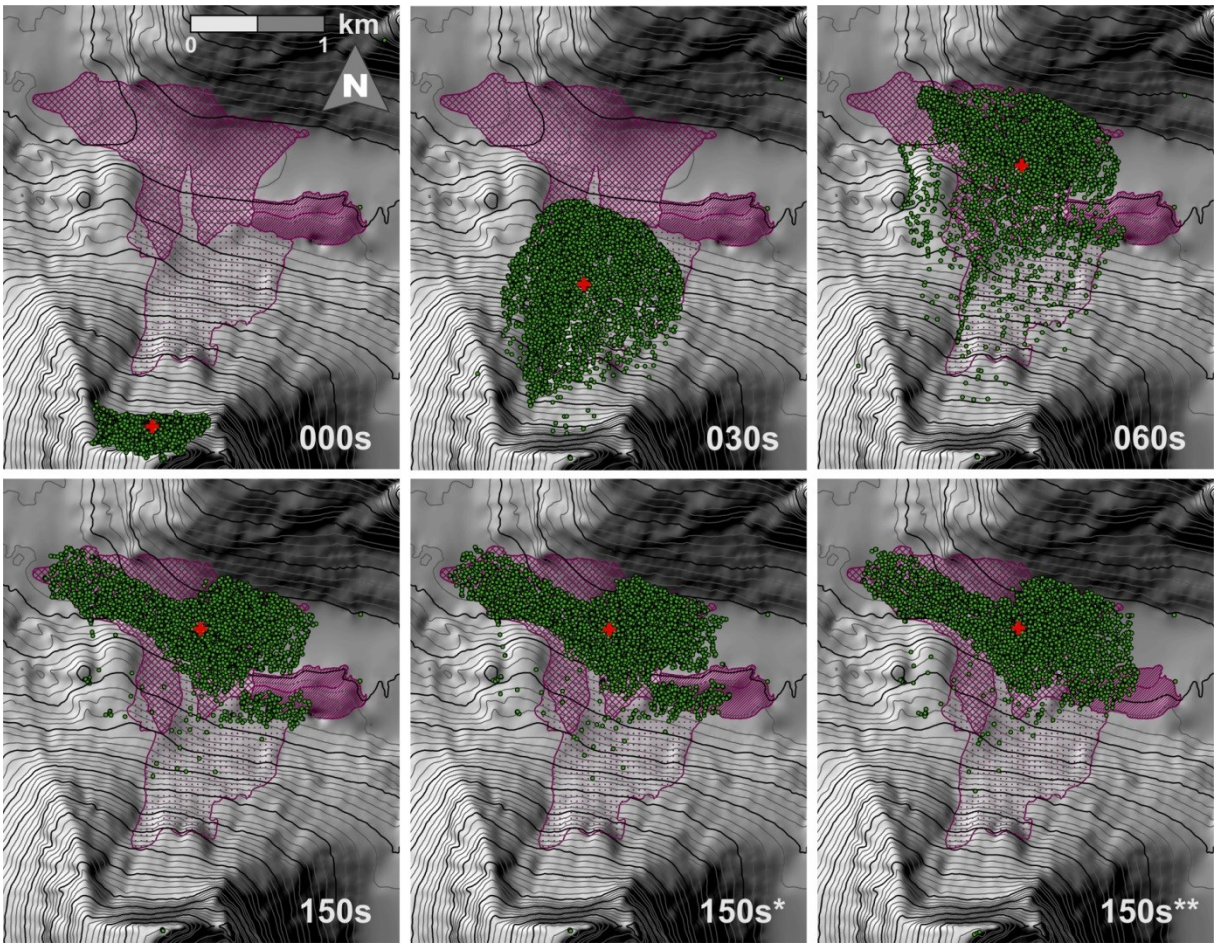

*Fig. 2.12: Propagation of the Holocene rock avalanche in Innerdalen simulated with DAN3D. The propagation into an ice-free valley is shown at four time steps (0, 30, 60 and 150 seconds) and is represented by the simulated particles (green dots) and center of gravity (red cross), superimposed on a hillshade and 25 m contour lines. The final time step of 150 s for two additional models with slightly different path topography, that is, removed valley-parallel ridges, are shown (marked with * and **). The mapped extents of the actual rock-avalanche deposits are indicated by polygons (crossed purple, main rock-avalanche deposit; dotted purple, shallow rock-avalanche deposit, that is, transit area; hatched purple, valley-parallel ridges of rock-avalanche material). For rheology settings, refer to Table 2.1. (Schleier et al., 2015)*

Table 2.8: Runout dynamics of the two rock avalanches in Innerdalen simulated with DAN3D (rock avalanche onto a glacier and such into an ice-free valley). The abbreviations are: t, modeled time step; v max., maximum velocity; av. th., average thickness.

	Rock avalanche onto a glacier (31.5×10^6 m^3)		Rock avalanche into an ice-free valley (23.5×10^6 m^3)	
t (s)	v max. (m/s)	av. th. (m)	v max. (m/s)	av. th. (m)
0	0.0	46.0	0.0	55.5
10	116.7	31.2	98.0	39.6

20	114.8	16.4	85.6	18.7
30	76.6	9.9	75.5	12.1
40	57.4	7.4	63.0	9.1
50	39.2	6.3	47.6	8.0
60	29.2	5.6	35.8	8.3
70	25.1	5.2	25.9	8.9
80	21.9	5.0	22.0	9.5
90	21.2	4.9	20.0	10.2
100	19.9	4.8	16.7	10.9
110	19.3	4.7	16.1	11.5
120	17.1	4.6	13.6	12.0
130	17.5	4.5	12.4	12.6
140	17.1	4.4	11.4	13.3
150	17.5	4.3	12.7	13.8
160	10.2	4.2	11.2	14.3
170	9.4	4.1	10.2	14.6
180	8.2	4.1	10.1	14.9
190	8.4	4.0	---	---
200	7.4	4.0		
210	10.4	4.0		
220	17.7	3.9		
230	8.0	3.9		
240	8.0	3.9		
250	6.8	3.8		
260	7.1	3.8		
270	5.5	3.8		
280	5.3	3.7		
290	6.0	3.7		
300	5.0	3.7		
310	4.6	3.7		
320	4.5	3.6		
330	4.4	3.6		
340	4.6	3.6		
350	4.4	3.6		
360	3.5	3.6		
370	4.0	3.6		
380	2.9	3.6		
390	4.2	3.6		
400	---	---		

Starting from the steep N-facing rock slope of Skarfjellet Mountain (0 s), the rock mass propagates toward NNE across the transit area following the steepest path of the natural topography and showing a maximum velocity of 75 m/s (30 s) (Table 2.8). After reaching the valley bottom, the flowing mass widens and a part of the mass starts to turn toward NW following the natural slope. The main bulk of the flow crosses the valley and runs up on the opposite slope, reaching the maximum runup height and showing a maximum velocity of 36 m/s (60 s). However, the first particles have already come to rest in the middle of the

valley. Following the runup, some particles flow back into the valley and the main mass finally turns around to follow the natural slope toward WNW. At 150 s almost all particles come to rest, and only some single ones still move with low velocities.

In order to test if it is possible to reproduce the valley-parallel ridges with the same rock-avalanche event, the model was applied with slightly different path topography, that is, the ridge deposits were removed. There were no significant differences in the propagation. Therefore, only the final time steps at 150 s of the additional models (indicated with * and **) are shown in Fig. 2.12. Time step 150 s* shows the modeled deposit obtained by using a path topography where the second morphological ridge was removed, whereas for 150 s** both ridges have been removed. The results indicate that more material would be deposited in the area of the ridges but only up to half of the area would be covered.

The mean runup height is estimated to be 80 m based on field estimates for the mean thickness of the deposit (Fig. 2.9 c). Because the lake water level is at 396 m a.s.l., and the maximum runup is mapped at 462 m a.s.l., the minimum runup height is 66 m. The maximum runup height is assumed to be 100 m, considering the depth to the bedrock under the lake and the erosion of the rock-avalanche deposits (Fig 2.10). Therefore, the calculated velocities for the flowing mass are 36 m/s for 66 m, 40 m/s for 80 m, and 44 m/s for 100 m height differences. This is in concordance with the modeled velocity of 36 m/s at the time step 60 s, which marks the maximum runup (Fig. 2.12).

Additionally, the Fahrböschung of the continuous rock-avalanche deposit and the modeled extent of particles were determined. For the most distal part of the deposits, the Fahrböschung is 23.0° for modeled particles, and 22.0° for mapped deposits (Table 2.9). For the runup area, it is 25.7° for modeled particles, and 25.3° for mapped deposits. Therefore, modeled and field-derived values are in concordance. The travel angle calculated by DAN3D is 26.6°.

Table 2.9: Runout characteristics of the rock avalanches in Innerdalen (rock avalanche onto a glacier and such into an ice-free valley). The Fahrböschung is determined by using the modeled most distal particle distribution or the mapped debris extent. h is the vertical fall height and l is the horizontal travel length. The travel angle and volume are calculated by the DAN3D simulation. The ages are based on TCN dating (Table 2.4). (modified after Schleier et al., 2015)

	Rock avalanche onto a glacier surface	Rock avalanche into an ice-free valley	
	Model	Model	Map
h (m)	1240	1493	1491
l (m)	5280	3510	3695
h/l	0.235	0.425	0.404
Fahrböschung (°)	13.2	23.0	22.0
Travel angle (°)	16.5	26.6	-
Volume (10^6 m^3)	31.5	23.5	-
Age (ka)	14.1 ± 0.4	7.97 ± 0.94	

2.5.4.2 Rock avalanche onto a glacier surface

Remnants of the rock avalanche onto the glacier surface are the preserved discontinuous rock-avalanche deposits. The material of the following deposits (geomorphological units) were interpreted to originate from this supraglacial rock avalanche: the boulder patch above the lake, the two valley-parallel ridges (G and H), the isolated boulder patches (D and E), the terminal-moraine ridges (A, B, and C), and the isolated mounds of kame deposits. These deposits have a total estimated volume of 28.9×10^6 m^3. This value was used as a reference to model the initial failure volume based on topographical constraints. However, the volume represents a minimum value because, besides the named deposits, similar boulders are distributed along all slopes of the valley and mixed with talus and till. For modeling the rock-avalanche propagation with DAN3D, an initial volume of 31.5×10^6 m^3 was finally assigned to account for these circumstances (Fig. 2.10). The results of the best-fitting model are shown as particle distribution of eight time steps in Fig. 2.13 and the modeled runout dynamics in Table 2.8. The associated rheology settings are summarized in Table 2.1.

Starting at the steep N-facing rock slope of Skarfjellet Mountain (0 s), the mass travels toward NNE, following the natural slope, and begins a slight shift, traveling more toward N after reaching the glacial-ice surface (30 s). At this time step, the mass shows a maximum velocity of 76 m/s and an average thickness of around 10 m (Table 2.8). The whole area of the boulder deposit above the lake is crossed by the flowing mass. Almost the whole mass propagates onto the glacier after 60 s, showing a mean flow direction toward NNW. The maximum velocity rapidly decreases to 29 m/s and the average thickness decreases to 6 m because of the widening of the propagating mass. After 90 s, the mass spans the glacier on its entire width as a shallow deposit with an average thickness of 5 m and a width of around 2 km. The main mass propagates toward NNE with a maximum velocity of 21 m/s. Almost the whole area of the preserved valley-parallel ridges is covered. The front of the mass now reaches the location of the isolated boulder deposit at the northern slope of the valley. Subsequently, the main propagation is characterized by the further widening of the extent of moving mass, with spreading over the entire glacial surface. At this point, the maximum velocities gradually decrease, and the average thickness is more or less constant at 4 m (since 150 s) until the central main part of mass stopped after 270 s. However, there are still movements but only in the frontal part, showing velocities up to 5 m/s. The final extent of the rock-avalanche propagation is reached after 390 s. At this time, almost the entire mass has stopped, and only single particles show small displacements. A huge part of this rock avalanche has now developed as relatively shallow supraglacial deposits. The whole rock-avalanche material was deposited below the contemporaneous equilibrium line altitude (ELA) (Fig. 2.13). The travel angle calculated by DAN3D is 16.5°, whereas the Fahrböschung was measured at 13.2° for the modeled particles (Table 2.9).

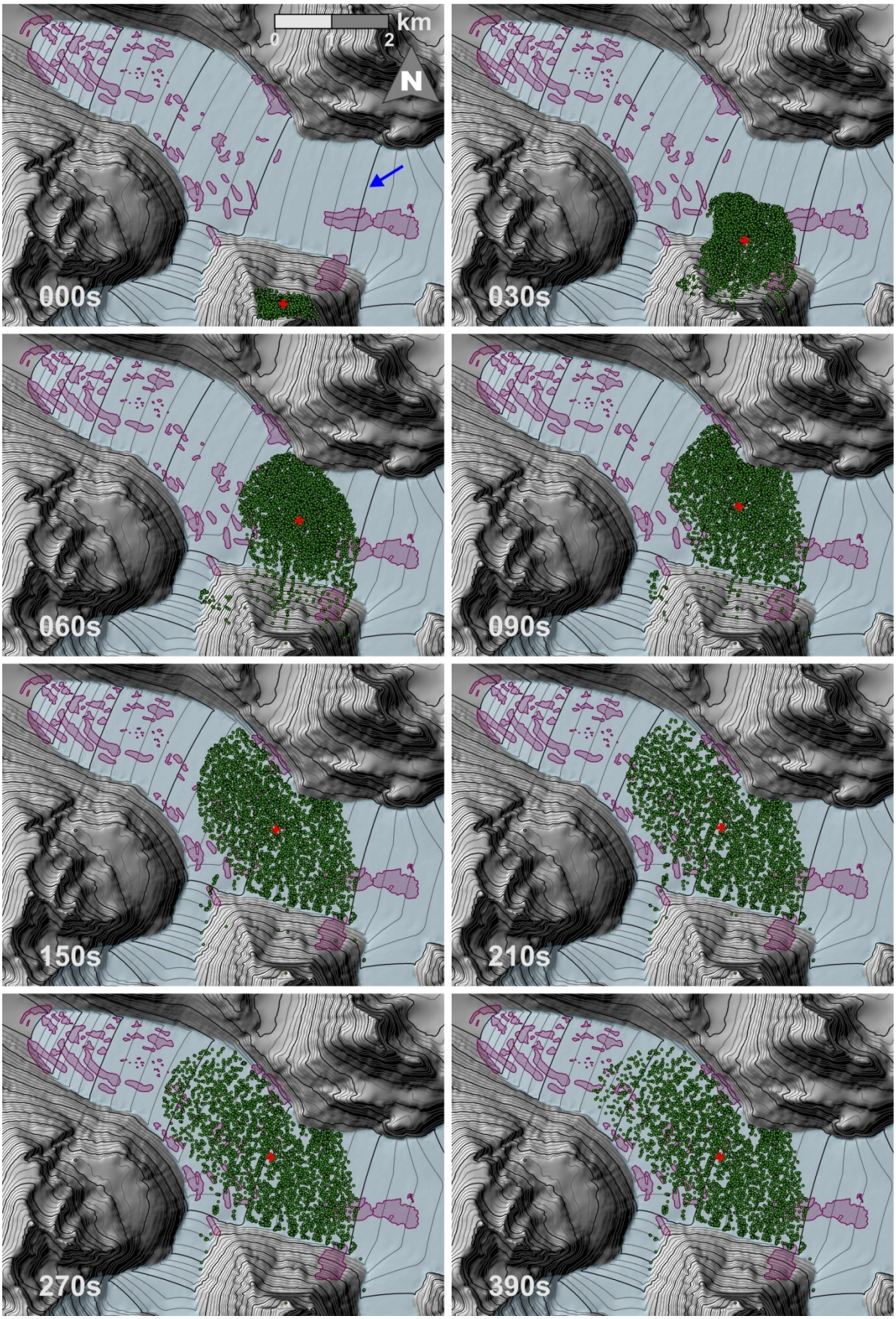

Fig. 2.13: Propagation of the Pleistocene supraglacial rock avalanche in Innerdalen simulated with DAN3D. The propagation onto a proposed glacial-ice body is shown at eight time steps (0, 30, 60, 90, 150, 210, 270 and 390 seconds) and is represented by the simulated particles (green dots) and center

of gravity (red cross), superimposed on a hillshade and 25 m contour lines, including the proposed glacial surface (light blue). The mapped extents of the preserved deposits of the supraglacial rock avalanche are indicated by polygons (hatched purple). For rheology settings, refer to Table 2.1. The blue arrow in time step 0 s indicates the approximate paleo-equilibrium-line altitude. (Schleier et al., 2015)

2.6 Discussion

The spatial distribution and interpretation of landforms already provided a hypothesis for the relative timing of multiple rock avalanches and paleoenvironments in Innerdalen, including rock avalanching onto a glacier (which is not present any more) and into the ice-free valley (Schleier et al., 2013b). Our additional mapping, orthophoto and DEM analyses, TCN dating, and runout modeling support this hypothesis and presents further details. The mean surface-exposure ages of boulders on the different deposits indicate that one large rock avalanche occurred in the Late Pleistocene (~14 ka) under paraglacial environmental conditions and another one during the Holocene (~8 ka) under a temperate climate. Deposits of uncertain genesis (perhaps glacially modified supraglacial rock-avalanche material) and landforms of rock-avalanche material are left as remnants in today's valley.

2.6.1 Kinematics of multiple rock-slope failures

Structural and kinematic analyses show that failure with the geometry of one large wedge does not provide a feasible solution because of the low persistence of the limiting joint sets. The main discontinuities and their intersections fragment the rock mass and detach rock blocks. Because the lower slope (dip ~40°) is gentler than the upper rock slope (dip ~80–85°) (Figs. 2.9 a, b, and 2.10) the very steep dipping intersections do not daylight on the slope. However, the sensitivity analyses reveal that planar failure along the foliation is possible alternative under specific, water saturated conditions. Because a shallow dipping main thrust fault is present at the rock slope (Figs. 2.2 and 2.9 a), tectonic stress might have weakened the rock mass or produced possible failure surfaces. It was not possible to detect this structure within the LiDAR data.

If different lithologies are involved, the stratigraphy of the source area is often preserved in the deposits because the former lowest lithology travels at the front of the rock avalanche and becomes the most distal deposit (Heim, 1932; Hewitt, 2009b). Unfortunately, in most of the deposits in the study area, the clast lithology is rather monolithic (similar gneisses). However, the conspicuous quartzitic boulders provide some indication of provenance. For instance, the northern isolated boulder deposit (D) shows a suspiciously high amount of quartzitic boulders and in the deposits of the terminal-moraine ridges it decreases from the outermost (A) to innermost (C) ridge (Fig. 2.5). This suggests that the quartzitic rocks mark the lower limit of the rock-slope failure source area, and that the influence of the main thrust fault on the planar sliding component is feasible. Geological constraints and changes in

stress field due to glaciation and glacial debuttressing are factors that increase destabilization. The paleostress field is therefore assumed to be complex, and strong changes are likely to have occurred as the rock face is located at the former margin of the main valley glacier in an area characterized by the confluence of several valleys (see valley topography in Figs. 2.6 and 2.13).

It appears that the final rock-slope failures were induced by climatic factors that reduced shear strength and might have increased shear stress. In paraglacial environments, it is common that the decay of ice bodies and the thawing of permafrost cause an increasing amount of meltwater and joint-water pressure and the disappearance of ice bridges connecting disaggregated rock mass (Ballantyne et al., 2014). Furthermore, permafrost limit, ice in fractures, water infiltration, and seasonal climatic pattern based on freeze-and-thaw cycles (e.g., frost cracking and expansion) are identified to strongly control rockslide deformation (Blikra & Christiansen, 2014). As an example, frost cracking and expansion of ice in fractures during winter freezing can decrease shear strength and trigger failure.

According to the mean surface-exposure ages, both rock avalanches occurred under such conditions. The earlier avalanche (~14 ka) failed during the Late Pleistocene Bølling/Allerød interstadial (~14.7–12.9 ka) under paraglacial environmental conditions. The younger avalanche (~8 ka) failed under a more temperate climate during the Atlantic chronozone often referred to as the mid-Holocene climatic optimum (~8–7 ka) (Nesje & Dahl, 1993; Wanner et al., 2008). This followed the Boreal period, a time of rapid climate change (9–8 ka) including the so-called 8.2 ka cooling event (Alley & Ágústsdóttir, 2005). It is noted that both events immediately followed significant cooling periods in the northern hemisphere (Older Dryas and the 8.2 ka event). The permafrost limit dropped to lower elevations during the cooling events, leading to more stable conditions. However, during the warming period, the permafrost limit moved upward (i.e., higher elevations) and increased the probability of failure, especially in the lower sections. Additionally, rock-slope deformation might be weaker during long-lasting glacial periods because of relatively stable cold temperatures but stronger during relatively warmer climatic periods because of more intensive seasonal temperature patterns. These behaviors are consistent with modern observations of rock slopes at the permafrost limit made by Blikra & Christiansen (2014). Furthermore, positive feedbacks may have been caused because the rock avalanches occurred from the same rock slope (Figs. 2.5 and 2.6) owing to accelerated decompression along the slope (Hermanns et al., 2006a).

2.6.2 Late Pleistocene rock avalanche onto a glacier

The Late Pleistocene rock avalanche (~14 ka) appears to have propagated onto a glacial landform that is not present any more. Remnant deposits of this event are the discontinuous rock-boulder deposits showing distinct geomorphological units (Figs. 2.5 and 2.6). Although they are separated from each other by several kilometers, these deposits are composed of identical material and have similar characteristics.

A carapace of large rock boulders of mainly angular and sub-angular forms with low sphericity onto fine grained material (Figs. 2.7 and 2.8) is typical for rock-avalanche deposits (c.f., Hewitt, 2009a). A high angularity and a low sphericity indicate relatively fresh material without reworking or transportation over long distances. Because the rock-avalanche runout crossed onto a glacial surface, the debris material was exposed to supraglacial processes; but due to the deposition in the ablation zone below the approximate paleo-ELA (equilibrium line altitude) it was not buried by snow (Fig. 2.13). Based on the lateral moraine deposits, the contemporaneous paleo-ELA is estimated to be around 700 m a.s.l. (around 800 m lower than today) which is in concordance to Lie et al. (2003) and Wasrud (2010), who proposed a paleo-ELA around 500 m lower than today during the YD, and 1 000 m lower during the LGM, respectively.

The debris material (e.g., rock-avalanche material) is modified by supraglacial processes and affects glacial behavior in different ways (Hewitt, 2009b; Shulmeister et al., 2009; Reznichenko et al., 2011; Shugar & Clague, 2011): Fine grained material is winnowed by supraglacial washing by meltwater flow and strong winds, leading to a concentration of large rock boulders and lack of fines on the surface. The shape of the rock-avalanche deposit is distorted, and elongated boulders are oriented with their long axis parallel to the glacial flow during supraglacial transportation. Melting of the ice body leads to a boulder accumulation at the margin. Supraglacial debris cover generally insulates the glacier and could induce air circulation in cavities that may significantly retard glacier ablation. If the debris is distributed irregularly on the glacial surface, it leads to an asymmetrical melting. Furthermore, a rock-boulder carapace is likely to lead to an acceleration of the glacial flow.

2.6.2.1 Isolated boulder patches

The isolated boulder patches (D, E), and the patch above the lake are remnant deposits of a rock avalanche that occurred onto a Late Pleistocene glacier (Figs. 2.5, 2.6 and 2.9a). The northern isolated boulder patch (D) is interpreted to be, at least partly, deposited directly along the opposite glacial-ice margin (Fig. 2.6), which is in concordance with the results of the runout modeling (Fig. 2.13). The granaulometric characteristics, in this case, the high angularity and the highest amount of large boulders (Figs. 2.7 and 2.8) confirm this interpretation as this type of boulders are reported to travel at the front of a rock avalanche propagating over a glacier (Delaney & Evans, 2014). Many large boulders lying broken but closely spaced (jigsaw boulder) also indicate that no secondary re-transportation took place. Therefore, the deposit's mean age of 14.1 ± 0.4 ka (deposit D, Table 2.4) is proposed to represent the minimum age of the rock avalanche and sets it into the Late Pleistocene.

In contrast, we hypothesize that the southern isolated boulder patch (E) was transported into the current position as supraglacial debris. The modeled runout extent shows that the rock avalanche could not reach the southern ice margin directly (Fig. 2.13). The lack of very angular boulders but the existence of sub-rounded ones and their smaller sizes (Figs. 2.7 and 2.8) suggest more reworking and an origin from the main bulk mass. The boulder patch above the lake was deposited directly by the rock avalanche. The runout model (Fig. 2.13) shows that the area was part of the transition area and was covered completely with debris

at least during the propagation. It is likely that some material was also deposited there. The deposit shows a sharp boundary to the lower slope that runs along a valley-parallel morphological edge. On the basis of the spatial distribution of the isolated boulder patches and their lower limits, the thickness of the glacial ice is estimated to have been around 300–350 m at time of occurrence (Figs. 2.5, 2.6 and 2.9a). However, the rock boulders in the till and talus material downslope of these deposits are interpreted to also belong to this supraglacial rock avalanche and to be deposited during the final melting of the glacier.

2.6.2.2 Moraine deposits

The prominent moraine ridges in the lower part of the valley (A, B and C) are interpreted as terminal moraines composed of primary supraglacial rock-avalanche material (Figs. 2.5 and 2.6). In contrast to typical moraine deposits or glacial till they have an inverse grading and a carapace of large angular and sub-angular rock boulders on top of a fine grained matrix (Fig. 2.9 d). The runout model indicates that the rock avalanche did not reach and overtopped the frontal ice margin (Fig. 2.13). Furthermore, the morphology of such deposition would be rather flat because of the spreading on an unconfined flat surface of valley-fill sediments, and it would not form distinct ridges. Also, the granulometric characteristics (Figs. 2.7 and 2.8) of the deposits (A, B, C) indicate a slightly longer transportation and reworking of material. These characteristics are, for instance, a higher amount of small boulders, sub-rounded forms, and high sphericity. This is in contrast with the directly deposited northern isolated boulder patch (D) but is comparable to the southern isolated patch deposit (E) for which a supraglacial transport is also assumed. The lack of overtopping of the glacial tongue and entrainment of moraine material makes this example different from other cases as, for example, those studied by Hermanns et al. (2014b) at the foot of Aconcagua Mountain.

According to the runout modeling, the rock-avalanche material was deposited as supraglacial debris on the glacial body spreading almost over its whole width but most material should have been deposited on the northern part of the glacier (Fig. 2.13). The large but non-uniform debris cover likely led to the acceleration of glacial flow and asymmetrical melting of the ice body (Hewitt, 2009b; Shugar & Clague, 2011) which can explain the limitation of the moraine ridges to the southern side, and the boulder accumulation in hummocky surfaces on the northern side of the outer valley (Figs. 2.5 and 2.6). The above-referenced historical examples show that the glacial flow is rather stagnant. The terminal-moraine ridges are interpreted to have developed during several small glacial advances and retreats, which partly were induced by the supraglacial debris of the rock avalanche. The isolated concentric mounds on the valley floor behind the recessional moraine show granulometric characteristics similar to those of the terminal-moraine ridges (Fig. 2.9 e) and are interpreted to be kames composed of supraglacial rock-avalanche material.

Because the material of terminal-moraine deposits has been re-deposited by glacial processes, the TCN-derived ages do not show the age of the rock-avalanche event itself. The ages of the outermost (A) and innermost (C) terminal-moraine deposits show slightly

different results (14.1 ± 1.1 ka and 13.2 ± 0.2 ka), but are indistinguishable within their 1σ error limits (Fig. 2.5 and Table 2.4). These ages suggest that the valley ice was at an intermediate deglacial extent between the LGM and YD cooling. However, the effects of erosion, snow, and moss cover might be overestimated or the boulders may have a significant concentration of inherited ^{10}Be. If so, the ages would be 13.6 ka and 12.8 ka, close to the beginning of the YD re-advance, as previously proposed for this site (Sollid & Sørbel, 1979).

It is interpreted that the last advance was followed by a relatively fast decay of the glacier, during which the remaining supraglacial rock-avalanche debris was deposited in till material along the valley slopes, as kame deposits and in glaciofluvial sediments in the valley bottom (Figs. 2.5 and 2.6). The lack of moraine ridges in the upper valley suggests that there was no further glacial advance and that the deglaciation proceeded through stagnation processes rather than a systematic ice marginal retreat back to the cirques or ice caps.

2.6.2.3 Valley-parallel ridges

The most curious deposits in Innerdalen but most difficult to interpret are rock-avalanche materials forming the prominent valley-parallel ridges (G, H) located along the lake in the upper valley (Figs. 2.5, 2.6, and 2.9 a). Their geomorphology and spatial distribution is not typical for the deposit of one large catastrophic rock avalanche. The runout model shows that such an origin is not reasonable (Fig. 2.12), but it yields solutions if the rock avalanche fell on a former valley glacier (Fig. 2.13). This explanation is supported by the irregular asymmetric distribution of the deposits within the valley that suggests a stagnant ice body that hindered the rock avalanche from spreading over the entire valley. Furthermore, the boulder concentration and lack of fines can be explained by the above mentioned modification of supraglacial debris. The large angular forms (Figs. 2.7 and 2.8) and jigsaw boulders indicate short transportation distances and less re-transportation. However, the surface-exposure ages of this deposit do not fit with the interpretation of being connected to the Late Pleistocene rock avalanche onto a glacier because they date it into the Holocene (7.65 ± 0.29 ka) (Table 2.4). It is remarkable that this age is similar to the Holocene rock avalanche (7.97 ± 0.94 ka), although the stratigraphic position of the ridge deposits rather suggests a relatively older age (Figs. 2.5 and 2.9 a). However, the sampling site shows evidence for a possible reactivation of the deposit, such as internal scarp and slide morphology. If reactivation occurred, the TCN ages would not represent the primary deposition of the rock-avalanche boulders.

Four alternative interpretations are proposed that explain the landform and the age. The first three are based on a re-deposition of the primary Pleistocene rock-avalanche material, and the fourth is based on a multiphase deposition of the Holocene rock avalanche.

(1) The rock-avalanche material was primarily deposited on the mountain slope and was entrained and re-deposited by snow avalanches. Hence, the ridges represent snow-avalanche impact ramparts, that is, landforms formed by erosion and deposition of a high-energy debris-rich snow-avalanche impact (Ballantyne, 1989; Matthews & McCarroll, 1994;

Owen et al., 2006). Typical features are valley-parallel ridges away from the valley wall. However, in other parts of the world, these described ramparts have been reported to be much lower in relative height and to also include fine grained sediments entrained by the snow avalanche.

(2) The rock-avalanche material was primarily deposited onto the glacial landform as supraglacial debris and/or crevasse infill, then modified and re-deposited. Supraglacial processes (Hewitt, 2009b; Shugar & Clague, 2011) led to the accumulation of boulders on the southern side of the valley, and the debris carapace favored the survival of a persistent stagnant ice body in the subsurface. Such a landform is also likely to survive in the shadow of the N-facing slope that limits direct insolation to only a few months per year. The dead ice body was preserved until the Holocene rock avalanche (7.97 ± 0.94 ka) formed a natural dam that impounded a lake. The increased water circulation caused its fast meltdown and the volume loss would have led to a destabilization and re-deposition of the ice-cored rock-boulder deposit. The re-deposition age postdates the Holocene rock avalanche by only a few hundred years, supporting this interpretation.

(3) The rock avalanche occurred similarly to the second alternative, but the development is slightly different. The material was deposited and accumulated along the ice margin during the glacial decay, forming a prominent ridge deposit. Again, the lake impoundment induced by the Holocene rock avalanche caused the destabilization and re-deposition. This interpretation as a gravitational slump due to rising water level and increased pore-water pressure requires fine grained sediments in the subsurface. However, glacial and fluvial valley-fill sediments are common along the valley bottom, and fine matrix sediments are likely to exist below a rock-avalanche carapace. Again, the time delay between the Holocene rock avalanche and the re-deposition is plausible for this interpretation.

(4) A Holocene multiphase rock-slope failure occurred and moved into the ice-free valley, forming both the ridge deposits and the continuous rock-avalanche deposit. Such a multiphase event might be composed of several sub-events and might have lasted over a time period of several days or weeks, similarly to the Randa rockslide (30×10^6 m^3) (Sartori et al., 2003; Willenberg et al., 2008b; Gischig et al., 2011). The complex interaction and the smaller volumes of the sub-events might develop atypical rockslide deposits such as a steep talus cone with a relatively short runout length according to its total volume. The probable overtopping of deposits might be misleading for age interpretation. Here, the ridges are related to the lateral spreading and differential movements within the dry granular flow and to secondary rockslides oblique to the initial flow direction as described by Strom (2006). Additionally, the process of rock-avalanche jumping (Strom, 2006; Strom & Abdrakhmatov, 2013) should be taken into consideration because the slope morphology might trigger such runout behavior and squashing and fluidizing of the debris at impact might form similar ridges. The main advantage of a multiphase interpretation is that it could simply explain the TCN ages of both the valley-parallel ridges and the continuous rock-avalanche deposit, which are similar within the error margins.

2.6.2.4 Flat boulder patch

The flat boulder patch (I) south of the river is interpreted to not be connected with the rock avalanche onto the glacier and certainly not with the Holocene event because of its geomorphology (i.e., relatively flat and partly hummocky surface) and the interaction with moraine deposits (Figs. 2.5 and 2.6). The material is proposed to be re-transported rock-fall and rock-avalanche material, which might also be affected by a secondary glacial advance as described by Cook et al. (2013). The source of this material is suspected to be located higher up in the catchment where other rock-avalanche deposits of considerable size exist (Hermanns et al., 2013a).

2.6.3 Holocene rock avalanche into an ice-free valley

The other rock avalanche is dated to the Holocene with an age of 7.97 ± 0.94 ka. On the basis of the geomorphology, this event is clearly identified by its continuous rock-avalanche deposit (F) composed of typical material (Figs. 2.7 and 2.8). It shows typical flow structures, for example, lateral levees and frontal rims (Dufresne & Davies, 2009), and a high runup area, indicating a high landslide mobility (Figs. 2.5, 2.6 and 2.9 c). These structures, the extent over the whole valley width, and the stratigraphic position overlying moraine deposits suggest the post-glacial origin and proposed propagation into the ice-free valley. The large jigsaw boulders indicate less post-depositional reworking. Furthermore, the rock avalanche forms a landslide dam that has been stable since its formation and can be classified as an IIa-ii-2-type event according to the classification of rockslide dams proposed by Hermanns et al. (2011c).

The runout model shows a good concordance with the mapping results such as the spatial distribution of the deposit (Fig. 2.12), the process velocities, and the Fahrböschung (Table 2.9). This verifies that the applied model represents reliable results for the propagation of rock avalanche in the ice-free valley. The final extent of modeled particles (150 s) fits well with the mapped extent, with special regard to runout length and runup height. Nevertheless, some areas mapped as rock-avalanche deposit are not covered by particles in this final time step, for instance, the transition area and the opposite slope west of the runup. However, almost all such areas have been crossed by particles during the mass propagation, especially at time step 60 s. It is likely that the material composed of large angular boulders would also have been deposited there because of its relatively high friction. This frictional effect might be underestimated because such changes in path rheology cannot be applied in the model.

The comparison of the modeled rock avalanche onto a Late Pleistocene glacier and the ice-free Holocene event shows obvious differences in runout behavior (Figs. 2.12 and 2.13). The Late Pleistocene rock avalanche shows longer duration of propagation (Table 2.8) and longer runout distances (Fahrböschung of 13° against 23°) (Table 2.9), although the travel path is very shallow and the fall height is much lower because of the modeled glacier surface. This indicates an increased landslide mobility due to a lower basal friction when propagating over the glacier. The model further shows a high component of spreading and

enlarged extent of the rock-avalanche mass because of propagation onto a relatively smooth, wide, and subsequently moving glacial surface. In contrast, the Holocene rock avalanche shows a more confined flow, constrained by the steep topography of the ice-free valley.

2.7 Conclusions

This study presents the first description of remnant deposits of a rock avalanche onto a Late Pleistocene glacial-ice body in a deglaciated valley that will improve the identification and interpretation of similar deposits in other areas of Norway and glacierized mountain areas around the world. The plausibility of the interpretation was proven by TCN dating and numerical runout modeling (DAN3D) that reveals consistency with field observations. Furthermore, the study contributes to the understanding of the paleoenvironmental conditions of rock-slope failures and Quaternary valley development in the Innerdalen Valley, which might be an example for similar valleys in western Norway.

(I) Complex deposits of rock avalanche onto Late Pleistocene glacier: The studied rock avalanche onto a Late Pleistocene glacier is preserved in discontinuous and complex boulder deposits that are composed of typical rock-avalanche material, that show distinct geomorphological characteristics, and are separated from each other by kilometers. Five distinguished types of deposits support the interpretation of supraglacial deposition, modification, re-transportation, and re-deposition of rock-avalanche debris and might further indicate the thickness, extent, and response of the former ice body: (1) isolated boulder patches high above the valley floor (e.g., runout across the whole glacier), (2) terminal-moraine ridges (e.g., no direct deposition by overtopping of the glacial tongue but due to landslide-induced glacial advance), (3) kame mounds (e.g., stagnation style deglaciation), (4) irregular hummocky boulder accumulations (e.g., irregular debris cover and asymmetrical ice decay), (5) valley-parallel ridges (e.g., irregular debris accumulation along the source slope and asymmetrical ice decay).

(II) Paleoenvironments and runout of multiple rock avalanches in Innerdalen Valley: At least two rock avalanches occurred from the same source area underlain in gneissic rocks at the N-facing steep rock slope of Skarfjellet Mountain since the Late Pleistocene. The feasible kinematic for the rock-slope failures are a combination of wedge failures related to three main joint sets and planar sliding along the shallow dipping foliation. Both events followed a significant cooling period, and destabilization was probably induced by increased joint water pressure due to the decay of glacial ice and permafrost (rising permafrost limit). (1) A rock avalanche with a volume of 31×10^6 m^3 occurred at 14.1 ± 0.4 ka under paraglacial environmental conditions between the Older and Younger Dryas. It propagated onto a glacial-ice body, which filled the entire valley with a thickness of 300–350 m and shows increased runout extent due to the wide area and low basal friction of the ice surface (Fahrböschung of 13°). The material was mainly deposited as supraglacial debris that was subsequently modified, re-transported and re-deposited, and affected the glacial behavior causing asymmetrical decay and glacial advance. The remnants of this event are the

complex discontinuous rock-avalanche deposits summarized above. (2) Another rock avalanche with a volume of 23×10^6 m^3 occurred at 7.97 ± 0.94 ka under temperate environmental conditions in the mid Holocene climatic optimum. It propagated into the ice-free valley and shows a Fahrböschung of 22°. The narrow topography constrained and confined the flow. The remnant of this event is the continuous rock-avalanche deposit that shows typical characteristics such as boulder carapace, frontal rims, lateral levees and runup deposit on the opposite slope. It further developed a natural dam that is assumed stable since origin. The associated lake impoundment might have induced destabilization and re-deposition of former Late Pleistocene rock-avalanche deposits.

3 Paleodynamics of multiple rock avalanches in Innfjorddalen: rock avalanching onto marine sediments exposed by isostatic rebound

This chapter is based on the manuscripts Schleier et al. (2013b) and Schleier et al. (2015, submitted).

Schleier, M., Hermanns, R.L. & Rohn, J. (2013b). Spatial distribution of rockslide deposits and their morphological features suggest timing and palaeo-environmental conditions for rock slope failures in Innerdalen and Innfjorddalen, Møre og Romsdal county, western Norway. *In:* R. Genevois & A. Prestininzi (Eds.), International Conference on Vajont – 1963-2013 – Thoughts and analyses after 50 years since the catastrophic landslide, Padua, Italy, 8-10. October 2013. *Italian Journal of Engineering Geology and Environment*, Book Series (6): 493-505.

Schleier, M., Hermanns, R.L., Oppikofer, T. & Rohn, J. (2015, submitted). Rock avalanching onto marine sediments exposed by isostatic rebound, the Innfjorddalen case, Western Norway. *Geomorphology*.

3.1 Abstract

Multiple rock avalanches and their deposits can create distinct geomorphological features that can be challenging to interpret if they occur in valleys affected by other fast geological processes such as glaciations and isostatic rebound. For the runout behavior of rock-avalanche events process volume and path topography is supposed to be the important factors. However, the material distribution along the travel path such as rock-boulder deposits or highly water saturated sediments is also of huge influence. This chapter presents a detailed description of deposits and geomorphological features of multiple rock-slope failures, including one rock avalanche that propagated onto water saturated sediments into the Innfjord and that was deposited below the former water level. As the deposits are exposed on the today's valley bottom as an effect of post-glacial isostatic rebound, this site depicts the first described example to study such deposits directly. At least three rock-slope failures occurred from the same source area at Gråfonnfjellet Mountain since the Late Pleistocene from which rock-boulder deposits are distributed over an area of around 1.44 km^2 along the valley bottom. These events were a rock avalanche with a volume of 15.1 × 10^6 m^3 that occurred at 14.3 ± 1.4 ka, one of 5.4 × 10^6 m^3 at 8.79 ± 092 ka, and a historic event of 0.3 × 10^6 m^3 in the year AD 1611/12. Typical deposits and landform

characteristics of the previous events are a stratified succession of continuous rock-boulder deposits (1.38 km^2) associated with the different rock-slope failures, showing lobate forms with a runup on opposite slope, frontal rims, parallel ridges and rockslide dams. The most conspicuous geomorphological features are isolated hills of rock-boulder deposits (0.61 km^2), interpreted to be “toma-hills”, which are disconnected from the main deposits by a 520 m wide area of deformed and a 180 m wide area of undeformed valley-fill sediments. Trenches and ground penetrating radar survey of these deposits indicate that these deposits are highly deformed or liquefied. Furthermore, numerical runout modeling of multiple rock-slope failures using DAN3D, confirms the interpretation of landforms and source areas, and exhibits their different runout behavior. Structural and kinematic analyses of high resolution LiDAR scans indicate a jointed source rock with four main discontinuity sets with dip/dip direction of 63°/156° ± 13° (sub-parallel to foliation), 60°/309° ± 11° (exfoliation), 69°/347° ± 12°, and 75°/098° ± 12°. The most feasible kinematics for large scale rock-slope failure is a wedge failure along an intersection of joint sets. However, planar sliding along exfoliation joints and a toppling along sub-parallel foliation joints are feasible for small-scale events. As this study is the first example that describes the characteristics of rock avalanches propagated into a fjord and exposed by isostasy, it will help to improve the identification and interpretation of similar deposits in other areas characterized by isostatic rebound.

3.2 Introduction

Large rock-slope failures are widespread hazardous phenomena in glacially overprinted mountain areas such as western Norway (Blikra et al., 2002; Braathen et al., 2004; Blikra et al., 2006; Longva et al., 2009; Böhme et al., 2011; Hermanns et al., 2012a; Saintot et al., 2012; Oppikofer et al., 2013). Especially rock avalanches pose a certain threat due to high energy release, long runout length and secondary effects such as displacement waves and formation of landslide dams with associated upriver and potential downriver flooding (Heim, 1932; Crosta et al., 2004; Evans et al., 2006b; Evans et al., 2011; Hermanns & Longva, 2012).

Rock-slope failures are a quite common phenomena in the Innfjorddalen Valley, as indicated by multiple landslide deposits in the lower part (Schleier et al., 2013b), and by an active unstable rock slope in the upper part (Krieger et al., 2013; Chapter 4). As proposed by Hermanns et al. (2006a), past rock-slope failures could increase the probability of a future failure in the vicinity. Therefore, detailed integrative investigation of deposits formed by multiple rock-slope failures and its morphologies is useful for hazard assessment (Welkner et al., 2010), as it provides information on the temporal pattern of those failures that can be related to climatic variability (Hermanns et al., 2000; Trauth et al., 2000; Soldati et al., 2004; Blais-Stevens et al., 2011), and as it is very important to be able to understand the post-failure behavior (Strom, 2006).

Furthermore, large rock avalanches and their deposits show a high impact on Quaternary landscape evolution in mountain areas (Hewitt et al., 2008; Hewitt et al., 2011), for instance, due to the effects of the formation of rockslide dams (Hewitt, 1998; Evans et al., 2011;

Hermanns et al., 2011c) or the interaction with glacial landforms (Hewitt, 2009b; Shulmeister et al., 2009; Shugar et al., 2012; Delaney & Evans, 2014) and associated cascading effects and phenomena. Besides rather typical continuous rock-boulder deposits, rock avalanches can also form more complex deposits and geomorphological features which are not easy to interpret. Their formation depends on the runout behavior including, for instance, complex emplacement histories and interaction of propagating rock mass with deformable substrates along the travel path (e.g., Hewitt et al., 2008; Hermanns et al., 2014b). Numerical dynamic runout modeling, for instance, DAN3D, can be used to back analyze rock avalanches to study their runout behavior over complex 3D terrain and to predict runouts for future hazard assessment (Hungr & Evans, 1996; McDougall & Hungr, 2004; Hungr, 2006; Sosio et al., 2008; Pedrazzini et al., 2012). Additionally, it is a useful tool to support the interpretation of paleodynamics of rock avalanches and associated landforms (Schleier et al., 2015).

Typical rock-avalanche deposits show a carapace of rock boulders meter to several meters large with high angularity (Hewitt, 2009a), along with frontal rims, lateral levees, parallel ridges, or also runups on the opposite valley side that indicate high mobility (Evans et al., 1989; Erismann & Abele, 2001; Poschinger, 2002; Dufresne & Davies, 2009). However, for example, rock avalanches that ran on water saturated sediments or into water bodies can form distinct geomorphological features such as isolated hills of rock-avalanche material, as proposed by Schleier et al. (2013b) for the deposits in Innfjorddalen.

These structures are named “toma hills” and have only been described for a few sites up to date, for instance, the rock avalanches of Elm, Fernpass and Flims, whereas the latter is the best known example (Abele, 1974; Poschinger, 2002; Poschinger et al., 2006; Masera et al., 2014). The definition of “toma hills” is based only on geomorphology and not on genesis of deposits. Abele (1991), Poschinger (2002) and Poschinger & Kippel (2009) correlate the deposits of Flims to the effects of undrained loading and secondary debris flow associated with rock-avalanche propagation onto water saturated sediments. However, the effects of interaction between propagating rock-avalanche mass and substrate along travel path and in deposition area are often not obvious.

To describe and understand the rock-avalanche runout that impacts into water bodies, the effects of landslide surfing as recently proposed by Mazzanti & De Blasio (2011) and Mazzanti & De Blasio (2013) should also be taken into consideration. However, in the case of deposition below water level access is generally limited, which impedes detailed studies. This is different in Innfjorddalen as deposits were exposed by the effects of the post-glacial isostatic rebound of the Fennoscandian landmass (Fjeldskaar et al., 2000; Olsen et al., 2013b) enabling an easy access to areas that initially deposited into a shallow fjord.

This chapter is based on the previous works of Seljesæter (2010) and Schleier et al. (2013b) but extends them and brings the different puzzle pieces together. It presents a detailed description of the landforms found in Innfjorddalen together with ^{10}Be cosmogenic ages and numerical runout modeling (DAN3D) of multiple rock-slope failures, of which one rock avalanche propagated onto water saturated sediments into the fjord. As the deposits are exposed on today’s land surface by isostasy, the study could help to improve identification and interpretation of similar deposits in other areas of the world that are characterized by

isostatic rebound, such as for instance, west or east Canada or Greenland. Furthermore, the study contributes to the dataset of surface-exposure ages of rock-slope failures in western Norway and might indicate the approximate age of the sea level drop due to post-glacial isostatic rebound in this valley.

3.3 Regional Setting

The Innfjorddalen Valley is located in Møre og Romsdal County in western Norway and develops into the Innfjord, which is a southern lappet of the Romsdalsfjord, located around 3.5 km NNE of the study area (Fig. 3.1). It is a typical glacial affected U-type shaped valley with oversteepened slopes and high topographic relief spanning a mean elevation difference of around 1 000 m between the valley bottom and surrounding mountain crests (Fig. 3.2). The valley bottom is located at around 15 m a.s.l., and the highest peak of Gråfonnfjellet Mountain at 1 475 m a.s.l.

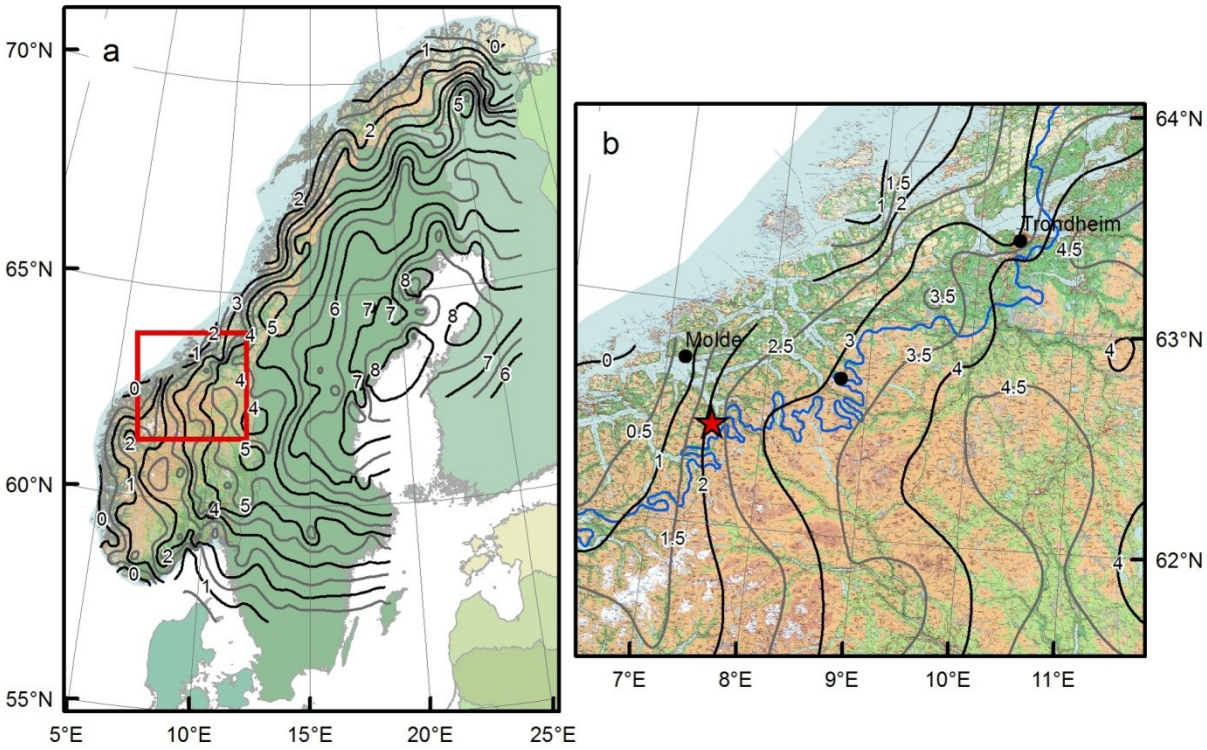

Fig. 3.1: Map of current apparent uplift rates of Fennoscandia in mm/yr (black contours) following Dehls et al. (2000). (a) Overview map of Norway, the red rectangle delimits area of (b). (b) Area around Innfjorddalen (red star). Additionally shown is the Younger Dryas ice extent (blue line) according to Sollid & Sørbel (1979).

Geologically, this area is located in the Western Gneiss Region (WGR) of Norway. The exposed lithologies are metamorphic rocks of the Caledonian orogeny with primary source rocks of Proterozoic gneisses which have been partly covered by oceanic and continental

sediments (Hacker et al., 2010). The bedrock and the rock-boulder deposits in Innfjorddalen are composed of the typical hard gneisses of this region (Fig. 3.2). According to the geological map of Ålesund by Tveten et al. (1998) the disclosed lithologies are: (1) undifferentiated gneisses which are chiefly quartzdioritic and partly migmatitic, (2) coarse grained granitic gneiss, augengneiss and gneissic granite, and (3) quartzitic gneiss, which contains sillimanite and partly kyanite. These gneisses, in general, have a well-developed foliation that is often involved in rock-slope failures in form of sliding surfaces or other main delimiting structures (Henderson & Saintot, 2011; Saintot et al., 2011b).

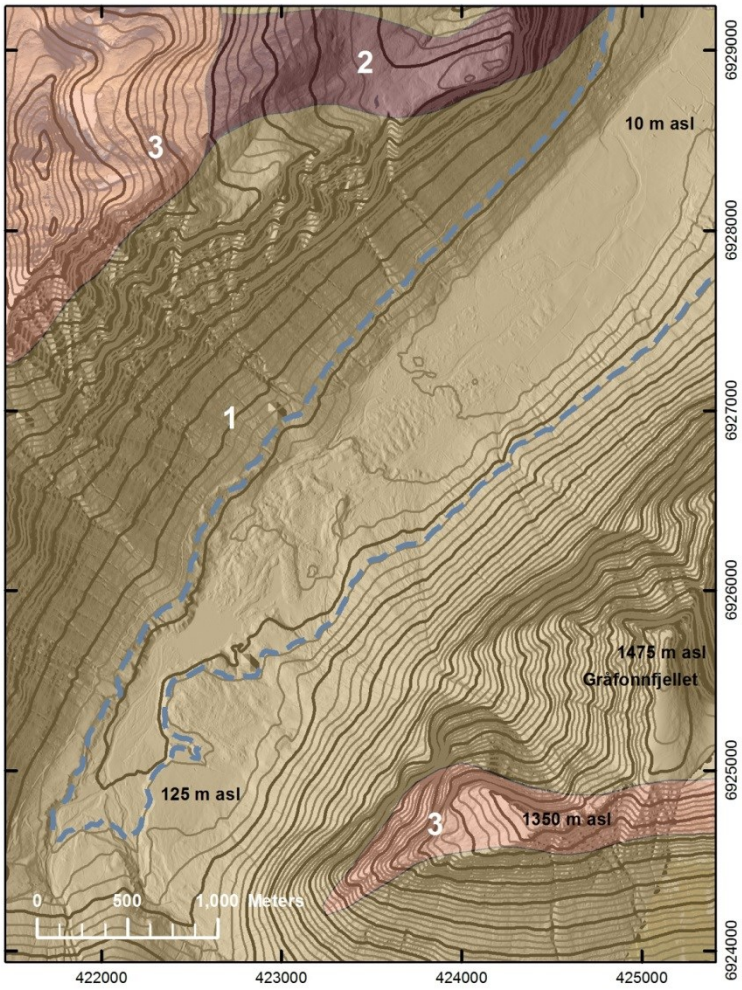

Fig. 3.2: Geological map of Innfjorddalen. The topography is represented by the hillshade and 25 m contour lines. The geology is based on Tveten et al. (1998): (1) undifferentiated quartzdioritic, partly migmatitic gneiss; (2) coarse grained granitic gneiss and augengneiss; (3) quartz-rich sillimanite and partly kyanite containing gneiss. The dashed blue line marks the approximate marine limit in account with NGU (2015). (Coordinate system: WGS1984, UTM Zone 32N)

During the Quaternary, the geomorphology of western Norway was intensively affected and modified by major glacial cycles that formed, for instance, characteristic U-shaped valleys, fjords, and alpine reliefs (Sollid & Sørbel, 1979; Fredin et al., 2013; Olsen et al., 2013b).

Besides erosive and sedimentary effects, these glaciations also had an impact on (neo-) tectonics (Olesen et al., 2013). Present day distribution of marine sediments at elevations up to 220 m a.s.l. indicate that the landmass in western Norway, formerly located near the shoreline, rose up several hundred meters since Last Glacial Maximum (Hansen et al., 2012; Hansen et al., 2014; NGU, 2015). The therein presented marine limit (i.e., the highest relative sea level following the Pleistocene glaciation), which is based on regional modeling, is indicated in Fig. 3.2 for Innfjorddalen Valley at around 120 m a.s.l.

This effect is associated to the dome-like post-glacial uplift of the Fennoscandian landmass and is explained by the movement of solid earth, originated in glacioisostatic rebound of the crust following the unloading due to decline of the thick glacial-ice sheet (Fjeldskaar et al., 2000). According to the neotectonic map of Norway (Dehls et al., 2000) the uplift is still an ongoing process in Fennoscandia and shows present apparent uplift rates of up to 8 mm/yr and values of 2–3 mm/yr for the study area (Fig. 3.1). Following this map and Blikra et al. (2002), the area around Innfjorddalen shows the highest land uplift gradient in western Norway which could be a cause for crustal instability and neotectonic faulting that could trigger rock-slope failures. Therein, and in Anda et al. (2002) a geomorphological lineament at Middagstinden Mountain around 3.5 km further up in Innfjorddalen Valley was proposed to be a neotectonic fault. However, more recent investigations (Krieger et al., 2013; Chapter 4) show that this lineament is not associated with neotectonic activity in Innforddalen.

3.4 Materials and Methods

3.4.1 Field investigations and previous studies

3.4.1.1 Field mapping and granulometric description

Field mapping and landform interpretation of the spatial distribution of rock-boulder deposits in Innfjorddalen Valley was carried out. Investigations were based on previous findings by Seljesæter (2010) to verify and improve the dataset. Therein, besides mapping the spatial extents, the granulometric characteristics were described for 13 locations to determine mean values for the different deposits by following a similar method as described in Chapter 2.4.1. Boulder size and roundness were estimated in the field by sampling around 100 connected rock boulders at each of the 13 locations to determine mean values for the different deposits. Boulder size distribution was presented in 20 classes of 0.5 m intervals ranging from class 0.5 m to class 10 m. Boulder roundness and sphericity was described qualitatively following the classification of Pettijohn & Doornkamp (1973) using the six classes very angular, angular, sub-angular, sub-rounded, rounded and well rounded and the two classes low and high sphericity.

Additionally, three trenches have been opened in the outer part of the valley in order to study sedimentology and deformation of valley-fill sediments besides or below the rock-boulder deposits (Seljesæter, 2010). These trenches have been around 1.5 m wide, 1 m deep and up to 5 m long.

3.4.1.2 Georadar profiling

Two ground penetrating radar (GPR) surveys were carried out by the Geological Survey of Norway in the year 1998 and 2009 to identify structures associated with rock avalanches and obtain more detailed subsurface information of the multiple landslide deposits (Mauring et al., 1998; Seljesæter, 2010). The GPR method is based on the theory that electromagnetic waves transmitted into the subsurface and its reflections provide information about layering and structures in the underground. According to Mauring et al. (1998) a rough description of the technique is as follows. A GPR antenna sends wave pulses into the ground. Part of this wave energy is reflected back to the surface when the wave hits a boundary that represents a change in the dielectric characteristics of the medium. The energy which is not reflected penetrates deeper into the subsurface enabling detection of reflected signal from several boundaries and depth. The reflections can be recorded by a receiving antenna placed on the surface. The GPR recordings deliver information about two-way travel time to the various reflectors and with known propagation velocity of the electromagnetic wave in the media, the depth of the various reflectors can be determined. For further details on the GPR technique and applications refer also to Keary et al. (2002) and Schrott & Sass (2008).

With regard to the investigations of landslide deposits in Innfjorddalen, two crossing GPR profiles were conducted in the year 2009 (Seljesæter, 2010). Results have been summarized in unpublished database of Geological Survey of Norway (Kartblad NR 1319 IV (2009): Georadaropptak G1 og G2, Innfjorddalen). These profiles are a 995 m long valley-parallel profile along the main road and a 595 m long valley-perpendicular profile along a track in the distal part of the rock-boulder deposits (Fig. 3.3).

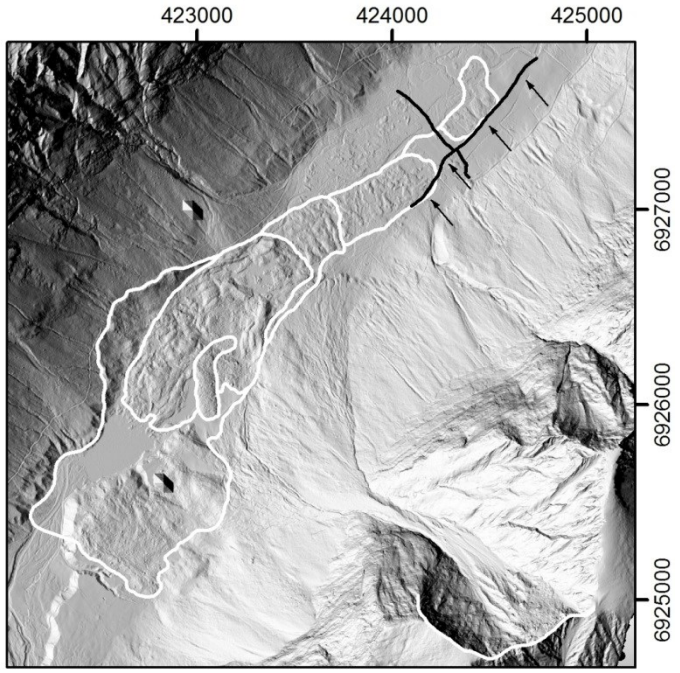

Fig. 3.3: Location of the ground penetrating radar profiles in Innfjorddalen (black line). Black arrows mark locations of exemplary sections presented in Fig. 3.13. The spatial extent of deposits formed by multiple rock-slope failures are indicated by white solid lines (for details, refer to Fig. 3.6).

3.4.2 GIS surface analyses and topographic modeling

Orthophotos and digital elevation models (DEMs) were used to support and improve mapping and landform interpretation (orthophotos and DEM with reference to the Geological Survey of Norway database). The raster datasets were implemented as layers in the geographical information system ArcGIS 10.x (Esri Inc.). Besides the high resolution orthophotos with a grid size of 0.5 m × 0.5 m, two DEMs with different resolution were provided. One DEM is based on topographical maps and has a grid size (spatial resolution) of 10 m × 10 m (Fig. 3.4), whereas the other is based on airborne laser scanning (ALS) with a grid size of 2 m × 2 m (Fig. 3.5).

DEM derivatives such as slope angle, slope aspect, slope curvature, and hillshade (i.e., shaded relief) with different azimuth and altitude for lighting, were created to visualize the topography. These datasets were used in ArcMap and ArcScene for landform interpretation, topographic modeling, and for detailed three-dimensional visualization. They give very useful information to determine spatial distribution of deposits, to identify and describe geomorphological features, and to identify possible source areas. They also enhance the quality of data as especially large-scale morphologies are often not well visible in the field due to, for instance, dense vegetation or steep and difficult terrain (e.g., Jaboyedoff et al., 2012). Furthermore, the ALS-derived DEM was used as the basis for topographic modeling with ArcGIS to prepare input data for dynamic runout analyses (i.e., runout path topography and initial volume) and to estimate volumes of rock-slope failures. The DEM-derived contour lines with 10 m intervals were modified manually to reconstruct the pre- and post-failure topographies. Field-estimated volumes of deposits and current topographic constraints were taken into account in both, local site and also in a more general valley specific scale. Those constraints are, for instance, distinct scarp morphologies, topographic edges, rivers, mean slope orientation, and mean slope gradient. Surface DEMs representing different conditions, for instance, pre-failure topography, were interpolated based on the modified contour lines. Volumes can be determined with ArcGIS by differences of DEMs, for instance, between pre- and post-failure stage (e.g., Oppikofer, 2012).

Additional to field investigations, the volumes of different events were assessed. Field-estimated deposit thickness was multiplied with spatial extent of mapped deposits. So the thickness is a rough subjective estimate that is based on field observations (e.g., valley topography and deposit characteristics) and supported by three-dimensional inspections of the DEM. The determined value represents an estimate for the bulked landslide volume. The approximate initial volume was derived by applying a bulking factor of 0.25 (i.e., 25% volume increase due to fragmentation) as proposed by Boultbee et al. (2006) and Hungr & Evans (2004).

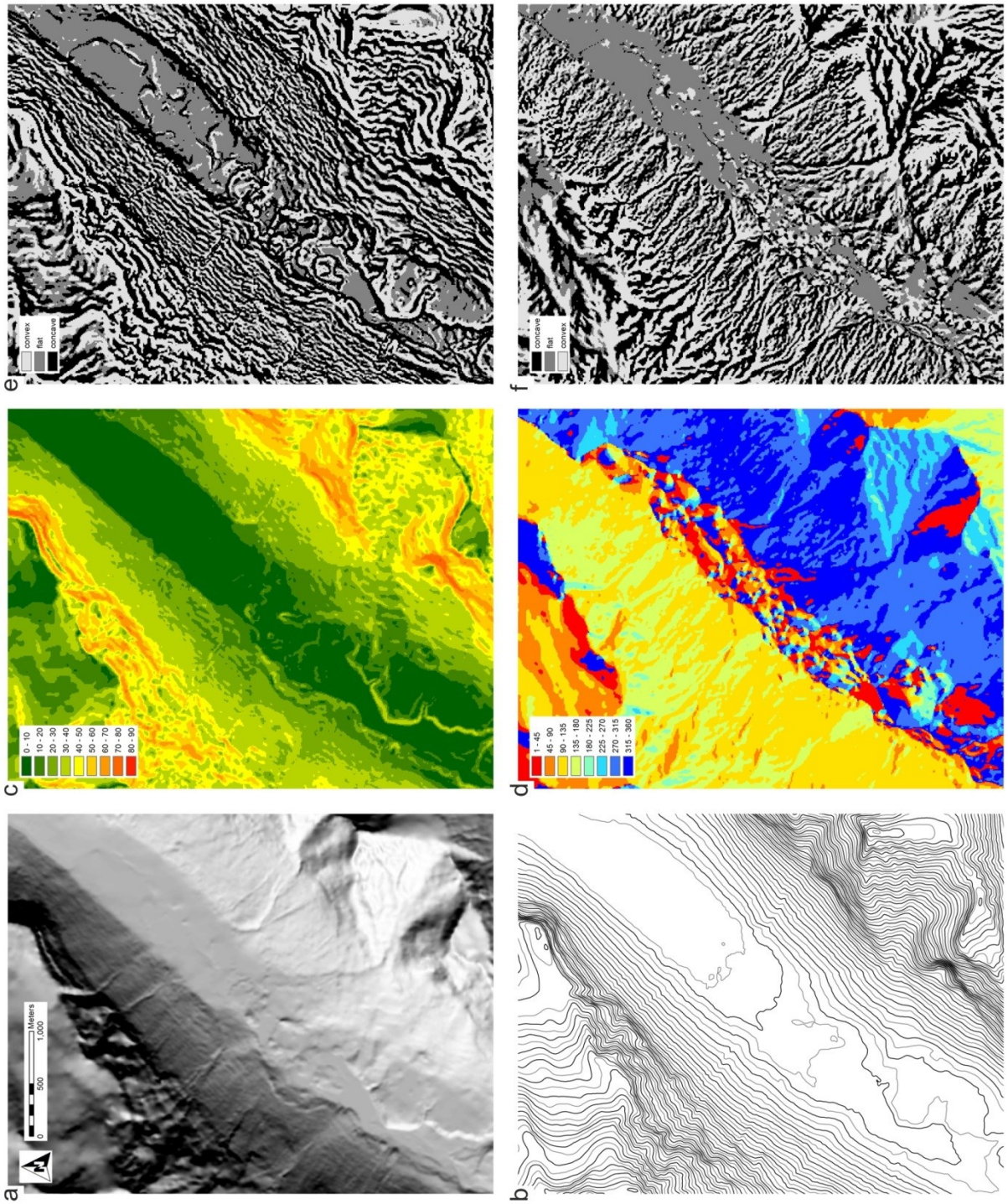

Fig. 3.4: Topographic characteristics of Innfjorddalen, represented by the DEM derivatives (10 m grid size). (a) hillshade, (b) 25 m contour lines, (c) slope angle in degree, (d) slope aspect in degree, clockwise from north, (e) profile slope curvature, and (f) planar slope curvature.

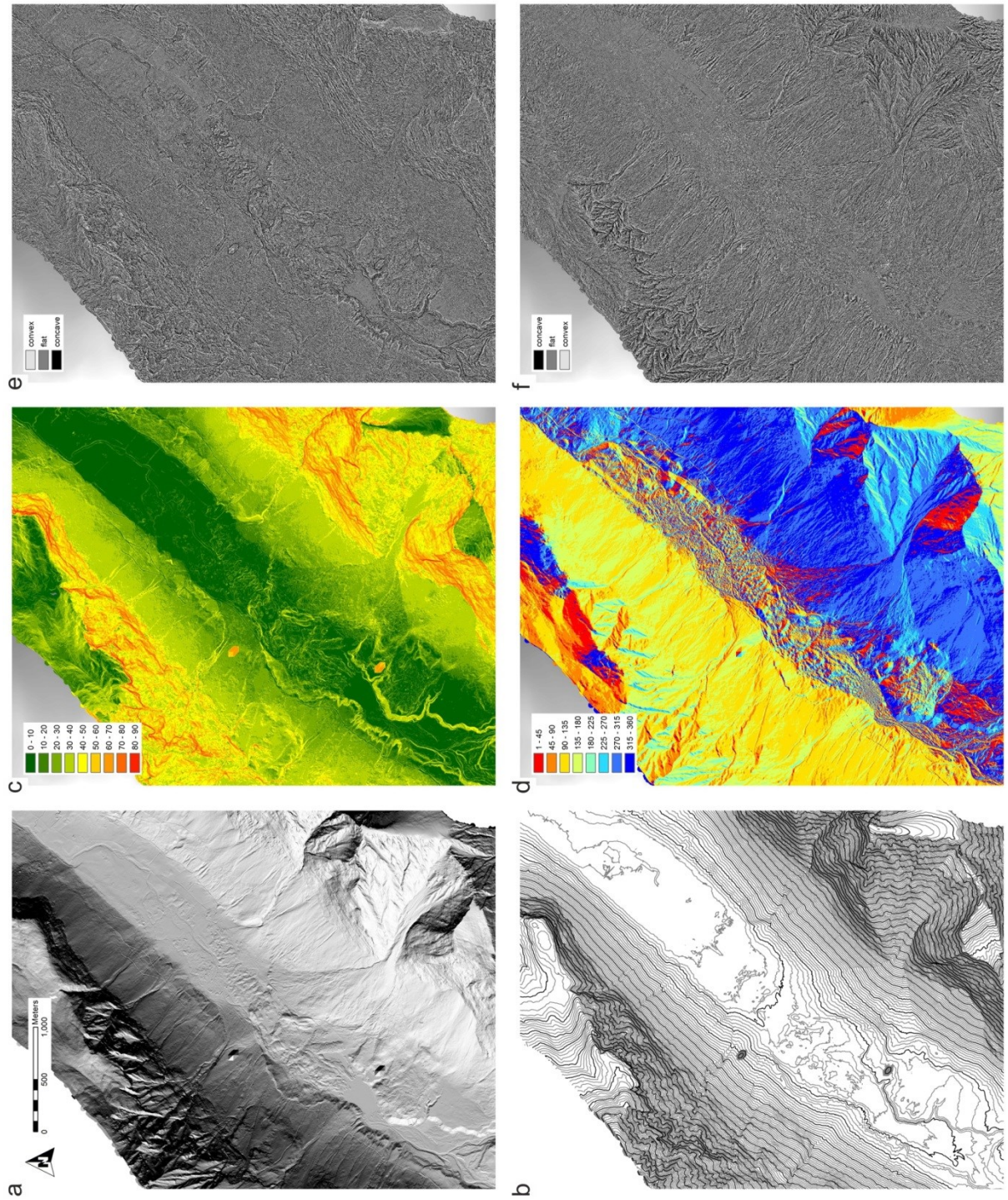

Fig. 3.5: Detailed topographic characteristics of Innfjorddalen, represented by the ALS derived DEM derivatives (2 m grid size). (a) hillshade, (b) 10 m contour lines, (c) slope angle in degree, (d) slope aspect in degree, clockwise from north, (e) profile slope curvature, and (f) planar slope curvature.

3.4.3 Surface-exposure dating

Surface-exposure dating using in-situ terrestrial cosmogenic nuclide (TCN) ^{10}Be was conducted to obtain absolute ages for the different boulder deposits that represent the different rock-slope failures in Innfjorddalen Valley. For basic theory, method and application of TCN dating refer to the review of Gosse & Phillips (2001), and for its application to landslide research refer to Ballantyne et al. (1998), Hermanns et al. (2001), Hermanns et al. (2004) and Ivy-Ochs et al. (2009).

The ^{10}Be surface-exposure dating in Innfjorddalen was conducted similarly as described in Chapter 2.4.2 and by Schleier et al. (2015). During the sampling campaign in 2011, in total 9 samples were taken, representing four different deposits according to sampling rules presented in Blais-Stevens et al. (2011) and Hermanns et al. (2012c). Thereby at least two independent rock boulders were sampled for each location. Samples were taken with hammer and chisel, if possible directly from quartz veins, to obtain rather pure quartz material. Sample preparation, analyses and age calculation was carried out by J.C. Gosse and the research groups at Dalhousie Geochronology Centre, Halifax (Canada) and Lawrence Livermore National Laboratory, Livermore (USA). Age calculation was conducted by using CRONUS calculator on the KU server, version 1.0 (Borchers et al., 2015) using ^{10}Be production systematics according to Sato, as described in Lifton et al. (2014) and following the principles outlined in Chapter 2.4.2 but without taking any erosion or snow cover into account. Additionally, in the year 2003 R.L. Hermanns took also a sample for surface-exposure dating of the stratigraphically highest rock-boulder deposit.

3.4.4 Terrestrial laser scanning and structural and kinematic analyses

The very steep and inaccessible rock slopes of the source area of the multiple rock-slope failures, that is, the large niche of Gråfonnfjellet Mountain, were investigated further by using terrestrial laser scanning (TLS) surveys. A detailed description of the TLS technique, methods and its application to landslide research are referred to in the review papers of Jaboyedoff et al. (2012) and Abellán et al. (2014). The following applied methods are similar to those as described in Chapter 2.4.3.

The scans were conducted with an Optech ILRIS LR (Optech Inc.) scanner using the last pulse time-of-flight measuring technique (for technical specifications see Optech, 2014). In total, six scans were carried out from three locations positioned rather at the valley bottom, looking upward to the large niche of the source area. The average spot spacing (or scan resolution) ranges from 97 mm to 180 mm for a mean distance between 1 200 m and 2 250 m. The raw 3D point clouds were post-processed using the software Polyworks (InnovMetric Software Inc.). The combined and georeferenced high resolution point cloud of the rock slope was used for structural analysis with the software Coltop3D (terr@num Inc.) to determine rock surfaces formed by discontinuity sets and measure their orientations.

Using the software Dips 6.0 (Rocscience Inc.), cluster analyses of each of the sampled discontinuity sets (in total 13 027 pole vector selections) were carried out for the TLS-derived structural data to determine their mean orientations. Simple kinematic analyses were conducted with the obtained discontinuity orientations to determine possible mechanisms for the rock-slope failures. Results are presented in Schmidt net stereoplots (lower hemisphere, equal area).

According to the topography of the source area, various slope orientations (the mean orientations were interpolated based on DEMs using ArcGIS 10.x) were applied for these kinematic feasibility tests. A friction angle of 20° along discontinuity surfaces, and lateral limits of 30° were applied to obtain conservative results that correspond to the requirements recommended by Hermanns et al. (2012b) for hazard and risk classification of large unstable rock slopes in Norway. Thereby, a lateral limit which is larger than the standard value of 20°, as generally adopted for rock-slope engineering (Wyllie & Mah, 2004), accounts for the more complex structures of large rock-slope failures.

3.4.5 Dynamic runout analyses

Back analyses of multiple rock-slope failures in Innfjorddalen using numerical runout modeling (DAN3D) were carried out to study runout behavior, to test reliability of landform interpretation, and to obtain reliable input data for forward runout modeling of future events. Therefore, dynamic runout modeling using the software code DAN3D was carried out to model the runout of multiple rock-slope failures, that are, rock avalanches. The DAN3D code was developed to model the propagation of landslides of the flow-type over complex three-dimensional terrain (McDougall & Hungr, 2004; McDougall, 2006). It is based on smoothed particle hydrodynamics (SPH) theory and implements a depth averaged meshless Lagrangian solution similar to the previous two-dimensional version DAN (Hungr, 1995; Hungr & Evans, 1996; Hungr & McDougall, 2009). For further details on the theory and method refer to Chapter 2.4.4 and the references presented above.

The different input raster datasets, that is, source volume, path topography and path material, were created using software ArcGIS 10.x (Esri Inc.) and Surfer 11 (GoldenSoftware Inc.). Pre- and post-failure topography was modeled as outlined in Chapter 3.4.2. The distribution of different materials (i.e., path rheology) along the runout path was interpreted by field-mapping results. To determine the most reliable model, several DAN3D runout models were run iteratively with different settings beginning with values similar as such proposed by Hungr & Evans (1996) and McDougall (2006) to be typical for rock avalanches (e.g., friction coefficient 0.1 and turbulence coefficient of 500 m/s²). The iterative models were verified manually with field-mapping results such as spatial extent of deposits.

Additionally, to compare and verify modeling against field mapping, event velocity was calculated for one rock avalanche using its runup height (Crandell & Fahnestock, 1965), and Fahrböschung angles (Heim, 1932) were determined for all deposits based on the mapping and modeling results as outlined in Chapter 2.4.4.

According to Schleier et al. (2013b), several rock-slope failures occurred from the large niche besides Gråfonnfjellet Mountain that created distinct rock-boulder deposits in the valley. Within this niche, different source areas were identified for the different events. Therefore, several runout models were applied to study the multiple rock-slope failures. Back analysis was conducted for the first rock avalanche that propagated onto the valley fill deposits into the fjord and the second and third rock avalanche that both propagated onto rock-boulder deposits of previous rock avalanches. For back analysis of the first rock avalanche, a two stage model was applied. One uses only one type of substrate for the valley sediments along the travel path and was used to calibrate the main model parameters. The other applies an additional type of substrate to account for the highly water saturated sediments along the travel path in the bottom of the valley. Furthermore, in consideration of the surface-exposure dating, a higher water level (marine limit) of the fjord is proposed for the time of this rock avalanche occurrence. As it is not possible with DAN3D to model rock-avalanche propagation after the impact into a water body, the modeling below the assumed water level is interpretive. The parameters of the best-fitting models derived by iterative modeling are summarized in Table 3.1.

Table 3.1: Rheology settings for materials used in the DAN3D models for Innfjorddalen.

Rock-slope failure	Volume (10^6 m^3)	Travel-path material	Rheology	Unit weight (kN/m^3)	Friction angle (°)	Friction coefficient	Turbulence coefficient (m/s^2)	Internal friction angle (°)
1st rock avalanche	15.1	1) talus	Voellmy	28	-	0.13	600	35
		2) valley-fill sediments	Voellmy	28	-	0.09	700	35
		3) water saturated sediments	Voellmy	28	-	0.03	1000	35
2nd rock avalanche	5.4	1) talus	Voellmy	28	-	0.1	600	35
		2) rock-avalanche deposits	Voellmy	28	-	0.11	400	35
3rd rock avalanche	0.3	1) talus	Frictional	28	25	-	-	35
		2) rock-avalanche deposits	Frictional	28	33	-	-	35

3.5 Results

3.5.1 Spatial distribution and characteristics of surface deposits

According to Seljesæter (2010) and Schleier et al. (2013b), a succession of deposits formed by multiple rock avalanches is preserved on the valley floor of Innfjorddalen. As the deposits overlay each other they indicate relative timing and three main rock-slope failure events can be distinguished by the spatial distribution and characteristics of deposits. However, also some suspicious deposits such as an isolated patch of rock-avalanche material are associated with these events. At least one event created a landslide dam and impounded a lake.

The observed rock-avalanche deposits cover an area of around 1.4 km^2. The spatial distribution and geomorphological characteristics of the deposits are shown in the map in Fig. 3.6, in oblique view in Fig. 3.7 and in schematic profiles in Fig. 3.8. Several morphological features (corresponding with different landslide events) can be distinguished. The stratigraphically lowest continuous rock-boulder deposit represented by (A) and (B) and the isolated rock-boulder deposit (C) which are disconnected by an area showing deformed (D) and undeformed (G) valley-fill sediments. The stratigraphically middle rock-boulder deposit (E) with smaller extent is located on the lower continuous deposit (A and B). On top of these deposits lies the stratigraphically highest rock-boulder deposit (F) showing a much smaller extension. The lowest base of these rock-avalanche deposits is represented by talus, valley-fill sediments and a marine terrace (H) at the SW margin.

The described deposits show distinct geomorphological features and granulometric characteristics. In general, these are lobate forms such as frontal rims and parallel ridges, and similar material composition with a carapace of rock boulders, meter to several meters in diameter, which is typical for rock-avalanche material.

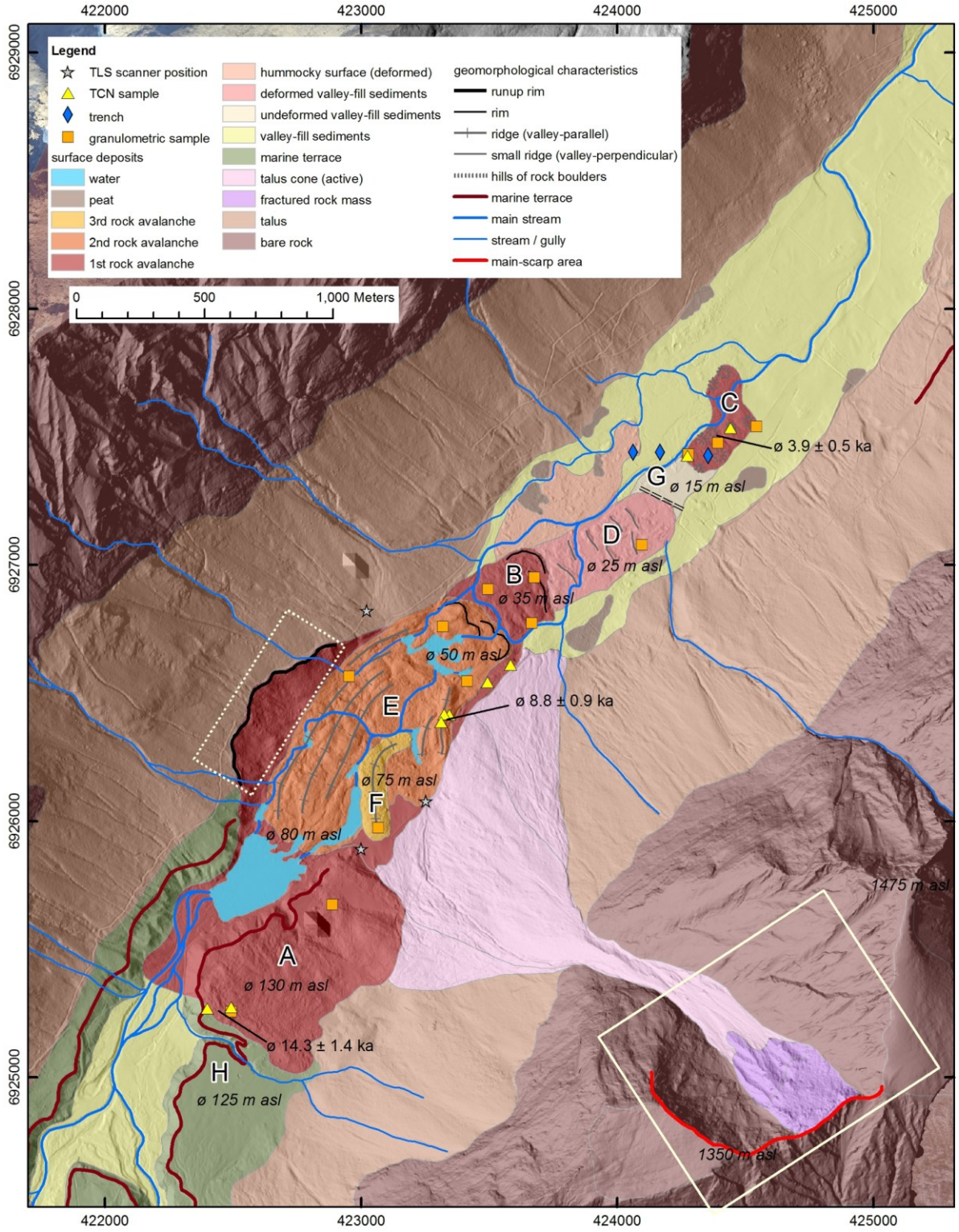

Fig. 3.6: Map of rock-avalanche deposits and surface sediments in Innfjorddalen, showing the spatial distribution of deposits, the geomorphological characteristics, the mean elevations, the different sampling locations, and the surface-exposure ages. Areas for granulometric description are labeled (A to F). The rock-avalanche source area located at the large niche of Gråfonnfjellet Mountain is outlined by the solid white rectangle (main scarp at around 1 350 m a.s.l.), and the runup area is indicated by the dotted white rectangle. (Coordinate system: WGS1984, UTM Zone 32N)

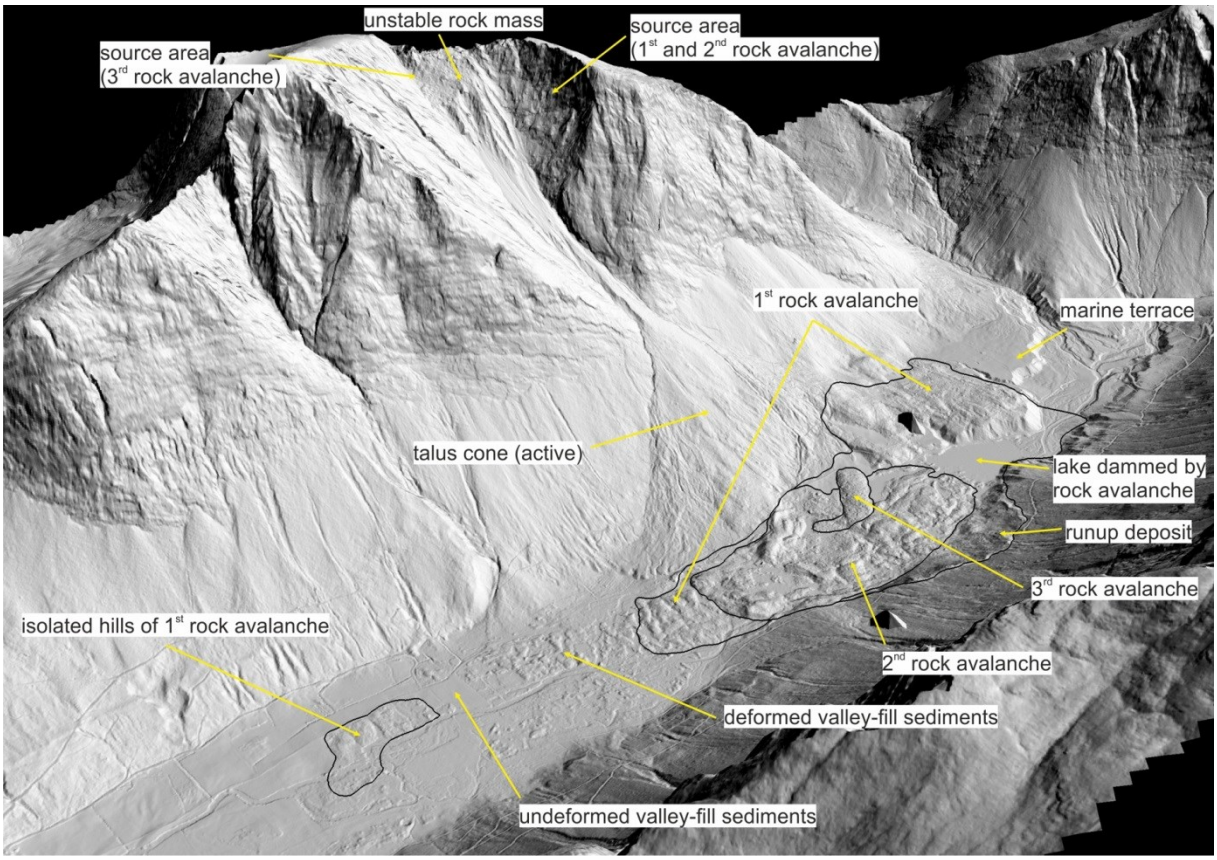

Fig. 3.7: Oblique three-dimensional view of the hillshade of Innfjorddalen (view direction toward SSE). The main geomorphological features are indicated and labeled (see text for detailed description). The spatial extent of rock-boulder deposits is outlined by black line. For scale, refer to Figs. 3.2 and 3.6.

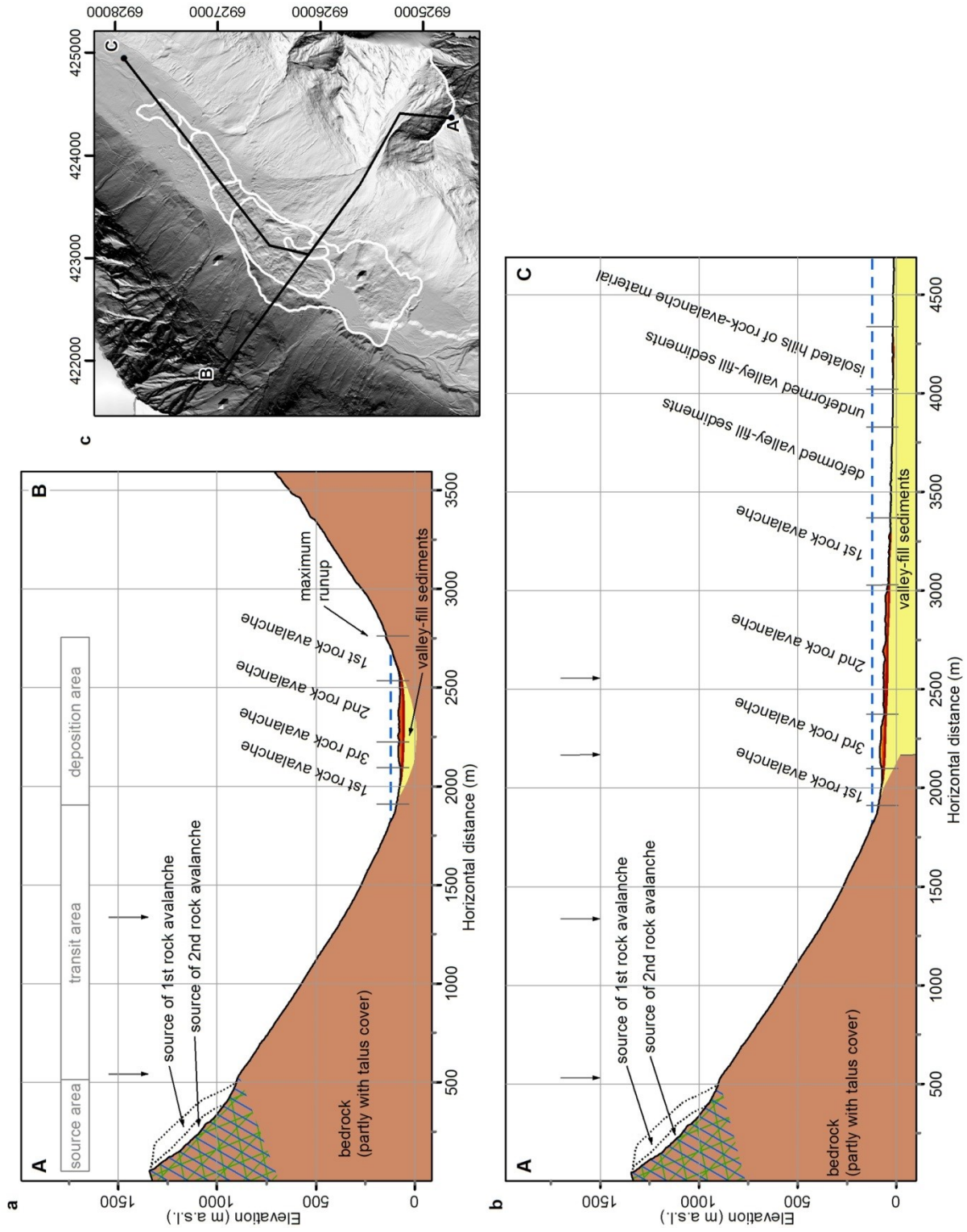

Fig. 3.8: Schematic profiles across the valley of Innfjorddalen, showing the today's topography, the extent of rock-avalanche deposits (red, orange), and main geomorphological features. Additionally indicated are the apparent dip of the main discontinuity sets including the foliation (solid blue line) and the joint sets (solid green line), and the modeled pre-failure topographies of the source area (dotted black line). The dashed blue line marks the approximate marine limit at 120 m a.s.l. (a) Cross valley profile (A–B) running from the source area to the maximum runup on the opposite slope. (b) Cross and valley-parallel profile (A–C) running from the source area to the most distal deposits (note that black arrows mark inflexion points along the profile line). (c) Traces of the profiles.

Granulometric characteristics, that is, boulder size, roundness and sphericity were measured by Seljesæter (2010). The results are summarized in Figs. 3.9 and 3.10 and are described for the deposits in the following sections. In general, the deposits (A to E) show similar characteristics whereas deposit (F) is different. According to the boulder size, 59–84% of the boulders are generally smaller than 2 m in diameter, 22% for deposit (F) respectively. Boulder sizes up to 8–10 m are common. Concerning the roundness and sphericity, the distribution is slightly different and shows concentration of sub-angular boulders (50–67%) for deposit (A, B and E), sub-rounded (57–58%) for deposit (C and D), and angular ones (68%) for deposit (F). The deposits show no distinct frequency pattern according to the boulder sphericity. Additionally, Table 3.2 shows mapped spatial extend, field-estimated thickness and the thereby derived bulked and initial volumes of multiple landslide deposits. The field-estimated thickness of the deposits varies between 5–15 m.

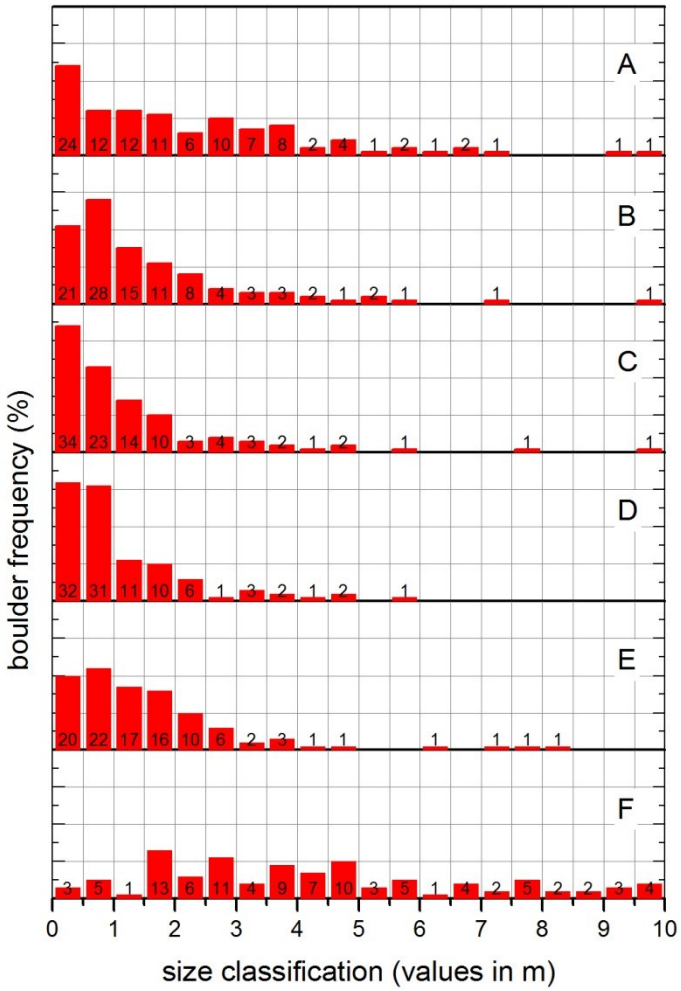

Fig. 3.9: Boulder size distribution for the sampled deposits (A to F) in Innfjorddalen. The horizontal grid lines mark 10% intervals. For location, refer to Fig. 3.6.

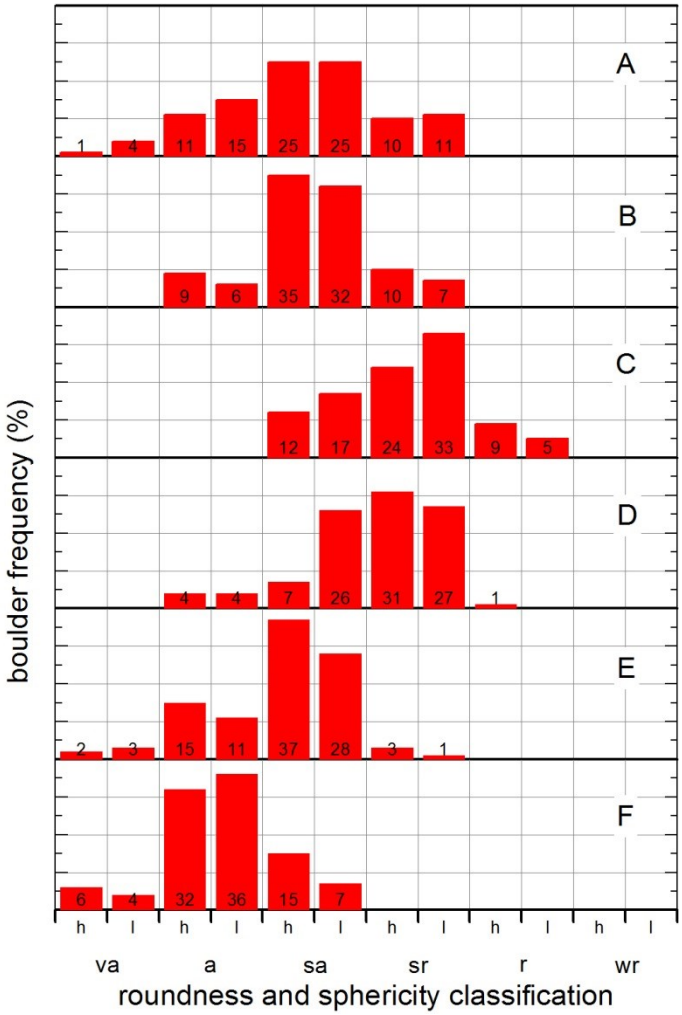

Fig. 3.10: Boulder roundness and sphericity distribution for the sampled deposits (A to F) in Innfjorddalen. The abbreviations are: va, very angular; a, angular; sa, sub-angular; sr, sub-rounded; r, rounded; wr, well rounded; l, low sphericity; h, high sphericity. The horizontal grid lines mark 10% intervals. For location, refer to Fig. 3.6.

Table 3.2: Field-estimated thickness, mapped spatial extent and calculated volume of deposits in Innfjorddalen. Extent of the first continuous rock avalanche includes also the second and third event (area A, B, E, F), and extent of the second rock avalanche includes also the third event (area E, F). Bulked volume is calculated by area and field-estimated thickness, initial volume is derived by assuming a bulking factor of 0.25. For location, refer to Fig. 3.6.

Deposit		Mapped spatial extent	Field-estimated mean thickness	Volume	
				bulked	initial
		(10^3 m^2)	(m)	(10^6 m^3)	(10^6 m^3)
1st rock avalanche	Continuous	1376	15	20.6	16.5
	Isolated hills	61	5	0.3	0.2
2nd rock avalanche		523	12	6.3	5.0
3rd rock avalanche		44	8	0.4	0.3
Total		-	-	27.6	22.0

3.5.1.1 Stratigraphically lowest rock-boulder deposit (A and B)

The stratigraphically lowest and also the largest of the succession of deposits formed by multiple rock avalanches is a continuous rock-boulder deposit, which covers an area of 1 376 × 10^3 m^2 and has an estimated bulked volume of around 20.6 × 10^6 m^3 (A and B in Figs. 3.6 and 3.7, and Table 3.2). The continuous deposit spans over the entire valley width and spreads longitudinal along the valley. The deposit shows lobate forms, longitudinal ridges and a runup on the opposite valley slope of around 100 m (Figs. 3.6 and 3.7), which are typical morphological structures of a high mobility rock avalanche. Today, the proximal part in the inner valley is located at 130 m a.s.l., and the most distal part at 35 m a.s.l. It is partly covered by younger rock-boulder deposits (E) and (F) (Fig. 3.8). Because of the deposit's extent that fills the entire valley, a previous rock-avalanche dam is proposed although it is not preserved because of modification during the younger event that formed deposit (E). In the case of rock-avalanche dam, associated lake sediments could have developed upstream, but unfortunately no such sediments were found. The deposit is characterized by geomorphological features (A) and (B) which show similar grain size and roundness distribution (Figs. 3.9 and 3.10). It shows a typical carapace of rock boulders, with a mean diameter of boulders of 1.5 m (ranging from <0.5 m to 10 m). Boulders are mainly sub-angular (at least 50%), but also show an even distribution of angular and sub-rounded forms (around 20%). Some very angular boulders (up to 5%) were also identified. The boulders show an equal frequency distribution of high (51%) and low sphericity (49%).

3.5.1.2 Isolated islands of rock-boulder deposits (C)

This part of rock-avalanche deposit is separated from the continuous rock-avalanche deposit (B) by valley fill deposits (D) and (G). This deposit is characterized by isolated islands composed of rock-avalanche material and covers an area of 61 × 10^3 m^2 (Figs. 3.6, 3.7 and 3.11, and Table 3.2). Mean thickness is estimated in the field to 5 m giving an estimated bulked volume of 0.3 × 10^6 m^3. The deposits are located at a mean elevation of 15 m a.s.l. These rather concentric hills are embedded in fine grained material and composed mainly of sub-rounded rock boulders, meter to several meters in diameter. The hills are up to three meters high (Fig. 3.11) and the deposit shows no direct connection to any other continuous landslide deposit (Fig. 3.8). The grain size distribution is similar to (A), (B) and (D) but with less large boulders (Fig. 3.9). The deposit shows a mean grain size of 1 m and a peak for 0.5–2 m. Remarkably, 10 m large boulders are common, whereas boulders >3.5 m are less abundant. They mainly show sub-rounded (57%) and sub-angular (29%) forms. However, even rounded boulders (14%) are also present (Fig. 3.10). The boulders show quite an equal frequency distribution of high (45%) and low sphericity (55%).

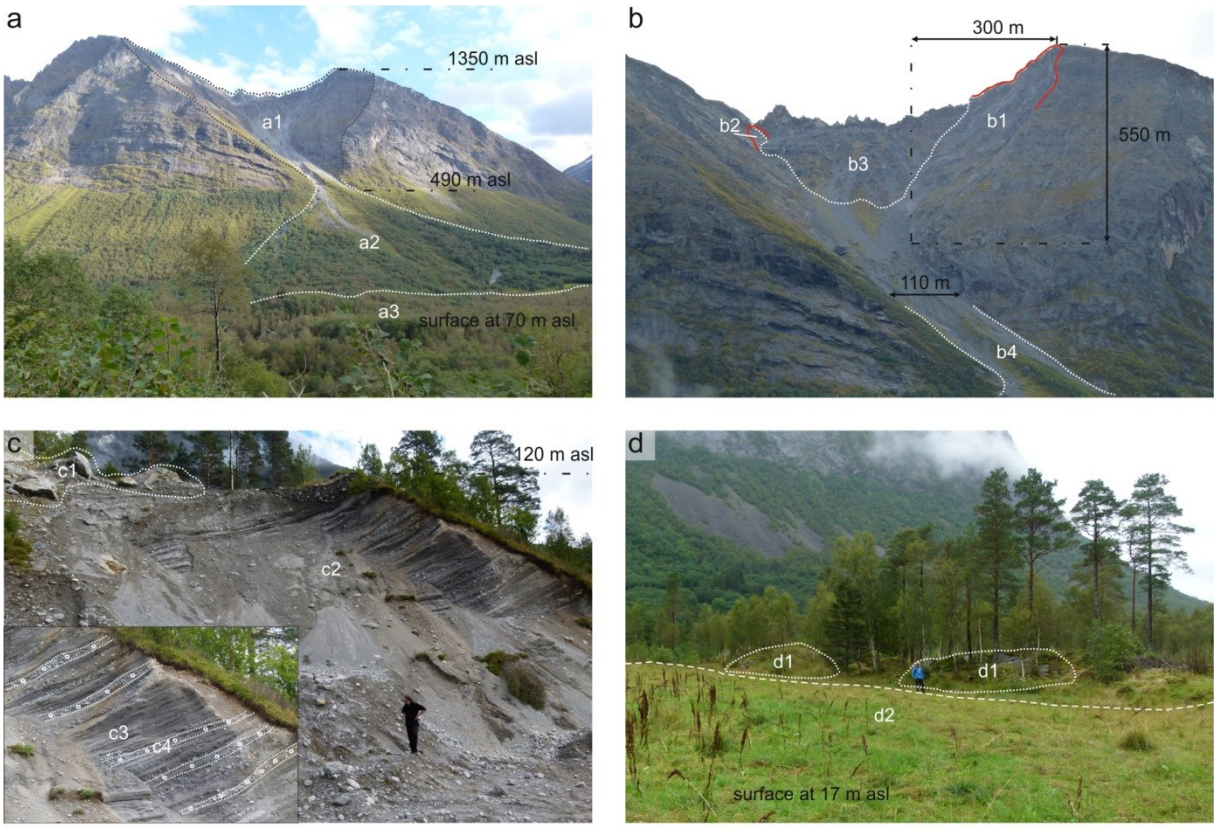

Legend of marked areas

a1: main niche of source area
a2: transit area of rock avalanches and active talus cone
a3: deposits of rock avalanches
b1: source area of 1st and 2nd rock avalanche
b2: source area of 3rd rock avalanche
b3: unstable rock mass
b4: transit area (active)

c1: rock-avalanche deposit (on marine terrace)
c2: marine terrace (delta deposits)
c3: layered sand and silt
c4: layered gravel
d1: island hills of rock-avalanche material
d2: undeformed valley-fill sediments

Fig. 3.11: Photographs of geomorphological units in Innfjorddalen. Geomorphological features are outlined by white dotted line and abbreviations are summarized in the legend. For scale, refer also to Fig. 3.2 and 3.6. (a) Gråfonnfjellet Mountain (view direction toward SE, from the TLS scanner position besides the runup area), showing the source area, the transit area and a part of the deposition area. (b) Closer view of the main niche of the source area, indicating main scarps of the rock-slope failures (red line) and the unstable rock mass. (c) Cut of marine terrace deposit (view direction toward SSE), showing rock-avalanche material lying on top of the layered delta sediments at around 120 m a.s.l. (upper left corner). The small inset shows a closer view of the typical layered bedding structures of the propagating delta sediments (modified after Schleier et al., 2013b). (d) Isolated hills of rock-avalanche material (view direction toward NNE) located at the boundary to the undeformed valley-fill sediments (modified after Schleier et al., 2013b).

3.5.1.3 Stratigraphically middle rock-boulder deposit (E)

The stratigraphically intermediate and second largest of the succession of multiple landslide deposits is the rock-boulder deposit (E). It covers an area of 523×10^3 m^2 and shows an estimated bulked volume of 6.3×10^6 m^3 (Figs. 3.6 and 3.7, and Table 3.2). It is deposited entirely on top of the first continuous deposit (A) and (B) (Fig. 3.8) and shows internal

morphological structures such as lobes and longitudinal ridges. Spanning over the whole width of the valley from around 50 m a.s.l. to 80 m a.s.l., it deposited as a rockslide dam and caused the impoundment of a lake. It is partly covered by the third rock-avalanche deposit (F). Deposit (E) also shows a carapace of rock boulders similar to (A) and (B). The mean grain size is around 2 m with a range from <0.5 m to 10 m (Fig. 3.9). The boulders show mainly sub-angular forms (65%). Around 25% are angular, and even very angular and sub-rounded clasts (both around 5%) were sampled (Fig. 3.10). The boulders show quite an equal frequency distribution of high (57%) and low sphericity (43%).

3.5.1.4 Stratigraphically highest rock-boulder deposit (F)

The rock-boulder deposit (F) is the stratigraphically highest and also the smallest deposit of the succession of multiple landslide deposits. It covers an area of 44×10^3 m^2, contains an estimated bulked volume of 0.4×10^6 m^3 and is located on top of deposit (A) and (E) at a mean elevation of around 75 m a.s.l. (Figs. 3.6 and 3.7, and Table 3.2). The deposit also presents a characteristic compact carapace of rock boulders similar to other rock-avalanche deposits. However, in contrast this deposit displays other grain size and roundness distribution and less vegetation (Figs. 3.9 and 3.10). The deposit shows a concentration of boulders between 2–5 m, but between the range of <0.5 m up to 10 m, all sizes are well distributed. However, the large boulders show a mean grain size of 4.5 m. Boulders are mainly of angular forms (68%), but also sub-angular (22%) and very angular (10%) boulders were sampled. Therefore, angularity is more pronounced in this deposit indicating a rather fresh rock-avalanche material. The boulders show an equal frequency distribution of high (53%) and low sphericity (47%).

3.5.1.5 Deformed (D) and undeformed (G) valley-fill sediments

The isolated distal part of the rock-avalanche deposit (C) is separated from the stratigraphically lowest continuous rock-avalanche deposit (A and B) by valley fill deposits (Figs. 3.6 and 3.7). These valley fill deposits are deformed (D) and undeformed (G) sediments. The deformed sediments (D) are located at elevations between 20–30 m a.s.l. adjacent to deposit (B) and are followed by undeformed sediments (G) below 20 m a.s.l. Area (D) is morphologically characterized by an undulated surface, showing small valleys and ridges, oriented perpendicular to the valley axis. In this area, no continuous boulder deposit is developed, but isolated boulders can be found. Embedded boulders show a mean diameter of 1 m. The grain size distribution shows a peak between <0.5 m to 1 m. The largest boulders have 6 m diameter (Fig. 3.9). Boulders mainly show sub-rounded (58%) and sub-angular (33%) forms. However, also some rounded and angular (8%) boulders were found (Fig. 3.10). The boulders display quite an equal frequency distribution of high (43%) and low sphericity (57%). The area between isolated hills of rock-avalanche deposit (C) and deformed valley-fill sediments (D) is characterized by valley fill deposits (G) (Fig. 3.8). These present no deformation and a relatively flat and even surface at a mean elevation of around 15 m a.s.l. No rock boulders are present within this area (Fig. 3.11).

In order to investigate and describe the deformation of valley fill deposits, two excavation pits were opened (Seljesæter, 2010). One within the deformed deposit (D) and one at the transition between deformed (D) and undeformed (G) deposits (Figs. 3.6 and 3.12). Both trenches show homogenized sand and gravel (fluvial or marine) material with lack of any layering. Clasts of rock-avalanche material or layered fine grained sediments are mixed up and swim isolated within this matrix. According to Seljesæter (2010), another trench was opened previously in the year 1997 by L.H. Blikra (not published), located in the area of isolated hill deposits (C). Sediments are described as a succession of gravel sediments (fluvial or marine), flood sediments and peat, and rock-boulder deposits on top (debris flow) which deformed and are partly mixed with the flood and gravel sediments.

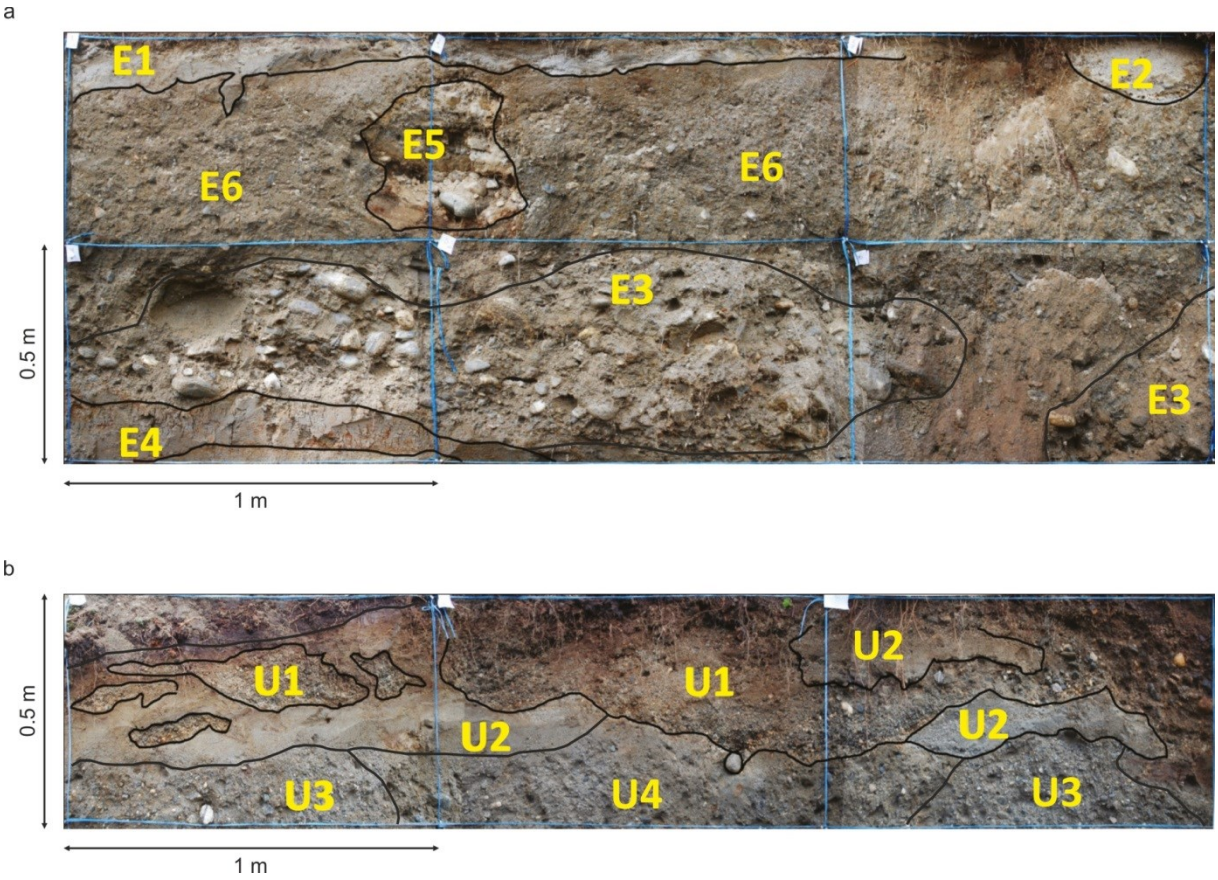

Fig. 3.12: Photographs of two trenches in Innfjorddalen, located in the area of deformed and undeformed valley-fill sediments (modified after Seljesæter, 2010 and Schleier et al., 2013b). For location, refer to Fig. 3.6. (a) Eastern trench, showing five different units that indicate disturbed sedimentation (E1 and E2, layered fine silt and clay mixed with sand, partly with iron precipitation; E3 and E5, islands of gravelly deposits without layering within sandy matrix; E4, layered clay and fine sand with iron precipitation; E6, homogenized sandy matrix). (b) Western trench, showing also disturbed sedimentation and four main units with varying grain size (U1, coarse sand with less fine grained material, iron colored; U2, fine sand and clay, also iron colored; U3, unsorted gravelly deposits similar to unit E3 from the eastern trench; U4, homogenized sandy matrix).

3.5.1.6 Marine terrace (H)

A marine terrace is recognized in the inner part of the valley, at the southern margin of the first rock-avalanche deposit (A) (Figs. 3.6 and 3.7). It is characterized morphologically by a distinct edge and an around 30 m high embankment. The material and internal structure is exposed at a fluvial cut (Fig. 3.11). The terrace is composed out of bedded fine grained material. These chiefly rounded and well rounded sand and gravel deposits are layered and show graded bedding structures which are inclined with 25° toward N, facing outside the valley. These structures are typical for a propagating marine delta deposit. The flat surface which marks the top of the terrace is located at around 120 m a.s.l. indicating an isostatic rebound of that area of at least 120 m. The deposit of the first rock avalanche (A) is situated on top of this terrace.

3.5.2 Georadar profile

Different areas of the deposits are visible in the ground penetrating radar (GPR) profiles from the outer part of the valley. Some sections are shown exemplarily in Fig. 3.13. The GPR profile in the area of deformed valley-fill sediments (D) shows irregular undulating reflectors with small valleys and ridges (Fig. 3.13a). These structures are relatively coherent down to around 8 m depth. Within the area of undeformed valley-fill sediments (G) the GPR profile displays very distinct characteristics (Fig. 3.13b). These are smooth, rather flat and regular sub-horizontal reflectors visible down to around 5 m depth. The GPR profile of the area of isolated hills of rock-avalanche material (C) also exhibits distinct structures, which are different from the other parts of the profile (Fig. 3.13c). Here again, larger hill-like structures are visible down to around 4 m depth. However, between these structures, also relatively flat sub-horizontal layers are visible. The most distal part of the GPR profile is beyond the limit of landslide deposits (Fig. 3.13d). In this area the profile shows smooth, sub-horizontal and partly undulating reflections. No large hill-like structures are visible.

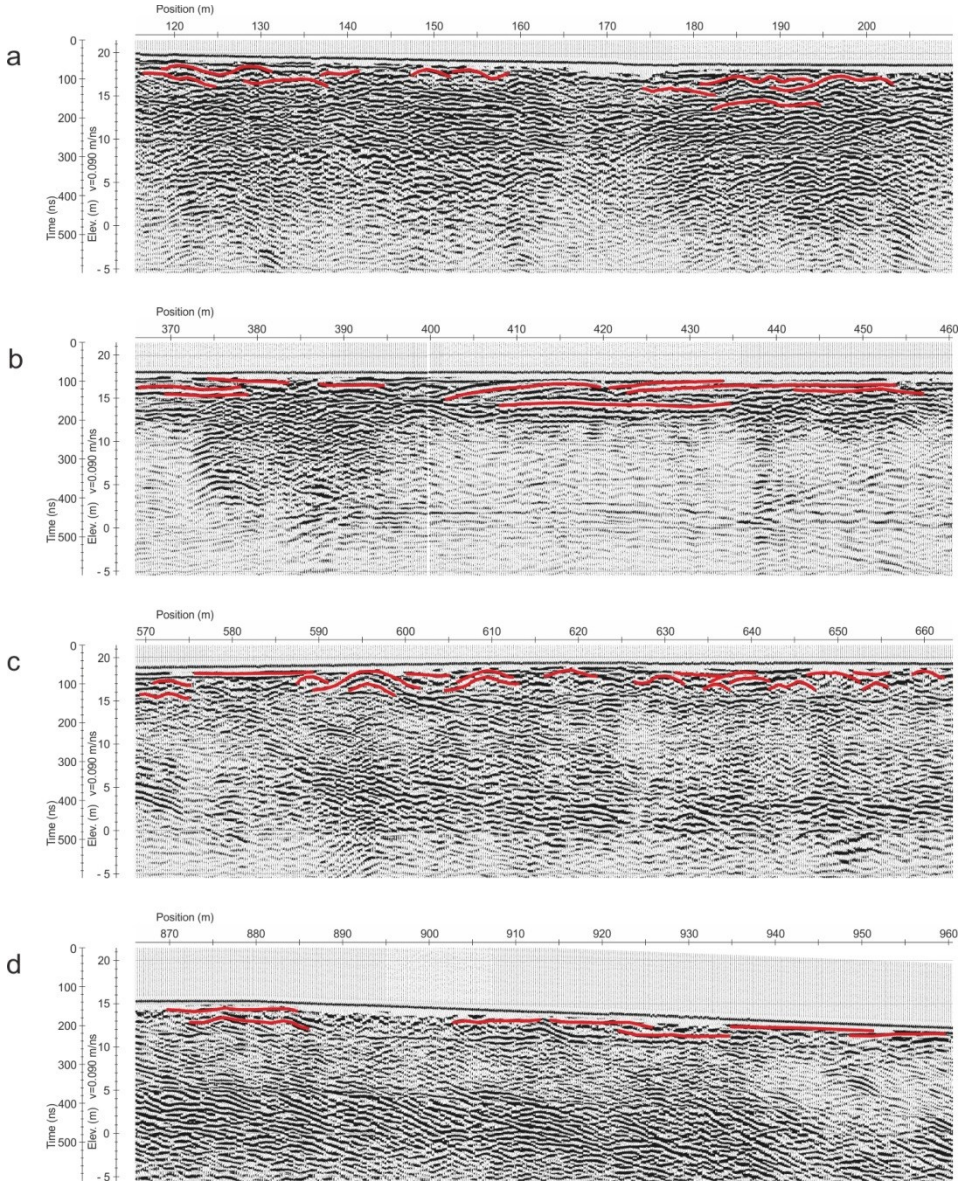

Fig. 3.13: Results of the GPR survey along the valley-parallel profile in Innfjorddalen. For location, refer to Fig. 3.3. The different deposits are shown by four representative sections: (a) deformed valley-fill sediments, (b) undeformed valley-fill sediments (c) isolated hills of rock-boulder deposits, and (d) valley-fill sediments beyond the distal limit of the rock-boulder deposits (sections are extracted from unpublished data: Kartblad NR 1319 IV (2009): Georadaropptak G1 og G2, Innfjorddalen, Geological Survey of Norway).

3.5.3 Chronology of rock-avalanche deposits

Surface-exposure dating using TCN ^{10}Be was conducted to derive absolute ages for the rock-boulder deposits, representing different rock-slope failures. The sample locations are shown in Fig. 3.6. Unfortunately, not all samples were analyzed, because of difficulties in sample preparation and unfavorable chemical composition of the samples. However, at least one age was calculated for each deposit. Therefore, available results are shown in Table 3.3 and deposit mean ages are summarized in Table 3.4.

A historic rock avalanche in Innfjorddalen Valley is recorded in church books from the year AD 1611/12 (Furseth, 2006). R.L. Hermanns applied surface-exposure dating of the stratigraphically highest deposit in the year 2003 and results correlate with this historic event (R.L. Hermanns, personal communication).

An additional age for rock-avalanche deposits in Innfjorddalen is presented in Blikra et al. (2002) and Seljesæter (2010). This age is derived by ^{14}C dating of organic material which was sampled in a trench in the area of isolated hills of boulder deposits (C) by L.H. Blikra in 1997. The mean age of dated rock-avalanche deposit is reported with <3 800 cal. yr BP.

Therefore, the various dating results indicate consistent ages for the succession of rock-avalanche deposits that confirm the plausibility of their interpretation. However, the islands of rock-boulder deposits (C) exhibit younger ages that need to be investigated.

Table 3.3: ^{10}Be exposure ages for samples in Innfjorddalen. Not all samples were analyzed due to difficulties in sample preparation and unfavorable chemical composition. The available ages are not calibrated for erosion (ε = 0 mm/ka), snow and moss cover. For sample location, refer to Fig. 3.6.

Deposit	Sample	Location (UTM 32V)		Elevation	^{10}Be age	Ext. Unc.
		x (m)	y (m)	(m a.s.l.)	(ka)	(1σ ka)
1st rock avalanche (lower limit; isolated hills)	INF-01	424 273	6 927 427	20	3.91	0.44
	INF-02	424 441	6 927 535	20	3.85	0.49
1st rock avalanche (upper limit; continuous deposit)	INF-06	422 489	6 925 276	130	5.05	0.61
	INF-07	422 399	6 925 271	125	14.3	1.4
1st rock avalanche (center; continuous deposit)	INF-08	423 583	6 926 612	50	-	-
	INF-09	423 494	6 926 544	55	-	-
2nd rock avalanche	INF-03	423 344	6 926 416	70	8.79	0.92
	INF-04	423 324	6 926 419	75	-	-
	INF-05	423 311	6 926 388	70	-	-

Table 3.4: ^{10}Be surface-exposure ages summarized for the rock-avalanche deposits in Innfjorddalen. Coordinates are in decimal degrees (d.d.). The 3rd rock avalanche coincides with the reported historic event of AD 1611/12. For sample location, refer to Fig. 3.6.

Description	Latitude (d.d.)	Longitude (d.d.)	Elevation (m a.s.l.)	^{10}Be surface-exposure age (ka)	External uncertainty (1σ ka)
1st rock avalanche (isolated hills)	62.470	7.531	20	3.88	0.47
1st rock avalanche (continuous deposit)	62.451	7.496	125	14.3	1.4
2nd rock avalanche	62.461	7.514	70	8.79	0.92

3.5.4 Source area and kinematics of rock-slope failures

3.5.4.1 Source areas of rock-slope failures

The source areas of the multiple rock-slope failures are identified to be located in the large niche on the western side of the valley which is generally the NW-facing slope of Gråfonnfjellet Mountain (Figs. 3.6, 3.7, 3.8 and 3.11). However, the niche itself is formed by three main slope faces (orientations in dip / dip direction), one NE-facing (50°/060°), one NW-facing (60°/310°) and one W-facing (45°/260°). According to topographic modeling and GIS-based analyses of the DEMs, the niche lacks a volume of approximately 47.0 × 10^6 m^3 of rock mass. Based on field observations, helicopter reconnaissance, and photo and DEM (hillshade) interpretation, several source areas were identified for the rock-slope failures that are concordant with the different bulked volumes of the deposits and the associated initial volumes (Table 3.2). A large distinct scarp was identified at the NE-facing slope of the niche and a small scarp at the W-facing slope (Fig. 3.11). The first is correlated to the source area of the stratigraphically lowest and middle deposits and the latter to such of the highest deposit.

Additionally, an unstable rock mass of around 1.8 × 10^6 m^3 (debris and disaggregated rock) is identified in the uppermost part of the central, NW-facing, slope of the niche (from around 1 050–1 320 m a.s.l.) that could fail in future as a rock avalanche. In the lower part of the niche and along the former transit areas of the rock-slope failures, a large talus cone has developed which displays a rather high activity, such as, for instance, gully erosion, debris flows and rock falls (Fig. 3.11).

However, a detailed hazard assessment was not carried out within the presented study. Those analyses are in the responsibility of the Geological Survey of Norway (NGU). They are conducted as standard investigations within the national project of mapping the unstable rock slopes in Norway, following the working approach presented in Hermanns et al. (2012b), Hermanns et al. (2013b) and Hermanns et al. (2014a). The results of these investigations for Innfjorddalen will be included in the upcoming NGU online database.

3.5.4.2 Kinematics of rock-slope failures

In the following descriptions on the kinematics, the orientations of discontinuity surfaces derived by TLS data are presented in degrees of dip/dip direction and trend/plunge for their intersections, respectively. Results are summarized in Tables 3.5 and 3.6. Four main discontinuity sets were identified using the TLS dataset: Joint set J1 (63°/156° ± 13°) is sub-parallel to the foliation, joint set J2 (60°/309° ± 11°) is sub-parallel to the slope and probably formed by exfoliation joints, and two joint sets J3 (69°/347° ± 12°) and J4 (75°/098° ± 12°) that are steeply dipping. J1 is well distinguishable along the rock face and is represented by small planar steps in the slope. J2 is characterized by distinct rather slope-parallel and planar, slightly undulating surfaces.

Table 3.5: Mean orientation of main discontinuity sets in Innforddalen. Mean surfaces are derived by Dips 6.0 cluster analysis of 13 027 pole vector selections made in Coltop3D based on the TLS-derived HRDEM.

Name	Type	Dip (°)	Dip direction (°)	1σ variability (°)
J1	Subparallel foliation	63	156	13
J2	Exfoliation	60	309	11
J3	Joint	69	347	12
J4	Joint	75	098	12

Table 3.6: Orientation of intersections formed by the mean surfaces of the main discontinuities in Innfjorddalen (Table 3.5).

Intersection	Trend (°)	Plunge (°)
J1#J2	233	23
J1#J3	072	12
J1#J4	156	63
J2#J3	298	59
J2#J4	018	32
J3#J4	035	60

Simple kinematic feasibility tests were conducted using different slope orientations in order to take into consideration the different possible pre-failure topographies. Results are shown in the stereoplots in Fig. 3.14.

Kinematic analyses for the NE-facing slope (mean slope orientation of 50°/060°) indicate that only wedge failures along the intersection of J2 and J4 (trend/plunge of the intersection line: 018°/32°) are kinematically feasible (Fig. 3.14 a). Additionally, the intersection of J3 and J4

(035°/60°) could become critical for a steeper slope with similar aspect. These wedge failures are also feasible for higher friction angles than the conducted value. Planar sliding or toppling failures are not kinematically feasible for this slope orientation.

Kinematic analyses for the NW-facing slope (mean slope orientation of 60°/310°) show feasibility for planar sliding along J2, even for higher friction angles (Fig. 3.14 b). Wedge failures are kinematically feasible mainly along J2 and J3 (298°/59°), but also partly along J2 and J4 (018°/32°) and J1 and J2 (233°/23°). Toppling is partly kinematically feasible along J1 (63°/156°) or even along J4 (75°/098°). However, due to intersections of discontinuity sets it is not probable that J4 will form long persisting rock slabs enabling a toppling.

Kinematic analyses for the W-facing slope (mean slope orientation of 45°/260°) show less feasible kinematics (Fig. 3.14 c). A wedge failure along intersection of J1 and J2 (233°/23°) could be feasible but only with the conducted low friction angle. Planar sliding is not kinematically feasible, but toppling would be feasible along J4 (75°/098°).

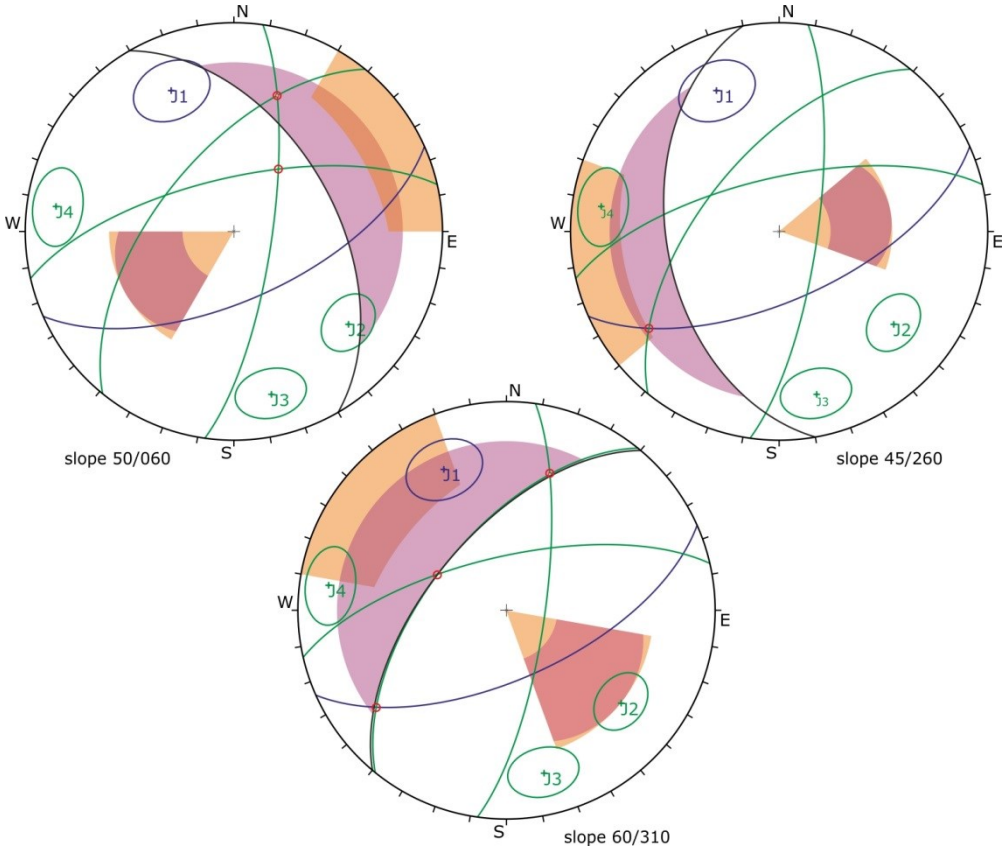

Fig. 3.14: Schmidt net plot of main discontinuity sets in Innfjorddalen (equal area, lower hemisphere). The discontinuities are four joint sets, J1 to J4, of which J1 is sub-parallel to the foliation (see Table 3.5). The circles display the 1σ variability of the mean orientations. The results of kinematic analyses (friction angle 20°, lateral limit 30°) for the three mean slope orientations are shown by the failure envelopes (red, planar sliding; purple, wedge sliding; orange, toppling failure).

3.5.5 Dynamics of rock-slope failures

3.5.5.1 1st rock-slope failure

The runout of a rock avalanche with an initial volume of 15.1×10^6 m^3 was modeled with DAN3D. The surface-exposure dating of the associated boulder deposit presents an age of ~14 ka that suggests different paleoenvironmental conditions. According to the research on the marine limit in western Norway, the relative sea level in this region was around 120 m higher at this time (Hansen et al., 2014; NGU, 2015) (Fig. 3.2). This is also in concordance with the stratigraphic position of the boulder deposit (A) on top of the marine terrace (H). This circumstance suggests a rock-avalanche propagation that impacted into the former water body at a today's elevation of around 120 m a.s.l. However, it is not possible with DAN3D to model the rock-avalanche propagation within a water body. Therefore, an alternative model was applied that had to be stopped manually when the mass reaches this elevation. This model shows the same path topography but assumes a sea level at time of rock-avalanche occurrence at a today's elevation of around 20 m a.s.l. that is based only on spatial distribution of deformed (D) and undeforemd (G) valley-fill sediments (Schleier et al., 2013b). Therefore, the rock-avalanche propagation occurred along the talus slope into the glacially affected smooth valley and into the shallow fjord. Besides the talus material along the path, the valley bottom is characterized by rather fine grained valley-fill (probably fjord) sediments which are water saturated. The modeling results are shown in Fig. 3.15 as particle distribution at selected time steps. Table 3.7 summarizes the modeled runout dynamics, that is, maximum particle velocities and average thicknesses. Associated model parameters are summarized in Table 3.1.

Starting from the source area (0 s), the rock-avalanche mass propagated down the slope in NW direction. After leaving the narrow niche, the material starts to spread over the whole debris fan, traveling over talus material and then the mass enters the valley-fill sediments.

To account for the former marine limit, the following comments have to be added. At around 25 s the propagating mass is still above the elevation of 120 m a.s.l. that equals the former marine limit. At 30 s it is partly below this elevation and the mass already reaches 60 m a.s.l. after 40 s. At this point, the center of mass is below the 120 m a.s.l. line. This signifies that the rock avalanche impacted in the water body after around 30 s resulting in a displacement wave. However, related deposits were not found in the valley. Therefore, the modeling needs to be stopped at this point, and the following descriptions of the alternative model can only be interpreted for these conditions.

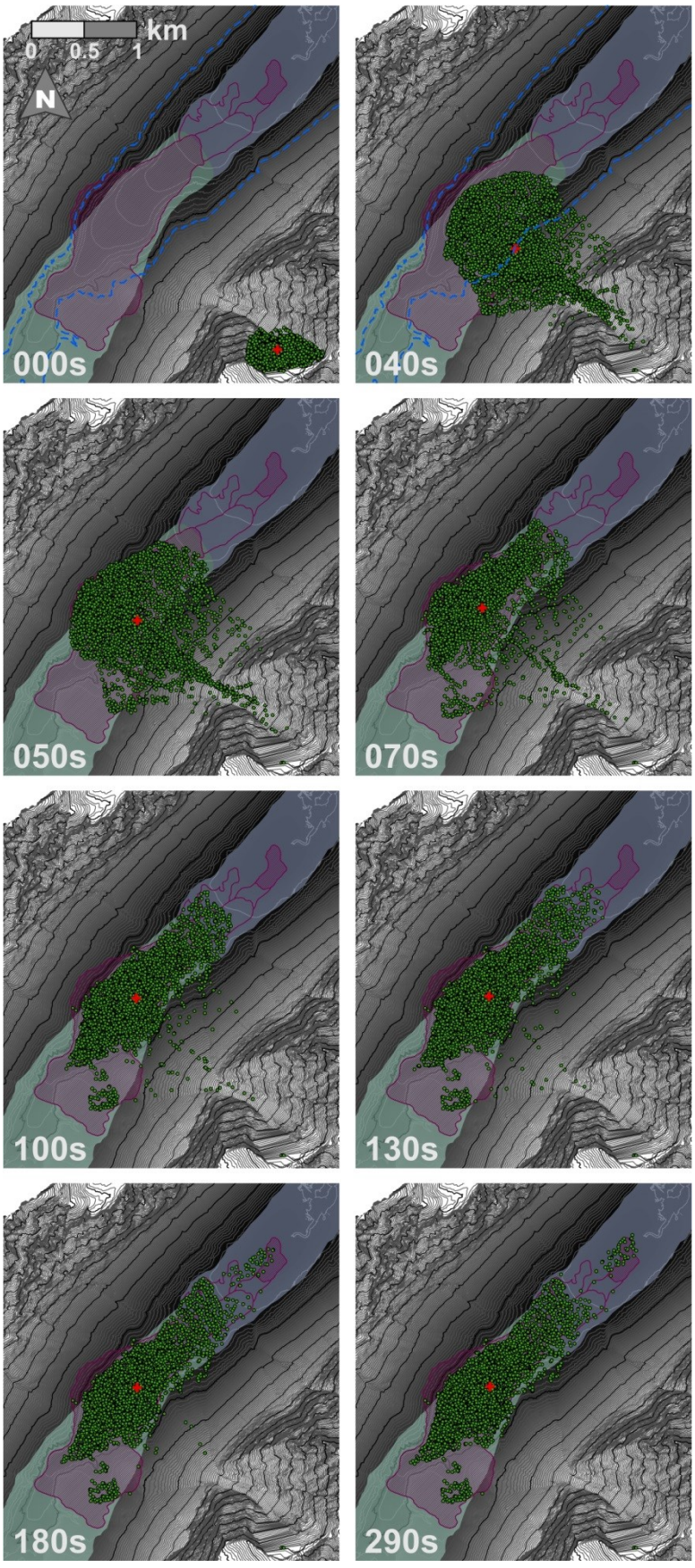

Fig. 3.15: Propagation of the 1st rock avalanche in Innfjorddalen simulated with DAN3D, using two different types of substrate for the valley-fill sediments. The propagation is shown at several time steps (indicated in the lower left corner) and is represented by the simulated particles (green dots) and

center of gravity (red cross), superimposed on a hillshade and 25 m contour lines. The background colors display the substrate along the travel path (no color, talus material; light green, valley-fill sediments; light blue, water saturated sediments). The mapped extent of deposits are indicated by polygons (hatched purple, 1st rock avalanche; purple outline, deformed and undeformed valley-fill sediments). For rheology settings, refer to Table 3.1. The dashed blue line marks the approximate marine limit at 120 m a.s.l. in account with NGU (2015).

Table 3.7: Runout dynamics of the first, second and third rock avalanche in Innfjorddalen simulated with DAN3D (rock avalanche onto water saturated sediments and such onto rock-avalanche deposits). The abbreviations are: ra, rock avalanche; t, modeled time step; v max., maximum velocity; av. th., average thickness.

	1st ra (15.1×10^6 m^3)		2nd ra (5.4×10^6 m^3)		3rd ra (0.3×10^6 m^3)	
t	v max.	av. th.	v max.	av. th.	v max.	av. th.
(s)	(m/s)	(m)	(m/s)	(m)	(m/s)	(m)
0	0.0	48.3	0.0	36.6	0.0	10.5
10	209.9	25.2	140.2	17.8	54.0	6.0
20	119.4	13.4	101.9	9.6	74.3	3.0
30	89.2	9.9	81.4	6.6	83.6	1.3
40	74.5	7.6	55.8	4.7	78.2	0.6
50	53.1	6.4	37.3	4.0	76.3	0.4
60	38.0	7.0	28.0	3.8	76.5	0.5
70	35.7	7.8	24.1	3.8	74.3	0.7
80	27.0	8.0	23.0	4.0	73.7	1.0
90	22.5	8.4	18.9	4.2	72.4	1.5
100	20.4	8.6	16.8	4.5	71.5	2.1
110	17.5	8.7	15.7	4.7	42.6	2.3
120	14.3	8.8	14.0	4.9	1.0	2.4
130	14.4	8.9	12.6	5.0	---	---
140	15.4	8.9	15.4	5.2		
150	13.4	8.9	12.7	5.3		
160	12.8	9.0	---	---		
170	11.3	9.1				
180	12.1	9.3				
190	10.5	9.3				
200	10.3	9.4				
210	9.5	9.4				
220	8.9	9.5				
230	12.0	9.5				
240	10.8	9.5				
250	10.9	9.6				
260	9.8	9.6				
270	10.1	9.6				
280	10.3	9.7				
290	8.0	9.7				
300	9.9	9.7				
310	---	---				

For the alternative model, a large amount of mass already reached the valley bottom after 40 s showing a mean velocity of 43.8 m/s. Here it starts spreading up and down the valley and in the back. Along its transition area, it still spread along the debris fan. The mass reached the maximum runup height after 50 s at the opposite slope and starts to turn around more toward N and finally shows a turn in propagation direction of around 90° toward NE (70 s). This is followed by a deceleration of the mass (<30 m/s). Once reaching the maximum runup parts of the mass also run back into the valley, which could slow down propagating material at the western margin and create valley-parallel compression ridges. While propagating and spreading still rather parallel to the valley, the frontal part of the rock avalanche reached the water saturated valley-fill sediments after 70 s. At this point, only small volumes of material are still running down from the debris fan. After 100 s the bulk of mass has already came to rest at the valley bottom (<5 m/s). The rock avalanche reached its maximum extent at the SW margin coming to rest onto the marine terrace and probably creating a landslide dam whilst still moving (<20 m/s) at its distal NE margin, where it propagated onto the water saturated sediments. At around 130 s some material at the distal margin starts to detach from the main continuous mass. Although the main continuous mass is at rest, some material still propagates isolated toward NE (180 s). This isolated propagation shows comparatively low velocities (<10 m/s) and finally no movement is displayed after 290 s anymore.

Deposits mark the maximum runup on opposite slope at an elevation of 149 m a.s.l. Today's elevation in the middle of the valley is around 76 m a.s.l. behind the third rock-avalanche deposit—this would have been below the water level of the fjord at ~14 ka (Fig. 3.8). Therefore, today's topography shows a runup height of 73 m. Taking into account an estimated thickness of deposits of 27 m (Table 3.2) the runup height would be extended to 100 m which is assumed to be the maximum. Assuming a constant slope angle of the previous valley topography, the interpolated valley bottom elevation would be at 50 m a.s.l. indicating a similar runup height. Calculation of velocity by runup height shows 37.8 m/s at a height of 73 m which is the minimum velocity and 44.3 m/s at height of 100 m. Dynamic runout modeling shows a mean velocity of 43.8 m/s at time step 40 s when the bulk of the mass travels through the bottom of the valley.

The most distal part of rock avalanche (isolated hills) indicates a Fahrböschung of 17.7° for mapped deposits and 17.5° for spatial extent of modeled particles. For the runup area the map shows 23.3° and the model 24.0°. Therefore, mapped and modeled values are in good concordance. Travel angle of 27.3° is calculated by DAN3D for the center of mass (Table 3.8).

Table 3.8: Runout characteristics of the multiple rock avalanches in Innfjorddalen. The Fahrböschung is determined by using the most distal modeled particle distribution or the mapped debris extent, respectively. The travel angle and volume are calculated during the DAN3D simulation. The ages are based on TCN dating (Table 3.4). The 3rd rock avalanche coincides with the reported historic event of the year AD 1611/12.

Event	Fahrböschung		Travel angle	Model volume	Age
	mapped	modeled			
	(°)	(°)	(°)	(10^6 m^3)	(ka)
1st rock avalanche (runup)	17.7 (23.3)	17.5 (24.0)	27.3	15.1	14.3 ± 1.4
2nd rock avalanche	24.5	23.7	29.1	5.4	8.79 ± 092
3rd rock avalanche	28.2	28.6	29.6	0.3	-

Fig. 3.16 also presents the results of runout modeling of this first rock avalanche using the same model parameters but only one type of rheology for the valley-fill sediments (Table 3.1). This model was rather used for back analysis of the event to determine parameters for propagation along talus slope and normal valley-fill sediments. This runout model shows similar results for the mass propagation and can explain the continuous deposit by reproducing the runup (50 s) and the spatial extent of the deposit (100 s). However, the propagation time and runout length is shorter than in the previously presented model where water saturated valley-fill sediments are taken into consideration. The rock avalanche comes to rest (140 s) at around the distal limit of the continuous deposit. This model does not reproduce the isolated hills.

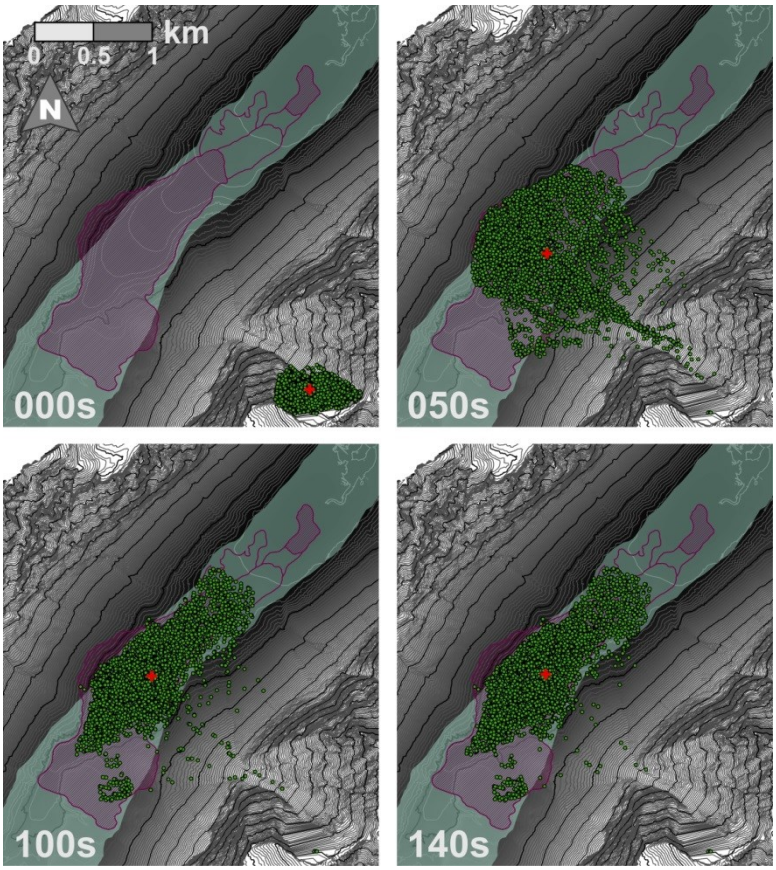

Fig. 3.16: Alternative propagation of the 1st rock avalanche in Innfjorddalen simulated with DAN3D, using only one type of substrate for the valley-fill sediments. The propagation is shown at several time steps (indicated in the lower left corner) and is represented by the simulated particles (green dots) and center of gravity (red cross), superimposed on a hillshade and 25 m contour lines. The background colors display the substrate along the travel path (no color, talus material; light green, valley-fill sediments). The mapped extent of deposits are indicated by polygons (hatched purple, 1st rock avalanche; purple outline, deformed and undeformed valley-fill sediments). For rheology settings, refer to Table 3.1.

3.5.5.2 2nd rock-slope failure

Dynamic runout modeling (DAN3D) was conducted of a rock avalanche with an initial volume of 5.4×10^6 m^3. It propagated over talus material and onto previous rock-avalanche deposits. The model parameters are summarized in Table 3.1 and the results are presented as particle distribution at selected time steps in Fig. 3.17, and runout dynamics in Table 3.7.

Starting from the source area (0 s), the rock-avalanche mass propagated through the narrow niche down the slope in NW direction, similar to the first rock avalanche. After passing the niche, the mass spread over the debris fan. Traveling over talus material the propagating mass reached the rock-boulder deposits of the previous rock avalanche and suddenly slowed down from >50 m/s to <30 m/s (40 s). This older and highly frictional deposit constrained the flow further to the SW and caused a slight shift in propagation toward N (50 s). At around 60 s the bulk of mass is situated in the valley bottom and the main part

decelerated to <10 m/s. After 80 s the bulk of mass came to rest (<5 m/s), marking the maximum extent of rock-avalanche runout. Only small volumes are still falling (<10 m/s) as an incoherent mass from the debris fan, accumulating at the deposits margin. Finally, after around 140 s no movement is observed anymore. The determined Fahrböschung values of this continuous rock-avalanche deposit are in good concordance, with 24.5° for the mapped and 23.7° for the modeled extent. The travel angle calculated by DAN3D is 29.1° (Table 3.8).

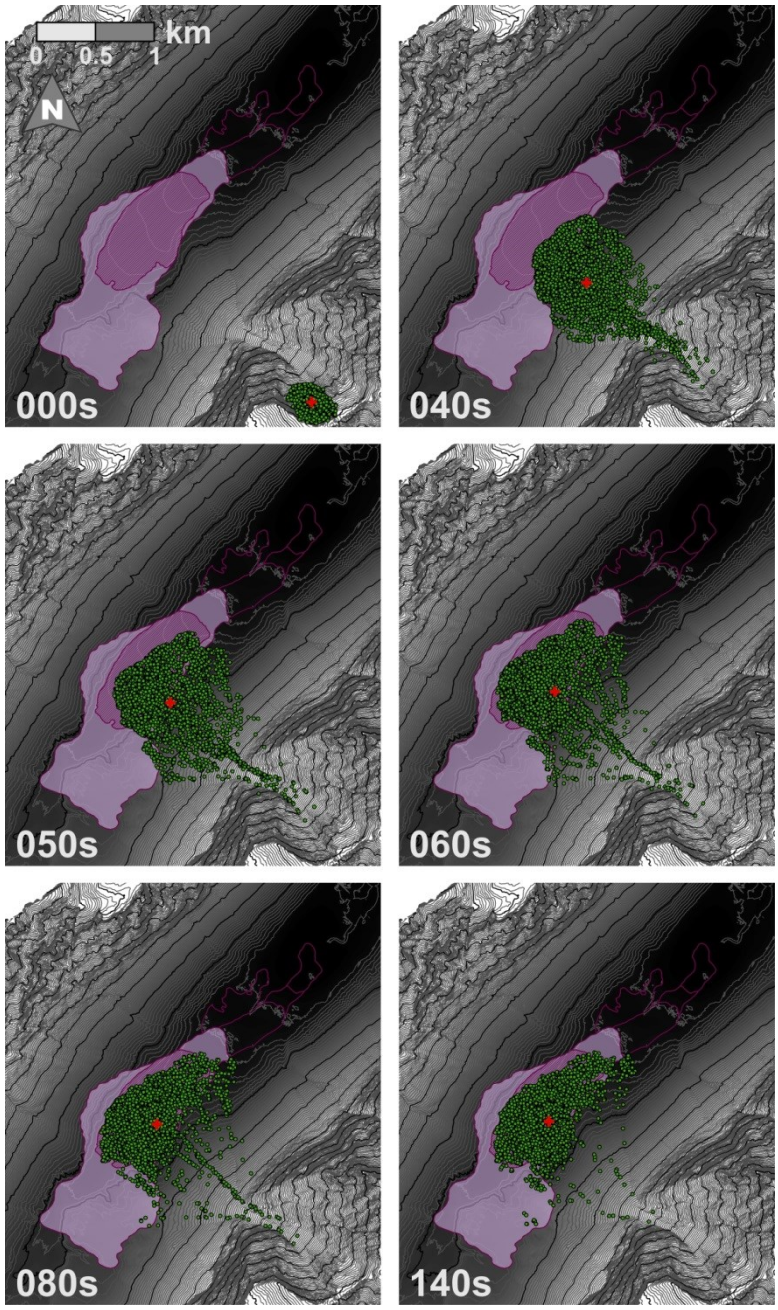

Fig. 3.17: Propagation of the 2nd rock avalanche in Innfjorddalen simulated with DAN3D. The propagation is shown at several time steps (indicated in the lower left corner) and is represented by the simulated particles (green dots) and center of gravity (red cross), superimposed on a hillshade and 25 m contour lines. The background color displays the substrate along the travel path (no color, talus material; light purple, previous rock-avalanche deposits). The mapped extent of deposits are indicated

by polygons (hatched purple, 2nd avalanche; purple outline, 1st rock avalanche, and deformed and undeformed valley-fill sediments). For rheology settings, refer to Table 3.1.

3.5.5.3 3rd rock-slope failure

The runout of a rock-avalanche event with an initial volume of 0.3×10^6 m^3 was modeled with DAN3D. The mass propagated over talus material and onto rock-avalanche deposits. Results are shown in Fig. 3.18 and in Table 3.7 by particle distribution at selected time steps and runout dynamics, respectively. The model parameters are summarized in Table 3.1.

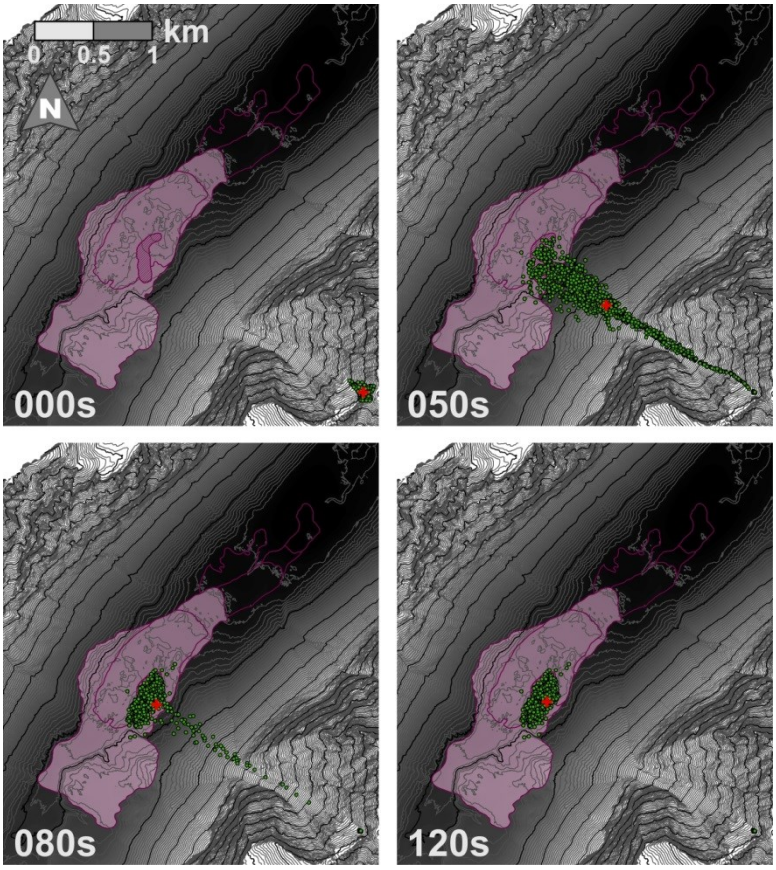

Fig. 3.18: Propagation of the 3rd rock avalanche in Innfjorddalen simulated with DAN3D. The propagation is shown at several time steps (indicated in the lower left corner) and is represented by the simulated particles (green dots) and center of gravity (red cross), superimposed on a hillshade and 25 m contour lines. The background color displays the substrate along the travel path (no color, talus material; light purple, previous rock-avalanche deposits). The mapped extent of deposits are indicated by polygons (hatched purple, 3rd rock avalanche; purple outline, 1st and 2nd rock avalanche, and deformed and undeformed valley-fill sediments). For rheology settings, refer to Table 3.1.

Starting from the source area (0 s) the mass propagates through the niche and across the debris fan over the talus material rather straight forward toward NW (50 s) and does not show much spreading over the debris fan. When entering the deposits of previous rock avalanches the mass suddenly decelerated from >50 m/s to <30 m/s. The coherent mass does not travel over a long distance across these rock-boulder deposits. After 80 s the bulk of the mass came to rest, marking the maximum runout extent. However, some single blocks are still running from the debris fan, accumulating at the deposits margin. No movement is observed for the whole slope anymore, at least after 120 s. The continuous rock-avalanche deposit shows a Fahrböschung of 28.2° for mapped and 28.6° for modeled extent, which is in good concordance. A travel angel of 29.6° is calculated by Dan3D (Table 3.8).

3.5.5.4 Possible future rock-slope failure

Dynamic runout modeling with DAN3D was conducted for a probable future rock avalanche with an initial volume of 1.8×10^6 m^3, resulting from possible failure of the unstable rock slope. The model parameters were selected based on the conducted back analyses of the previous events. In this case, they are most similar to the 2nd rock avalanche. The results are consistent with expected runout behavior. However, the results are not presented in this thesis in detail because, as previously stated, no detailed hazard assessment was carried out within the framework of this study. Hazard and risk assessment is in responsibility of the Geological Survey of Norway (NGU).

3.6 Discussion

3.6.1 General comments on the multiple rock-slope failures

At least three rock-slope failures occurred from same source area since the valley was ice free after last glaciations. The source areas are located at the eastern slope of the valley above a highly active debris fan in the large niche north of Gråfonnfjellet Mountain (Figs. 3.6, 3.7 and 3.11). The deposits of these rock-avalanche events are preserved on today's valley floor due to post glacio-isostatic uplift, either as a succession of continuous rock-boulder deposits and as discontinuous rock-boulder deposits which are disconnected from the main deposits (Schleier et al., 2013b). All of these deposits show a distinct carapace of large, mainly sub-angular and angular rock boulders which are typical for rock-avalanche material (Hewitt, 2009a). They also partly exhibit distinct geomorphological features indicating the mobility of rock avalanches, such as frontal rims, parallel ridges, and runup on the opposite slope (Evans et al., 1989; Erismann & Abele, 2001; Poschinger, 2002; Dufresne & Davies, 2009). Some further comments on the conducted investigations and uncertainties are addressed in the following subchapters.

3.6.1.1 Rock-avalanche volume and activity

The preserved deposits have a field-estimated total bulked volume of around $27.6x10^6$ m^3. Taking into consideration a bulking factor of around 0.25 (equals 25%) as proposed by Hungr & Evans (2004) and Boultbee et al. (2006), the bulked volume is in concordance with an initial volume of around 22.0×10^6 m^3 (Table 3.2), which fits well with the topographic modeling of the source area. However, volume estimates based on preserved deposits are only rough estimates and contain uncertainties (Hermanns et al., 2014b). These are, for instance, according to field estimation, topographic modeling, and effects such as material entrainment, bulking and post depositional erosion. Nevertheless, the uncertainties are assumed to be relatively low in accordance to the large volumes of several tens of 10^6 m^3 and therefore can be neglected.

However, volume estimations by GIS-based topographic modeling and DEM analyses present a total volume of around 47.0×10^6 m^3 which is missing in the large niche of the source area. This results in a lack of an initial volume of around 25.0×10^6 m^3 that needs to be investigated. This observed volume discrepancies between the deposits and the whole niche of the source area can be explained by alternative interpretations. However, a complex combination is also possible.

(1) Several large rock-slope failures occurred additionally from this niche prior or during last Pleistocene glaciations. This is assumed as no rock-boulder deposits of such previous events are preserved in the entire valley and its outer part (Fig. 3.6). If the rock-slope failures occurred prior to glaciation, the deposits might have been eroded and re-deposited by the valley glaciers due to sub- and englacial processes. Alternatively, if rock-slope failures occurred during glaciations they might have propagated and deposited onto a glacial-ice body. Then the supraglacial debris would have been modified, transported and re-deposited by supraglacial processes and glacial activity. Both would have led to deposition in the outer valley but however, some boulder deposits should be preserved as remnants along the valley bottom or the slopes of the lower valley, or in the fjord below the water level. Taking into account the change of the sediment basin due to the effects of glacio-isostatic rebound, it could be possible that these deposits are also covered by thick valley-fill sediments and are therefore not visible in the GPR profile (Fig. 3.13).

(2) Alternatively, the findings imply that the first rock avalanche propagated onto soft to liquid fjord sediments. Therefore, it is likely that portions of the involved rock-avalanche material subsided into these deposits and thus are not visible on the today's surface anymore. Therefore, large volumes of rock-avalanche material could be buried below the fine grained sediments. This leads to an underestimated volume of the first rock avalanche. This effect is probable although such deposits are not visible in the trenches or the GPR profile (Figs. 3.12 and 3.13). Anyway, it might explain at least a part of the volume discrepancy. Nevertheless, further detailed investigations are required to verify such interpretations.

However, the lack of large volume of material indicates that rock-slope failures are highly frequent at this slope. This is also shown by the recently active large debris cone below the niche and the additional unstable rock mass which was identified in the center of the niche and poses a possible future hazard (Figs. 3.6 and 3.11). The observed high activity in source

area and multiple rock-slope failures support hypothesis of Hermanns et al. (2006a) that the occurrence of rock-slope failures could increase the probability for future failure due to accelerated decompression along the rock slope.

3.6.1.2 Terrestrial laser scanning

Results of the conducted kinematic analyses show that the most feasible kinematics for rock-slope failure are rather simple for the different slope orientations, and are wedge failure along intersections between exfoliation joint set (J2) and the two main joint sets J3 or J4 (Fig. 3.14). This is valid at least for slope orientations of 50°/060° and 60°/310°. However, for a slope orientation more to the west, only a wedge along intersection between foliation (J1) and exfoliation joint set (J2) is feasible.

Additionally, the analyses indicate feasibility for a toppling failure along J1 or the joint set J4, and planar sliding along J2. However, these discontinuity planes are delimited in their extent by the other discontinuity sets with relatively small persistence, which can be seen in the field observation (photo interpretation). This means that these structures could disaggregate rock mass and detach rather small rock blocks from the rock face. Therefore, it is assumed that these types of failure are more feasible for small rock-fall volumes (e.g., single blocks) than for large volume rock-slope failures. Nevertheless, the exfoliation joint set is supposed to represent an important structure for rock-slope failure at this mountain. The proposed kinematics for large scale failure could be a combination of wedge and planar failure.

However, those kinematic analyses can only provide basic ideas but are not exhaustive and often cannot describe kinematics of complex rock-slope failure properly. Furthermore, the reliability of structural input data, that is, type and orientation of discontinuity sets, orientation of mean slope, and mechanical properties, are the main limitations for the analyses and contain various uncertainties. Analyses can be improved by using solid datasets derived by detailed field investigations (Böhme et al., 2013; Booth et al., 2014). Anyway, structural data is then mainly based on surface data and presents uncertainties according to their reliability for the subsurface rock mass. For the presented case, only structural data derived by terrestrial laser scanning (TLS) was available in a statistical amount, because of limited access to the rock face. Those TLS-derived orientations of discontinuities exhibit uncertainties due to data acquisition preparation and processing (Jaboyedoff et al., 2012; Abellán et al., 2014). However, these can be considered rather small compared with the error margins of spatial variability of discontinuity orientation. More importantly, some structures might not be detectable or will be under represented in the TLS dataset due to factors of scan resolution, spatial variability, or shadow zone (Oppikofer et al., 2009; Sturzenegger & Stead, 2009; Fisher et al., 2014). These structures could be very important for the interpretation of kinematics of rock-slope failure as the example of Krieger et al. (2013) displays for the rock-slope instability of Middagstinden Mountain in the upper part of Innfjorddalen Valley (Chapter 4). However, for areas with limited access to the steep rock face such as in the presented case, remote sensing techniques, for instance, TLS are often the only source to derive structural data for kinematic analyses to gain increased knowledge on the rock-slope failure.

During helicopter reconnaissance, a stop was performed and some manual structural measurements were collected using a compass at the backside (E-facing slope) of the niche. The limited dataset on discontinuity orientation does not show a statistically significant distribution. However, values for foliation (61°/170°) are in good correlation with TLS-derived orientation for discontinuity set J1 (63°/156°) which is interpreted as sub-parallel to foliation. Structural data from the upper part of the valley (Chapter 4) also shows similar orientation for the foliation (50°/160° for TLS-derived and 49°/158° for field measurements). Therefore, TLS-derived orientations of discontinuity sets are verified by additional field values and are reliable for the study site.

3.6.1.3 Surface-exposure dating

Terrestrial cosmogenic nuclide ages always exhibit some uncertainties due to various effects such as erosion, re-deposition, pre-exposition, or analytical problems (Gosse & Phillips, 2001; Ivy-Ochs et al., 2009; Hermanns et al., 2014b). The presented ^{10}Be surface-exposure ages of deposits (Table 3.3) are not exhaustive, because unfortunately not all rock samples were analyzed due to unfavorable chemical composition such as high feldspar content and associated difficulties in chemical sample preparation. Therefore, for some deposits the ages are only based on one single sample. According to applied multiple sample technique this circumstance increases the probability that the obtained age does not represent the age of deposition due to the effects named above. However, the available results correlate well with presented hypothesis and the observed stratigraphy and relative chronology of rock-avalanche deposits. Nevertheless, as the results of surface-exposure dating are used for the further interpretation of valley development and the assumptions for the numerical runout modeling, they also imply uncertainties within these studies as outlined in the following chapter.

3.6.1.4 Dynamic runout modeling

Numerical modeling generally exhibits various uncertainties. The main limiting factors for dynamic runout modeling with DAN3D are related to the topographic datasets (e.g., initial volume and runout path) and the applied mechanical properties (Hungr & Evans, 1996; McDougall & Hungr, 2004; Hungr & McDougall, 2009) of which all show uncertainties to some extent.

The input topographic datasets present the main uncertainties, because of topographic modeling with numerical interpolation errors and basic assumptions due to lack of knowledge of pre- or post-failure topography. Initial volumes can be estimated by differences in the interpolated pre- and post-failure topography, or, in the case of back analyses also by using the observed volumes of deposits. The distribution of different substrates along the travel path (rheology distribution) can be assessed by field mapping. Thorough two-dimensional and three-dimensional interpretations of topographic and geomorphologic constraints of the source area in site specific but also valley specific scale (orthophoto, field photo, DEM) are suggested to improve topographic modeling. This interpretation helped to identify and model

the source areas in correlation with the bulked deposit volumes, and to decrease uncertainties. Uncertainties according to topographic modeling are assumed to be relatively low and can be neglected due to the very large volumes of rock mass. However, the modeled volumes represent the trend of the volumes.

The runout model itself can be calibrated by back analyses of known examples and iterative adjustment of model settings, for instance, material parameters. Conducted model parameters are in concordance with such as recommended by Hungr & Evans (1996) and McDougall (2006) (e.g., friction coefficient of 0.1 and turbulence coefficient of 500 m/s²) for typical rock avalanches (Table 3.1). Based on verification and good correlation with mapping data, for instance, spatial extent of deposits and Fahrböschung (Table 3.8), the presented models are interpreted to give reliable results for the analyzed rock-slope failures.

Besides these general uncertainties, additional uncertainties occur for the special case of the presented dynamic runout modeling of the first rock avalanche due to the interpretation of paleoenvironmental conditions. This model is highly dependent on the assumptions made based on the results of the surface-exposure dating such as the location of the former sea level at time of rock-avalanche occurrence. Based on the spatial distribution of marine terrace deposits (H) and the research on the regional marine limit (Hansen et al., 2014; NGU, 2015) it is likely that the relative sea level was around 120 m higher at this time. This means that it is very likely that the rock avalanche impacted the water body of an ancient fjord and caused a displacement wave. However, as it is not possible to model the rock-avalanche propagation within a water body with DAN3D, the model had to be stopped manually at the point when the propagating mass impacts the water body. Therefore, the modeling results below this assumed water level are considered to be interpretive.

3.6.2 1st rock avalanche (~14.3 ka): propagation into a shallow fjord

A rock avalanche of around 15.1 × 10^6 m^3 volume (initial, model) occurred 14.3 ± 1.4 ka ago from the NE-facing slope of the large niche (Figs. 3.6 and 3.11, and Table 3.8). The observed age is similar to the age of a rock avalanche in Innerdalen Valley (located ~70 km WNW of Innfjorddalen) that occurred around 14.1 ka ago onto a Late Pleistocene glacier (Schleier et al., 2015; Chapter 2). However, the Innfjorddalen case shows in contrast different paleoenvironmental conditions.

According to research on the marine limit in western Norway, the highest relative sea level in this region was around 120 m following the Pleistocene glaciation (Hansen et al., 2014; NGU, 2015) (Fig. 3.2). Therefore, the observed first rock avalanche propagated onto highly water saturated sediments located at the former coast line into the shallow fjord and then was at least partly deposited below the water level. However, the deposits of this event are exposed on today's valley floor due to post-glacial isostatic uplift of the landmass. The preserved deposits form a continuous deposit (A,B) which is the stratigraphically lowest of the succession of rock-boulder deposits, and a discontinuous deposit (C) which are the isolated hills in the distal part composed of rock-boulder deposits (i.e., rock-avalanche

material) (Figs. 3.6, 3.7 and 3.8). This interpretation is suggested by the spatial distribution of the rock-boulder deposits and it is further supported by additional findings such as the numerical runout modeling and TCN dating.

3.6.2.1 Continuous rock-boulder deposit

Rock-avalanche material (A) is deposited directly on top of the marine terrace (H) (Figs. 3.6 and 3.11). Lack of soil material along this sediment contact indicates that the terrace was not exposed above the sea level, or at least not for a long time period prior to deposition. This implies that the land was close to sea level at the time of rock-avalanche occurrence. The head of terrace is located today at around 120 m a.s.l. This indicates that the sea level was at least 120 m higher at time of deposition of these delta sediments and that the landmass in this valley was affected by uplift due to post-glacial isostatic rebound following last major Pleistocene glaciation. The post-glacial rebound of Fennoscandia (Fjeldskaar et al., 2000) is an ongoing process and the study area still shows current apparent uplift rates of 2–3 mm/yr (Dehls et al., 2000).

These findings together with the ^{10}Be surface-exposure age of 14.3 ± 1.4 ka for deposit (A) and the results of the research on marine limit (Hansen et al., 2014; NGU, 2015) suggest a sea level that was around 120 m higher at time of rock-avalanche occurrence. It is very likely that the rock avalanche propagated directly into the shallow fjord and also created a displacement wave. Based on the ^{10}Be surface-exposure age it is further assumed that this area was above water level since ~14.3 ka ago, at least. Furthermore, the lack of glacial sediments and the presence of the not modified continuous rock-avalanche deposit suggest that no glacial landform was developed in Innfjorddalen after the LGM, and for certain not after ~14.3 ka.

The continuous deposit spans the valley along its entire width. Although it is partly covered by younger rock-avalanche deposits (Fig. 3.8) it is proposed that the event created a rockslide dam that probably impounded a lake or at least divided the sedimentation basin of the shallow fjord. However, no associated lake sediments were found as the area is still covered by a lake impounded by the second rock avalanche. The deposit further shows structures typical for high mobility of rock avalanche such as runup on opposite slope and longitudinal ridges (Evans et al., 1989; Legros, 2002; Dufresne & Davies, 2009). Latter are described as kind of levees due to internal differential shearing during movement (Poschinger, 2002) and are typical for large rock avalanches propagating onto deformable substrates (Dufresne & Davies, 2009). These ridges are located mainly on the valley side opposite to the source area below the runup area. They are perpendicular to the main direction of propagation (Figs. 3.6 and 3.7). Therefore, these ridges could be explained as structures of compression in the main movement direction. This is because part of the rock-avalanche material propagates back into the valley after reaching the maximum runup height and highly interacts with rock-avalanche material still propagating down from the source area. It forms a kind of barrier that stops the following propagating mass. This behavior and

interaction is also indicated by numerical dynamic runout modeling (Table 3.1 and Figs. 3.15 and 3.16).

The dynamic runout model also reproduced the spatial runout extent which showed good concordance with field observations especially with height and extent of the runup. Furthermore, the modeled (43.8 m/s) and calculated (37.8–44.3 m/s) velocities are in the same range. With these characteristics, the applied model is verified and demonstrates good reliability. The runout model taking into account only one type of valley-fill sediments (Fig. 3.16) can explain the continuous deposit. Furthermore, the model with additional material showing less friction (e.g., water saturated sediments) can also explain the discontinuous deposits of the isolated hills of rock boulders being disconnected from the main deposit.

3.6.2.2 Discontinuous rock-boulder deposits

Although composed of similar material, the distinct conspicuous deposits of the isolated hills and the deformed and undeformed valley-fill sediments in between these hills and the continuous rock-avalanche deposit require more discussion (Figs. 3.6, 3.7, 3.8 and 3.11).

According to Seljesæter (2010) and Schleier et al. (2013b) the isolated hills of rock-avalanche material are interpreted to be formed by rock avalanche and described as “toma hills”. With reference to Abele (1974) and Poschinger (2002), “toma hills” are defined as isolated and concentric hills of rock-avalanche material and are only described from few locations up to now, as, for instance, the rock avalanches of Elm, Flims and Fernpass. However, the definition is only based on its geomorphology and not on the genesis of deposits. Several explanations for origin are given, including direct deposition of rock avalanche, vertical internal re-deposition, reworking by fluvial effects, influence of dead ice under rock-avalanche deposits, glacial advance across such deposit, or deposition onto highly water saturated alluvial sediments (Abele, 1974; Erismann & Abele, 2001; Poschinger, 2002; Poschinger et al., 2006; Poschinger & Kippel, 2009).

Based on findings, the “toma hills” are interpreted to be deposits of a rock avalanche which propagated onto water saturated fjord deposits (valley-fill sediments) and into the shallow fjord. To explain the discontinuous deposits in Innfjorddalen, two alternative interpretations are suggested, but also the combination of both effects could be reliable.

(1) The “toma hills“ are deposits of rock-avalanche material that was transported by the mobilization and liquefaction of water saturated sediments (fjord or valley-fill sediments) as kind of secondary effect. The material was thereby detached from the continuous rock-avalanche body. Abele (1991), Poschinger (2002), Poschinger et al. (2006) and Poschinger & Kippel (2009) describe similar effects for the Flims rock avalanche. Water saturated alluvial deposits in the underground were mobilized by the rockslide deposits, causing, for instance, development of a debris flow. Isolated parts of rock-avalanche material were transported on top of these mobilized sediments, leading to isolated deposits of this material. According to Poschinger (2002) the driving factor of this mobilization is the effect of undrained loading, that is, the weight of the rock-avalanche material on the water saturated valley fills causes an

excess of pore water pressure which reduces shear strength and thus induces mobilization. As the spatial distribution of deposits indicates a location close to sea level, such water saturated sediments along the travel path would have been highly likely for this event. Abele (1991), Poschinger (2002), Poschinger et al. (2006) further describe other typical associated deposits called “Bonaduz gravel” placed between “toma hills” and the main landslide deposit. These are homogenized and unlayered sediments of coarse silt, sand and gravel matrix with clasts of fine layered lacustrine sediments and sub-vertical pipes of fines which represent dewatering structures. Sometimes clasts of rock-avalanche material also occur. They interpret these sediments as re-sedimented alluvium, partly mixed with rock-avalanche material and report similar structures also for the Fernpass and Köfels sites. Rock-avalanche material could have traveled onto or with the valley-fill sediments. Thus, the deformed valley-fill sediments (D) in Innfjorddalen are interpreted to represent deposits that are similar to “Bonaduz gravel”, as the trenches (Fig. 3.12) show distinct characteristics of a mixture of sediments, for instance, islands of gravel deposits swim in unlayered fine grained sediments. The undeformed valley-fill sediments along the path between deformed sediments and “toma hills” show no sign of mobilization. The deformed sediments as well as the undeformed sediments are well visible in the GPR profile (Fig. 3.13). The isolated hills were deposited below water level and it is possible that the undeformed valley-fill sediments were deposited by marine and fluvial sedimentation after the rock-avalanche occurrance. No thick cover of fine grained layered sediments was found in the trenches. This was not expected as there was a rock-avalanche dam upriver that formed a sink for sediments and hence strongly restricted the sediment flow into the fjord. However, it is very likely that fluvial processes affected the rock-avalanche deposits after deposition. This is also reflected by a slightly higher amount of sub-rounded boulder forms in isolated hills (Figs. 3.9 and 3.10). Furthermore, dynamic runout modeling (Fig. 3.15) confirms the interpretation of a rock avalanche onto highly water saturated sediments as reliable that could form similar deposits.

(2) Alternatively, the “toma hills” could be direct deposits of a rock avalanche which reached the water level of the fjord, and surfed on the water head for a short distance until it was deposited below the water level. This effect of “landslide surfing” is described by Mazzanti & De Blasio (2011) and Mazzanti & De Blasio (2013). Therein, landslide propagation into water body was investigated using observations, photographs, laboratory experiments and numerical modeling. They suggest that a landslide could flow horizontally along the water surface for a distance before the material plunges into water. The effect is proposed to be limited to particular conditions, such as, for instance, landslide impact into a water body with high velocity and low impact angle that reduces the vertical acceleration (Mazzanti & De Blasio, 2013). Such propagation into the water at a low transition angle could be possible for the Innfjorddalen case due to the location on the shallow inclined valley bottom close to the previous shore line and the presence of a water body. Furthermore, this surfing effect could explain the presence of undeformed valley-fill sediments between the “toma hills” and rock-avalanche deposit, but it does not properly explain the deformed valley-fill sediments. However, this interpretation is only possible if the water level was at around 20 m at the time of rock-avalanche occurrence. This is in concordance with the interpretation of spatial distribution of deformed (D) and undeformed (G) valley-fill sediments but contradicts the

surface-exposure dating and the thereby suggested marine limit. Nevertheless, a combination of both effects could be reliable.

Other effects which cause long runout distances of rock avalanches such as dynamic fragmentation, acoustic and mechanical fluidization, or lubrication by air or water (Erismann & Abele, 2001; Legros, 2002; Hungr, 2006; McSaveney & Davies, 2006) could be feasible to explain the runout length and high mobility of this event which is also shown by the distinct runup and the small Fahrböschung of 17.7° (Table 3.8). The latter can be determined assuming that this deposit is of the same origin as the stratigraphically lowest rock avalanche (A and B). Especially the effects of lubrication, by water extruded from valley-fill sediments (Abele, 1991; Erismann & Abele, 2001), or lubrication due to entrainment of liquefied saturated soil form landslide path (Abele, 1974; Legros, 2002; Hungr, 2006) would be highly probable for the conditions in Innfjorddalen. However, all of these effects could explain the runout length but do not properly explain the suspicious deposits along the runout path which are the deformed and undeformed valley-fill sediments and the isolated “toma hills”.

Furthermore, Abele (1974) also suggests glacial effects that could have formed “toma hills” such as primary supraglacial rock-avalanche deposition and secondary deposition as a type of kame hills during the melting of the glacial ice, or modification of rock-avalanche deposits by glacial crossing. However, these explanations are not feasible for deposits found in Innfjorddalen, because of the lack of moraine material and the marine terrace in underground suggest that no glacial landform was present at time of landslide occurrence. Schleier et al. (2013b) also named the possibility that the whole deposit of the first rock avalanche is a continuous deposit. This would mean that the isolated hills of rock-avalanche material and main continuous rock-avalanche deposit are connected in the underground and are partly covered by alluvial and fluvial sediments, especially in the area of undeformed valley-fill sediments. However, this interpretation is not plausible for Innfjorddalen, as such a sediment structure with cover of layered sediments on top of rock-boulder deposits was not visible either in the trenches, nor in the GPR profiles (Figs. 3.12 and 3.13).

The described deposits of deformed and undeformed valley-fill sediments, and the “toma hills” are well determined in the subsurface by the GPR profile (Fig. 3.13). The irregular hill-like structures in the reflections can be interpreted as rock bouders of rock-avalanche material. The deformed valley-fill sediments are represented by coherent undulating reflection. Smooth and flat sub-horizontal reflectors are interpreted to represent the layered undeformed valley-fill sediments. The “toma hills” are indicated by hill-like structures of boulder deposits within rather smooth, undulating and partly sub-horizontal flat layers.

Results of ^{10}Be surface-exposure dating of the landslide deposits do not directly show similar ages for the first continuous deposit with 14.3 ± 1.4 ka and the discontinuous deposit of isolated hills with 3.88 ± 0.47 ka (Fig. 3.6 and Table 3.4). However, these ages are in concordance with the presented interpretation. When the rock avalanche occurred, the distal part propagated into the fjord and was deposited below the water level. This reduces cosmic radiation causing less production of cosmogenic nuclides and therefore a younger exposure age. Because of that, the surface-exposure age of the isolated boulders (3.88 ± 0.47 ka) represents the time when the deposit was exposed out of the water following the post-glacial

isostatic uplift. This age is also in concordance with the ^{14}C age of around 3 800 cal. yr BP presented by Blikra et al. (2002). The isostatic rebound and therefore the adjacent sea level drop is not dated well for Innfjorddalen. Anyway, for other areas of western Norway it is reported that sea level was around 25 m higher around 3.0 ka ago (Maiforth, 2010). Based on the findings it is interpreted that sea level in Innfjorddalen was around 15 m higher around 3.9 ka ago. However, impact of post depositional uplift or subsidence of landmass on TCN dating causes an age difference of around 10.4 ka for a deposit interpreted to be of the same origin. This shows that these effects should be taken into consideration, especially in areas with similar conditions.

3.6.3 2nd rock avalanche (~8.79 ka): propagation onto a rock-avalanche deposit

A second rock avalanche with a volume of around 5.4×10^6 m^3 (initial, model) occurred at 8.79 ± 0.92 ka, again from the NE-facing slope of the large niche (Figs. 3.6, 3.8 and 3.11, and Table 3.8). Within uncertainty limits, this age is similar to the age of a rock avalanche in Innerdalen Valley that occurred around 7.97 ± 0.94 ka ago, also into an ice-free valley (Schleier et al., 2015; Chapter 2). Since the first rock avalanche also shows an age similar to the other one in Innerdalen, the ^{10}Be surface-exposure dating indicates a similar temporal pattern in both valleys with mean event ages of ~14.2 ka and ~8.38 ka. This suggests similar trigger mechanisms that could be correlated to major climate changes as discussed in Chapter 2.6.

The continuous deposit represented by stratigraphically middle rock-boulder deposit (E) shows typical characteristics of a rock avalanche. These are, for instance, a carapace of large rock boulders of mainly angular and sub-angular forms (Hewitt, 2009a), frontal rims, lateral levees and parallel ridges. Latter can be explained by internal differential shearing during the movement of the granular rock mass (Abele, 1974; Poschinger, 2002; Dufresne & Davies, 2009). However, the propagation is also highly constrained by the older rock-avalanche deposit along the travel path which represents an irregular and high frictional surface. Therefore, the distinct longitudinal ridges can be explained by interaction of propagating rock mass and underlying rock-boulder deposits. They could also represent some geomorphological structures of the previous rock avalanche, for instance, compressional ridges perpendicular and below runup, instead of being only flow structures of the second event.

This second rock avalanche shows no distinct runup on the opposite slope, despite of the proposed high mobility of such an event. This is explained by the higher friction of substrate along the travel path causing a higher basal friction which reduces the mobility and runout extent of rock avalanche. This runout behavior is also represented in the results of the dynamic runout model (Fig. 3.17). The higher Fahrböschung of 24° (Table 3.8) can be concluded by both the smaller process volume (Scheidegger, 1973) and the mentioned runout behavior. The findings indicate that the substrate along the runout path has a high impact on the runout behavior although the path topography of the events is similar.

The rock avalanche created a landslide dam and impounded a little lake. The dam has been rather stable since origin (Figs. 3.6 and 3.7). However, as the older deposits of the first rock avalanche span over the entire valley it is assumed that landslide dams already occurred before.

3.6.4 3rd rock avalanche (AD 1611): propagation onto rock-avalanche deposits

A rock-slope failure of 0.3×10^6 m^3 in volume (initial, model) occurred in form of a smaller rock avalanche from the large niche (in this case, at the transition between the NW-facing and the W-facing slope) and is preserved as the stratigraphically highest rock-boulder deposit (F) (Figs. 3.6, 3.8 and 3.11, and Table 3.8). This third rock avalanche coincides with the historic event of the year AD 1611/12 reported in church books for the year, because it led to the death of farmers by suffocation due to the enormous dust cloud (Furseth, 2006). The deposit can be determined by its geomorphology and shows a distinct contact to the underlying deposits. The pronounced angularity and larger boulder size (Figs. 3.9 and 3.10) of this material also supports the interpretation of a younger and less reworked deposit. Less fine grained material can be explained by less interaction between rock boulders during propagation of a small volume rock avalanche compared to a large volume event with higher energy release.

According to the smaller volume and associated different dynamics, the deposit shows a smaller runout extent for the event (Fig. 3.6) which is also represented by the relatively high Fahrböschung of 28° (Table 3.8). Besides the smaller volume (Scheidegger, 1973), this small runout length could also be affected by the higher basal friction due to the substrate along the travel path, in this case rock-boulder deposits of previous rock avalanches. The dynamic runout model indicates such an effect, as the mass is stopped rather suddenly when impacting these higher frictional materials after propagation over the talus material. However, this effect seems only to be reliable for a relatively small propagating volume, representing a lower energy release. For instance, the previously discussed second rock avalanche (5.4×10^6 m^3 in volume) does not show the same distinct effect when impacting the deposits of older rock avalanche.

Furthermore, spatial extent (Fig. 3.6) and runout model (Fig. 3.18) show that the mass is rather compact and does not spread very wide over the valley. This could also be indicated by the similarity of Fahrböschung and travel angle which are 28.2° and 29.6°, respectively (Table 3.8). The ratio of Fahrböschung to travel angle is 0.95. This high ratio close to one can be interpreted to represent a smaller amount of spreading of rock-avalanche mass compared, for example, with lower ratios of 0.84 for the second or 0.65 for the first rock avalanche.

3.7 Conclusions

The study presents the description and interpretation of multiple rock-avalanche deposits in Innfjorddalen Valley including the suspicious deposits of a rock avalanche which propagated onto water saturated sediments into the shallow fjord that were exposed within the course of the post-glacial isostatic rebound. Plausibility of this interpretation is confirmed by surface-exposure dating (^{10}Be) and numerical runout modeling (DAN3D). It also describes the first application of numerical runout modeling to back analyze multiple rock-slope failures in order to analyze runout behavior and to support landform interpretation. Furthermore, the study contributes to understanding the Quaternary development in Innfjorddalen Valley which can also enhance to understand the more regional effects in western Norway with regard to glaciation and post-glacial isostatic rebound. The main conclusions are as follows.

(I) Temporal distribution and kinematics of multiple rock-slope failures: The western slope of Gråfonnfjellet Mountain shows high activity of rock-slope failures. At least three rock-slope failures with total volume of 22.0 × 10^6 m^3 occurred from the same source area, since Late Pleistocene (14.3 ka) and additionally volume of around 25.0 × 10^6 m^3 failed prior to last Pleistocene glaciations. One rock avalanche with a volume of 15.1 × 10^6 m^3 occurred at 14.3 ± 1.4 ka, one of 5.4 × 10^6 m^3 at 8.79 ± 0.92 ka, and one of 0.3 × 10^6 m^3 in the year AD 1611/12 which had a historic impact. The rock-slope failures are controlled by four main discontinuity sets of which one is sub-parallel to foliation and one is an exfoliation joint set. The most feasible kinematics for a failure is wedge failure along intersection of joint sets, but also planar sliding along exfoliation joint and toppling along foliation sub-parallel joint are feasible for rather small-scale failures.

(II) Runout and deposits of multiple rock-slope failures: The deposits of multiple rock-slope failures are preserved on the valley floor as a succession of continuous rock-boulder deposits (1.38 km^2) and discontinuous deposits. The first rock avalanche (14.3 ± 1.4 ka) propagated into the valley, onto marine terrace deposits, over water saturated sediments (low friction) into the shallow fjord and was partly deposited below the water level. The associated effects of undrained loading and/or rock-avalanche surfing caused the longer runout extent (Fahrböschung 17.7°) and the distinct geomorphological features of isolated hills of rock-avalanche material (0.61 km^2) (“toma hills“), which are separated by 700 m from the main continuous rock-avalanche deposit by deformed (520 m) and undeformed (180 m) valley-fill sediments. The rock-avalanche deposit spans the entire width of the valley and shows a runup on the opposite slope of around 100 m. The deposits (including the “toma hills”) are exposed due to post-glacial isostatic uplift of the landmass. The following rock-slope failures propagated into the valley onto the previously deposited rock-boulder material (high friction) of former rock avalanches. This high friction substrate along the travel path affected the runout behavior of propagating mass, which can be seen in reduced runout extent (Fahrböschung of 24.5° and 28.2°). The second rock avalanche (8.79 ± 092 ka) created a rockslide dam which impounded a lake and is stable since origin. Large valley-parallel ridges right below the runup area and perpendicular to the primary flow direction are compressional structures of mass interactions during rock-avalanche runout. These large structures still can be preserved and visible in the topography even if overlain by following

rock-avalanche deposits. Besides initial volume, the path topography and especially large primary geomorphological structures, and type of substrate along travel path have a strong impact on runout behavior of rock-slope failures. Ratio of modeled Fahrböschung to travel angle indicate the amount of spreading of the propagating mass. Dynamic runout modeling (DAN3D) can reproduce the runout behavior and deposits of multiple rock-slope failures. Therefore, back analyses provide reliable model parameters for forward modeling of possible future rock avalanches. Furthermore, DAN3D runout modeling is well applicable to support and confirm interpretation of geomorphological landforms and quaternary valley development.

(III) Insights for regional Quaternary valley development: No glacial landform (valley glacier) covered the valley of Innfjorddalen following the Last Glacial Maximum, for certain not after 14.3 ka ago. The relative sea level was around 120 m higher around 14.3 ka ago and around 15 m higher around 3.9 ka ago, representing the post-glacial uplift of this area. The ^{10}Be exposure age of isolated hills of rock-avalanche material reflects the time when the deposits were exposed out of the water, rather than the time of rock-avalanche occurrence itself. Therefore, the effect of post-glacial isostatic uplift causes an age difference of around 10.4 ka for a deposit interpreted to be of the same origin. This indicates that effects such as uplift or subsidence of the landmass could have an important influence on the surface-exposure dating.

4 Kinematics of the active rock-slope instability in Innfjorddalen: gravitational reactivation of a pre-existing tectonic fault

This chapter is based on the manuscripts Schleier et al. (2013a), Krieger et al. (2013) and Schleier et al. (in preparation), and contains material included in the master thesis of Krieger (2013) that was carried out based on field investigations and co-supervised in the framework of this doctoral study.

Krieger, I., Hermanns, R.L., Schleier, M., Yugsi Molina, F.X., Oppikofer, T., Rønning, J.S., Eiken, T. & Rohn, J. (2013). The Berill fault and its relation to a deep seated gravitational slope deformation (DSGSD). *In:* R. Genevois & A. Prestininzi (Eds.), International Conference on Vajont – 1963-2013 – Thoughts and analyses after 50 years since the catastrophic landslide, Padua, Italy, 8-10. October 2013. *Italian Journal of Engineering Geology and Environment*, Book Series (6): 265-273.

Schleier, M., Hermanns, R.L., Krieger, I., Rohn, J. & Eiken, T. (2013a). Geotechnical investigations of a complex rock slope instability by use of field mapping and high resolution digital elevation models in West Norway (in German with English abstract). *Proceedings of the 19th Conference on Engineering Geology with Forum for Young Engineering Geologists*, Munich, Germany, 13-15. March 2013: 607-612.

Schleier, M., Hermanns, R.L., Krieger, I., Oppikofer, T. & Rohn, J. (in preparation). The deep seated gravitational slope deformation of Middagstinden Mountain, western Norway: evidence of gravitational reactivation of a pre-existing fault system.

4.1 Abstract

The origin of linear features in mountain terrain that form distinct vertical steps is often not obvious and has been discussed to be either related to tectonic faulting or gravitational slope deformation. Furthermore, inherited tectonic structures could have a strong influence on kinematics of rock-slope instabilities. A strong linear feature is located at the SE-facing slope of Middagstinden Mountain in Innfjorddalen Valley, western Norway. It is 1.5 km long, strikes SSW – NNE (30°oblique to the SE-facing slope), forms a 3–4 m high convex step in the topography, and is one of the limiting structures of a rock-slope instability. In previous studies it has been interpreted as a Holocene reverse fault indicating the first example of neotectonic activity in this area. However, the intense structural field mapping rather exhibits the existence of a normal fault which shows the orientation of the Caledonian collapse. Four

main discontinuity sets (dip/dip direction) can be determined: The fault plane (43°/271° ± 16°) with slickensides, the foliation (49°/158° ± 17°), and two steep joint sets (77°/309° ± 16° and 84°/039° ± 20°). Except for the fault, all other discontinuities were detected in the high resolution digital elevation model derived by terrestrial laser scanning (LiDAR). Kinematic feasibility tests indicate a wedge failure along the intersection of the fault plane and the foliation (trend/plunge of 218°/29°). However, this intersection line lies below the valley bottom and does not daylight on the slope, hence simple wedge or translational sliding is not possible over the entire slope, except in its uppermost part. Therefore, the deformation is changing along the slope suggesting a complex kinematics composed of three main processes including (1) planar sliding in the uppermost part, (2) wedge sliding in the middle part, and (3) hindered wedge sliding causing creep-like deformation and pressing out in the lower part. The complex deformation mechanisms are indicated by the observed displacements and the various geomorphological areas distributed along the slope that show distinct characteristics such as up to 20 m deep counterscarps, small-scale superficial mass movements, large coherent slide blocks, and morphological slope bulging. The complex kinematics and observed geomorphological characteristics account for the definition of a deep seated gravitational slope deformation (DSGSD). Differential global navigation satellite system (dGNSS) surveys show a current movement activity with a mean velocity of 6.6 ± 0.9 mm/yr for the main part of the DSGSD and 20.9 ± 1.0 mm/yr for an adjacent newly opened cleft. Three electric resistivity tomography profiles of the valley floor and the thereto parallel trenches down to glacial deposits or bedrock confirm the regional extent of the fault. Furthermore, the sediments observed in the trenches do not exhibit any Holocene activity. Therefore, the linear geomorphological structure oblique to the slope that was previously proposed as the first evidence for neotectonic faulting in southern Norway has to be reinterpreted. This linear feature is rather formed by the gravitational reactivation of the fault system due to the DSGSD and not by neotectonic activity and hence is an example of pseudotectonics (“apparent reverse fault”). This requires further need for future discussions on triggering factors other than neotectonic seismicity for cluster of rock-slope failures in this area. The detailed description of geomorphological features can further enable improved identification and interpretation of complex kinematics and linear features along deforming rock slopes in other high mountain areas.

4.2 Introduction

Large rock-slope instabilities such as deep seated gravitational slope deformations show typical geomorphological structures (e.g., morphostructures) and often complex kinematics and deformation processes (Dramis & Sorriso-Valvo, 1994; Agliardi et al., 2001; Agliardi et al., 2009b; Chigira et al., 2013; Crosta et al., 2013). These phenomena are typical in mountain ranges throughout the world, especially in areas with high topographic relief composed of anisotropic fractured and tectonized rocks.

Mass movements, in general, are influenced and controlled by tectonics and geology (Hutchinson, 1988) and it is proven that large rock-slope instabilities are often strongly

controlled by preexisting and inherited geological structures such as bedding, foliation, joint sets of various origin, or tectonic faults (Dramis & Sorriso-Valvo, 1994; Bovis & Evans, 1996) (Agliardi et al., 2001; Braathen et al., 2004; Saintot et al., 2011b; Agliardi et al., 2013; Bianchi Fasani et al., 2014). Especially major tectonic features could lead to a spatial cluster (concentration) of rock-slope failures (e.g., Hermanns & Strecker, 1999; Ambrosi & Crosta, 2006; Agliardi et al., 2009a) because of tectonic activity and damage (Brideau et al., 2009) that could have caused distinct weakness zones in the rocks or even could have triggered the failure. Neotectonic activity and seismicity (Hermanns et al., 2001; Blikra et al., 2002; Galadini, 2006; Penna et al., 2011) and active tectonics (Osmundsen et al., 2009; Gori et al., 2014) are identified and discussed as triggers for rock-slope deformations and failures that are recorded within its spatial and temporal distribution.

Besides tectonic activity, glacial processes (mainly erosion and deglaciation) and progressive failure also have a strong influence on rock-slope failures. Especially glacial debuttressing (Evans & Clague, 1994; Holm et al., 2004; Cossart et al., 2008; Agliardi et al., 2009a; Crosta et al., 2013) and the decay of permafrost (Fischer et al., 2006; Fischer et al., 2012; Krautblatter et al., 2013; Blikra & Christiansen, 2014) and the following progressive failure (Bjerrum, 1967; Eberhardt et al., 2004; Hermanns et al., 2012b) are suggested to favor or trigger large rock-slope failures in (previous) glacierized high mountain areas.

Increased knowledge on rock-slope failures and their complex processes (including e.g., geomorphological features, and type, mechanism and amount of deformation) can be gained by detailed integrative site studies (Willenberg et al., 2008a; Welkner et al., 2010; Blikra, 2012; Böhme et al., 2013; Booth et al., 2014) combining field investigations (geomorphological and geomechanical mapping) and modern investigation and monitoring techniques such as remote sensing (TLS, photogrammetry, dGNSS) (Oppikofer et al., 2009; Oppikofer et al., 2012b; Yugsi Molina et al., 2012; Booth et al., 2013; Wolter et al., 2014), geophysics (Ganerød et al., 2008; Willenberg et al., 2008b), numerical modeling (pre- and post-failure) (Hürlimann et al., 2006; Stead et al., 2006; Bachmann et al., 2009; Gischig et al., 2011), and surface-exposure dating (terrestrial cosmogenic nuclides) (El Bedoui et al., 2009; Hippolyte et al., 2009; Hermanns et al., 2012c; Hermanns et al., 2013c).

Nevertheless, geomorphological analysis of the slope is the main key to classify large gravitational rock-slope deformations and to understand their development, complex processes and morpho-tectonic control. Depending on the different study approaches, various terms have been applied throughout the years to describe the phenomena of such slope instabilities (Agliardi et al., 2001; Agliardi et al., 2012; Chigira et al., 2013) including rockslides, rock slumps, lateral spreads, rock (mass) creep, rock flow and “Sackung” (sagging) (Zischinsky, 1969a; Zischinsky, 1969b; Radbruch-Hall et al., 1976; Varnes, 1978; Hutchinson, 1988; Hungr et al., 2014). Within older literature the term “Sackung” is sometimes further described with the special types of “Bergzerreißung” and “Talzuschub” (Ampferer, 1939; Stini, 1941; Zischinsky, 1969a). Thereby, the first is related more to the deformation structures in the upper part of the slope, and the second describes the slope deformation with special feature of distinct slope bulging in the lower slope section.

Nowadays, the term deep seated gravitational slope deformation (DSGSD) is generally used to describe large rock-slope deformations with small displacement rates but large cumulative deformations (non-catastrophic mass movements), irrespective of the presence of a major sliding plane (Dramis & Sorriso-Valvo, 1994; Agliardi et al., 2001; Agliardi et al., 2012). The two main types of DSGSD are “Sackung” and lateral spread. According to the review of the definition by Agliardi et al. (2012) most of the observed DSGSDs are “Sackung” (i.e., sagging) that occur within igneous, metamorphic or layered sedimentary rocks in alpine areas. Nevertheless, the phenomena show no unique mechanisms but a large variability.

However, all the definitions are mainly based on surface observations of geomorphological features and generally show common characteristics (morphostructures). These are, for instance, a distinct back scarp (back crack), double ridges, large slide blocks, tension cracks, counterscarps (or uphill-facing scarps), grabens, collapsed block fields, and irregular slope profiles with, for instance, slope bulging at the toe (Zischinsky, 1969b; Bovis & Evans, 1996) (Gutiérrez-Santolalla et al., 2005; Agliardi et al., 2009a; Reitner & Linner, 2009; Crosta et al., 2013; Jomard et al., 2014). The type and distribution of this morphostructures often distinguish different areas along the slope indicating various types and intensity of deformation and hence supporting interpretation of complex kinematics.

Following the classification by Dramis & Sorriso-Valvo (1994), Agliardi et al. (2001), Agliardi (2012) and Agliardi et al.(2012), a DSGSD can be summarized as a large, non-catastrophic, long-lasting landslide and can be identified by the following diagnostic features whereby the surface deformation features are the most important indicators: (1) Large size of the phenomena that involves the entire slope from ridge to toe; (2) relatively low displacement rates (up to tens of mm/a) that sum up to large cumulative displacements; (3) morphostructures such as double ridges, scarps, counterscarps, etc.; (4) geomorphological characteristics such as slope bulging and enhanced rock fracturing; (5) minor secondary, often catastrophic landslides within the deformed mass and the lower part of the slope.

However important these morphostructures are, their origin along slopes in high mountain terrain is often not clearly understood and discussed. Because as mentioned by Jomard et al. (2014) the geomorphological expression of morphostructures of a DSGSD are often close to neotectonic features. Especially several kilometer-long linear features that build a vertical step (either uphill- or downhill-facing) along the slope, for instance, counterscarps (uphill-facing scarps), have been discussed to be related either to tectonic faulting (tectonic surface ruptures) or to gravitational slope deformation (e.g., gravitational sackung) which sometimes led to the reinterpretation of structures (Thompson et al., 1997; Hippolyte et al., 2006; Agliardi et al., 2009b; Li et al., 2010). Such structures can show characteristics of both origins (Thompson et al., 1997). However, various mechanisms, including gravitational deformation, folding and faulting are described by Li et al. (2010) who also highlights the influence of mountain topography on kinematics of deformation. Therein, flexural toppling along sub-vertical bedding planes is suggested to be the primary origin for a swarm of counterscarps, similar to Hippolyte et al. (2006) who additionally considers the gravitational reactivation of inherited fault structures.

A distinct morphostructure is well developed at the Middagstinden Mountain as a prominent 1.5 km long linear feature that strikes SSW – NNE with 30° oblique to the SE-facing slope and that forms a 3–4 m high convex step in the topography. In previous studies this structure was interpreted as a Holocene reverse fault (the "Berill fault") and as the first evidence of neotectonic activity (surface deformation due to faulting) in southern Norway (Anda et al., 2002; Olesen et al., 2004). Furthermore, this interpretation was used to explain the cluster of rock-slope failures in this area by suggesting neotectonic seismicity as the triggering factor (Blikra et al., 2002). However, conducted preliminary investigations indicate that the linear feature does not show any neotectonic activity, but strongly limits a DSGSD that has developed in the upper part west of it by forming its lower boundary (Krieger, 2013; Krieger et al., 2013). The DSGSD is controlled by geological structures and shows several different morphological areas with, for instance, coherent slide blocks, rather slope-parallel and up to 20 m deep counterscarps, and large block-fields that indicate various amounts of deformation and complex deformation style.

This chapter presents results of detailed integrative site investigations of the DSGSD at Middagstinden Mountain, including geomorphological field mapping, remote sensing, geomechanical analyses, geophysical resistivity tomography, and differential global navigation satellite system displacement measurements, in order to describe the morphostructures, to discover their origin (either tectonic or gravitational) and to relate them to the complex kinematics and deformation processes. The findings and the proposed geological model will be an important input for more advanced analyses such as numerical stability and runout modeling that can be applied to study the deformation and failure processes in more detail. The presented case study further contributes to the understanding of the complex deformation mechanisms and morphostructures of a DSGSD and can improve interpretation of linear features along slopes in other high mountain areas.

4.3 Regional setting

The study area is located in the upper part of Innfjorddalen Valley, Møre og Romsal County in western Norway (Fig 4.1). The rock-slope instability is situated at the southern slope of Middagstinden Mountain, directly above the artificial Berrilvatnet Lake. This area was significantly affected by Pleistocene glaciations with strong erosion and post-glacial isostatic uplift (Olsen et al., 2013a) and the crust still shows a current apparent uplift rate of several mm/yr (Dehls et al., 2000). The valley is a typical U-type shaped valley with steep slopes and a high topographic relief (here ranging elevations from 370 m a.s.l. to 1568 m a.s.l.). In this area of Møre og Romsal County, large rock-slope failures are common phenomena (Blikra et al., 2002; Saintot et al., 2012). The deposits of multiple rock-slope failures that are preserved in the lower part of Innfjorddalen Valley indicate post-glacial failure activity (Schleier et al., 2013b; Chapter 3).

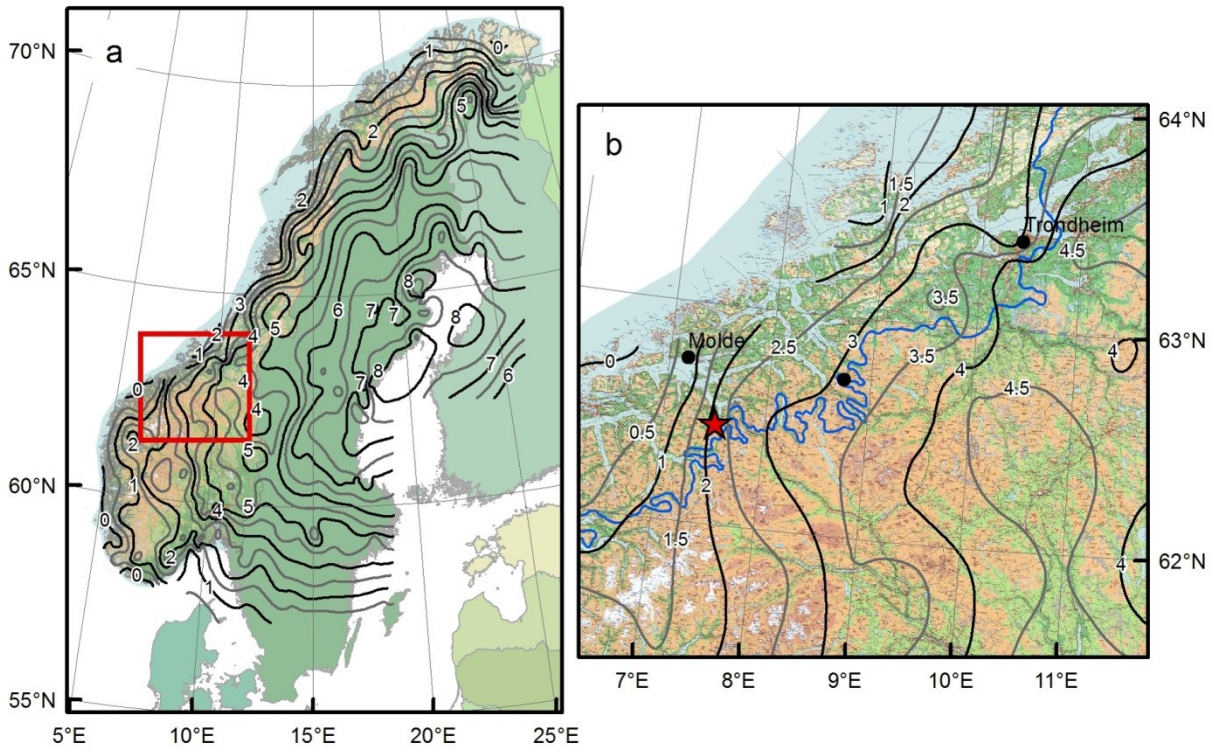

Fig. 4.1: Map of current apparent uplift rates of Fennoscandia in mm/yr (black contours) following Dehls et al. (2000). (a) Overview of Norway, the red rectangle delimits area of (b). (b) Area around Middagstinden Mountain in Innfjorddalen (red star). Additionally shown is the Younger Dryas ice extent (blue line) following Sollid & Sørbel (1979).

Geologically, this area is part of the Western Gneiss Region (WGR) of Norway. The bedrock consists mainly of Proterozoic gneisses with a magmatic origin, which is locally covered by oceanic and continental sediments. The deformation and metamorphisation of the neo- and mesoproterozoic rocks took place during the Caledonian orogeny (Nordgulen & Andresen, 2008). The most prevalent rock types in the WGR are tonalitic and granodioritic gneisses (Hacker et al., 2010). The disclosed bedrock in Innfjorddalen is mainly composed of different types of gneisses (Fig. 4.2). Several lithologies can be distinguished following Tveten et al. (1998). The Middagstinden Mountain is mainly composed of undifferentiated, chiefly quartzdioritic gneisses that show local migmatitic structures. In the uppermost part, quartzitic gneisses that contain sillimanit and partly kyanite also occur. These gneisses have, in general, a well-developed foliation that is often involved in rock-slope failures as sliding surfaces or other main delimiting structures (Henderson & Saintot, 2011; Saintot et al., 2011b). The region also shows a variety of tectonic structures (Fig. 4.2) that originate from different Caledonian and post-Caledonian tectonic activities (e.g., orogeny or post-orogenic collapse) (Tveten et al., 1998; Gabrielsen et al., 2002).

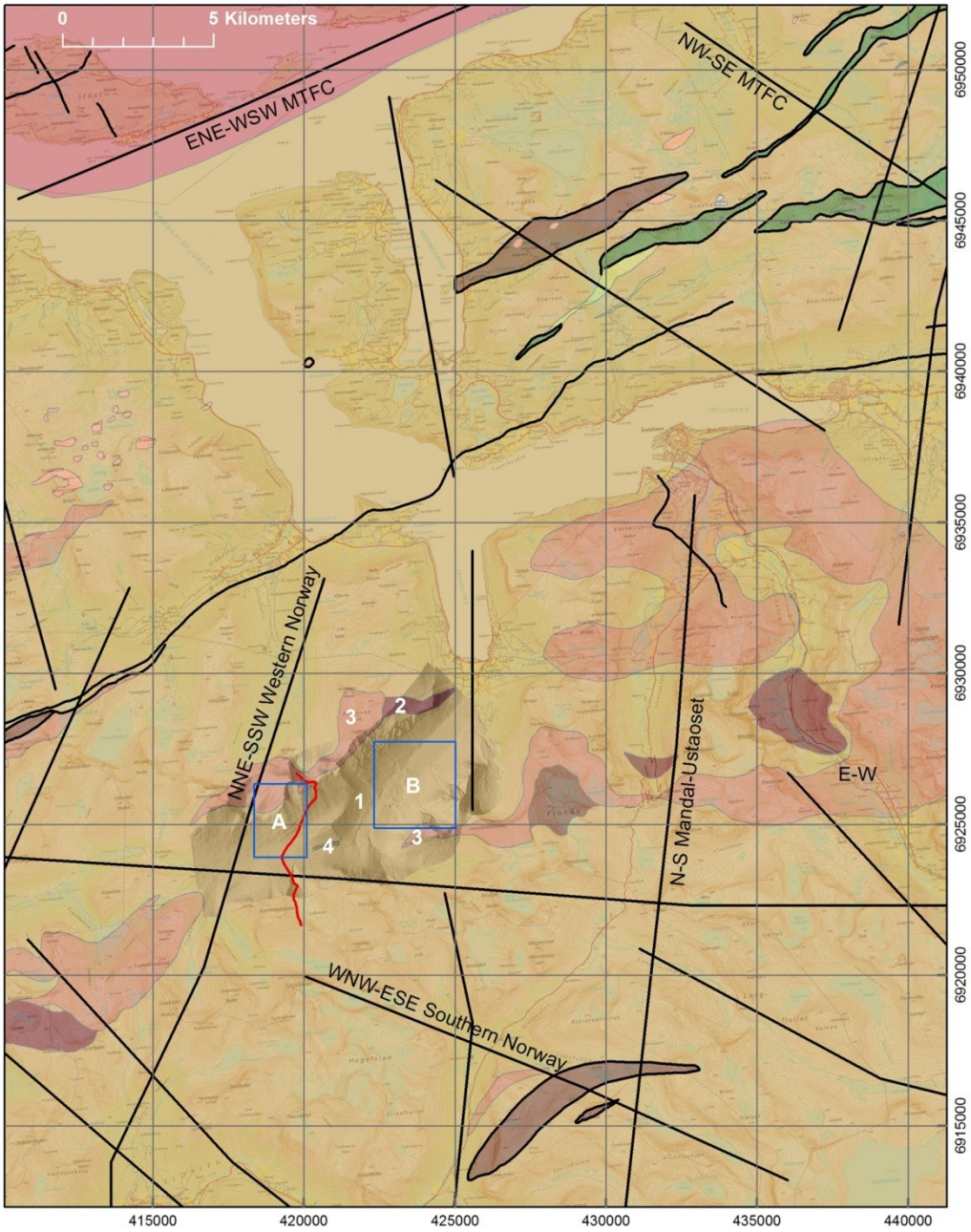

Fig. 4.2: Geological map of Innfjorddalen and Midagstinden Mountain. The main lithologies (labeled 1-4) and major tectonic lineaments (solid black line) are based on Tveten et al. (1998) and Gabrielsen et al. (2002): (1) undifferentiated gneiss, chiefly quartzdioritic, partly migmatitic; (2) coarse grained granitic gneiss, augengneiss, gneissic granite; (3) quartzitic gneiss, containing sillimanit and partly kyanite; (4) eclogite. For regional overview, refer to Fig. 1.3 and Table 1.3. The observed fault lineament at Middagsinden Mountain is marked by solid red line. The blue rectangles delimit the study areas of: (A) Middagstinden instability; (B) Gråfonfjellet Mountain (Chapter 3). (Coordinate system: WGS1984, UTM Zone 32N)

4.4 Materials and Methods

4.4.1 Field investigations and used data

Detailed geomorphological and structural field mapping was carried out at the unstable rock slope of Middagstinden Mountain to characterize the different areas within the slope, to identify geomorphological features and limiting structures of the rock-slope instability.

Field mapping was supported and improved by remote sensing data such as orthophotos with grid size of 0.5 m × 0.5 m and airborne laser scanning (ALS) derived digital elevation model (DEM) with grid size of 2 m × 2 m (both with reference to Geological Survey of Norway database). This data was implemented in the geographical information system ArcGIS 10.x (Esri Inc.) for surface analyses. Orthophotos and especially the DEM derivatives such as hillshade (i.e., shaded relief), slope angle, slope aspect and slope curvature (Fig. 4.3) enable a better overview over the whole site, and an improved identification of prominent geomorphological structures throughout the instability.

Detailed structural field mapping of the whole investigation area with rock outcrops was performed at 35 locations (marked in Fig. 4.5). In total, 1 126 plane measurements were conducted with a Clar-type geological compass to determine the orientation of discontinuity surfaces (e.g., foliation, fault sets, joint sets). To obtain a comprehensive dataset, the geological strength index (GSI) of the outcrop and characteristics of discontinuities such as spacing, persistence and roughness were recorded at these locations following the classification of Wyllie & Mah (2004). This data increases the understanding of possible movements within the rock mass and are important rock mechanical parameters for future stability analyses.

Supplementary data for structural analyses was gained from airborne- and ground based LiDAR (Light Detection and Ranging) data in order to create a high resolution digital elevation model (HRDEM). To create a HRDEM by terrestrial laser scanning (TLS), the site was scanned with the long range Optech ILRIS LR (Optech Inc.) scanner device (Optech, 2014) using the time-of-flight technique. 14 scans were conducted from five positions (marked in Fig. 4.5) with different lines of sight to obtain a preferably dense 3D point cloud of the slope. Scan direction was generally upward with a mean distance and point spacing ranging from 700 m with 80 mm up to 1 650 m with 130 mm, respectively. To minimize the disturbing factor of vegetation only the last reflected impulse of the pulsed laser was recorded. Postprocessing of the LiDAR point clouds (i.e., removal of disturbing reflections such as vegetation, aligning and georeferencing of the point clouds) was conducted by using the Polyworks software package (InnovMetric Software Inc.). The LiDAR technique, methods, data treatment and its application to landslide research are reviewed in detail by Jaboyedoff et al. (2012) and Abellán et al. (2014) and in Chapter 2.4.3.

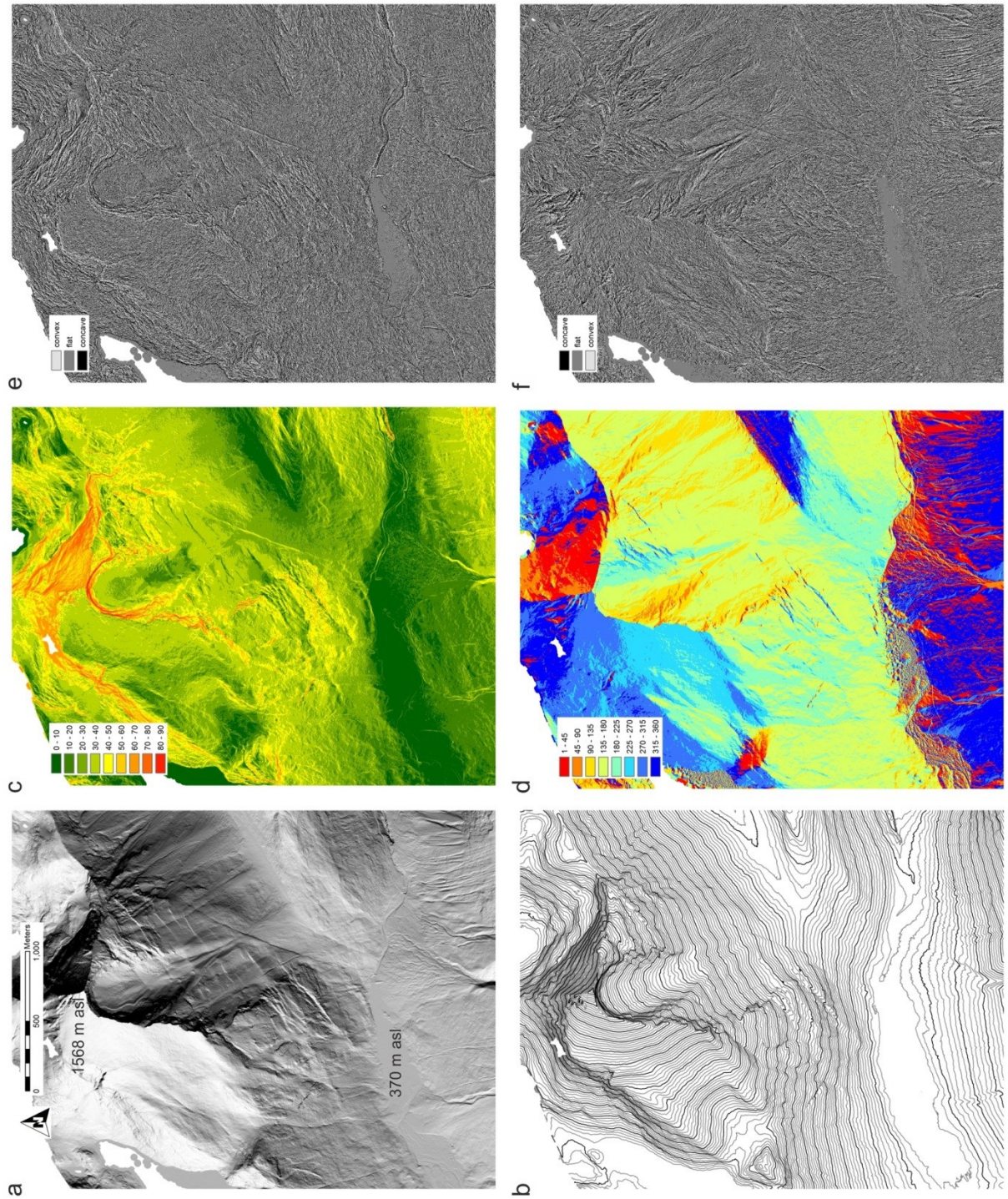

Fig. 4.3: Topographic characteristics of Middagstinden Mountain, represented by the DEM derivatives (2 m grid size). (a) hillshade (lake water level at 370 m a.s.l., mountain top at 1 568 m a.s.l.), (b) 10 m contour lines, (c) slope angle in degree, (d) slope aspect in degree, clockwise from north, (e) profile slope curvature, and (f) planar slope curvature.

4.4.2 Structural and kinematic analyses

The orientation of discontinuity sets can be obtained directly by field measurements. In order to determine discontinuity sets and their orientation based on the HRDEM, the software Coltop3D (terr@num Inc.) was used (Jaboyedoff et al., 2007). This software computes plane normals out of the point cloud and provides them with an orientation-specific colour. By manual selection of plane normals with similar color (representing surface planes), the orientation of discontinuity surfaces were obtained. In this case 22 124 pole vector selections were made. The results were exported in a text file as dip and dip direction for further analyses (Oppikofer et al., 2012b).

Structural data (either derived by field measurements or analysis of the HRDEM) was analyzed by using the software Dips 6.0 (Rocscience Inc.). Cluster analysis was conducted to determine mean orientations and 1σ variability of the main discontinuity sets. Additionally, field measurements of the sampling locations were assigned either to 12 representative morphological areas within the slope (e.g., coherent rock blocks), or to one whole dataset to determine mean values for these areas or the whole slope, respectively. Results were plotted in Schmidt net (equal area, lower hemisphere) and depicted as great circles, pole points and 1σ variability cones and are presented with dip/dip direction.

Furthermore, kinematic feasibility tests for planar, wedge and toppling failures (Turner & Schuster, 1996; Wyllie & Mah, 2004) were carried out based on the field measurements by using Dips 6.0. For analyses, the slightly changing topography along the slope has to be taken in consideration. Surface analyses with ArcGIS 10.x (Esri Inc.) show that the slope angle (dip) is rather constant with mean value of 35° but the slope aspect (dip direction) changes along the slope from the eastern (~151°) to the western (~182°) part. Therefore, a mean slope orientation of 40°/175° (dip/dip direction) was used. A friction angle of 20° along discontinuity surfaces and lateral limits of 30° (for planar sliding and toppling) were applied for kinematic analyses to obtain conservative results. These values are in accordance with recommendations by Hermanns et al. (2012b) on the hazard and risk classification of large unstable rock slopes in Norway. Thereby, the lateral limit (30°) that is larger than the standard value of 20°, a value generally adopted for rock-slope engineering (Wyllie & Mah, 2004), accounts for the more complex structures of large rock-slope failures.

4.4.3 Displacement measurements

Displacements within the rock-slope instability have been monitored periodically by the Geological Survey of Norway (NGU) using the differential global navigation satellite system (dGNSS) technique (the yearly measurements were conducted by Trond Eiken, University of Oslo). The monitoring network consists of one fix point in a stable part above the main scarp and three rover points that are installed within the apparently unstable parts of the mountain slope (Fig. 4.5). This setup enables to derive a vector network indicating the relative point movement. Uncertainties for measurements in the horizontal direction of 3–6 mm and in the vertical direction of 10–20 mm are assumed in this method (Hermanns et al., 2011a).

A movement is considered to be significant when it is larger than the uncertainty value range. Because of large differences in height between the rover points and the fix point, as well as annual systematic trends from un-modeled meteorological effects, the vertical uncertainty is much higher than the horizontal and must be interpreted carefully (Böhme et al., 2012).

For displacement monitoring at Middagstinden Mountain annual measurements were conducted between 2008 and 2013 (without measurement in 2012 due to bad weather conditions). Measurements provide 2D horizontal and vertical displacements. By regression analyses of the measured displacements against time, a trend for the movement rate (mm/yr) can be determined. Furthermore, a 3D movement vector was obtained by regression analyses of the N – S against E – W displacements (showing its trend) and vertical against horizontal displacements (showing its plunge) (Böhme et al., 2013).

4.4.4 Geophysical investigations

A distinct geomorphological lineament observed at the slope of Middagstinden Mountain, was interpreted as the trace of a neotectonic reverse fault (Anda et al., 2002). Therefore, geoelectric resistivity tomography technique was applied to investigate the continuation and orientation in the subsurface of the observed fault structure. Three 2D geoelectric resistivity profiles were measured by the NGU at the lower slope and the valley bottom (Fig. 4.5) using the Lund system (Dahlin, 1993), a gradient electrode configuration and an ABEM SAS Terrameter 4000 (ABEM, 1999) instrumentation. Electrode separation was set at two meters (profile 1 and 2) and at five meters (profile 3) giving a penetration depth of 25 m and 60 m, respectively. This method is proven to be a powerful tool for mapping drift deposits and fracture zones in bedrock (Solberg et al., 2008; Rønning et al., 2009; Rønning et al., 2014).

In addition, the NGU opened two trenches down to glacial deposits or bedrock on the valley bottom where the geoelectric profile P3 suggests the position of the fault, to study the deformation of the soft sediments (Fig. 4.5).

4.5 Results

Preliminary results according to investigation of the rock-slope instability at Middagstinden Mountain have already been described and discussed in Krieger (2013) and Krieger et al. (2013). However, this data and the interpretation were improved by detailed structural cluster analyses, further remote sensing (orthophoto and DEM) analyses and additional dGNSS displacement measurements.

4.5.1 Geomorphology and morphostructures

Based on field mapping, DEM (ALS derived) and orthophoto analyses, several main areas (1 to 11) can be distinguished within the S-facing slope of Middagstinden Mountain that are characterized by different morphologies and types and/or amount of deformation (Fig. 4.4).

All the described areas that show deformation at the rock slope are located NW (i.e., above) of the linear morphological feature previously described by Anda et al. (2002) as the “Berill fault”. These areas can be roughly distinguished as the eastern part (1 to 4), the main part of active rock-slope instability (5 to 10) and an active moving rock block west of the main part (11) and can be described as follows.

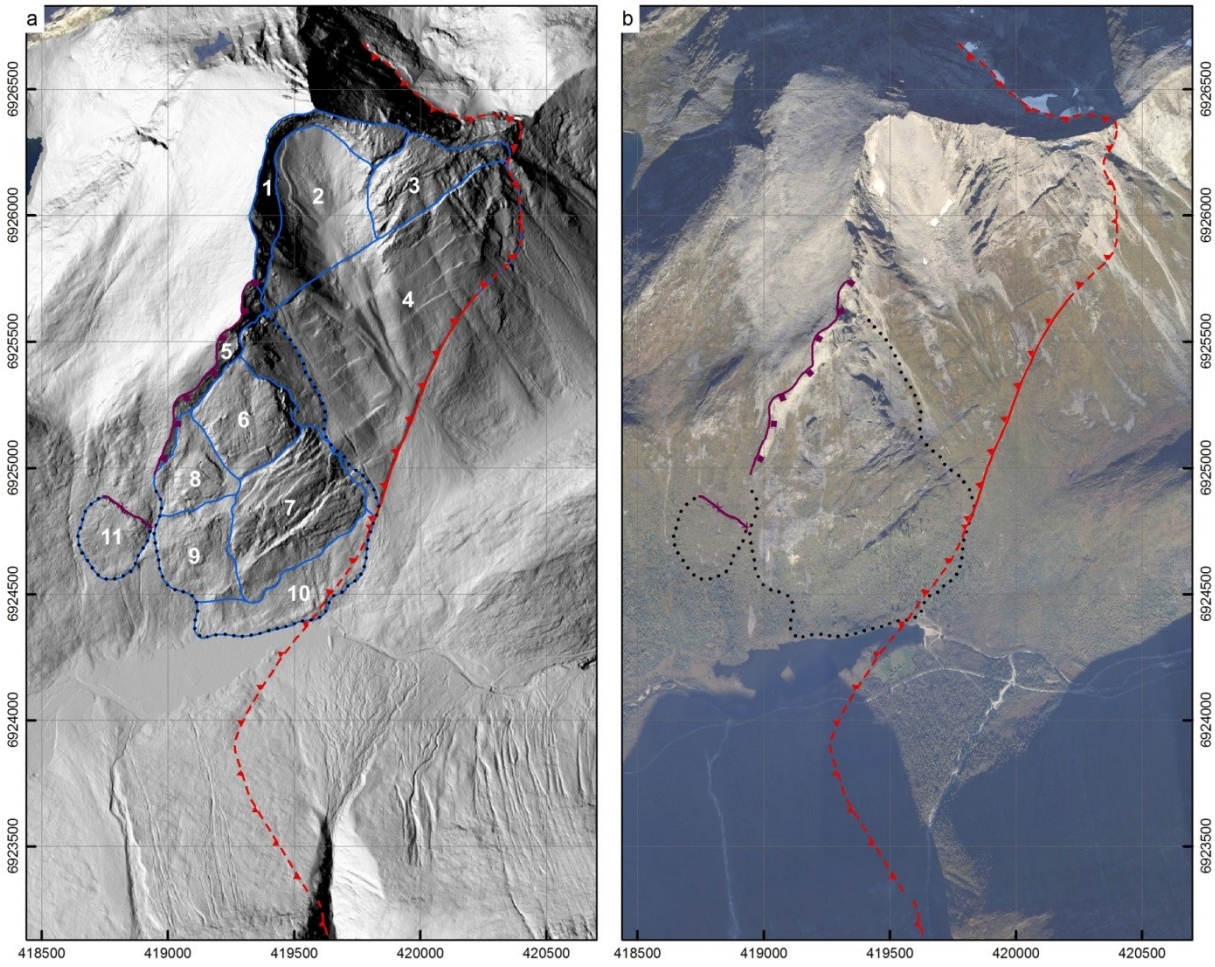

Fig. 4.4: Overview map of Middagstinden Mountain. (a) hillshade and (b) orthophoto, showing the extent of the main rock-slope instabilities (black dotted line), the associated main scarps (purple line), and the trace of the fault lineament (red line). Additionally, the geomorphological areas are outlined in (a) as described in the text. For an oblique view, refer to Fig. 4.6. (Coordinate system: WGS1984, UTM Zone 32N)

4.5.1.1 Northeastern part (1 to 4)

(1 to 3) Upper northeastern part: The large niche is limited at the back by a steep and high rock face (1). Small-scale failures such as rock fall could be likely for this fractured steep rock slope. Area (2) is covered by debris and talus material and shows moraine deposits indicating the existence of a previous cirque glacier that could have formed the niche. The

niche is limited toward NE by fractured bedrock material (3) that shows fractures and joints rather parallel to the foliation.

(4) Lower northeastern part: This area is covered by surficial sediment deposits and shows morphological lineaments that strike NE – SW (parallel to the counterscarps) and the main scarp of the active instability (5 to 10) (Figs. 4.5 and 4.6). The lineaments are around 3 m deep depressions (sackungs) that limit toward the fault and partly deform the surficial deposits. These depressions are partly filled by alluvial debris (avalanche deposits). Furthermore, lateral moraine deposits that are associated to the Younger Dryas cirque glacier are preserved and active avalanche tracks and associated debris cones were identified. This morphological area is limited toward SE by a prominent morphological lineament ("Berill fault"). This lineament strikes SSW – NNE and can be traced as a 3–4 m high convex morphological step oblique to the slope. The lineament is around 1.4 km long but disappears in the valley bottom.

4.5.1.2 Main part (5 to 10)

Several sub-areas are distinguished within the main rock-slope instability (Figs. 4.4 and 4.5). Besides the morphological areas, rather coherent rock blocks were identified within the instability showing different deformations and movements.

(5) Main scarp and sliding surface: The back bounding limit of the rock-slope instability is formed by its main scarp (Fig. 4.5). Below the crest, the sliding surface is exposed. In this case, it is mainly composed by the foliation and sub-parallel surfaces (Fig. 4.6). Scarp offset was measured in ArcGIS based on DEM and orthopohoto inspections. The mean horizontal displacements between the main scarp and the moving mass (i.e., horizontal width of the exposed sliding surface) are approximately 50 m but slightly varying along the scarp (e.g., smaller at the SW limit of the scarp). The mean height of the scarp is around 60 m. This results in a 3D offset of around 78 m.

(6) Upper eastern part: This area is composed of several rather coherent slide blocks that cover an area of around 130 000 m^2 (Fig. 4.5). The rocks are fractured (Fig. 4.6) and the slide blocks are mainly delimited by the major joint sets. These blocks show no surficial sediment cover. Small-scale rock-fall activity is frequent at the lateral and frontal margins where large block-fields with up to several meter sized blocks have developed. This area shows the lowest amount of rock deformation throughout the instability.

(7) Lower eastern part: Main morphological characteristics of this area are the prominent counterscarps (uphill-facing scarps) formed by fractured bedrock (Fig. 4.6). These lineaments mainly strike NE – SW, sub-parallel to the depressions (sackung) in area (4). Furthermore, they run sub-parallel to the foliation. Morphologically, these lineaments are graben-like structures that are up to 20 m deep and tens of meters wide (varying between 10–50 m). High small-scale rock-fall activity is present at the associated rock faces. Hence, the scarps are filled with meter sized blocks that masks their real depth. This area can be distinguished into the areas of upper and lower counterscarps (Fig. 4.5). These structures are more frequent in the upper area and also two rather coherent slide blocks can be

determined in the lower area. One of these blocks marks the lowermost limit of the lower eastern part. This area shows a higher amount of rock deformation than the upper part (6). Bulging of the slope is characteristic for the large scale slope topography in this area.

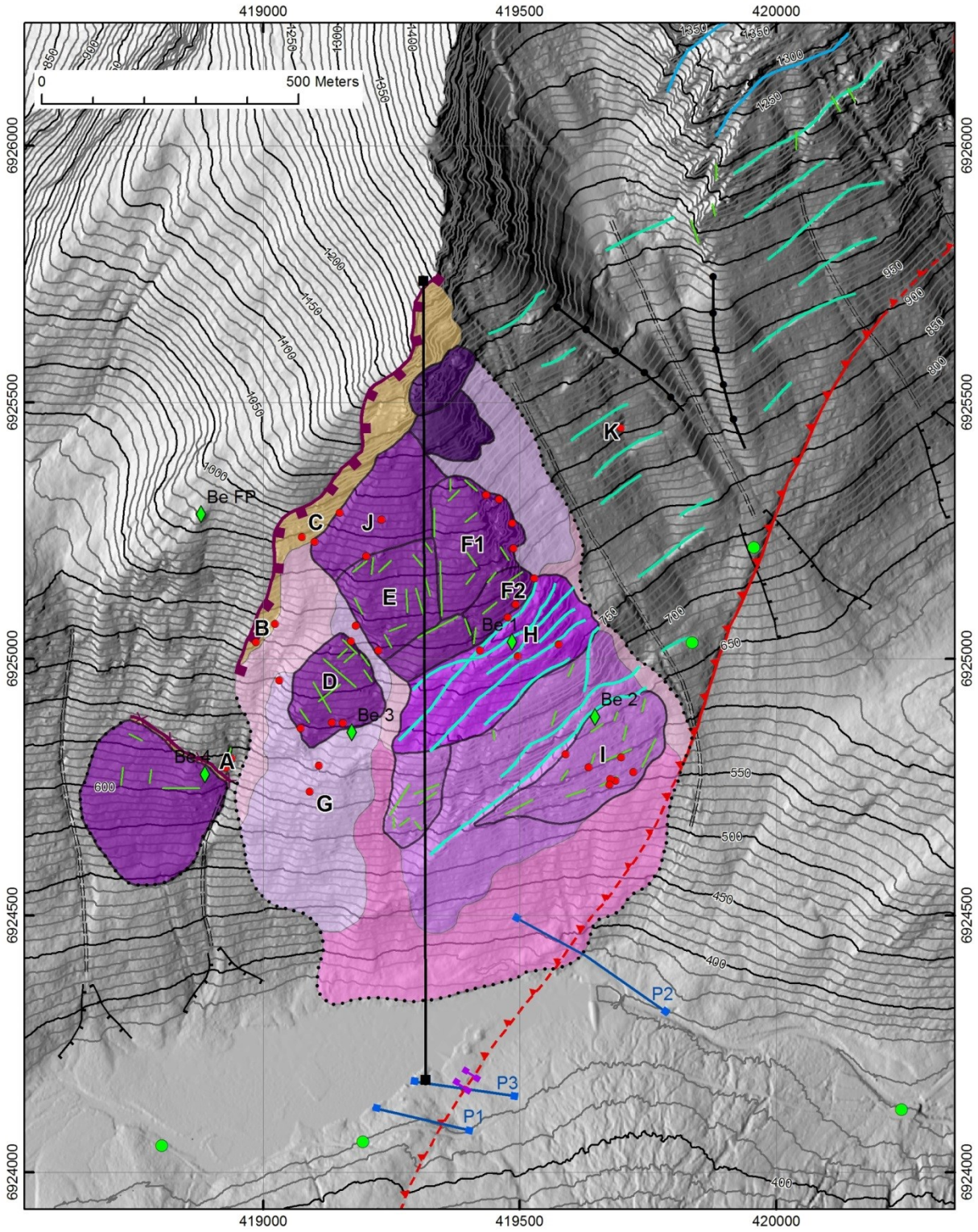

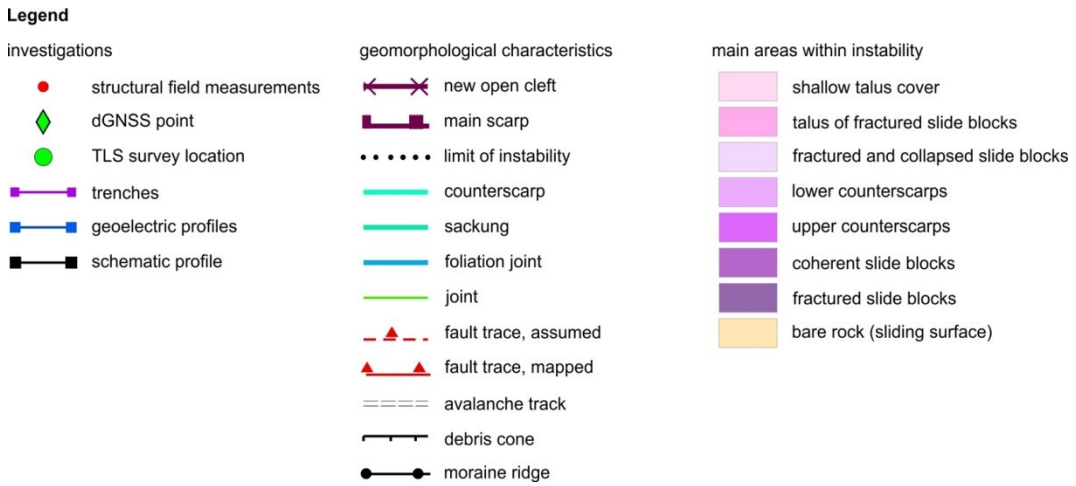

Fig. 4.5 (previous page): Map of the rock-slope instability of Middagstinden Mountain, showing the locations of conducted investigations, the geomorphological characteristics and the distinguished areas of deformation. The labels A to K mark the areas determined for structural analyses as presented in Fig. 4.7. (Coordinate system: WGS1984, UTM Zone 32N)

(8) Upper western part: This area is limited by the main scarp (5) and the lateral limit of the coherent slide blocks of area (6). The upper part, directly below the scarp (sliding surface) is characterized by shallow talus cover. One distinct coherent slide block with defined lateral limits is located in the main part of this area (Fig. 4.5). This block is composed of fractured bedrock, similar to the blocks in area (6). The opened cleft between this block and the blocks of area (6) indicate a slight rotation (Fig. 4.6). Besides this large slide block, many single and mainly highly fractured bedrock outcrops (small slide blocks) are found randomly distributed within this area, especially at the western and frontal limit. Small-scale rock fall occurs at the margins of these blocks. These slide blocks are surrounded by large block-fields of fractured and collapsed slide blocks that are composed of meter sized boulders (mainly angular and very angular forms). The lack of repositioning structures and highly fractured bedrock outcrops within the deposits suggest an origin by in situ fragmentation rather than rock-fall activity from above. This area shows the highest amount of large scale rock deformation throughout the instability.

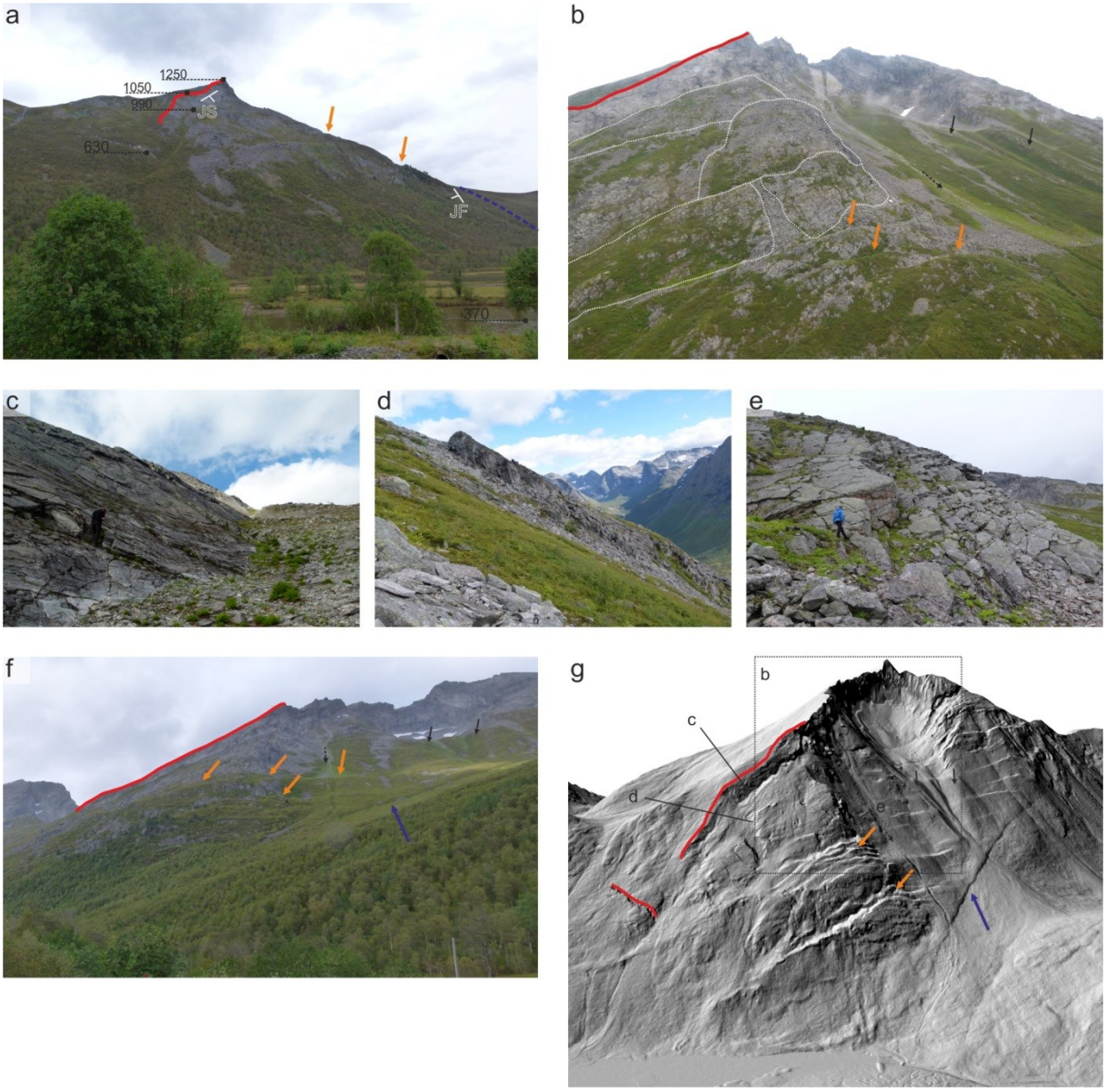

Fig. 4.6: Photographs and oblique view of Middagstinden Mountain, showing geomorphological characteristics of the rock-slope instability (red line, main scarp; blue dashed line and blue arrow, morphological trace of the fault; orange arrow, counterscarp; black solid arrow, moraine ridge; black dashed arrow, avalanche track). For scale and areas within the instability, refer to Figs. 4.4 and 4.5. (a) Overview from the valley bottom (view direction toward NNE). The labels mark elevations in m a.s.l. Further indicated are the dip of the foliation (JS) and the fault (JF), forming a wedge failure. (b) Upper part of the instability as seen from helicopter (view direction toward N), showing coherent slide blocks (white dotted line) above the area of upper counterscarps. (c) Sliding surface below the main scarp, parallel to JS. (d) Western limit of a coherent rock block in the upper eastern part of the instability. (e) Fractured bedrock as exposed on the coherent rock block in the upper eastern part of the instability. (f) Overview from the valley bottom (view direction toward NNW). The marked trace of the fault forms a 4 m convex topographic step running oblique to the slope. (g) Oblique 3D view of the hillshade (view direction toward N). Black dotted rectangle indicates the area shown in (b), and labels mark locations of (c), (d) and (e).

(9) Lower western part: This area is mainly characterized by large block-fields (meter sized boulders) of fractured and collapsed slide blocks that show local repositioning structures (Figs. 4.5 and 4.6). Besides that, areas with a lack of large boulders but talus of fractured slide blocks were also identified. In some areas of the loose rock deposits with smaller boulder size and increased amount of soil, surficial mass movements (e.g., shallow debris flows) also occur. Bedrock outcrops can be only found in a few locations within the block-fields, and are highly fractured and weathered. An accumulation of such outcrops imbedded in large block-fields is observed at the transition to the upper area (8). Together with the upper part this area shows the largest amount of rock deformation / fragmentation within the instability.

(10) Lowermost part: The area that forms the lower limit of the rock-slope instability is characterized by talus material (mainly meter sized rock boulders) of the fractured and partly collapsed slide blocks. This material could be mixed up with previous (pre-failure) talus material of the slope. No large rock outcrops or large slide blocks are found within this area. However, the deposits show lobate deformation structures (Fig. 4.6), such as, for instance, compression ridges at the lowermost margin of the instability.

(11) Independently moving rock block: An active moving rock block is identified located west of the main instability (Figs. 4.5 and 4.6). This rather coherent slide block shows less distinct fractures of the surface and is limited by a NW – SE striking back crack. The newly opened crack is around 5 m wide and from several meters up to tens of meters deep.

4.5.2 Structural analyses

Four main discontinuity sets that are developed throughout the whole slope were identified by structural analyses of the field data and the HRDEM data as summarized in Table 4.1 and Table 4.2. Original data of structural field measurements are presented in Krieger (2013). The observed discontinuities are mainly the foliation (JS), a fault set (JF), two major joint sets (J1, J2) and one random varying minor joint set (Jx). 1σ variability of mean orientations is generally between 10–20°, whereas field measurements show higher variability (>16°). With reference to the geomorphological areas within the rock-slope instability (Fig. 4.5), variations of the mean orientations and 1σ variabilities are identified for the representative areas A toK (Fig. 4.7).

Table 4.1: Summary of the main discontinuity sets of the rock-slope instability at Middagstinden Mountain. Orientation of the mean surfaces is reported in dip/dip direction ± 1σ variability (in degree). The values are determined by structural cluster analyses (using Dips 6.0) of TLS-derived HRDEM data (n = 22 124 pole vector selections made in Coltop3D), and field measurements (n = 1 126 planes), respectively. Discontinuity characteristics, that is, spacing, persistence and roughness were observed in the field and are expressed qualitatively with reference to the classification of Wyllie & Mah (2004). JF shows lineations with trend/plunge of 31°/245° ± 11°. Groove marks with trend/plunge of 42°/138° ± 16° are observed on JS below the main scarp area. For location of structural field measurements and TLS scanner positions, refer to Fig. 4.5.

Type	Orientation		Spacing	Persistence	Roughness
	TLS (°)	Field (°)			
Fault (JF)	-	43/271 ± 16	Moderate to extremely wide	High	Slickensided, planar
Foliation (JS)	50/160 ± 11	49/158 ± 17	Close to moderate	High	Smooth, planar–undulating
Joint set (J1)	80/315 ± 8	77/309 ± 16	Wide to very wide	High	Rough, planar (undulating)
Joint set (J2)	81/048 ± 14	84/039 ± 20	Wide to very wide	High	Rough, planar (undulating)

Table 4.2: Orientation of intersections between mean surfaces of the main discontinuity sets at Middagstinden Mountain (Table. 4.1).

Intersection	Trend (°)	Plunge (°)
JF#JS	218	29
JF#J1	227	34
JF#J2	313	34
JS#J1	224	24
JS#J2	123	43
J1#J2	333	75

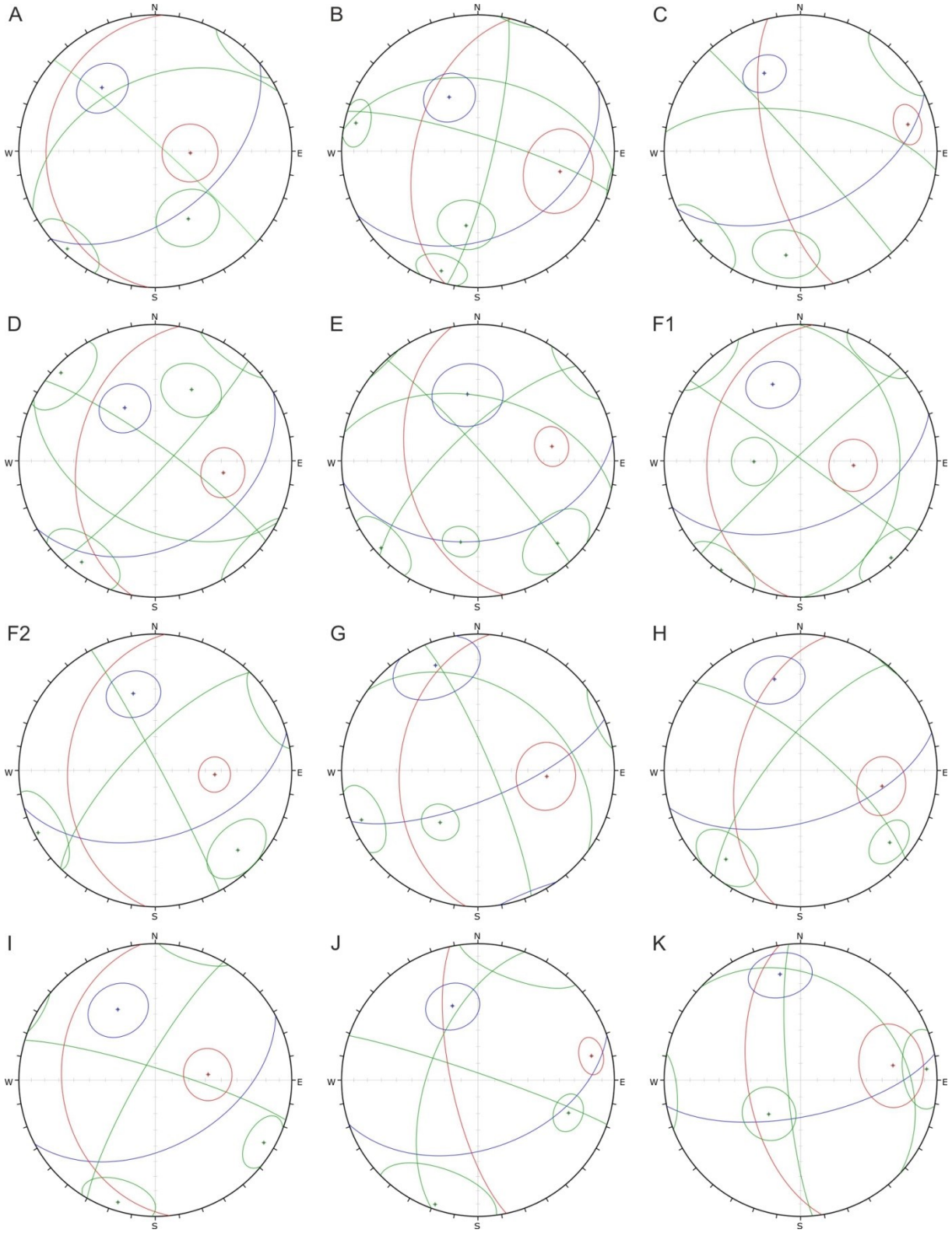

Fig. 4.7: Schmidt net plots of main discontinuity sets at various areas along the slope of Middagstinden Mountain (equal area, lower hemisphere). The discontinuities are indicated by different colors (blue, foliation; red, fault; green, major joint set), and the circles display the 1σ variability cones of their mean orientations. The values are derived by cluster analysis of the structural field measurements conducted for the distinguished areas labeled A to K. For location of structural field measurements and areas, refer to Fig. 4.5.

4.5.2.1 Foliation (JS)

The orientation of foliation (JS) shows a mean dip/dip direction of 49°/158° ± 17° based on field measurements, and varies over the whole area of the instable slope. This value is concordant to the mean orientation derived by the TLS dataset (50°/160° ± 11°) but shows a higher variability. Within areas (6) and (8), the foliation forms distinct smooth and planar–undulating discontinuity surfaces with high persistence, close–moderate spacing and little variability in orientation. The foliation forms prominent structures, both the main scarp and the counterscarp that limits area (6). Groove marks with a trend/plunge of 42°/138° ± 16° are found on the sliding surface below the main scarp that is formed by the foliation. However, the foliation shows higher variability in orientation, higher spacing and smaller persistence within the lower parts of the instability, especially the area of counterscarps (7). Dip direction varies between NNE and SSW with dip angle between 5° and 40°. This is due to folding in cm- but also m-scale with an E-striking axis that can be observed qualitatively but unfortunately cannot be measured in the rock outcrops.

4.5.2.2 Fault (JF)

A mean dip/dip direction of 43°/271° ± 16° (field value) was determined for the orientation of the fault set (JF). This discontinuity set was not detected within the TLS data because of its orientation with a relatively shallow dipping into the mountain slope that does not form distinct surfaces. However, field investigations gained further important information. The discontinuity set shows high, occasionally even very high persistence and the spacing varies very much depending on the area. In some parts the outcrops recur on the surface in meter scale, in other parts it is not existent. In the lower parts (i.e., area of counterscarps) it plunges about 16° shallower than further up the slope. Generally, the roughness can be described as slickensided, planar. The surfaces of this discontinuity set show a strong lineation (trend/plunge of 31°/245° ± 11°) and a distinct quartz–feldspar remineralisation with frequent break offs that indicate a normal fault movement (Fig. 4.8). These lineaments do not occur continuously on all surfaces of the fault set and the planes are partly undulated with varying orientations (Fig. 4.7).

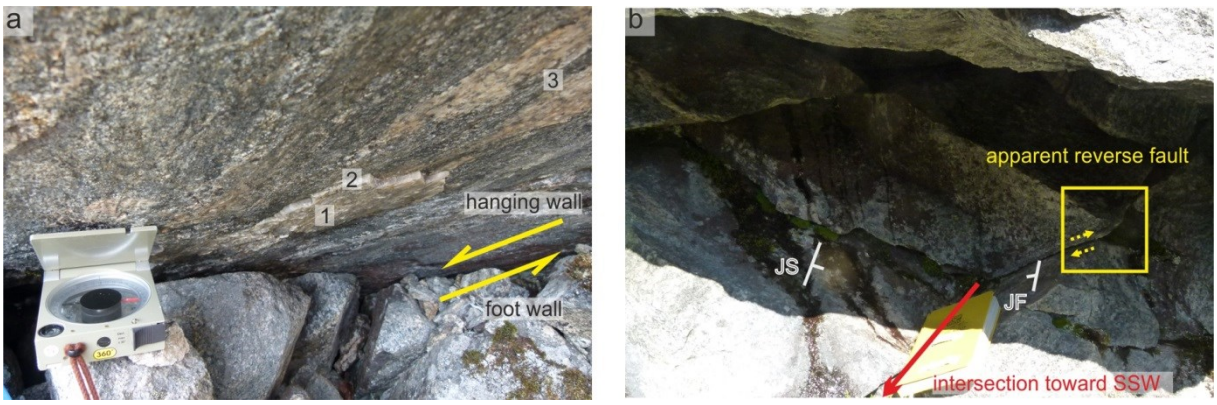

Fig. 4.8: Photographs of the fault plane and the wedge sliding along its intersection formed with the foliation observed at Middagstinden Mountain. (a) Fault plane JF showing (1) quartz re-mineralisation

(2) distinct break offs, and (3) lineations, which indicate a normal fault movement. (b) Wedge sliding along the intersection between JF and the foliation (JS) (red arrow, field measurement with trend/plunge of 201°/21°) as observed in a small-scale field example. The sliding causes the geomorphological structure of the apparent reverse fault because of gravitational reactivation. For mean orientation of discontinuity sets along the slope, refer to Table 4.1.

4.5.2.3 Joint sets (J1, J2)

Two prominent major joint sets (J1, J2) are developed throughout the slope. Both dip steeply with a field-measured mean dip/dip direction of 77°/309° ± 16° and 84°/039° ± 20°, respectively. Additionally, a random joint set (Jx) 45°/019° ± 15° can be found in some areas within the slope. These discontinuity sets were also detected in the TLS data with similar mean values but smaller 1σ variability. The major joint sets show wide to very wide spacing with high persistence. The surface roughness of the joint sets can be described as generally rough, planar and occasionally undulating. At the main scarp, these joint sets do not occur as frequently as in the deforming parts, and their persistence is much lower. Most of the prominent structures such as large fractures, cracks, or morphological lineaments that are visible in the field and on the DEM developed along these joint sets. Single small blocks or outcrops in the instability are mainly limited by J1 and J2 or a combination of both.

4.5.3 Kinematic analyses and schematic model

Kinematic analyses conducted with the mean orientations of discontinuity sets for the whole slope show that various types of failure are kinematically feasible (Fig. 4.9). A wedge failure is highly feasible as discontinuity sets show various intersections (Table 4.2) that outline within the failure envelope. The critical intersections are JS#JF, JS#J1 for the mean slope orientation of 40°/175° (dip/dip direction). In case of the slightly steeper slope angle (dip 50°), intersection JF#J1 is also critical. Wedge failure is feasible for the mean slope orientation but also for the changing aspects along the slope (i.e., ranging from 151−182° from the eastern to the western part). Toppling failure would be kinematically feasible along J1 when the slope aspect is more to the southeast (e.g., 150°). Planar failure along JS is kinematically feasible for the observed slope orientations. However, 1σ variabilities (generally >10°) indicate that also the variability of intersections has to be taken into consideration.

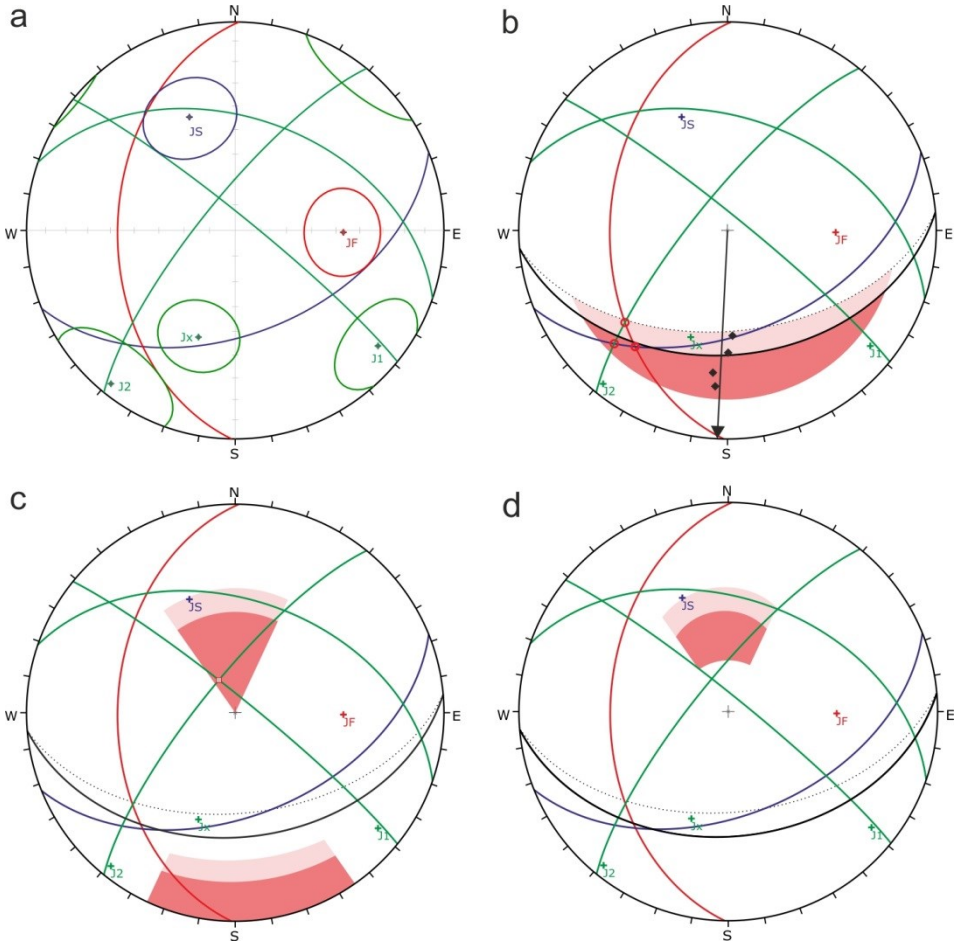

Fig. 4.9: Schmidt net plot of main discontinuity sets at Middagstinden Mountain (equal area, lower hemisphere). The discontinuities are the foliation (JS), the fault (JF), and two major (J1 and J2) and one random (Jx) joint set (see Table 4.1). The values are derived by cluster analysis of the structural field measurements conducted for the whole slope. (a) Mean orientation and 1σ variability (displayed by circles). The results of the kinematic feasibility tests (friction angle 20°, lateral limit 30°) are shown by the failure envelopes for (b) wedge failure, (c) toppling failure, and (d) planar failure, by using a mean slope aspect of 175° and mean slope angles of 40° (dark color) and 50° (light color).

A schematic geological model for the deep seated gravitational slope deformation of Middagstinden Mountain was established based on the geomorphological and structural findings (Fig. 4.10). This 2D model is based on a topographic profile that is drawn in direction of the movement. The model indicates the apparent dip of the foliation (JS) and the fault (JF). The intersection line between these two discontinuity surfaces is critical according to the kinematic analyses (trend/plunge of 218°/29°). However, this intersection line does not daylight at the slope but lies below the valley bottom. Hence, simple wedge sliding is not possible and other deformation mechanisms are necessary to explain the complex movements of this rock slope, and thus the geomorphological characteristics such as counter scarps and slope bulging.

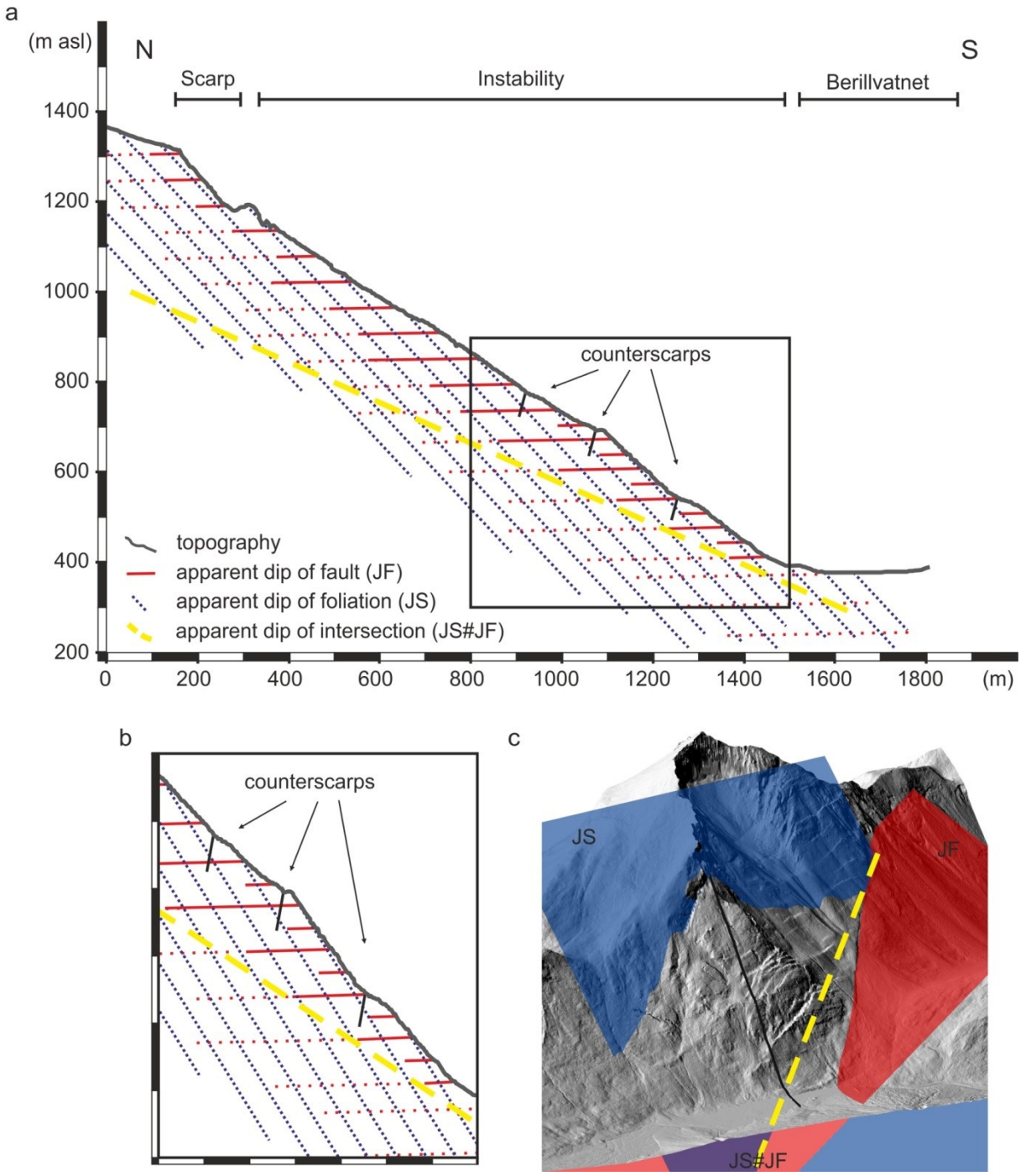

Fig. 4.10: Schematic profile of the rock-slope instability at Middagstinden Mountain, drawn parallel to the main movement direction (N–S). For location, refer to Fig. 4.5. The figures represent the current topography, the apparent dip of the two main limiting discontinuity sets (JS, foliation; JF, fault), and the apparent intersection line. (a) Profile along the whole slope, running from the uppermost scarp to the valley bottom. Black rectangle delimits area of (b). (b) Closer view of the lower slope section, drawn with a vertical exaggeration of 1.5. (c) Oblique 3D view of the slope, indicating aditionally the trace of the profile, running N–S.

4.5.4 dGNSS displacement measurements

The displacement measurements using periodic dGNSS surveys reveal that all rover points (BER-1, BER-3, BER-3 and BER-4) show significant displacements in horizontal direction, ranging between 4.2 and 14.1 mm/yr with an error of 0.5 mm/yr (Table 4.3). In vertical direction, only the points BER-1, BER-3 and BER-4 show significant displacements, ranging from -3.9 to -15.5 mm/yr with an error of 0.7 mm/yr. The negative displacements indicate downward-directed movement. All points show significant displacements in 3D, ranging between 4.6 and 20.9 mm/yr with an error of around 0.9 mm/yr. The highest 3D displacement rates were determined for BER-4 (around 20.9 ± 1.0 mm/yr), representing the slide block below the newly opened cleft located west of the main rock-slope instability. It shows a downward S-directed movement (trend/plunge of 177°/48°) (Fig. 4.11 d). The other rover points (BER-1, BER-2, and BER-3) that represent the main instability show varying displacements. BER-1 and BER-3 (trend/plunge of 179°/41° and 185°/34°) move toward S and down, whereas BER-2 (trend/plunge of 185°/34°) shows S-directed but no downward movement because of insignificant vertical displacements, although the interpolated plunge would indicate a downward movement (Fig. 4.11 a, b, and c). Therefore, the average 3D movement rate for the main instability is around 6.6 ± 0.9 mm/yr with mean horizontal direction generally toward S (179–185°) but with varying inclinations (34–41°).

Additional to these periodic measurements, new monitoring data obtained by satellite based DInSAR using RADASAT-2 images indicate active deformation of the entire slope with about the same rate, in the range of several mm/yr (J. Dehls, personal communication).

Table 4.3: Summarized results of the periodic dGNSS displacement measurements at Middagstinden Mountain for the years 2008–2013. The associated regression plots of the observed displacements are shown in Fig. 4.11. For location of the survey points, refer to Fig. 4.5.

dGNSS point	Coordinates UTM32N (m)			Movement (mm/year)			Error (mm/year)			3D-movement	
	Easting	Northing	Altitude	Horizontal	Vertical	3D	Horizontal	Vertical	3D	Trend (°)	Plunge (°)
BER-1	419485.9159	6925033.2275	844.7852	6.0	-5.3	8.0	0.5	0.7	0.9	179	41
BER-2	419646.5779	6924887.0769	712.1617	4.2	-2.0	4.6	0.5	0.7	0.9	185	34
BER-3	419173.2247	6924857.1432	740.1638	6.3	-3.9	7.4	0.5	0.7	0.9	185	34
BER-4	418886.5785	6924775.1287	671.7474	14.1	-15.5	20.9	0.5	0.8	1.0	177	48

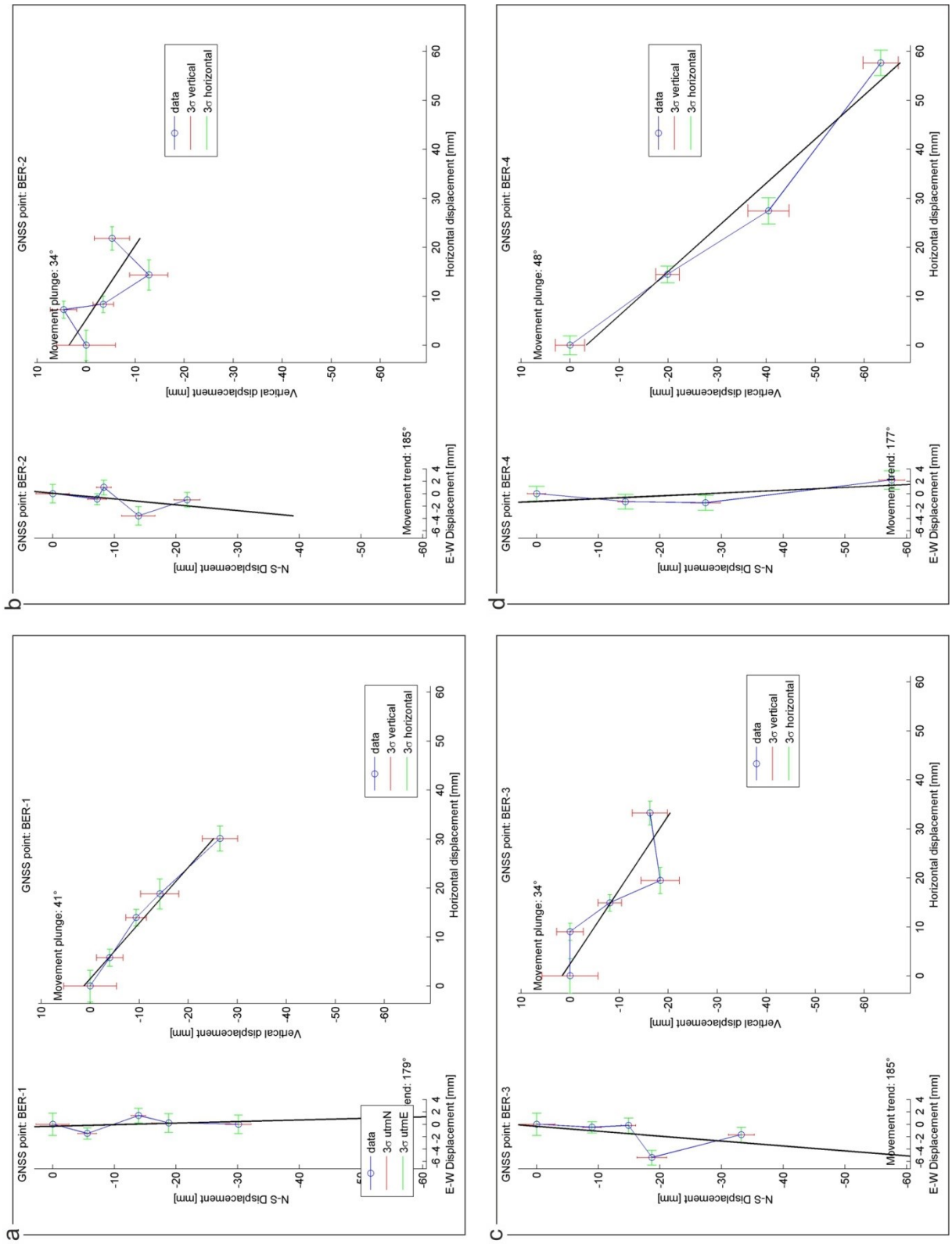

Fig. 4.11: Regression plots of the observed dGNSS displacements at Middagstinden Mountain, showing trend/plunge of the 3D movement vectors of the different rover points. (a) BER-1, (b) BER-2, (c) BER-3, and (d) BER-4 (modified after Geological Survey of Norway database). The measurements are summarized in Table 4.3. For location, refer to Fig. 4.5.

4.5.5 Geoelectric resistivity tomography

All three geoelectric resistivity profiles generally show a low resistivity on the surface (i.e., water saturated sediments) and higher resistivity in a few meters of depth (i.e., bedrock) (Fig. 4.12). In addition, in all profiles a pronounced zone (10–30 m wide) of low resistivity is determined that separates areas of high resistivity and that can be traced as a rather sub-vertical structure into depth. Within profile P1 the structure is well pronounced. Here, an around 10 m wide low resistivity zone can be traced into the depth showing the proposed dip direction of the fault. Additionally, a second but less pronounced zone of lower resistivity runs parallel to this structure.

P1

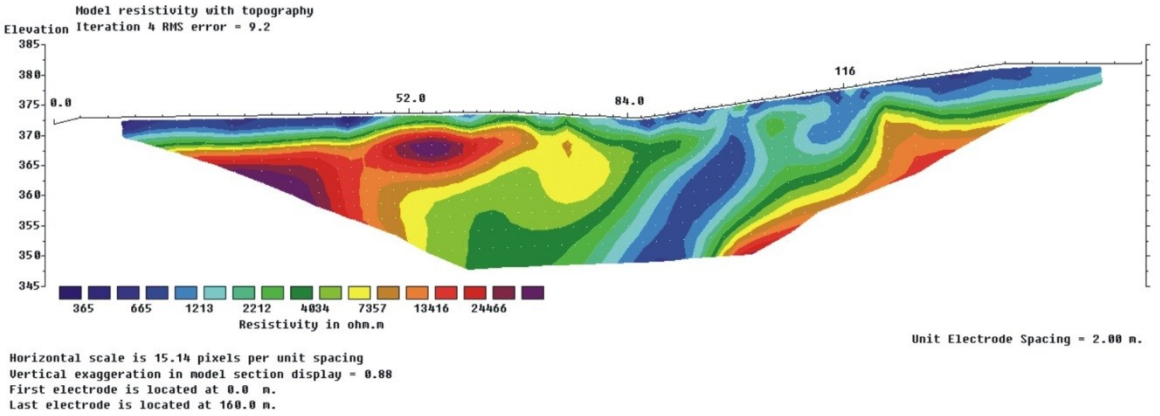

P2

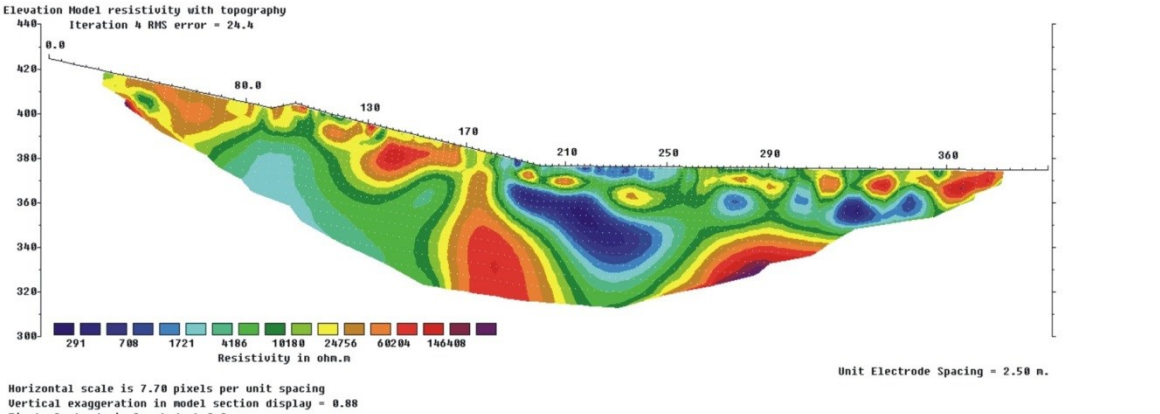

P3

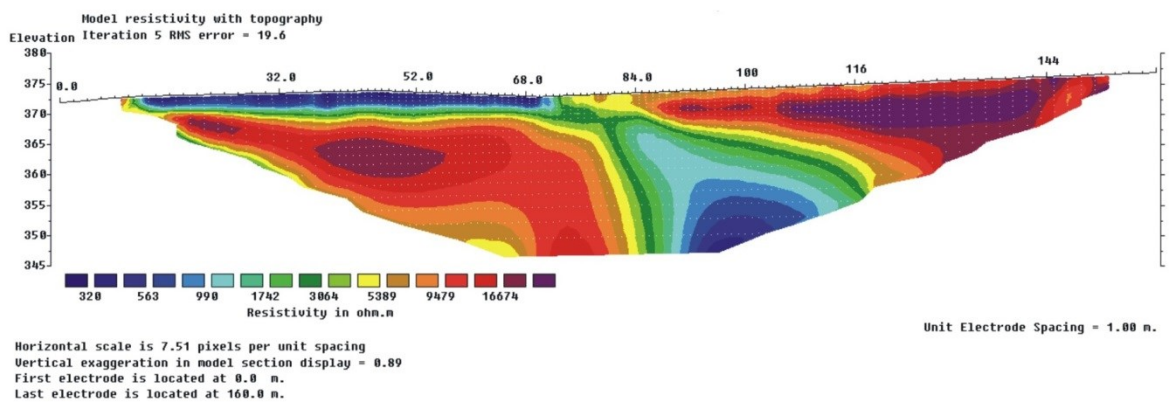

Fig. 4.12 (previous page): Results of the geoelectric resistivity tomography along the three profiles P1, P2, and P3 at Middagstinden Mountain (modified after Geological Survey of Norway database). For profile location, refer to Fig. 4.5. Relatively low resistivity (blue colors) indicates either water saturated peat sediments near the lake (P1 and P2) and/or zones of fractured bedrock (P1, P2 and P3).

The two trenches that run parallel to the geoelectric profiles and cross the position of the fault in this profile were dug down to glacial deposits or the bedrock. In both trenches, no deformation structures were detected within the soft sediments (Fig. 4.13).

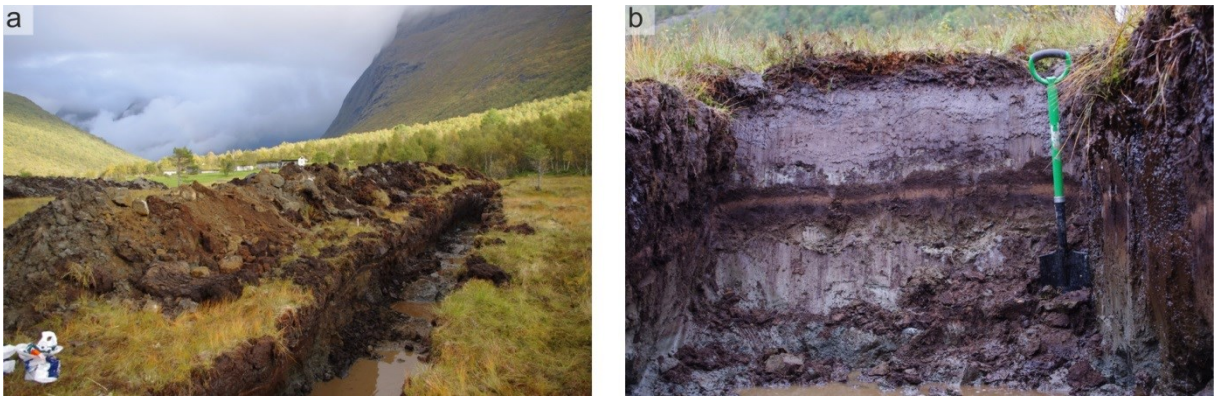

Fig. 4.13: Exemplary photographs of one trench on the valley bottom below Middagstinden Mountain running parallel to the geoelectric profile P3. (a) Overview of the around 20 m long, 1.5 m wide and 1.3 m deep trench in soft sediments. (b) Closer view of the layered soft-sediments. The observed sediments do not show any distinct deformation structures. For location, refer to Fig. 4.5.

4.6 Discussion

4.6.1 Origin of the fault

The fault plane is found in the field throughout the whole rock-slope instability with a mean orientation of 43°/271° ± 16° but slightly varying (Table 4.1). However, this structure was not detected within the TLS-derived HRDEM due to the shallow dipping into the slope and lack of visible surfaces. Since the fault structure is very important for kinematics of the investigated rock-slope instability, this circumstance states a main problem for structural investigations by using only remote sensing data. Because, according to Oppikofer et al. (2009) and Fisher et al. (2014), some structures might not be detectable or will be under-represented in the TLS dataset because of factors of scan resolution, spatial variability, or shadow zone. Nevertheless, detailed field investigation gained important information about the fault. Significant quartz-feldspar remineralisation and the distinct quartz-feldspar lineation indicate tectonic fault activity in depth prior to exhumation to its present position. Additionally,

frequent break offs indicate a down-dip direction of the hanging wall block and therefore a normal fault process (Fig. 4.8).

The orientation of the lineation (trend/plunge of 31°/245° ± 11°), and consequently the direction of fault movement, are sub-parallel to the direction of the post Caledonian collapse of the orogen and the major fault structures in western Norway (Fig. 4.2). However, the lineation does not occur continuously on all surfaces of the fault set and the planes are partly undulated and show varying orientations throughout the slope (Fig. 4.7). Therefore, it is interpreted that the planes of the fault set could follow a pre-existing discontinuity (e.g., a joint set) that was a preconditioned zone of weakness in the course of faulting during the Caledonian collapse.

The distinct morphological trace of the fault is slightly oblique to the measured structures and the slope (Figs. 4.5 and 4.7). The fault trace is also detectable at the backside (NE-dipping slope) of Middagstinden Mountain (Fig. 4.4) (Anda et al., 2002). The low electric resistivity zones detected in the valley (Fig. 4.12) are interpreted to represent the prolongation of the fault (especially P1 shows the same dip direction). Furthermore, with knowledge of fault orientation it is even possible to trace the lineament further on the opposite valley slope (Fig. 4.4). Therefore, the extent of the fault is suggested to be more regional.

As neotectonic (i.e., Holocene) activity was proposed by Anda et al. (2002), two trenches were opened along the resistivity profiles (Fig. 4.5) by the Geological Survey of Norway to investigate deformation in the valley sediments. The trenches were dug into glacial deposits or down to the basement rocks. No fault offset or any soft sediment deformation features that indicate seismic activity were observed within the trenches (Fig. 4.13). Thus, the fault is interpreted to have been active during the post Caledonian collapse but was not seismically reactivated in post-glacial (i.e., Holocene) times. Therefore, the lineament at Middagstinden Mountain (“Berill fault”) can no longer be considered as the first evidence of neotectonic activity in southern Norway as proposed by Anda et al. (2002). Furthermore, the trigger factors for the cluster of large rock-slope failures in this region (i.e., Møre og Romsdal County) have to be reinvestigated and newly discussed since Anda et al. (2002) and Blikra et al. (2002), who previously suggested neotectonic seismicity as the main cause based on this interpretation. Detailed investigations of the neighboring DSGSD provide further new insights on the fault and its trace forming a distinct geomorphological lineament.

4.6.2 Kinematics of the rock-slope instability

Because of new data analyses, that is, improved cluster analyses of structural data and kinematic feasibility tests, the presented results show some variations in contrast to the results already presented in Krieger et al. (2013). This led further to improved interpretation of the kinematics of the rock-slope instability. Field investigations, structural measurements and the additional TLS data reveal that the main sliding plane (exposed below the scarp) is mainly formed by the foliation JS (mean dip/dip direction of 49°/158° ± 17°) (Figs. 4.5 and 4.6). Simple kinematic feasibility tests conducted for the mean slope suggest a planar sliding along JS and wedge failure along the intersection of JS#JF (trend/plunge of 218°/29°) as

main processes for the rock-slope instability (Fig. 4.9). Because of the variability of structures (i.e., mainly foliation and fault), also other deformation styles could have developed on the slope in various sectors. The slope aspect is slightly changing from east to west (area 4: 151°, areas 6 and 7: 169°, and areas 8 and 9: 182°) with a rather constant mean slope angle (35°). Planar sliding and wedge failure are feasible for all slope aspects, but the wedge failure gets to the limit of the failure envelope for slope aspects directed more to SSE. For these slope orientations also flexural toppling along J1 is kinematically feasible. However, these feasibility tests are only indications (Turner & Schuster, 1996; Wyllie & Mah, 2004) and the results are strongly limited by input data and are generally applicable for simple kinematics but often not useful to explain complex slope deformations.

Based on the findings, a coherent sliding plane composed only of JS and also the intersection line formed by JS and JF are not daylighting at the slope (Fig. 4.10). Therefore, simple planar or wedge sliding is not possible over the entire slope, except in the upper part, and other deformation mechanisms are necessary to explain the deformation of the rock slope and thus the geomorphological characteristics. Different main processes that interact with each other are assumed to control the complex kinematics and the slope deformation.

(1) In the uppermost part of the slope, the deformation is controlled by a planar sliding component of rather coherent slide blocks along the foliation JS toward SSE. This is also marked by the groove marks (trend/plunge of 42°/138° ± 16°) found on the sliding plane below the main scarp (Table 4.1). Therefore, this movement is 45° oblique to the observed general movement directed toward S (~183°) (Table 4.3 and Figs. 4.5 and 4.11) as indicated by the dGNSS measurements. However, groove marks could also be formed by small-scale slide activity and thus should be interpreted carefully.

(2) In the middle part of the slope, the deformation is controlled by the large wedge failure formed by JS and JF (trend/plunge of 218°/29°) and movement along the intersection (Table 4.2 and Fig. 4.9). This type of movement is supported by the dGNSS measurements of the rover points BER-1 and BER-3 that show significant 3D displacements toward S and down (Fig. 4.5 and 4.11 and Table 4.3). Furthermore, the variability of structural data (Fig. 4.7) indicates that, for instance, the wedge intersection between JS and JF is steeper in the upper part supporting sliding in this area. In contrast, it is less steep in the lower part supporting rather horizontal movement. This is also in consistency with the intersection of 201°/21° (trend/plunge) presented in Krieger et al. (2013) that was measured at a small-scale example in the field (Fig. 4.8) located in the lower part of the slope in area I (Fig. 4.5).

(3) In the lower part of the slope, the sliding along the intersection is stuck because, as stated above, this intersection line is not daylighting at the slope but lies below the valley bottom (Fig. 4.10). This causes the S-directed but no downward movement that is also indicated by the observed dGNSS displacement of the rover point BER-2. This deformation further causes the slope bulging in the lower section by pressing the rock mass out of the slope. This creep-like deformation in the lower part is not concentrated on any distinct failure plane but is taken up by multiple structures.

This complex kinematics with the toe of the deformation lying below the valley floor suggest the classification of a deep seated gravitational slope deformation (Agliardi et al., 2012) for this rock-slope instability.

4.6.3 Morphology of the rock-slope instability

The slope morphology at Middagstinden Mountain shows typical geomorphological features such as counterscarps, grabens, tension cracks and irregular slope profile including slope bulging. These geomorphological characteristics that are changing along the slope, together with the size of the instability, the discussed complex kinematics, and the relatively slow deformation rate account for the definition of a deep seated gravitational slope deformation (DSGSD) following the introduced classification of Dramis & Sorriso-Valvo (1994), Agliardi et al. (2001) and Agliardi et al. (2012). Thereby, the surface geomorphology (i.e., deformation features) provides the most important diagnostic characteristics for this definition. However, the distinguished areas show distinct geomorphological differences along the slope that need to be explored.

4.6.3.1 Morphostructure of the “apparent reverse fault”

The described areas (1 to 4) are located in the northeastern part of the slope, outside of the main active rock-slope instability (Fig. 4.4). The bedrock in area (4) is covered by surficial glacial and alluvial deposits. Because of the lack of bedrock outcrops it was neither possible to collect structural data in the field nor to install representative dGNSS points for displacement measurements. However, this part of the slope could follow a similar slope deformation process as the main slope (area 7), since area (4) also shows depressions (sackung) that strike in the same direction like the counterscarps in area (7). Furthermore, the new InSAR data (i.e., satellite based DInSAR using RADASAT-2 images) indicate that the whole slope deforms with the same rate of several mm/yr (J.Dehls, personal communication).

A distinct linear morphostructure that runs 30° oblique to the slope (Figs. 4.5 and 4.6) strongly limits the slope deformation toward SE. This structure was previously interpreted as the trace of a neotectonic reverse fault (Anda et al., 2002). However, the origin of linear morphostructures along a slope should be discussed because it could be related either to tectonic and/or to gravitational processes. Length and linearity of such structures could indicate tectonic origin (Thompson et al., 1997). In concordance to this work, the observed lineament (i.e., the traced convex step) indicates to rather be of gravitational origin since it is relatively short and no similar offset is found in other stable parts of the mountain. A gravitational model is further supported, as no activity (i.e., deformation) is found in lower parts of the slope or down on the valley floor (neither in topography, nor in the trenches), similar to the study of Hippolyte et al. (2006). The sackung features (area 4) at the slope above this main lineament (Figs. 4.5 and 4.6) also suggest a gravitational origin because of the typical characteristics proposed by Hippolyte et al. (2006) and Li et al. (2010), that are,

swarms of relatively short, mainly uphill-facing scarps that cut scree deposits and occur rather parallel to the ridge crest and the contours.

Moreover, the proposed kinematic model can be used to explain this distinct morphostructure. The sliding rock mass moves along the wedge intersection (218°) out of the slope in a direction 43° oblique to the mean slope aspect (175°). This movement, in combination with the sliding component along JS and the low friction along JF (slickensided, planar, and sub-horizontal apparent dip in direction of movement) produces a positive offset (Fig. 4.8). This offset appears similar to an apparent thrusting along the fault plane in an eastward direction. This would be similar to a flexural slip on bedding planes due to gravitational load in a syncline (Li et al., 2010), but in the presented case not related to folding but to gravitational reactivation of a shallow dipping (shallow apparent dip in movement direction) preexisting fault, similar to Hippolyte et al. (2006). However, no E-directed displacement is observed on the entire slope (e.g., InSAR data). Nevertheless, the observed S-directed movement can result in such a positive relief step along the fault because it is oblique to the wedge intersection. Thereby, the rock mass is not pushed upwards but it is pushed toward S causing the offset that is therefore not reverse but oblique, however still producing a positive step in the relief. This offset is largest along the SE boundary of the instability and forms the distinct convex step in the topography that strikes slightly oblique to the fault plane (Fig. 4.6).

Therefore, the observed geomorphological lineament is interpreted to be an “apparent reverse fault” (pseudotectonics) as it is formed by gravitational reactivation of the preexisting Caledonian fault.

4.6.3.2 Morphostructures within the unstable rock slope

The areas (5 to 10) are interpreted to be subareas within the active rock-slope instability (Fig 4.5). Area (6) is composed of several coherent slide blocks that are delimited by the joint set J1 in the front and by J2 at its lateral limits. Block movement is generally sliding along foliation toward SSE nearly in dip direction of the slope as indicated by groove marks at the sliding plane below the back bounding scarp (Table 4.1). The block movement causes compressive and stresses in the lower areas, especially area (7).

Distinct morphological features (morphostructures) characteristic for area (7) are the prominent sub-parallel counterscarps and the slope bulging. Counterscarps are typical morphological lineaments of large scale slope deformations (Bovis & Evans, 1996; Agliardi et al., 2001) but could have different origins such as either tectonic or gravitational (Gutiérrez-Santolalla et al., 2005; Hippolyte et al., 2006; Li et al., 2010). The latter describes various processes including gravitational deformation (i.e., spreading of fractures, bending of bedding planes, flexural toppling, and normal faulting by spreading of rock mass), tectonic folding (i.e., bending or flexural slip due to anticline or syncline) and faulting (i.e., either normal or reverse faulting due to earthquake ground motion). However, gravitational origin is implied for the counterscarps at Middagstinden Mountain in concordance to the characteristics addressed by Hippolyte et al. (2006) and Li et al. (2010) as stated above

(e.g., swarms, parallel to the contours). For instance, gravitational flexural toppling failure is suggested by several authors to cause counterscarps (Hippolyte et al., 2006; Reitner & Linner, 2009; Li et al., 2010). Latter further suggests that gravitational flexural toppling could even cause and contribute to the development of a basal sliding plane in complex large scale slope deformation. However, the examples show that these processes are limited to sedimentary rocks or well foliated metamorphic rocks with high persisting, sub-vertical structures of bedding or foliation. Based on kinematic feasibility tests, Krieger (2013) suggests a flexural toppling along the high persisting joint set J1 toward SE as the cause for the counterscarps at Middagstinden Mountain. However, the question arises, if the well-developed foliation that intersects with J1 will allow the formation of large rock columns that are required for flexural toppling as proposed by Turner & Schuster (1996); Wyllie & Mah (2004).

For the Middagstinden case, it is interpreted that unregular basal sliding planes together with high pressure, due to sliding block movement in the upper slope sections and hindered movement in the lower ones, are most likely to cause the morphostructures of grabens and counterscarps. For instance, sliding planes with a succession of flat and ramp areas (i.e., shallow dipping parts followed by steeper dipping parts) are proposed for listric-style complex fields (Braathen et al., 2004) that are typical type for large scale slope deformations in Norway. This could be reliable for this site, because the main sliding plane is formed by the varying and partly folded foliation (Fig. 4.7).

Spreading of fractures due to tensional stresses and brittle failure during block sliding and erosion of the uphill side can cause counterscarps (Li et al., 2010) even in the case of sliding along a shallow dipping sliding plane. Furthermore, at a transition where the dip gets steeper, higher tensional stresses increase brittle failure and rock fragmentation along preexisting structures (e.g., JS and J1), similar as proposed by Li et al. (2010) for bending moment faults caused by folding at the hinge of an anticline. Preexisting structures as in this case JS and J1, will favor such processes. Furthermore, a steeper sliding plane (i.e., foliation) could cause acceleration of the sliding block. This leads to different slide velocities and differential movements throughout the rock slope with slower velocity of the sliding blocks in the upper part (i.e., shallow foliation) and faster velocity in the lower part (i.e., steeper foliation). This movement behavior favors the opening of large cracks and the development of counterscarps, similar to bending moment fractures and spreading of fractures as kind of lateral spreading as proposed by Gutiérrez-Santolalla et al. (2005) and Li et al. (2010).

Moreover, a basal sliding plane, neither for planar nor wedge sliding does not outline at the slope, and the intersection for wedge sliding lies in the valley bottom. Therefore, obstructed slope deformation and pressure due to pushing blocks from behind (area 6) cause high internal stresses. This might encourage the formation of counterscarps by stress release due to a kind of “normal faulting” (Li et al., 2010) along J1. The southward movement without a downward component causes the slope bulging in the lower slope section (Fig. 4.10) due to sliding or tolling out. Thereby, the creep-like deformation is taken up by multiple structures in the subsurface, which further explains the lack of a distinct failure plane daylighting at the slope.

Additionally, the counterscarps indicate different amounts of deformation along the slope that are in coherence with this interpretation. Within the area of lower counterscarps (within area 7) these morphostructures are more distinct, deeper and longer as above (Figs. 4.5 and 4.6). They seem to be slightly stretched and tilted. This can be explained by larger displacement and tension stress in the lower part of the slope due to the complex slope movement as discussed above.

The depressions (sackung) in area (4) that strike rather in the same direction but that are much smaller and less deep are caused by similar slope deformation processes but with smaller amount of deformation. A large displacement toward S or toward SW is either hindered by the slope orientation or the large unstable rock masses, respectively. This effect is in concordance to Li et al. (2010) who proposed a strong influence of the mountain morphology (i.e., topography) on stress orientations and kinematics during gravitational deformations (e.g., angle between slope and sliding or toppling surfaces). Therefore, this area could be rather in a kind of initial state that shows smaller amount of tensional stress. However, because of the hindered displacement in direction of the intersection, the S-directed movement and stress release causes the geomorphological lineation of the “apparent reverse fault” that is more distinct in this part of the slope. This structure is not so strongly developed in the lower part, because of increased possibilities of stress release and for higher amounts of deformation.

Within area (7) the dGNSS measurements of BER-1 and BER-2 indicate average block movement toward S, but with different dip angles of the 3D movement vector (Fig. 4.5 and Table 4.3). Thereby, BER-1 also shows a significant downward movement whereas BER-2 only shows horizontal movements. These observations support the described interpretation of varying processes along the slope. However, the survey points installed on top of rock faces of the counterscarps could rather represent the movement of the counterscarp and not the whole instability. The counterscarps indicate toppling along J1 toward SE and the combination of this toppling with the SSW-directed wedge sliding (i.e., along intersection JF#JS) could explain the observed S-directed movement.

The coherent block in the upper western part (area 8) is separated from the block of area (6) along joint set J2 (Fig. 4.5). The dGNSS measurements of BER-3 (Table 4.3) show movement rather toward S (185°). The morphology of the opened cleft also indicates a slightly rotational component that might mask the original movement direction. The surrounding large block-fields are results of fractured and collapsed slide blocks that indicate high amount of deformation and fragmentation.

As the lower area (9) is mainly composed of large block-fields, no dGNSS point could be installed due to lack of either coherent blocks or un-fractured outcrops. Only a few outcrops exist, but these show highly fractured rocks with widely opened discontinuities. These are likely to be related to high strain rates induced by stresses due to the surrounding coherent slide blocks that push on this part of the slope. The large block-fields are interpreted to be deposits of fractured and collapsed slide blocks. High compressive stress due to block movement in the upper areas (8 and 6) would also explain why the highest amount of deformation and fragmentation is found within this area.

4.6.4 Displacements of the rock-slope instability

The DSGSD of Middagstinden Mountain shows complex slope movements that can be interpreted based on surface geomorphology, structural investigations and displacement measurements. However, the observed displacements are based on periodic dGNSS measurements conducted at single rover points along the surface. Those measurements can provide indications for the movements of slope deformation but they only represent the displacements of the observed blocks that could also move independently, such as counterscarps. Uncertainties due to the influence by superficial movements were strongly reduced or even eliminated by careful choice of the point location prior to the installation.

To overcome this issue, multitemporal TLS surveys can be applied in the future based on the developed HRDEM to improve the understanding of the complex rock-slope deformation (Oppikofer et al., 2009; Oppikofer et al., 2012b) including, for instance, overall slope displacements and internal slide block rotations. Furthermore, the detailed analyses of available InSAR data will also contribute to the understanding of deformations distributed over the whole slope. However, all these monitoring methods can only detect surface displacements.

The main sliding plane (area 5) is built by the foliation (Figs. 4.5 and 4.6). The mean 3D displacement along the sliding plane is around 78 m. By assuming continuous activity since the end of Younger Dryas (app. 11 500 yr), this displacement indicates an average Holocene movement rate of 6.8 mm/yr. In the case of continuous activity since the Last Glacial Maximum (LGM, app. 22 000 yr) the averaged movement rate is 3.5 mm/yr. These values are in the range of measured dGNSS displacements.

The valley was filled by Pleistocene glacier but rather ice free since LGM. Considering that deformation took place after glacial retreat similar to the model suggested by Agliardi et al. (2009a), the observed dGNSS values could indicate increasing activity (i.e., higher current movement rates than averaged rate of 3.5 mm/yr). Anyway, the movement below the new crack (BER-4) shows increasing activity. However, these estimates only state rough indications. More detailed investigations such as surface-exposure dating of the sliding plane (Hermanns et al., 2012c) using, for instance, terrestrial cosmogenic nuclide ^{10}Be would be necessary to increase understanding of long term displacement velocities.

4.7 Conclusions

The rock-slope instability of Middagstinden Mountain shows diagnostic characteristics of a deep seated gravitational slope deformation (DSGSD) that is controlled by preexisting geological structures. Based on findings of detailed investigations the following conclusions can be drawn.

(I) The Fault: The morphological lineament at Middagstinden Mountain, previously described as the “Berill fault” has to be reinterpreted. Associated fault planes are found throughout the unstable slope, and quartz-feldspar remineralisation with lineation and break offs indicate a normal fault process dipping toward the west instead of a reverse fault movement as

previously proposed. Therefore, the fault set is proposed to be a pre-existing discontinuity set (e.g., joint set) that has been exploited as weakness zone during post Caledonian collapse of the orogeny. The observed fault trace suggests a rather more regional extent. The fault was not tectonically reactivated (neither normal nor reverse movement) in post-glacial times, that is, the Holocene. Hence, the "Berill fault" can no longer be considered as the first evidence for neotectonic activity in southern Norway. Furthermore, neotectonic seismicity and associated earthquakes might no longer be the reliable trigger for the cluster of large rock-slope failures in this region (i.e., Møre og Romsdal County, western Norway). Thus, other triggers have to be discussed.

(II) The DSGSD: The S-facing slope of Middagstinden Mountain shows complex slope deformation processes and distinct geomorphological features. The slope deformation is controlled by preexisting geological structures (i.e., discontinuity sets) that are the foliation (JS), the fault (JF) and two major joint sets (J1 and J2). Structural field measurements generally correlate with TLS-derived data. However, one major discontinuity (i.e., the fault set) was not detected with the TLS dataset. This shows that detailed field investigations are essential for increased understanding of the failure kinematics. Either planar failure along JS or wedge sliding along intersection of JS and JF (JS#JF) are kinematically feasible, but the necessary structures are not daylighting at the slope and the intersection line lies below the valley bottom. Hence, simple wedge or translational sliding is not possible. Therefore, a complex kinematics has developed that consists of three main deformation mechanisms changing along the slope, including (1) planar sliding along JS in the uppermost part, (2) wedge sliding along JS and JF in the middle part, and (3) creep-like deformation on multiple structures due to hindered wedge sliding in the lower part. The complex deformation is represented by distinct geomorphological characteristics such as large coherent slide blocks, up to 20 m deep counterscarps, small-scale superficial mass movements, and morphological slope bulging, which are distributed over various areas of the slope. The observed geomorphological characteristics, the complex kinematics and the deformation rate account for the definition of a deep seated gravitational slope deformation (DSGSD). Therefore, the fault plane is gravitationally reactivated as a weakness zone by the DSGSD (exploitation of preexisting tectonic structures). This inherited structure of a Caledonian fault strongly limits the slope deformation. Because of the type of deformation, with S-directed movement that is oblique to the fault plane, and varying slope orientations, the sliding rock mass forms a positive offset (morphological convex step in topography) along its SE boundary that is described as an "apparent reverse fault" (pseudotectonics). In consideration of average movement rates since Younger Dryas or Last Glacial Maximum, the observed current displacements (dGNSS) indicate either constant deformation or slight acceleration. However, further investigations such as surface-exposure dating of the sliding plane are recommended to increase understanding of long term displacements.

5 General conclusions

This thesis presents the detailed description and interpretation of multiple large rock-slope failures in the two valleys of Innerdalen and Innfjorddalen in western Norway, with regard to its paleodynamics, kinematics, geomorphological characteristics and chronology.

The Innerdalen case (Chapter 2) presents the first description of remnant deposits formed by a rock avalanche onto a Late Pleistocene glacial-ice body in a today deglaciated valley. The findings will improve the identification and interpretation of similar deposits in glacierized high mountain areas around the world such as, for instance, the Norwegian mountains, the Alps, Himalayas, Andes, and the Rockies.

The Innfjorddalen case (Chapter 3) presents the first example of remnant deposits of a rock avalanche onto water saturated sediments and into the water body of the ancient fjord that are exposed on today's surface due to the post-glacial isostatic rebound. This enables a direct study of such rock-slope failures that deposited at the land/water interface. The findings will improve the identification and interpretation of similar deposits in other regions around the world that show a similar geological history such as, for instance, western Norway, west and east Canada and Greenland.

In both studies, the plausibility of the interpretations is confirmed by surface-exposure dating (^{10}Be) and numerical runout modeling (DAN3D). The studies further present an application of DAN3D modeling to back analyze multiple rock-slope failures in order to study their paleodynamics and to support the geomorphological landform interpretation.

The Middagstinden rock-slope instability in Innfjorddalen (Chapter 4) shows characteristics of a complex deep seated gravitational slope deformation (DSGSD) and causes a morphological lineament by gravitational reactivation of a Caledonian fault plane ("pseudotectonic"). The findings contribute to the understanding of complex processes of active rock-slope instabilities and will be useful for the interpretation of associated geomorphological features.

Therefore, shortly summarized, the findings of this thesis contribute to the understanding of large rock-slope failures in landscapes strongly influenced by glacial processes. They improve the identification and interpretation of complex deposits and geomorphological features associated with rock avalanches and rock-slope instabilities in order to derive their paleodynamics and kinematics. They further contribute to the understanding of Quaternary landscape development in the valleys of Innerdalen and Innfjorddalen and provide implications for more regional effects in western Norway regarding the Late Pleistocene glaciations, the post-glacial isostatic rebound, and neotectonic activity.

5.1 Paleodynamics of rock avalanches and related deposits

Remnant deposits of rock avalanches, show distinct characteristics and complex distribution depending on their paleodynamics. In general, rock-avalanche deposits are composed of typical rock-boulder material such as large angular rock boulders and show typical geomorphological characteristics, for instance, a distinct boulder carapace, lobate forms, frontal rims, lateral levees, longitudinal ridges, and runup deposits on the opposite slope. However, these characteristics depend on the mobility and runout behavior of the propagating mass.

In the case of a rock avalanche onto a glacial-ice body which has meanwhile disappeared (Innerdalen case), the deposits show a complex distribution with discontinuous boulder deposits that are separated from each other by kilometers. Five distinguished types of deposits support the interpretation of the interaction between the rock avalanche and a glacier, including the supraglacial and glacial modification of the rock debris: (1) Isolated boulder patches on the slopes high above the valley floor; (2) terminal-moraine ridges; (3) kame mounds behind the moraine ridges; (4) irregular boulder accumulations such as isolated hummocky deposits; (5) distinct valley-parallel ridges at the valley bottom.

These remnant deposits and its spatial distribution provide further implications concerning the valley development and the complex landform interaction such as: (1) The spatial extent and the thickness of the former glacier; (2) the runout path and the deposition zone (e.g., only supraglacial deposition or crossing and overtopping the glacier at its margin); (3) the style of deglaciation (e.g., stagnation style); (4) the effects of supraglacial debris on glacial activity (e.g., boulder accumulation, asymmetrical decay, and landslide induced glacial advance).

In the case of a rock avalanche over water saturated sediments into a water body (Innfjorddalen case), the deposits again show a complex distribution with a separation between discontinuous and continuous boulder deposits. Several distinct geomorphological features suggest the interpretation: (1) Isolated concentric hills of rock-avalanche material (“toma hills”) in the most distal part that are separated for several hundred meters by (2) deformed and (3) undeformed valley-fill sediments from (4) the main continuous rock-avalanche deposit which is located onto (5) marine terrace deposits. These remnant deposits and their spatial distribution provide further implications for the valley development such as paleoenvironmental conditions and in this case the post-glacial isostatic uplift of the landmass.

In the case of multiple rock avalanches depositing onto each other (Innfjorddalen case), the deposits rather exhibit a succession of continuous boulder deposits. Geomorphological features of the older events are often masked by the younger deposits. However, the observed deposits indicate that strong features, such as large longitudinal ridges, are preserved and visible in the surface structures of the covering deposits providing implications for the paleodynamics of the older events.

The extended runout length in the presented examples is mainly caused by the propagation over low frictional substrates that cause a reduced basal friction, as the path topography shows a relatively shallow inclined and smooth surface. Such substrates are: (1) A wide glacial-ice surface that also encourages the spreading of the propagating mass (Innerdalen case, Fahrböschung of 13°); (2) water saturated sediments that probably also cause a higher mobility by the additional effect of undrained loading (Innfjorddalen case, Fahrböschung 17.7°). On the contrary, the propagation over substrate with higher friction reduces the runout extent. Such substrates are, for instance: (1) The talus and till material (Innerdalen case, Fahrböschung of 22°); (2) the boulder deposits of previous rock avalanches (Innfjorddalen case, Fahrböschung of 24.5° and 28.2°).

Numerical dynamic runout modeling (DAN3D) is consistent with field observations and shows reliable results for the rock-avalanche propagations. Therefore, it is considered an appropriate tool to study runout behavior and paleodynamics of rock avalanches, to support the interpretation of complex landforms associated with those processes, and to prove its plausibility. Furthermore, the presented results of runout back analyses provide reliable parameters which can be used for model calibration of future forward runout modeling.

5.2 Kinematics of rock-slope instabilities and related geomorphological characteristics

The type and distribution of geological structures and the geomorphological characteristics on the surface are important implications for the interpretation of complex kinematics and deformation mechanisms of large rock-slope failures. Therefore, remote sensing techniques are useful to support field investigations and to collect data from inaccessible areas such as steep and high rock slopes. However, the results exhibit uncertainties that occur due to data collection and processing (e.g., limited visibility), and that careful interpretation and verification by field data is necessary, when possible.

Different feasible kinematics, which are of rather simple types, can be determined for the previous rock slope instabilities that failed as rock avalanches: (1) Planar sliding along the shallow dipping foliation in combination with wedge failures related to the main joint sets (Innerdalen case, foliation and three joint sets); (2) wedge failure along various intersections of the joint sets with also planar sliding along the exfoliation and toppling along the foliation for small-scale failures (Innfjorddalen case, foliation, exfoliation and two joint sets).

The active rock-slope instability at Middagstinden Mountain in Innfjorddalen Valley shows more complex kinematics. This deformation is controlled by the preexisting geological structures formed by the foliation, two major joint sets and a fault set that was not detected within the TLS data. Both, planar failure along the foliation and wedge sliding along the intersection of the foliation and the fault are kinematically feasible. However, the necessary structures such as a basal sliding plane or the intersection line are not daylighting at the slope, hence simple wedge or translational sliding is not possible. The intersection line between the foliation and the fault lies below the valley bottom and therefore a complex

kinematics has developed. The deformation is changing along the slope consisting of: (1) Planar sliding along foliation in the uppermost part; (2) wedge sliding along intersection in the middle part; (3) creep-like deformation on multiple structures because of hindered wedge sliding in the lower part. Distinct geomorphological characteristics such as large coherent slide blocks, up to 20 m deep counterscarps, small-scale superficial mass movements, and the slope bulging are distributed over various areas of the slope and represent the complex kinematics and deformation mechanisms. The observed diagnostic characteristics of this site such as geomorphology, kinematics and deformation rate account for the definition of a deep seated gravitational slope deformation (DSGSD). Therefore, the preexisting tectonic structure of the fault, which is associated with the Caledonian collapse, is gravitationally reactivated as a weakness zone by the DSGSD and its S-directed movement that is oblique to the orientation of this fault plane. The complex deformation mechanisms together with the varying slope orientations caused the distinct linear geomorphological feature that is a positive offset (i.e., convex step) in the topography, running oblique to the slope along the SE boundary of the DSGSD. This lineament, previously described as the “Berill fault”, has to be reinterpreted to be of gravitational and not neotectonic origin and is described as an “apparent reverse fault”

The example of Middagstinden Mountain further states that, although simple kinematic analyses based on subsurface structural data provide useful indications, they often cannot be applied to explain complex slope deformations. Therefore, the investigation of the geomorphological characteristics and the deformation monitoring of an active rock-slope instability are important tools to understand and to interpret the kinematics and subsurface deformation mechanisms in order to establish a reliable geological model. In the case of the Middagstinden Mountain, distinct characteristics that support the interpretation are the types and distribution of the main scarp, main sliding planes, coherent slide blocks, rock boulder fields, slope topography (e.g., bulging), and the linear features such as counterscarps and the “apparent reverse fault”.

5.3 Chronology and characteristics of rock-slope failures and Quaternary landscape development

Detailed investigations of multiple rock-slope failures in the valleys of Innerdalen and Innfjorddalen contribute to the knowledge of local Quaternary valley development. Moreover, the results provide new implications for Quaternary history such as deglaciation, post-glacial crustal uplift and neotectonics to be considered in a more regional context for western Norway.

In Innerdalen Valley at least two rock avalanches occurred from the same source area at Skarfjellet Mountain during the Late Pleistocene and the Holocene, indicating a temporal pattern similar to the large rock avalanches in Innfjorddalen. (1) A rock avalanche with a volume of around 31×10^6 m^3 occurred at 14.1 ± 0.4 ka under paraglacial environmental conditions between the Late Glacial Maximum (LGM) and the Younger Dryas (YD), and

propagated onto the surface of a valley glacier that was around 300 m thick. The material was mainly deposited in form of supraglacial debris. It was re-transported and modified by supraglacial and glacial processes, and affected the glacial behavior by causing asymmetrical decay of the ice body and glacial advance. Remnants of this event are the complex deposits as summarized above. (2) A rock avalanche with a volume of around 23×10^6 m^3 occurred at 7.97 ± 0.94 ka under more temperate environmental conditions during the Mid Holocene climatic optimum and propagated into the ice free narrow valley. The material was deposited as a continuous rock-avalanche deposit with distinct runup on the opposite slope. The event also caused secondary effects such as the development of a natural dam and the associated lake impoundment, which could have induced a reactivation of former rock-avalanche deposits.

In summary, further insights concerning the Quaternary valley development of Innerdalen are: (1) An around 300 m thick glacier covered the lower valley during the Late Pleistocene; (2) no glacial re-advance occurred during the YD; (3) the upper valley was ice free at least since 7.97 ± 0.94 ka.

In the lower part of Innfjorddalen Valley, the western slope of Gråfonnfjellet Mountain shows high activity of rock-slope failures. A total rock mass volume of around 25.0×10^6 m^3 failed prior to Last Pleistocene glaciations and around 22.0×10^6 m^3 volume failed later from the same source area in at least three events since the Late Pleistocene. The age of the first two rock avalanches indicate a temporal pattern similar to the large rock avalanches in Innerdalen. (1) A rock avalanche with a volume of around 15.1×10^6 m^3 occurred at 14.3 ± 1.4 ka and propagated into the ice-free valley, onto marine terrace deposits and water saturated sediments into the ancient fjord. The material was partly deposited below the water level. The rock-avalanche deposit further shows a runup on the opposite slope and a natural dam that probably impounded a lake. The most distal deposits have been lifted above the sea level by isostasy (post-glacial isostatic uplift). Remnants on the today's valley bottom are the complex deposits summarized above. (2) A rock avalanche with a volume of around 5.4×10^6 m^3 occurred at 8.79 ± 092 ka and propagated onto the former rock-avalanche deposit. The deposit created a natural dam that has been stable since its origin and impounds a lake. (3) A rock avalanche with a volume of around 0.3×10^6 m^3 occurred in AD 1611/12 and propagated onto the former rock-avalanche deposits. It had a historic impact by causing loss of lives. The high rock-slope failure activity of this slope is further indicated by the large debris cone that shows high activity of small-scale mass movements such as rock falls and debris flows.

In summary, further insights concerning the Quaternary valley development of Innfjorddalen are: (1) The lower valley was ice free following the LGM, at least since 14.3 ka. No YD valley glacier developed; (2) the post-glacial uplift was at least up to 120 m that confirms the regional modeling of the marine limit; (3) the relative sea level was around 120 m higher ~14.3 ka ago and around 15 m higher ~3.9 ka ago. Furthermore, surface-exposure dating indicates that regional effects such as uplift or subsidence of landmasses and the associated cover by water could strongly influence dating results. In the presented case, it causes an age difference of around 10.4 ka for deposits of the same origin.

In the upper part of Innfjorddalen Valley, a large rock-slope instability has developed at Middagstinden Mountain. This rock-slope instability shows currently active deformations and distinct geomorphological characteristics that indicate complex kinematics of a DSGSD (summarized in the previous Chapter). In consideration of average movement rates since the LGM or YD, the observed current displacements of several mm/yr (dGNSS) indicate either constant deformation or only a slight acceleration.

In summary, further insights concerning the geology at Middagstinden Mountain (i.e., the origin of the tectonic fault and its influence on the formation of the DSGSD) and regional perspective of rock-slope failures can be drawn. (1) The fault planes are distributed along the entire unstable slope and indicate a normal fault process with dip direction toward the west. (2) The fault set is proposed to be a pre-existing discontinuity set such as a joint set that has been exploited as a weakness zone during the post-Caledonian collapse of the orogeny. (3) The fault was not tectonically reactivated in post-glacial times and hence does not indicate any neotectonic activity. However, it was reactivated gravitationally. (4) The distinct geomorphological lineament, previously described as the “Berill fault”, has to be reinterpreted. It is not the geomorphological imprint of a neotectonic reverse fault. In contrast it is caused by the gravitational reactivation of the preexisting Caledonian normal fault. It is thus of gravitational origin and is described as an “apparent reverse fault” (pseudotectonic feature). (5) The “Berill fault” can no longer be considered as the first evidence of neotectonic activity in southern Norway. Consequently, the previously assumed neotectonic seismicity could no longer be a reliable trigger for the observed cluster of large rock-slope failures in this region (Møre og Romsdal County, western Norway), and hence other regional mechanisms have to be investigated and discussed.

References

Aa, A.R., Sjåstad, J., Sønstegaard, E. & Blikra, L.H. (2007). Chronology of Holocene rock-avalanche deposits based on Schmidt-hammer relative dating and dust stratigraphy in nearby bog deposits, Vora, inner Nordfjord, Norway. *The Holocene*, 17(7): 955-964. doi:10.1177/0959683607082411.

Abele, G. (1974). Bergstürze in den Alpen, ihre Verbreitung, Morphologie und Folgeerscheinungen. *Wiss. Alpenvereinshefte*, 25: 230.

Abele, G. (1991). Durch Bergstürze mobilisierte Muren und durch Muren transportierte Bergsturzmassen. *Österreichische Geographische Gesellschaft, Zweigverein Innsbruck*, Jahresbericht 1989/1990: 33-39.

Abellán, A., Oppikofer, T., Jaboyedoff, M., Rosser, N.J., Lim, M. & Lato, M.J. (2014). Terrestrial laser scanning of rock slope instabilities. *Earth surface processes and landforms*, 39(1): 80-97. doi:10.1002/esp.3493.

ABEM (1999). ABEM Terrameter SAS 4000/SAS 1000. Instruction Manual. *ABEM Printed Matter 93101*.

Agliardi, F., Crosta, G. & Zanchi, A. (2001). Structural constraints on deep-seated slope deformation kinematics. *Engineering Geology*, 59(1–2): 83-102. doi:10.1016/s0013-7952(00)00066-1.

Agliardi, F., Crosta, G.B., Zanchi, A. & Ravazzi, C. (2009a). Onset and timing of deep-seated gravitational slope deformations in the eastern Alps, Italy. *Geomorphology*, 103(1): 113-129. doi:10.1016/j.geomorph.2007.09.015.

Agliardi, F., Zanchi, A. & Crosta, G.B. (2009b). Tectonic vs. gravitational morphostructures in the central Eastern Alps (Italy): Constraints on the recent evolution of the mountain range. *Tectonophysics*, 474(1–2): 250-270. doi:10.1016/j.tecto.2009.02.019.

Agliardi, F. (2012). Slow, deep-seated rock slope deformation (DSGSD). *Educational Project Geological Field Trip and Workshop: Koefels - Suedtirol - Matrei*.

Agliardi, F., Crosta, G.B. & Frattini, P. (2012). Slow rock-slope deformation. In: J.J. Clague & D. Stead (Eds.), Landslides: Types, Mechanisms and Modeling. Cambridge University Press, pp. 207-221.

Agliardi, F., Crosta, G.B., Meloni, F., Valle, C. & Rivolta, C. (2013). Structurally-controlled instability, damage and slope failure in a porphyry rock mass. *Tectonophysics*, 605: 34-47. doi:10.1016/j.tecto.2013.05.033.

Alley, R.B. & Ágústsdóttir, A.M. (2005). The 8k event: cause and consequences of a major Holocene abrupt climate change. *Quaternary Science Reviews*, 24(10–11): 1123-1149. doi:10.1016/j.quascirev.2004.12.004.

Ambrosi, C. & Crosta, G.B. (2006). Large sackung along major tectonic features in the Central Italian Alps. *Engineering Geology*, 83(1–3): 183-200. doi:10.1016/j.enggeo.2005.06.031.

Ampferer, O. (1939). Über einige Formen der Bergzerreißung. *Sitz.-Ber. Akad. d. Wiss.*, 148: 1-14.

Anda, E., Blikra, L.H. & Braathen, A. (2002). The Berill Fault - first evidence of neotectonic faulting in southern Norway. *Norwegian Journal of Geology*, 82(3): 175-182.

Andersen, B.G. & Mangerud, J. (1989). The last interglacial-glacial cycle in fennoscandia. *Quaternary International*, 3–4(0): 21-29. doi:10.1016/1040-6182(89)90070-0.

Andersen, B.G., Mangerud, J., Sørensen, R., Reite, A., Sveian, H., Thoresen, M. & Bergström, B. (1995). Younger Dryas ice-marginal deposits in Norway. *Quaternary International*, 28(0): 147-169. doi:10.1016/1040-6182(95)00037-J.

Antinao, J.L. & Gosse, J. (2009). Large rockslides in the Southern Central Andes of Chile (32–34.5°S): Tectonic control and significance for Quaternary landscape evolution. *Geomorphology*, 104(3–4): 117-133. doi:10.1016/j.geomorph.2008.08.008.

Bachmann, D., Bouissou, S. & Chemenda, A. (2009). Analysis of massif fracturing during Deep-Seated Gravitational Slope Deformation by physical and numerical modeling. *Geomorphology*, 103(1): 130-135. doi:10.1016/j.geomorph.2007.09.018.

Bakke, J., Dahl, S.O. & Nesje, A. (2005a). Lateglacial and early Holocene palaeoclimatic reconstruction based on glacier fluctuations and equilibrium-line altitudes at northern Folgefonna, Hardanger, western Norway. *Journal of Quaternary Science*, 20(2): 179-198. doi:10.1002/jqs.893.

Bakke, J., Dahl, S.O., Paasche, Ø., Løvlie, R. & Nesje, A. (2005b). Glacier fluctuations, equilibrium-line altitudes and palaeoclimate in Lyngen, northern Norway, during the Lateglacial and Holocene. *The Holocene*, 15(4): 518-540. doi:10.1191/0959683605hl815rp.

Ballantyne, C.K. (1989). Avalanche impact landforms on Ben Nevis, Scotland. *Scottish Geographical Magazine*, 105(1): 38-42. doi:10.1080/00369228918736750.

Ballantyne, C.K., Stone, J.O. & Fifield, L.K. (1998). Cosmogenic Cl-36 dating of postglacial landsliding at The Storr, Isle of Skye, Scotland. *The Holocene*, 8(3): 347-351. doi:10.1191/095968398666797200.

Ballantyne, C.K., Sandeman, G.F., Stone, J.O. & Wilson, P. (2014). Rock-slope failure following Late Pleistocene deglaciation on tectonically stable mountainous terrain. *Quaternary Science Reviews*, 86(0): 144-157. doi:10.1016/j.quascirev.2013.12.021.

Bhasin, R. & Kaynia, A.M. (2004). Static and dynamic simulation of a 700-m high rock slope in western Norway. *Engineering Geology*, 71(3-4): 213-226. doi:10.1016/s0013-7952(03)00135-2.

Bianchi Fasani, G., Di Luzio, E., Esposito, C., Evans, S.G. & Scarascia Mugnozza, G. (2014). Quaternary, catastrophic rock avalanches in the Central Apennines (Italy): Relationships with inherited tectonic features, gravity-driven deformations and the geodynamic frame. *Geomorphology*, 211(0): 22-42. doi:10.1016/j.geomorph.2013.12.027.

Bjerrum, L. (1967). Progressive failure in slopes of overconsolidated plastic clay and clay shales. *Journal of Soil Mechanics & Foundations Division*, 93(SM5): 1-49.

Bjerrum, L. & Jørstad, F.A. (1968). Stability of rock slopes in Norway. *Norwegian Geotechnical Institute, Tech. Rep.*, 79.

Blais-Stevens, A., Hermanns, R.L. & Jermyn, C. (2011). A 36Cl age determination for Mystery Creek rock avalanche and its implications in the context of hazard assessment, British Columbia, Canada. *Landslides*, 8: 407-416. doi:10.1007/s10346-011-0261-0.

Blikra, L.H., Braathen, A., Anda, E., Stalsberg, K. & Longva, O. (2002). Rock avalanches, gravitational bedrock fractures and neotectonic faults onshore northern West Norway: Examples, regional distribution and triggering mechanisms. *Geological Survey of Norway, Report*, 2002.016: 48.

Blikra, L.H., Longva, O., Harbitz, C. & Løvholt, F. (2005). Quantification of rock-avalanche and tsunami hazard in Storfjorden, western Norway. In: K. Senneset, K. Flaate & J.O. Larsen (Eds.), Landslides and Avalanches: ICFL 2005 Norway. Taylor & Francis Group, London.

Blikra, L.H., Longva, O., Braathen, A., Anda, E., Dehls, J.F. & Stalsberg, K. (2006). Rock slope failures in Norwegian fjord areas: examples, spatial distribution and temporal

pattern. In: S.G. Evans, G. Scarascia Mugnozza, A. Strom & R.L. Hermanns (Eds.), Landslides from Massive Rock Slope Failure. NATO Science Series IV: Earth and Environmental Sciences - Vol. 49. Springer Netherlands, pp. 475-496.

Blikra, L.H. (2012). The Åknes rockslide, Norway. In: J.J. Clague & D. Stead (Eds.), Landslides: Types, Mechanisms and Modeling. Cambridge University Press, pp. 323-335.

Blikra, L.H., Kristensen, L. & Lovisolo, M. (2013). Subsurface monitoring of large rockslides in Norway: A key requirement for early warning. *Italian Journal of Engineering Geology and Environment*, Book Series (6): 307-314. doi:10.4408/IJEGE.2013-06.B-28.

Blikra, L.H. & Christiansen, H.H. (2014). A field-based model of permafrost-controlled rockslide deformation in northern Norway. *Geomorphology*, 208(0): 34-49. doi:10.1016/j.geomorph.2013.11.014.

Bøe, R., Longva, O., Lepland, A., Blikra, L.H., Sønstegaard, E., Haflidason, H., Bryn, P. & Lien, R. (2004). Postglacial mass movements and their causes in fjords and lakes in western Norway. *Norwegian Journal of Geology*, 84: 35-55.

Böhme, M., Saintot, A., Henderson, I.H.C., Henriksen, H. & Hermanns, R.L. (2011). Rock slope instabilities in Sogn and Fjordane County, Norway: a detailed structural and geomorphological analysis. *Geological Society, London, Special Publications*, 351(1): 97-111. doi:10.1144/sp351.5.

Böhme, M., Hermanns, R.L., Fischer, L., Oppikofer, T., Bunkholt, H., Derron, M.-H., Carrea, D., Jaboyedoff, M. & Eiken, T. (2012). Detailed assessment of the deep-seated gravitational deformation at Stampa above Flåm, Norway. In: E. Eberhardt, C. Froese, K. Turner & S. Leroueil (Eds.), Landslides and Engineered Slopes: Protecting Society through Improved Understanding. Taylor & Francis Group, London, pp. 647-652.

Böhme, M., Hermanns, R.L., Oppikofer, T., Fischer, L., Bunkholt, H.S.S., Eiken, T., Pedrazzini, A., Derron, M.-H., Jaboyedoff, M., Blikra, L.H. & Nilsen, B. (2013). Analyzing complex rock slope deformation at Stampa, western Norway, by integrating geomorphology, kinematics and numerical modeling. *Engineering Geology*, 154(0): 116-130. doi:10.1016/j.enggeo.2012.11.016.

Böhme, M. (2014). Spatial and temporal variability of rock slope instability in western Norway: Implications for susceptibility and hazard assessment. Doctoral thesis, Norwegian University of Science and Technology (NTNU), Trondheim, Norway.

Booth, A., Dehls, J., Eiken, T., Fischer, L., Hermanns, R. & Oppikofer, T. (2014). Integrating diverse geologic and geodetic observations to determine failure mechanisms and deformation rates across a large bedrock landslide complex: the Osmundneset landslide, Sogn og Fjordane, Norway. *Landslides*: 1-12. doi:10.1007/s10346-014-0504-y.

Booth, A.M., Lamb, M.P., Avouac, J.-P. & Delacourt, C. (2013). Landslide velocity, thickness, and rheology from remote sensing: La Clapière landslide, France. *Geophysical Research Letters*, 40(16): 4299-4304. doi:10.1002/grl.50828.

Borchers, B., Marrero, S., Balco, G., Caffee, M., Goehring, B., Lifton, N., Nishiizumi, K., Phillips, F., Schaefer, J. & Stone, J. (2015). Geological calibration of spallation production rates in the CRONUS-Earth project. *Quaternary Geochronology*. doi:10.1016/j.quageo.2015.01.009.

Boultbee, N., Stead, D., Schwab, J. & Geertsema, M. (2006). The Zymoetz River rock avalanche, June 2002, British Columbia, Canada. *Engineering Geology*, 83(1–3): 76-93. doi:10.1016/j.enggeo.2005.06.038.

Bovis, M.J. & Evans, S.G. (1996). Extensive deformations of rock slopes in southern Coast Mountains, southwest British Columbia, Canada. *Engineering Geology*, 44(1-4): 163-182. doi:10.1016/s0013-7952(96)00068-3.

Bowman, E.T., Take, W.A., Rait, K.L. & Hann, C. (2012). Physical models of rock avalanche spreading behaviour with dynamic fragmentation. *Canadian Geotechnical Journal*, 49(4): 460-476. doi:10.1139/t2012-007.

Braathen, A., Blikra, L.H., Berg, S.S. & Karlsen, F. (2004). Rock-slope failures in Norway; type, geometry, deformation mechanisms and stability. *Norwegian Journal of Geology*, 84: 67-88.

Brideau, M.-A., Yan, M. & Stead, D. (2009). The role of tectonic damage and brittle rock fracture in the development of large rock slope failures. *Geomorphology*, 103(1): 30-49. doi:10.1016/j.geomorph.2008.04.010.

Bungum, H., Lindholm, C.D., Dahle, A., Woo, G., Nadim, F., Holme, J.K., Gudmestad, O.T., Hagberg, T. & Karthigeyan, K. (2000). New Seismic Zoning Maps for Norway, the North Sea, and the United Kingdom. *Seismological Research Letters*, 71(6): 687-697. doi:10.1785/gssrl.71.6.687.

Bungum, H., Olesen, O., Pascal, C., Gibbons, S., Lindholm, C. & VestØl, O. (2010). To what extent is the present seismicity of Norway driven by post-glacial rebound? *Journal of the Geological Society*, 167(2): 373-384. doi:10.1144/0016-76492009-009.

Bunkholt, H., Osmundsen, P.T., Redfield, T., Oppikofer, T., Eiken, T., L'Heureux, J.-S., Hermanns, R.L. & Lauknes, T.R. (2011). ROS Fjellskred i Troms: status og analyser etter feltarbeid 2010. *Geological Survey of Norway, Report*, 2011-031.

Bunkholt, H., Otterå, S., Yugsi Molina, F.X., Hermanns, R.L., Dehls, J., Osmundsen, P.T., Redfield, T. & Eiken, T. (2013). Undersøkelser av ustable eller potensielt ustabile fjellpartier i Troms - status og planer etter feltarbeid 2011 og 2012. *Geological Survey of Norway, Report*, 2013.021.

Bunkholt, H.S.S., Redfield, T.F., Osmundsen, P.T., Oppikofer, T., Hermanns, R.L. & Dehls, J. (2012). Landslide processes in hard rock in Troms, Norway. In: E. Eberhardt, C. Froese, K. Turner & S. Leroueil (Eds.), Landslides and Engineered Slopes: Protecting Society through Improved Understanding. Taylor & Francis Group, London, pp. 855-861.

Burbank, D.W., Leland, J., Fielding, E., Anderson, R.S., Brozovic, N., Reid, M.R. & Duncan, C. (1996). Bedrock incision, rock uplift and threshold hillslopes in the northwestern Himalayas. *Nature*, 379(6565): 505-510.

Chigira, M., Hariyama, T. & Yamasaki, S. (2013). Development of deep-seated gravitational slope deformation on a shale dip-slope: Observations from high-quality drill cores. *Tectonophysics*, 605: 104-113. doi:10.1016/j.tecto.2013.04.019.

Cook, S.J., Porter, P.R. & Bendall, C.A. (2013). Geomorphological consequences of a glacier advance across a paraglacial rock avalanche deposit. *Geomorphology*, 189(0): 109-120. doi:10.1016/j.geomorph.2013.01.022.

Corfu, F., Gasser, D. & Chew, D.M. (2014). New perspectives on the Caledonides of Scandinavia and related areas: introduction. *Geological Society, London, Special Publications*, 390(1): 1-8. doi:10.1144/sp390.28.

Cossart, E., Braucher, R., Fort, M., Bourlès, D.L. & Carcaillet, J. (2008). Slope instability in relation to glacial debuttressing in alpine areas (Upper Durance catchment, southeastern France): Evidence from field data and 10Be cosmic ray exposure ages. *Geomorphology*, 95(1–2): 3-26. doi:10.1016/j.geomorph.2006.12.022.

Crandell, D.R. & Fahnestock, R.K. (1965). Rockfalls and Avalanches from Little Tahoma Peak on Mount Rainier Washington. *Geological Survey Bulletin*, 1221-A: 30.

Crosta, G.B., Imposimato, S. & Roddeman, D.G. (2003). Numerical modelling of large landslides stability and runout. *Nat. Hazards Earth Syst. Sci.*, 3(6): 523-538. doi:10.5194/nhess-3-523-2003.

Crosta, G.B., Chen, H. & Lee, C.F. (2004). Replay of the 1987 Val Pola Landslide, Italian Alps. *Geomorphology*, 60(1–2): 127-146. doi:10.1016/j.geomorph.2003.07.015.

Crosta, G.B., Frattini, P. & Fusi, N. (2007). Fragmentation in the Val Pola rock avalanche, Italian Alps. *J. Geophys. Res.*, 112(F1): F01006. doi:10.1029/2005jf000455.

Crosta, G.B., Imposimato, S. & Roddeman, D. (2009). Numerical modelling of entrainment/deposition in rock and debris-avalanches. *Engineering Geology*, 109(1-2): 135-145. doi:10.1016/j.enggeo.2008.10.004.

Crosta, G.B., Frattini, P. & Agliardi, F. (2013). Deep seated gravitational slope deformations in the European Alps. *Tectonophysics*, 605: 13-33. doi:10.1016/j.tecto.2013.04.028.

Dahl, S.O. & Nesje, A. (1992). Paleoclimatic implications based on equilibrium-line altitude depressions of reconstructed Younger Dryas and Holocene cirque glaciers in inner Nordfjord, western Norway. *Palaeogeography, Palaeoclimatology, Palaeoecology*, 94(1–4): 87-97. doi:10.1016/0031-0182(92)90114-K.

Dahlin, T. (1993). On the Automation of 2D Resistivity Surveying for Engineering and Environmental Applications. PhD thesis, Lund University, 187 pp.

Davies, T.R. & McSaveney, M.J. (2009). The role of rock fragmentation in the motion of large landslides. *Engineering Geology*, 109(1-2): 67-79. doi:10.1016/j.enggeo.2008.11.004.

De Blasio, F.V. (2014). Friction and dynamics of rock avalanches travelling on glaciers. *Geomorphology*, 213: 88-98. doi:10.1016/j.geomorph.2014.01.001.

Dehls, J.F., Olesen, O., Bungum, H., Hicks, E.C., Lindholm, C.D. & Riis, F. (2000). Neotectonic map: Norway and adjacent areas. *Geological Survey of Norway, Trondheim*.

Dehls, J.F., Fischer, L., Böhme, M., Saintot, A., Hermanns, R.L., Oppikofer, T., Lauknes, T.R., Larsen, Y. & Blikra, L.H. (2012). Landslide monitoring in western Norway using high resolution TerraSAR-X and Radarsat-2 InSAR. In: E. Eberhardt, C. Froese, K. Turner & S. Leroueil (Eds.), Landslides and Engineered Slopes: Protecting Society through Improved Understanding. Taylor & Francis Group, London, pp. 1321-1325.

Delaney, K. & Evans, S. (2014). The 1997 Mount Munday landslide (British Columbia) and the behaviour of rock avalanches on glacier surfaces. *Landslides*, 11(6): 1019-1036. doi:10.1007/s10346-013-0456-7.

Deline, P. (2009). Interactions between rock avalanches and glaciers in the Mont Blanc massif during the late Holocene. *Quaternary Science Reviews*, 28(11–12): 1070-1083. doi:10.1016/j.quascirev.2008.09.025.

Derron, M.-H., Jaboyedoff, M. & Blikra, L.H. (2005). Preliminary assessment of rockslide and rockfall hazards using a DEM (Oppstadhornet, Norway). *Nat. Hazards Earth Syst. Sci.*, 5: 285-292.

Dramis, F. & Sorriso-Valvo, M. (1994). Deep-seated gravitational slope deformations, related landslides and tectonics. *Engineering Geology*, 38: 231-243.

Dufresne, A. & Davies, T.R. (2009). Longitudinal ridges in mass movement deposits. *Geomorphology*, 105(3-4): 171-181. doi:10.1016/j.geomorph.2008.09.009.

Dunning, S.A., Mitchell, W.A., Rosser, N.J. & Petley, D.N. (2007). The Hattian Bala rock avalanche and associated landslides triggered by the Kashmir Earthquake of 8 October 2005. *Engineering Geology*, 93(3-4): 130-144. doi:10.1016/j.enggeo.2007.07.003.

Eberhardt, E., Stead, D., Coggan, J.S. & Willenberg, H. (2003). Hybrid finite-/discrete-element modelling of progressive failure in massive rock slopes. *ISRM 2003 - Technology roadmap for rock mechanics, South African Institute of Mining and Metallurgy*.

Eberhardt, E., Stead, D. & Coggan, J.S. (2004). Numerical analysis of initiation and progressive failure in natural rock slopes—the 1991 Randa rockslide. *International Journal of Rock Mechanics and Mining Sciences*, 41(1): 69-87. doi:10.1016/S1365-1609(03)00076-5.

Eidsvig, U.M., Medina-Cetina, Z., Kveldsvik, V., Glimsdal, S., Harbitz, C.B. & Sandersen, F. (2011). Risk assessment of a tsunamigenic rockslide at Åknes. *Natural Hazards*, 56(2): 529-545. doi:10.1007/s11069-009-9460-6.

El Bedoui, S., Guglielmi, Y., Lebourg, T. & Pérez, J.-L. (2009). Deep-seated failure propagation in a fractured rock slope over 10,000 years: The La Clapière slope, the south-eastern French Alps. *Geomorphology*, 105(3-4): 232-238. doi:10.1016/j.geomorph.2008.09.025.

Erismann, T.H. & Abele, G. (2001). Dynamics of Rockslides and Rockfalls. Springer, Berlin.

Esri, http://www.esri.com/ (access 20. Jan. 2015).

Evans, S., Scarascia Mugnozza, G., Strom, A. & Hermanns, R.L. (2006a). Landslides from Massive Rock Slope Failure NATO Science Series IV Earth and Environmental Science - Vol. 49. Springer.

Evans, S.G., Clague, J.J., Woodsworth, G.J. & Hungr, O. (1989). The Pandemonium Creek rock avalanche, British Columbia. *Canadian Geotechnical Journal*, 26(3): 427-446. doi:10.1139/t89-056.

Evans, S.G. & Clague, J.J. (1994). Recent climatic change and catastrophic geomorphic processes in mountain environments. *Geomorphology*, 10: 107-128.

Evans, S.G., Scarascia Mugnozza, G., Strom, A.L., Hermanns, R.L., Ischuk, A. & Vinnichenko, S. (2006b). Landslides from massive rock slope failure and associated phenomena. In: S.G. Evans, G. Scarascia Mugnozza, A. Strom & R.L. Hermanns (Eds.), Landslides from Massive Rock Slope Failure. NATO Science Series IV: Earth and Environmental Sciences - Vol. 49. Springer Netherlands, pp. 03-52.

Evans, S.G., Bishop, N.F., Fidel Smoll, L., Valderrama Murillo, P., Delaney, K.B. & Oliver-Smith, A. (2009a). A re-examination of the mechanism and human impact of catastrophic mass flows originating on Nevado Huascarán, Cordillera Blanca, Peru in 1962 and 1970. *Engineering Geology*, 108(1–2): 96-118. doi:10.1016/j.enggeo.2009.06.020.

Evans, S.G., Roberts, N.J., Ischuk, A., Delaney, K.B., Morozova, G.S. & Tutubalina, O. (2009b). Landslides triggered by the 1949 Khait earthquake, Tajikistan, and associated loss of life. *Engineering Geology*, 109(3-4): 195-212.

Evans, S.G., Delaney, K.B., Hermanns, R.L., Strom, A. & Scarascia-Mugnozza, G. (2011). The formation and behaviour of natural and artificial rockslide dams; implications for engineering performance and hazard management. In: S.G. Evans, R.L. Hermanns, A. Strom & G. Scarascia-Mugnozza (Eds.), Natural and Artificial Rockslide Dams, Lecture Notes in Earth Sciences 133. Springer, Berlin Heidelberg, pp. 1-75.

Evenson, E.B., Burkhart, P.A., Gosse, J.C., Baker, G.S., Jackofsky, D., Meglioli, A., Dalziel, I., Kraus, S., Alley, R.B. & Berti, C. (2009). Enigmatic boulder trains, supraglacial rock avalanches, and the origin of “Darwin's boulders,” Tierra del Fuego. *GSA Today*, 19(12): 4-10. doi:10.1130/GSATG72A.1.

Fenton, C.R., Hermanns, R.L., Blikra, L.H., Kubik, P.W., Bryant, C., Niedermann, S., Meixner, A. & Goethals, M.M. (2011). Regional 10Be production rate calibration for the past 12 ka deduced from the radiocarbon-dated Grøtlandsura and Russenes rock avalanches at 69° N, Norway. *Quaternary Geochronology*, 6(5): 437-452. doi:10.1016/j.quageo.2011.04.005.

Fischer, L., Kääb, A., Huggel, C. & Noetzli, J. (2006). Geology, glacier retreat and permafrost degradation as controlling factors of slope instabilities in a high-mountain rock wall: the Monte Rosa east face. *Nat. Hazards Earth Syst. Sci.*, 6(5): 761-772.

Fischer, L., Purves, R.S., Huggel, C., Noetzli, J. & Haeberli, W. (2012). On the influence of topographic, geological and cryospheric factors on rock avalanches and rockfalls in high-mountain areas. *Nat. Hazards Earth Syst. Sci.*, 12: 241-254. doi:10.5194/nhess-12-241-2012.

Fischer, L., Huggel, C., Kääb, A. & Haeberli, W. (2013). Slope failures and erosion rates on a glacierized high-mountain face under climatic changes. *Earth surface processes and landforms*, 38(8): 836-846. doi:10.1002/esp.3355.

Fisher, J.E., Shakoor, A. & Watts, C.F. (2014). Comparing discontinuity orientation data collected by terrestrial LiDAR and transit compass methods. *Engineering Geology*, 181(0): 78-92. doi:10.1016/j.enggeo.2014.08.014.

Fjeldskaar, W., Lindholm, C., Dehls, J.F. & Fjeldskaar, I. (2000). Postglacial uplift, neotectonics and seismicity in Fennoscandia. *Quaternary Science Reviews*, 19(14–15): 1413-1422. doi:10.1016/S0277-3791(00)00070-6.

Fossen, H. (2000). Extensional tectonics in the Caledonides: Synorogenic or postorogenic? *Tectonics*, 19(2): 213-224. doi:10.1029/1999tc900066.

Fossen, H., Dallmann, W. & Andersen, T.B. (2008a). The mountain chain rebounds and founders - The Caledonides are worn down; 405-359 Ma. In: I.B. Ramberg, I. Bryhni, A. Nøttvedt & K. Rangnes (Eds.), The Making of a Land - Geology of Norway. Norsk Geologisk Forening, Trondheim, pp. 232-259.

Fossen, H., Pedersen, R.-B., Bergh, S. & Andresen, A. (2008b). Creation of mountain chain – The building up of the Caledonides; about 500-405 Ma. In: I.B. Ramberg, I. Bryhni, A. Nøttvedt & K. Rangnes (Eds.), The Making of a Land - Geology of Norway. Norsk Geologisk Forening, Trondheim, pp. 178-231.

Fredin, O., Bergstrøm, B., Eilertsen, R., Hansen, L., Longva, O., Nesje, A. & Sveian, H. (2013). Glacial landforms and Quaternary landscape development in Norway. In: L. Olsen, O. Fredin & O. Olesen (Eds.), Quaternary Geology of Norway. Geological Survey of Norway Special Publication, Trondheim, pp. 5-25.

Furseth, A. (2006). Skredulykker i Norge. Tun Forlag, Oslo.

Gabrielsen, R.H., Braathen, A., Dehls, J. & Roberts, D. (2002). Tectonic lineaments of Norway. *Norwegian Journal of Geology*, 82: 153-174.

Galadini, F. (2006). Quaternary tectonics and large-scale gravitational deformations with evidence of rock-slide displacements in the Central Apennines (central Italy). *Geomorphology*, 82(3–4): 201-228. doi:10.1016/j.geomorph.2006.05.003.

Ganerød, G.V., Grøneng, G., Rønning, J.S., Dalsegg, E., Elvebakk, H., Tønnesen, J.F., Kveldsvik, V., Eiken, T., Blikra, L.H. & Braathen, A. (2008). Geological model of the Åknes rockslide, western Norway. *Engineering Geology*, 102(1-2): 1-18. doi:10.1016/j.enggeo.2008.01.018.

Ganerød, G.V. (2013a). Geological logging of drill cores from borehole KH-08-12 at Åknes, Møre og Romsdal, Western Norway. *Geological Survey of Norway, Report*, 2013.039.

Ganerød, G.V. (2013b). Geological logging of drill core from borehole NN-01-12 at Jettan, Nordnes mountain in Troms county, Northern Norway. *Geological Survey of Norway, Report*, 2013.042.

Geertsema, M., Clague, J.J., Schwab, J.W. & Evans, S.G. (2006). An overview of recent large catastrophic landslides in northern British Columbia, Canada. *Engineering Geology*, 83(1–3): 120-143. doi:10.1016/j.enggeo.2005.06.028.

Gischig, V., Amann, F., Moore, J.R., Loew, S., Eisenbeiss, H. & Stempfhuber, W. (2011). Composite rock slope kinematics at the current Randa instability, Switzerland, based on remote sensing and numerical modeling. *Engineering Geology*, 118(1-2): 37-53. doi:10.1016/j.enggeo.2010.11.006.

GoldenSoftware, http://www.goldensoftware.com/ (access 20. Jan. 2015).

Gori, S., Falcucci, E., Dramis, F., Galadini, F., Galli, P., Giaccio, B., Messina, P., Pizzi, A., Sposato, A. & Cosentino, D. (2014). Deep-seated gravitational slope deformation, large-scale rock failure, and active normal faulting along Mt. Morrone (Sulmona basin, Central Italy): Geomorphological and paleoseismological analyses. *Geomorphology*, 208(0): 88-101. doi:10.1016/j.geomorph.2013.11.017.

Gosse, J.C. & Evenson, E.B. (1994). Reinterpretation of the evidence for a significant mid-Holocene ice advance in the Rio Atuel valley, Mendoza Province, Argentina. *Z. Geomorph. N. F.*, 38(3): 327-338.

Gosse, J.C. & Phillips, F.M. (2001). Terrestrial in situ cosmogenic nuclides: theory and application. *Quaternary Science Reviews*, 20(14): 1475-1560. doi:10.1016/s0277-3791(00)00171-2.

Grøneng, G. (2010). Stability analyses of the Åknes rock slope, Western Norway. Doctoral thesis, Norwegian University of Science and Technology (NTNU), Trondheim, Norway.

Gutiérrez-Santolalla, F., Acosta, E., Ríos, S., Guerrero, J. & Lucha, P. (2005). Geomorphology and geochronology of sackung features (uphill-facing scarps) in the Central Spanish Pyrenees. *Geomorphology*, 69(1–4): 298-314. doi:10.1016/j.geomorph.2005.01.012.

Hacker, B.R., Andersen, T.B., Johnston, S., Kylander-Clark, A.R.C., Peterman, E.M., Walsh, E.O. & Young, D. (2010). High-temperature deformation during continental-margin subduction and exhumation: The ultrahigh-pressure Western Gneiss Region of Norway. *Tectonophysics*, 480(1-4): 149-171. doi:10.1016/j.tecto.2009.08.012.

Hansen, L., Sveian, H., Olsen, L., Høgaas, F., Rindstad, B.I., Wiig, T. & Lyche, E. (2012). The marine limit as a basis for mapping of landslide susceptibility in fine-grained, fjord deposits, onshore Norway. In: E. Eberhardt, C. Froese, K. Turner & S. Leroueil (Eds.), Landslides and Engineered Slopes: Protecting Society through Improved Understanding. Taylor & Francis Group, London, pp. 1833-1838.

Hansen, L., Høgaas, F., Sveian, H., Olsen, L. & Rindstad, B.I. (2014). Quaternary Geology as a Basis for Landslide Susceptibility Assessment in Fine-Grained, Marine Deposits, Onshore Norway. In: J.-S.e.a. L'Heureux (Ed.), Landslides in Sensitive Clays: From Geosciences to Risk Management, Advances in Natural and Technological Hazards Research 36,. Springer Science+Business Media, Dordrecht, pp. 369-381.

Harbitz, C.B., Glimsdal, S., Løvholt, F., Kveldsvik, V., Pedersen, G.K. & Jensen, A. (2014). Rockslide tsunamis in complex fjords: From an unstable rock slope at Åkerneset to tsunami risk in western Norway. *Coastal Engineering*, 88(0): 101-122. doi:10.1016/j.coastaleng.2014.02.003.

Heim, A. (1932). Bergsturz und Menschenleben. *Beiblatt zur Vierteljahresschrift der Naturforschenden Gesellschaft in Zürich*, 77: 218.

Henderson, I. & Saintot, A. (2007). Fjellskredundersøkelser i Møre og Romsdal. *Geological Survey of Norway, Report*, 2007.043.

Henderson, I.H.C., Saintot, A. & Derron, M.H. (2006). Structural mapping of potential rockslide sites in the Storfjorden area, western Norway: the influence of bedrock geology on hazard analysis. *Geological Survey of Norway, Report*, 2006.052.

Henderson, I.H.C., Lauknes, T.R., Osmundsen, P.T., Dehls, J., Larsen, Y. & Redfield, T.F. (2011). A structural, geomorphological and InSAR study of an active rock slope failure development. *Geological Society, London, Special Publications*, 351(1): 185-199. doi:10.1144/sp351.10.

Henderson, I.H.C. & Saintot, A. (2011). Regional spatial variations in rockslide distribution from structural geology ranking: an example from Storfjorden, western Norway. *Geological Society, London, Special Publications*, 351(1): 79-95. doi:10.1144/sp351.4.

Hermanns, R., Oppikofer, T., Molina, F.Y., Dehls, J. & Böhme, M. (2014a). Approach for Systematic Rockslide Mapping of Unstable Rock Slopes in Norway. In: K. Sassa, P. Canuti & Y. Yin (Eds.), Landslide Science for a Safer Geoenvironment. Springer International Publishing, pp. 129-134.

Hermanns, R.L. & Strecker, M.R. (1999). Structural and lithological controls on large Quaternary rock avalanches (sturzstroms) in arid northwestern Argentina. *Geological*

Society of America Bulletin, 111(6): 934-948. doi:10.1130/0016-7606(1999)111<0934:salcol>2.3.co;2.

Hermanns, R.L., Trauth, M.H., Niedermann, S., McWilliams, M. & Strecker, M.R. (2000). Tephrochronologic constraints on temporal distribution of large landslides in NW-Argentina. *Journal of Geology*, 108: 35-52.

Hermanns, R.L., Niedermann, S., Garcia, A.V., Gomez, J.S. & Strecker, M.R. (2001). Neotectonics and catastrophic failure of mountain fronts in the southern intra-Andean Puna Plateau, Argentina. *Geology*, 29(7): 619-622. doi:10.1130/0091-7613(2001)029<0619:nacfom>2.0.co;2.

Hermanns, R.L., Niedermann, S., Ivy-Ochs, S. & Kubik, P.W. (2004). Rock avalanching into a landslide-dammed lake causing multiple dam failure in Las Conchas valley (NW Argentina) - evidence from surface exposure dating and stratigraphic analyses. *Landslides*, 1(2): 113-122. doi:10.1007/s10346-004-0013-5.

Hermanns, R.L., Blikra, L.H., Naumann, M., Nilsen, B., Panthi, K.K., Stromeyer, D. & Longva, O. (2006a). Examples of multiple rock-slope collapses from Köfels (Ötz valley, Austria) and western Norway. *Engineering Geology*, 83(1-3): 94-108. doi:10.1016/j.enggeo.2005.06.026.

Hermanns, R.L., Niedermann, S., Garcia, A.V. & Schellenberger, A. (2006b). Rock avalanching in the NW Argentine Andes as a result of complex interactions of lithologic, structural and topographic boundary conditions, climate change and active tectonics. In: S.G. Evans, G. Scarascia Mugnozza, A. Strom & R.L. Hermanns (Eds.), Landslides from Massive Rock Slope Failure. NATO Science Series IV: Earth and Environmental Sciences - Vol. 49. Springer Netherlands, pp. 497-520.

Hermanns, R.L., Blikra, L.H., Anda, E., Saintot, A., Dahle, H., Oppikofer, T., Fischer, L., Bunkholt, H., Böhme, M., Dehls, J.F., Lauknes, T.R., Redfield, T.F., Osmundsen, P.T. & Eiken, T. (2011a). Systematic mapping of large unstable rock slopes in Norway. *Proceedings of the Second World Landslide Forum, Rome*.

Hermanns, R.L., Fischer, L., Oppikofer, T., Böhme, M., Dehls, J., Henriksen, H., Booth, A., Eilertsen, R., Longva, O. & Eiken, T. (2011b). Mapping of unstable and potentially unstable rock slopes in Sogn og Fjordane (work report 2008-2010). *Geological Survey of Norway, Report*, 2011.055.

Hermanns, R.L., Hewitt, K., Strom, A., Evans, S.G., Dunning, S.A. & Scarascia-Mugnozza, G. (2011c). The Classification of Rockslide Dams. In: S.G. Evans, R.L. Hermanns, A. Strom & G. Scarascia-Mugnozza (Eds.), Natural and Artificial Rockslide Dams, Lecture Notes in Earth Sciences 133. Springer, Berlin-Heidelberg, pp. 581-593.

Hermanns, R.L., Hansen, L., Sletten, K., Böhme, M., Bunkholt, H.S.S., Dehls, J.F., Eilertsen, R.S., Fischer, L., L'Heureux, J.-S., Høgaas, F., Nordahl, B., Oppikofer, T., Rubensdotter, L., Solberg, I.-L., Stalsberg, K. & Yugsi Molina, F.X. (2012a). Systematic geological mapping for landslide understanding in the Norwegian context. In: E. Eberhardt, C. Froese, K. Turner & S. Leroueil (Eds.), Landslides and Engineered Slopes: Protecting Society through Improved Understanding. Taylor & Francis Group, London, pp. 265-271.

Hermanns, R.L. & Longva, O. (2012). Rapid rock-slope failures. In: J.J. Clague & D. Stead (Eds.), Landslides: Types, Mechanisms and Modeling. Cambridge University Press, pp. 59-70.

Hermanns, R.L., Oppikofer, T., Anda, E., Blikra, L.H., Böhme, M., Bunkholt, H., Crosta, G.B., Dahle, H., Devoli, G., Fischer, L., Jaboyedoff, M., Loew, S., Sætre, S. & Yugsi Molina, F.X. (2012b). Recommended hazard and risk classification system for large unstable rock slopes in Norway. *Geological Survey of Norway, Report*, 2012.029.

Hermanns, R.L., Redfield, T.F., Bunkholt, H.S.S., Fischer, L., Oppikofer, T., Gosse, J. & Eiken, T. (2012c). Cosmogenic nuclide dating of slow moving rockslides in Norway in order to assess long-term slide velocities. In: E. Eberhardt, C. Froese, K. Turner & S.

Leroueil (Eds.), Landslides and Engineered Slopes: Protecting Society through Improved Understanding. Taylor & Francis Group, London, pp. 849-854.

Hermanns, R.L., Dahle, H., Bjerke, P.L., Crosta, G.B., Anda, E., Blikra, L.H., Saintot, A., Longva, O. & Eiken, T. (2013a). Rock slide dams in Møre og Romsdal county, Norway: Examples for the hazard and potential of rock slide dams. In: C. Margottini, P. Canuti & K. Sassa (Eds.), Landslide Science and Practise. Springer, Berlin.

Hermanns, R.L., Oppikofer, T., Anda, E., Blikra, L.H., Böhme, M., Bunkholt, H., Crosta, G., Dahle, H., Devoli, G., Fischer, L., Jaboyedoff, M., Loew, S., Sætre, S. & Yugsi Molina, F.X. (2013b). Hazard and risk classification for large unstable rock slopes in Norway. *Italian Journal of Engineering Geology and Environment*, Book Series (6): 245-254. doi:10.4408/IJEGE.2013-06.B-22.

Hermanns, R.L., Oppikofer, T., Dahle, H., Eiken, T., Ivy-Ochs, S. & Blikra, L.H. (2013c). Understanding long-term slope deformation for stability assessment of rock slopes: the case of the Oppstadhornet rockslide, Norway. *Italian Journal of Engineering Geology and Environment*, Book Series (6): 255-264. doi:10.4408/IJEGE.2013-06.B-23.

Hermanns, R.L., Fauqué, L. & Wilson, C.G.J. (2014b). 36Cl terrestrial cosmogenic nuclide dating suggests Late Pleistocene to Early Holocene mass movements on the south face of Aconcagua mountain and in the Las Cuevas–Horcones valleys, Central Andes, Argentina. *Geological Society, London, Special Publications*, 399. doi:10.1144/sp399.19.

Hermanns, R.L., Oppikofer, T., Roberts, N.J. & Sandøy, G. (2014c). Catalogue of Historical Displacement Waves and Landslide-Triggered Tsunamis in Norway. In: G. Lollino, A. Manconi, J. Locat, Y. Huang & M. Canals Artigas (Eds.), Engineering Geology for Society and Territory – Volume 4: Marine and Coastal Processes. Springer International Publishing Switzerland, pp. 63-66.

Hewitt, K. (1998). Catastrophic landslides and their effects on the Upper Indus streams, Karakoram Himalaya, northern Pakistan. *Geomorphology*, 26(1-3): 47-80. doi:10.1016/S0169-555X(98)00051-8.

Hewitt, K., Clague, J.J. & Orwin, J.F. (2008). Legacies of catastrophic rock slope failures in mountain landscapes. *Earth-Science Reviews*, 87(1–2): 1-38. doi:10.1016/j.earscirev.2007.10.002.

Hewitt, K. (2009a). Catastrophic rock slope failures and late Quaternary developments in the Nanga Parbat-Haramosh Massif, Upper Indus basin, northern Pakistan. *Quaternary Science Reviews*, 28(11-12): 1055-1069. doi:10.1016/j.quascirev.2008.12.019.

Hewitt, K. (2009b). Rock avalanches that travel onto glaciers and related developments, Karakoram Himalaya, Inner Asia. *Geomorphology*, 103(1): 66-79. doi:10.1016/j.geomorph.2007.10.017.

Hewitt, K., Gosse, J. & Clague, J.J. (2011). Rock avalanches and the pace of late Quaternary development of river valleys in the Karakoram Himalaya. *Geological Society of America Bulletin*, 123(9/10): 1836-1850. doi:10.1130/B30341.1.

Hippolyte, J.-C., Brocard, G., Tardy, M., Nicoud, G., Bourles, D., Braucher, R., Menard, G. & Souffache, B. (2006). The recent fault scarps of the Western Alps (France): Tectonic surface ruptures or gravitational sackung scarps? A combined mapping, geomorphic, levelling, and 10Be dating approach. *Tectonophysics*, 418: 255 - 276. doi:10.1016/j.tecto.2006.02.009.

Hippolyte, J.-C., Bourlès, D., Braucher, R., Carcaillet, J., Léanni, L., Arnold, M. & Aumaitre, G. (2009). Cosmogenic 10Be dating of a sackung and its faulted rock glaciers, in the Alps of Savoy (France). *Geomorphology*, 108(3–4): 312-320. doi:10.1016/j.geomorph.2009.02.024.

Holm, K., Bovis, M.J. & Jakob, M. (2004). The landslide response of alpine basins to post-Little Ice Age glacial thinning and retreat in southwestern British Columbia. *Geomorphology*, 57: 201-216. doi:10.1016/S0169-555X(03)00103-X.

Hungr, O. (1995). A model for the runout analysis of rapid flow slides, debris flows, and avalanches. *Can. Geotech. J.*, 32: 610-623.

Hungr, O. & Evans, S.G. (1996). Rock avalanche runout prediction using a dynamic model. In: K. Senneset (Ed.), Proceedings of the 7th International Symposium on Landslides. A.A. Balkema, Rotterdam, pp. 233-238.

Hungr, O., Evans, S.G., Bovis, M.J. & Hutchinson, J.N. (2001). A review of the classification of landslides of the flow type. *Environmental and Engineering Geoscience*, 7(3): 221-238. doi:10.2113/gseegeosci.7.3.221.

Hungr, O. & Evans, S.G. (2004). Entrainment of debris in rock avalanches: An analysis of a long run-out mechanism. *Geological Society of America Bulletin*, 116(9-10): 1240-1252. doi:10.1130/b25362.1.

Hungr, O. (2006). Rock avalanche occurrence, process and modelling. In: S.G. Evans, G. Scarascia Mugnozza, A. Strom & R.L. Hermanns (Eds.), Landslides from Massive Rock Slope Failure. NATO Science Series IV: Earth and Environmental Sciences - Vol. 49. Springer Netherlands, pp. 243-266.

Hungr, O. & McDougall, S. (2009). Two numerical models for landslide dynamic analysis. *Computers & Geosciences*, 35(5): 978-992. doi:10.1016/j.cageo.2007.12.003.

Hungr, O., Leroueil, S. & Picarelli, L. (2014). The Varnes classification of landslide types, an update. *Landslides*, 11(2): 167-194. doi:10.1007/s10346-013-0436-y.

Hürlimann, M., Ledesma, A., Corominas, J. & Prat, P.C. (2006). The deep-seated slope deformation at Encampadana, Andorra: Representation of morphologic features by numerical modelling. *Engineering Geology*, 83(4): 343-357. doi:10.1016/j.enggeo.2005.11.008.

Hutchinson, J.N. (1988). General Report: morphological and geotechnical parameters of landslides in relation to geology and hydrogeology. In: C. Bonnard (Ed.), Fifth International Symposium on Landslides. A.A. Balkema, Rotterdam, pp. 3-36.

InnovMetric, http://www.innovmetric.com/ (access 20. Jan. 2015).

Ivy-Ochs, S., Poschinger, A.v., Synal, H.A. & Maisch, M. (2009). Surface exposure dating of the Flims landslide, Graubünden, Switzerland. *Geomorphology*, 103(1): 104-112. doi:10.1016/j.geomorph.2007.10.024.

Jaboyedoff, M., Metzger, R., Oppikofer, T., Couture, R., Derron, M.-H., Locat, J. & Turmel, D. (2007). New insight techniques to analyze rock-slope relief using DEM and 3Dimaging cloud points: COLTOP-3D software. In: E. Eberhardt, D. Stead & T. Morrison (Eds.), Rock mechanics: Meeting Society's challenges and demands. Taylor & Francis, London, pp. 61-68.

Jaboyedoff, M., Couture, R. & Locat, P. (2009). Structural analysis of Turtle Mountain (Alberta) using digital elevation model: Toward a progressive failure. *Geomorphology*, 103(1): 5-16. doi:10.1016/j.geomorph.2008.04.012.

Jaboyedoff, M., Oppikofer, T., Derron, M.-H., Blikra, L.H., Böhme, M. & Saintot, A. (2011). Complex landslide behaviour and structural control: a three-dimensional conceptual model of Åknes rockslide, Norway. *Geological Society, London, Special Publications*, 351(1): 147-161. doi:10.1144/sp351.8.

Jaboyedoff, M., Oppikofer, T., Abellán, A., Derron, M.-H., Loye, A., Metzger, R. & Pedrazzini, A. (2012). Use of LIDAR in landslide investigations: a review. *Natural Hazards*, 61(1): 5-28. doi:10.1007/s11069-010-9634-2.

Jarman, D. (2006). Large rock slope failures in the Highlands of Scotland: Characterisation, causes and spatial distribution. *Engineering Geology*, 83(1–3): 161-182. doi:10.1016/j.enggeo.2005.06.030.

Jarman, D. (2009). Paraglacial rock slope failure as an agent of glacial trough widening. *Geological Society, London, Special Publications*, 320: 103-131. doi:10.1144/SP320.8.

Jibson, R.W., Harp, E.L., Schulz, W. & Keefer, D.K. (2006). Large rock avalanches triggered by the M 7.9 Denali Fault, Alaska, earthquake of 3 November 2002. *Engineering Geology*, 83(1–3): 144-160. doi:10.1016/j.enggeo.2005.06.029.

Jomard, H., Lebourg, T. & Guglielmi, Y. (2014). Morphological analysis of deep-seated gravitational slope deformation (DSGSD) in the western part of the Argentera massif. A morpho-tectonic control? *Landslides*, 11(1): 107-117. doi:10.1007/s10346-013-0434-0.

Keary, P., Brooks, M. & Hill, I. (2002). An introduction to geophysical exploration. Blackwell Science.

Korup, O., Densmore, A.L. & Schlunegger, F. (2010). The role of landslides in mountain range evolution. *Geomorphology*, 120(1-2): 77-90. doi:10.1016/j.geomorph.2009.09.017.

Krautblatter, M., Funk, D. & Günzel, F.K. (2013). Why permafrost rocks become unstable: a rock–ice-mechanical model in time and space. *Earth surface processes and landforms*, 38: 876-887. doi:10.1002/esp.3374.

Krieger, I. (2013). Die Berill Störung und ihr Einfluss auf eine tiefgreifende Massenbewegung in Norwegen (in German). Unpublished master thesis, Friedrich-Alexander-Universität Erlangen-Nürnberg, Erlangen.

Krieger, I., Hermanns, R.L., Schleier, M., Yugsi Molina, F.X., Oppikofer, T., Rønning, J.S., Eiken, T. & Rohn, J. (2013). The Berill fault and its relation to a deep seated gravitational slope deformation (DSGSD). In: R. Genevois & A. Prestininzi (Eds.), International Conference on Vajont – 1963-2013 – Thoughts and analyses after 50 years since the catastrophic landslide, Padua, Italy, 8-10. October 2013. Italian Journal of Engineering Geology and Environment, Book Series (6), pp. 265-273.

Kristensen, L., Rivolta, C., Dehls, J. & Blikra, L.H. (2013). GB InSAR measurement at the Åknes rockslide, Norway. *Italian Journal of Engineering Geology and Environment*, Book Series (6): 339-348. doi:10.4408/IJEGE.2013-06.B-32.

Kveldsvik, V. (2008). Static and dynamic stability analyses of the 800 m high Åknes rock slope, western Norway. Doctoral thesis, Norwegian University of Science and Technology (NTNU), Trondheim, Norway.

Kveldsvik, V., Kaynia, A.M., Nadim, F., Bhasin, R., Nilsen, B. & Einstein, H.H. (2009). Dynamic distinct-element analysis of the 800 m high Åknes rock slope. *International Journal of Rock Mechanics and Mining Sciences*, 46(4): 686-698. doi:10.1016/j.ijrmms.2008.10.007.

Lauknes, T.R. (2010). Rockslide mapping in Norway by means of interferometric SAR time series analysis. PhD thesis, University of Tromsø, Trondheim, Norway.

Lauknes, T.R., Piyush Shanker, A., Dehls, J.F., Zebker, H.A., Henderson, I.H.C. & Larsen, Y. (2010). Detailed rockslide mapping in northern Norway with small baseline and persistent scatterer interferometric SAR time series methods. *Remote Sensing of Environment*, 114(9): 2097-2109. doi:10.1016/j.rse.2010.04.015.

Lebrouc, V., Schwartz, S., Baillet, L., Jongmans, D. & Gamond, J.F. (2013). Modeling permafrost extension in a rock slope since the Last Glacial Maximum: Application to the large Séchilienne landslide (French Alps). *Geomorphology*, 198: 189-200. doi:10.1016/j.geomorph.2013.06.001.

Legros, F. (2002). The mobility of long-runout landslides. *Engineering Geology*, 63(3-4): 301-331. doi:10.1016/s0013-7952(01)00090-4.

Li, Z., Bruhn, R.L., Pavlis, T.L., Vorkink, M. & Zeng, Z. (2010). Origin of sackung uphill-facing scarps in the Saint Elias orogen, Alaska: LIDAR data visualization and stress

modeling. *Geological Society of America Bulletin*, 122(9): 1585-1599. doi:10.1130/B30019.1.

Lie, Ø., Dahl, S.O. & Nesje, A. (2003). Theoretical equilibrium-line altitudes and glacier buildup sensitivity in southern Norway based on meteorological data in a geographical information system. *The Holocene*, 13(3): 373-380. doi:10.1191/0959683603hl630rp.

Lifton, N., Sato, T. & Dunai, T.J. (2014). Scaling in situ cosmogenic nuclide production rates using analytical approximations to atmospheric cosmic-ray fluxes. *Earth and Planetary Science Letters*, 386(0): 149-160. doi:10.1016/j.epsl.2013.10.052.

Longva, O., Blikra, L.H. & Dehls, J.F. (2009). Rock avalanches - distribution and frequencies in the inner part of Storfjorden, Møre og Romsdal County, Norway. *Geological Survey of Norway, Report*, 2009.002: 23.

Maiforth, J. (2010). Kulturminner på Flakk (in Norwegian). unpublished MSc Thesis, Norges teknisk-naturvitenskapelige universitet, Trondheim.

Mangerud, J.A.N., Larsen, E., Longva, O. & SØNstegaard, E. (1979). Glacial history of western Norway 15,000–10,000 B.P. *Boreas*, 8(2): 179-187. doi:10.1111/j.1502-3885.1979.tb00798.x.

Martinsen, O. & Nøttvedt, A. (2008). Norway rises from the sea - Palaeogene and Neogene (Cenozoic): the modern continents take shape; 66-2.5 Ma. In: I.B. Ramberg, I. Bryhni, A. Nøttvedt & K. Rangnes (Eds.), The Making of a Land - Geology of Norway. Norsk Geologisk Forening, Trondheim, pp. 442-479.

Masera, D., Giardino, M., Perotti, L., Poschinger, A.v., Calhoun, N. & Clague, J.J. (2014). Application of geomorphology and geomatics in the study of the Flims and Tamins landslides, Switzerland. In: R.L. Hermanns, A. Liinamaa-Dehls, J.F. Dehls & T. Oppikofer (Eds.), 3rd Slope Tectonics conference - Program and abstract book. Geological Survey of Norway, Report, Trondheim, pp. 42.

Matthews, J.A. & McCarroll, D. (1994). Snow-Avalanche Impact Landforms in Breheimen, Southern Norway: Origin, Age, and Paleoclimatic Implications. *Arctic and Alpine Research*, 26(2): 103-115. doi:10.2307/1551773.

Mauring, E., Lauritsen, T. & Tønnesen, J.F. (1998). Georadarmålinger I formindelse med undersøkelser av fjellskred I Tafjord, Romsdalen, Hellesylt og Innfjorden, Møre og Romsdal. *Geological Survey of Norway, Report*, 98.047.

Mazzanti, P. & De Blasio, F. (2011). The dynamics of coastal landslides: insights from laboratory experiments and theoretical analyses. *Bulletin of Engineering Geology and the Environment*, 70(3): 411-422. doi:10.1007/s10064-010-0322-y.

Mazzanti, P. & De Blasio, F.V. (2013). Landslide surfing on water: a preliminary study. *Italian Journal of Engineering Geology and Environment*, Book Series (6): 425-435. doi:10.4408/IJEGE.2013-06.B-41.

McDougall, S. & Hungr, O. (2004). A model for the analysis of rapid landslide motion across three-dimensional terrain. *Canadian Geotechnical Journal*, 41(6): 1084-1097. doi:10.1139/t04-052.

McDougall, S. & Hungr, O. (2005). Dynamic modelling of entrainment in rapid landslides. *Canadian Geotechnical Journal*, 42(5): 1437-1448. doi:10.1139/t05-064.

McDougall, S. (2006). A new continuum dynamic model for the analysis of extremely rapid landslide motion across complex 3D terrain. Doctoral thesis, The University of British Columbia, Vancouver, Canada, 253 pp.

McDougall, S., Boultbee, N., Hungr, O., Stead, D. & Schwab, J.W. (2006). The Zymoetz River landslide, British Columbia, Canada: description and dynamic analysis of a rock slide–debris flow. *Landslides*, 3: 195-204. doi:10.1007/s10346-006-0042-3.

McKinnon, M., Hungr, O. & McDougall, S. (2008). Dynamic Analyses Of Canadian Landslides. In: P. Locat, D. Perret, D. Turmel, D. Demers & S. Leroueil (Eds.),

Proceedings of the 4th Canadian Conference on Geohazards : From Causes to Management.

McSaveney, M.J. & Davies, T.R.H. (2006). Rapid rock mass flow with dynamic fragmentation: inferences from the morphology and internal structure of rockslides and rock avalanches. In: S.G. Evans, G. Scarascia Mugnozza, A. Strom & R.L. Hermanns (Eds.), Landslides from Massive Rock Slope Failure. NATO Science Series IV: Earth and Environmental Sciences - Vol. 49. Springer Netherlands, pp. 285-304.

Mörner, N.A. (1979). The Fennoscandian uplift and late cenozoic geodynamics: geological evidence. *GeoJournal*, 3(3): 287-318. doi:10.1007/bf00177634.

Mosar, J., Eide, E.A., Osmundsen, P.T., Sommaruga, A. & Torsvik, T.H. (2002). Greenland - Norway separation: A geodynamic model for the North Atlantic. *Norwegian Journal of Geology*, 82: 281-298.

Mosar, J. (2003). Scandinavia's North Atlantic passive margin. *Journal of Geophysical Research: Solid Earth*, 108(B8): 2360. doi:10.1029/2002jb002134.

Nesje, A. & Dahl, S.O. (1993). Lateglacial and Holocene glacier fluctuations and climate variations in western Norway: A review. *Quaternary Science Reviews*, 12(4): 255-261. doi:10.1016/0277-3791(93)90081-V.

Nesje, A. (2009). Latest Pleistocene and Holocene alpine glacier fluctuations in Scandinavia. *Quaternary Science Reviews*, 28(21–22): 2119-2136. doi:10.1016/j.quascirev.2008.12.016.

NGU (2011). Geologisk oversiktskart over Norge. Norges geologiske undersøkelse, http://www.ngu.no/no/hm/Kart-og-data/Berggrunn/ (access 17. Nov. 2014).

NGU (2014). Online database: Nasjonal berggrunnsdatabase - Standardkart: Berggrunn N250. Norges geologiske undersøkelse, http://www.geo.ngu.no/kart/berggrunn/ (access 17. Nov. 2014).

NGU (2015). Online database: Nasjonal løsmassedatabase - Standardkart: marin grense. Norges geologiske undersøkelse, http://geo.ngu.no/kart/losmasse/ (access 13. Jan. 2015).

Nordgulen, Ø. & Andresen, A. (2008). The Precambrian – The oldest rocks are formed; 4600-850 Ma. In: I.B. Ramberg, I. Bryhni, A. Nøttvedt & K. Rangnes (Eds.), The Making of a Land - Geology of Norway. Norsk Geologisk Forening, Trondheim, pp. 62-119.

Nordvik, T., Blikra, L.H., Nyrnes, E. & Derron, M.-H. (2010). Statistical analysis of seasonal displacements at the Nordnes rockslide, northern Norway. *Engineering Geology*, 114(3-4): 228-237. doi:10.1016/j.enggeo.2010.04.019.

Olesen, O., Dehls, J., Bungum, H., Riis, F., Hicks, E., Lindholm, C., Blikra, L.H., Fjeldskaar, W., Olsen, L., Longva, O., Faleide, J.I., Bockmann, L., Rise, L., Roberts, D., Braathen, A. & Brekke, H. (2000). Neotectonics in Norway, Final Report. *Geological Survey of Norway, Report*, 2000.002: 135.

Olesen, O., Blikra, L.H., Braathen, A., Dehls, J.F., Olsen, L., Rise, L., Roberts, D., Riis, F., Faleide, J.I. & Anda, E. (2004). Neotectonic deformation in Norway and its implications: a review. *Norwegian Journal of Geology*, 84: 3-34.

Olesen, O., Bungum, H., Dehls, J., Lindholm, C., Pascal, C. & Roberts, D. (2013). Neotectonics, seismicity and contemporary stress field in Norway – mechanisms and implications. In: L. Olsen, O. Fredin & O. Olesen (Eds.), Quaternary Geology of Norway. Geological Survey of Norway Special Publication, Trondheim, pp. 145-174.

Olsen, L., Fredin, O. & Olesen, O. (2013a). Quaternary Geology of Norway. NGU Special Publication, 13. Geological Survey of Norway, Trondheim.

Olsen, L., Sveian, H., Bergstrøm, B., Ottesen, D. & Rise, L. (2013b). Quaternary glaciations and their variations in Norway and on the Norwegian continental shelf. In: L. Olsen,

O. Fredin & O. Olesen (Eds.), Quaternary Geology of Norway. Geological Survey of Norway Special Publication, Trondheim, pp. 27-78.

Olsen, L., Sveian, H., Ottesen, D. & Rise, L. (2013c). Quaternary glacial, interglacial and interstadial deposits of Norway and adjacent onshore and offshore areas. In: L. Olsen, O. Fredin & O. Olesen (Eds.), Quaternary Geology of Norway. Geological Survey of Norway Special Publication, Trondheim, pp. 79-144.

Oppikofer, T., Jaboyedoff, M., Blikra, L.H. & Derron, M.-H. (2008). Characterization and monitoring of the Aknes rockslide using terrestrial laser scanning. In: J. Locat, D. Perret, D. Turmel, D. Demers & S. Leroueil (Eds.), Proceedings of the 4th Canadian Conference on Geohazards : From Causes to Management. Presse de l'Université Laval, Québec.

Oppikofer, T. (2009). Detection, analysis and monitoring of slope movements by high-resolution digital elevation models. Doctoral thesis, Université de Lausanne, Lausanne, Switzerland.

Oppikofer, T., Jaboyedoff, M., Blikra, L.H., Derron, M.-H. & Metzger, R. (2009). Characterization and monitoring of the Aknes rockslide using terrestrial laser scanning. *Natural Hazards and Earth System Sciences*, 9: 1003-1019.

Oppikofer, T., Jaboyedoff, M., Pedrazzini, A., Derron, M.-H. & Blikra, L.H. (2011). Detailed DEM analysis of a rockslide scar to characterize the basal sliding surface of active rockslides. *Journal of Geophysical Research: Earth Surface*, 116(F2): F02016. doi:10.1029/2010jf001807.

Oppikofer, T. (2012). Morphologic description of the Punta Cola rock avalanche and associated minor rockslides caused by the 21 April 2007 Aysén earthquake (Patagonia, Southern Chile). 2012, 69.

Oppikofer, T., Bunkholt, H., Ganerød, G.V. & Engvik, A.K. (2012a). Mannen unstable rock slope (Møre og Romsdal): Geological and engineering geological logging of drill core KH-02-11 & grain size distribution and XRD analysis of fine-grained breccia. *Geological Survey of Norway, Report*, 2012.036.

Oppikofer, T., Bunkholt, H.S.S., Fischer, L., Saintot, A., Hermanns, R.L., Carrea, D., Longchamp, C., Derron, M.-H., Michoud, C. & Jaboyedoff, M. (2012b). Investigation and monitoring of rock slope instabilities in Norway by terrestrial laser scanning. In: E. Eberhardt, C. Froese, K. Turner & S. Leroueil (Eds.), Landslides and Engineered Slopes: Protecting Society through Improved Understanding. Taylor & Francis Group, London, pp. 1235-1241.

Oppikofer, T., Saintot, A., Otterå, S., Hermanns, R.L., Anda, E., Dahle, H. & Eiken, T. (2013). Investigations on unstable rock slopes in Møre og Romsdal - status and plans after field surveys in 2012. *Geological Survey of Norway, Report*, 2013.014.

Oppikofer, T., Böhme, M., Saintot, A., Hermanns, R.L. & Longva, O. (2014). Hazard Assessment of Unstable and Potential Unstable Rock Slopes in Storfjord (Western Norway). In: G. Lollino, D. Giordan, G. Crosta, J. Corominas, R. Azzam, J. Wasowski & N. Sciarra (Eds.), Engineering Geology for Society and Territory – Volume 2: Landslide processes. Springer International Publishing Switzerland, pp. 243-248.

Optech, http://www.optech.com/ (access 20. Jan. 2015).

Optech (2014). ILRIS-LR Summary Specification Sheet, http://www.optech.com/wp-content/uploads/specification_ilris-lr.pdf (access 03. March 2014).

Osmundsen, P.T., Henderson, I., Lauknes, T.R., Larsen, Y., Redfield, T.F. & Dehls, J. (2009). Active normal fault control on landscape and rock-slope failure in northern Norway. *Geology*, 37(2): 135-138. doi:10.1130/g25208a.1.

Ostermann, M., Sanders, D., Ivy-Ochs, S., Alfimov, V., Rockenschaub, M. & Römer, A. (2012). Early Holocene (8.6 ka) rock avalanche deposits, Obernberg valley (Eastern Alps): Landform interpretation and kinematics of rapid mass movement. *Geomorphology*, 171–172(0): 83-93. doi:10.1016/j.geomorph.2012.05.006.

Owen, G., Matthews, J.A., Shakesby, R.A. & He, X. (2006). Snow-avalanche impact landforms, deposits and effects at Urdvatnet, southern Norway: implications for avalanche style and process. *Geografiska Annaler: Series A, Physical Geography*, 88(4): 295-307. doi:10.1111/j.0435-3676.2006.00302.x.

Pascal, C. & Olesen, O. (2009). Are the Norwegian mountains compensated by a mantle thermal anomaly at depth? *Tectonophysics*, 475(1): 160-168. doi:10.1016/j.tecto.2009.01.015.

Pedrazzini, A., Froese, C.R., Jaboyedoff, M., Hungr, O. & Humair, F. (2012). Combining digital elevation model analysis and run-out modeling to characterize hazard posed by a potentially unstable rock slope at Turtle Mountain, Alberta, Canada. *Engineering Geology*, 128(0): 76-94. doi:10.1016/j.enggeo.2011.03.015.

Penna, I.M., Hermanns, R.L., Niedermann, S. & Folguera, A. (2011). Multiple slope failures associated with neotectonic activity in the Southern Central Andes (37°–37°30′S), Patagonia, Argentina. *Geological Society of America Bulletin*, 123(9-10): 1880-1895. doi:10.1130/B30399.1.

Penna, I.M., Hermanns, R.L., Daicz, S., Suriano, J. & Tedesco, A.M. (2015). Effects of tectonic deformation and landslides in the erosion of a mountain plateau in the transitional zone between the central and Patagonian Andes. *American Journal of Science*, 315(3): 257-274. doi:10.2475/03.2015.03.

Pettijohn, E.J. & Doornkamp, J.C. (1973). Sand and sandstone. Springer-Verlag, Berlin.

Pirulli, M. (2009). The Thurwieser rock avalanche (Italian Alps): Description and dynamic analysis. *Engineering Geology*, 109(1-2): 80-92. doi:10.1016/j.enggeo.2008.10.007.

Poisel, R., Preh, A. & Hungr, O. (2008). Run Out of Landslides – Continuum Mechanics versus Discontinuum Mechanics Models. *Geomechanik und Tunnelbau*, 1(5): 358-366. doi:10.1002/geot.200800036.

Poschinger, A.v. (2002). Large rockslides in the Alps: A commentary on the contribution of G.Abele (1937-1994) and a review of some recent developments. In: S.G. Evans & J.V. DeGraff (Eds.), Catastrophic landslides: Effects, occurrence, and mechanisms. Geological Society of America Reviews in Engineering Geology, Boulder, Colorado, pp. 237-255.

Poschinger, A.v., Wassmer, P. & Maisch, M. (2006). The Flims rockslide: history of interpretation and new insights. In: S.G. Evans, G. Scarascia Mugnozza, A. Strom & R.L. Hermanns (Eds.), Landslides from Massive Rock Slope Failure. NATO Science Series IV: Earth and Environmental Sciences - Vol. 49. Springer Netherlands, pp. 329-356.

Poschinger, A.v. & Kippel, T. (2009). Alluvial deposits liquefied by the Flims rock slide. *Geomorphology*, 103(1): 50-56. doi:10.1016/j.geomorph.2007.09.016.

Pudasaini, S.P. & Miller, S.A. (2013). The hypermobility of huge landslides and avalanches. *Engineering Geology*, 157(0): 124-132. doi:10.1016/j.enggeo.2013.01.012.

Radbruch-Hall, D.H., Varnes, D.J. & Savage, W.Z. (1976). Gravitational spreading of steep-sided ridges (“sackung”) in Western United States. *Bulletin of the International Association of Engineering Geology - Bulletin de l'Association Internationale de Géologie de l'Ingénieur*, 13(1): 23-35. doi:10.1007/bf02634754.

Ramberg, I.B., Bryhni, I., Nøttvedt, A. & Rangnes, K. (2008). The Making of a Land - Geology of Norway. Norsk Geologisk Forening, Trondheim.

Redfield, T.F. & Osmundsen, P.T. (2009). The Tjellefonna fault system of Western Norway: Linking late-Caledonian extension, post-Caledonian normal faulting, and Tertiary rock column uplift with the landslide-generated tsunami event of 1756. *Tectonophysics*, 474(1-2): 106-123. doi:10.1016/j.tecto.2009.02.006.

Reitner, J.M. & Linner, M. (2009). Formation and preservation of large scale toppling related to alpine tectonic structures - Eastern Alps. *Austrian Journal of Earth Sciences*, 102(2): 69-80.

Reznichenko, N.V., Davies, T.R.H. & Alexander, D.J. (2011). Effects of rock avalanches on glacier behaviour and moraine formation. *Geomorphology*, 132(3–4): 327-338. doi:10.1016/j.geomorph.2011.05.019.

Roberts, D. & Gee, D.G. (1985). An introduction to the structure of the Scandinavian Caledonides. In: D.G. Gee & B.A. Sturt (Eds.), The Caledonide Orogen - Scandinavia and Related Areas. Wiley, Chichester, pp. 55-68.

Roberts, D. (2003). The Scandinavian Caledonides: event chronology, palaeogeographic settings and likely modern analogues. *Tectonophysics*, 365(1–4): 283-299. doi:10.1016/S0040-1951(03)00026-X.

Rocscience, https://www.rocscience.com (access 20. Jan. 2015).

Romstad, B., Harbitz, C.B. & Domaas, U. (2009). A GIS method for assessment of rock slide tsunami hazard in all Norwegian lakes and reservoirs. *Natural Hazards and Earth System Sciences*, 9(2): 353-364.

Rønning, J., Ganerød, G., Dalsegg, E. & Reiser, F. (2014). Resistivity mapping as a tool for identification and characterisation of weakness zones in crystalline bedrock: definition and testing of an interpretational model. *Bulletin of Engineering Geology and the Environment*, 73(4): 1225-1244. doi:10.1007/s10064-013-0555-7.

Rønning, J.S., Dalsegg, E., Elvebakk, H., Ganerød, G.V. & Heincke, B.H. (2009). Characterization of fracture zones in bedrock using 2D resistivity, Proceedings from 5th Seminar on Strait Crossings, Trondheim, pp. 439-444.

Saintot, A., Böhme, M., Redfield, T. & Dahle, H. (2008). Field studies of unstable slopes in Sunndalen Valley. *Geological Survey of Norway, Report*, 2008.049.

Saintot, A., Elvebakk, H., Oppikofer, T., Ganerød, G.V. & Farsund, T.Ø. (2011a). Mannen unstable rock slope (Møre & Romsdal): Logging of borehole and drill core KH-0l-10, geomorphologic digital elevation model interpretation & displacement analysis by terrestrial laser scanning. *Geological Survey of Norway, Report*, 2011.026.

Saintot, A., Henderson, I.H.C. & Derron, M.-H. (2011b). Inheritance of ductile and brittle structures in the development of large rock slope instabilities: examples from western Norway. *Geological Society, London, Special Publications*, 351(1): 27-78. doi:10.1144/sp351.3.

Saintot, A., Oppikofer, T., Derron, M.H. & Henderson, I. (2012). Large gravitational rock slope deformation in Romsdalen Valley (Western Norway). *Revista de la Asociación Geológica Argentina*, 69(3): 354-371.

Sartori, M., Baillifard, F., Jaboyedoff, M. & Rouiller, J.-D. (2003). Kinematics of the 1991 Randa rockslides (Valais, Switzerland). *Nat. Hazards Earth Syst. Sci.*, 3: 423-433.

Scheidegger, A.E. (1973). On the prediction of the reach and velocity of catastrophic landslides. *Rock Mechanics*, 5: 231-236.

Schleier, M., Hermanns, R.L., Krieger, I., Rohn, J. & Eiken, T. (2013a). Geotechnical investigations of a complex rock slope instability by use of field mapping and high resolution digital elevation models in West Norway (in German with English abstract). *Proceedings of the 19th Conference on Engineering Geology with Forum for Young Engineering Geologists, Munich, Germany, 13-15. March 2013*: 607-612.

Schleier, M., Hermanns, R.L. & Rohn, J. (2013b). Spatial distribution of rockslide deposits and their morphological features suggest timing and palaeo-environmental conditions for rock slope failures in Innerdalen and Innfjorddalen, Møre og Romsdal county, western Norway. In: R. Genevois & A. Prestininzi (Eds.), International Conference on Vajont – 1963-2013 – Thoughts and analyses after 50 years since the catastrophic

landslide, Padua, Italy, 8-10. October 2013. Italian Journal of Engineering Geology and Environment, Book Series (6), pp. 493-505.

Schleier, M., Hermanns, R.L., Rohn, J. & Gosse, J. (2015). Diagnostic characteristics and paleodynamics of supraglacial rock avalanches, Innerdalen, Western Norway. *Geomorphology*, 245: 23-39. doi:10.1016/j.geomorph.2015.04.033.

Schleier, M., Hermanns, R.L., Oppikofer, T. & Rohn, J. (2015, submitted). Rock avalanching onto marine sediments exposed by isostatic rebound, the Innfjorddalen case, Western Norway. *Geomorphology*.

Schleier, M., Hermanns, R.L., Krieger, I., Oppikofer, T. & Rohn, J. (in preparation). The deep seated gravitational slope deformation of Middagstinden Mountain, western Norway: evidence of gravitational reactivation of a pre-existing fault system.

Schrott, L. & Sass, O. (2008). Application of field geophysics in geomorphology: Advances and limitations exemplified by case studies. *Geomorphology*, 93(1–2): 55-73. doi:10.1016/j.geomorph.2006.12.024.

Seljesæter, S. (2010). Diskusjon av opprinnelsen til deformasjonsstrukturane i dalbotnsedimenta i Innfjorden (in Norwegian). unpublished Master thesis, Norges teknisk-naturvitenskapelige universitet, Trondheim, 113 pp.

Shakesby, R.A., Matthews, J.A. & Winkler, S. (2004). Glacier variations in Breheimen, southern Norway: relative-age dating of Holocene moraine complexes at six high-altitude glaciers. *The Holocene*, 14(6): 899-910. doi:10.1191/0959683603hl766rp.

Shakesby, R.A., Matthews, J.A., Karlén, W. & Los, S.O. (2011). The Schmidt hammer as a Holocene calibrated-age dating technique: Testing the form of the R-value-age relationship and defining the predicted-age errors. *The Holocene*, 21(4): 615-628. doi:10.1177/0959683610391322.

Shakun, J.D. & Carlson, A.E. (2010). A global perspective on Last Glacial Maximum to Holocene climate change. *Quaternary Science Reviews*, 29(15–16): 1801-1816. doi:10.1016/j.quascirev.2010.03.016.

Shugar, D.H. & Clague, J.J. (2011). The sedimentology and geomorphology of rock avalanche deposits on glaciers. *Sedimentology*, 58(7): 1762-1783. doi:10.1111/j.1365-3091.2011.01238.x.

Shugar, D.H., Rabus, B.T., Clague, J.J. & Capps, D.M. (2012). The response of Black Rapids Glacier, Alaska, to the Denali earthquake rock avalanches. *Journal of Geophysical Research: Earth Surface*, 117(F1): F01006. doi:10.1029/2011jf002011.

Shulmeister, J., Davies, T.R., Evans, D.J.A., Hyatt, O.M. & Tovar, D.S. (2009). Catastrophic landslides, glacier behaviour and moraine formation – A view from an active plate margin. *Quaternary Science Reviews*, 28(11–12): 1085-1096. doi:10.1016/j.quascirev.2008.11.015.

Solberg, I.L., Rønning, J.S., Dalsegg, E., Hansen, L., Rokoengen, K. & Sandven, R. (2008). Resistivity measurements as a tool for outlining quick clay extents and valley fill stratigraphy: feasability study from Buvika, Central Norway. *Canadian Geotechnical Journal*, 45: 210-225.

Soldati, M., Corsini, A. & Pasuto, A. (2004). Landslides and climate change in the Italian Dolomites since the Late glacial. *Catena*, 55(2): 141-161. doi:10.1016/s0341-8162(03)00113-9.

Solli, A. & Nordgulen, Ø. (2006). Berggrunnskart over Norge og kaledonidene i Sverige og Finland – M 1:2,000,000. Norges geologiske undersøkelse.

Sollid, J.L. & Sørbel, L. (1979). Deglaciation of western Central Norway. *Boreas*, 8(2): 233-239. doi:10.1111/j.1502-3885.1979.tb00805.x.

Sosio, R., Crosta, G.B. & Hungr, O. (2008). Complete dynamic modeling calibration for the Thurwieser rock avalanche (Italian Central Alps). *Engineering Geology*, 100(1-2): 11-26.

Sosio, R., Crosta, G.B., Chen, J.H. & Hungr, O. (2012). Modelling rock avalanche propagation onto glaciers. *Quaternary Science Reviews*, 47(0): 23-40. doi:10.1016/j.quascirev.2012.05.010.

Stead, D., Eberhardt, E., Coggan, J. & Benko, B. (2001). Advanced numerical techniques in rock slope stability analysis - applications and limitations. *Landslides - Causes, Impacts and Countermeasures, June 2001, Davos*.

Stead, D., Eberhardt, E. & Coggan, J.S. (2006). Developments in the characterization of complex rock slope deformation and failure using numerical modelling techniques. *Engineering Geology*, 83(1–3): 217-235. doi:10.1016/j.enggeo.2005.06.033.

Stini, J. (1941). Unsere Täler wachsen zu. *Geol. u. Bauwes.*, 13: 71-79.

Strom, A. (2006). Morphology and internal structure of rockslides and rock avalanches: grounds and constraints for their modelling. In: S.G. Evans, G. Scarascia Mugnozza, A. Strom & R.L. Hermanns (Eds.), Landslides from Massive Rock Slope Failure. NATO Science Series IV: Earth and Environmental Sciences - Vol. 49. Springer Netherlands, pp. 305-326.

Strom, A. & Abdrakhmatov, K. (2013). International Summer School on Rockslides and Related Phenomena in the Kokomeren River Basin, Kyrgyzstan. In: K. Sassa, B. Rouhban, S. Briceño, M. McSaveney & B. He (Eds.), Landslides: Global Risk Preparedness. Springer Berlin Heidelberg, pp. 85-94.

Sturzenegger, M. & Stead, D. (2009). Quantifying discontinuity orientation and persistence on high mountain rock slopes and large landslides using terrestrial remote sensing techniques. *Nat. Hazards Earth Syst. Sci.*, 9: 267-287.

Sturzenegger, M., Stead, D., Gosse, J.C., Ward, B. & Froese, C. (2014). Reconstruction of the history of the Palliser Rockslide based on 36Cl terrestrial cosmogenic nuclide dating and debris volume estimations. *Landslides*. doi:10.1007/s10346-014-0527-4.

terr@num, http://www.terranum.ch/ (access 20. Jan. 2015).

Thompson, S.C., Clague, J.J. & Evans, S.G. (1997). Holocene Activity of the Mt. Currie Scarp, Coast Mountains, British Columbia, and Implications for its Origin. *Environmental and Engineering Geoscience*, III(3): 329-348.

Trauth, M.H., Alonso, R.A., Haselton, K.R., Hermanns, R.L. & Strecker, M.R. (2000). Climate change and mass movements in the NW Argentine Andes. *Earth and Planetary Science Letters*, 179(2): 243-256. doi:10.1016/s0012-821x(00)00127-8.

Turner, A.K. & Schuster, R.L. (1996). Landslides: investigation and mitigation (Special Report 247). Transportation Research Board (EUA), National Research Council, Washington, DC.

Tveten, E., Lutro, O. & Thorsnes, T. (1998). Geologisk kart over Norge, Berggrunnskart Ålesund, 1:250,000. *Geological Survey of Norway, Trondheim*.

Valle, P., Færseth, R.B. & Fossen, H. (2002). Devonian-Triassic brittle deformcition based on dyke geometry and fault kinematics in the Sunnhordland region, SW Norway. *Norwegian Journal of Geology*, 82: 3-17.

Varnes, D.J. (1978). Slope movement types and processes. In: R.L. Schuster & R.J. Krizek (Eds.), Landslides - Analysis and control. Special Report. National Research Council, Transportation Research Board, Washington, D.C., pp. 11-33.

Voellmy, A. (1955). Über die Zerstörungskraft von Lawinen (On breaking force of avalanches). *Schweizerische Bauzeitung*, 73: 212-285.

Vorren, T.O. & Mangerud, J. (2008). Glaciations come and go - Quaternary to Holocene (Pleistocene); 2.6 Ma-11,500 years ago. In: I.B. Ramberg, I. Bryhni, A. Nøttvedt & K. Rangnes (Eds.), The Making of a Land - Geology of Norway. Norsk Geologisk Forening, Trondheim, pp. 480-533.

Wanner, H., Beer, J., Bütikofer, J., Crowley, T.J., Cubasch, U., Flückiger, J., Goosse, H., Grosjean, M., Joos, F., Kaplan, J.O., Küttel, M., Müller, S.A., Prentice, I.C., Solomina,

O., Stocker, T.F., Tarasov, P., Wagner, M. & Widmann, M. (2008). Mid- to Late Holocene climate change: an overview. *Quaternary Science Reviews*, 27(19–20): 1791-1828. doi:10.1016/j.quascirev.2008.06.013.

Wasrud, J. (2010). Kvartær tid i vestre Trollheimen (in Norwegian). unpublished Master thesis, Norges Teknisk - Naturvitenskapelige Universitet, Trondheim.

Welkner, D., Eberhardt, E. & Hermanns, R.L. (2010). Hazard investigation of the Portillo Rock Avalanche site, central Andes, Chile, using an integrated field mapping and numerical modelling approach. *Engineering Geology*, 114(3-4): 278-297. doi:10.1016/j.enggeo.2010.05.007.

Willenberg, H., Evans, K.F., Eberhardt, E., Spillmann, T. & Loew, S. (2008a). Internal structure and deformation of an unstable crystalline rock mass above Randa (Switzerland): Part II -- Three-dimensional deformation patterns. *Engineering Geology*, 101(1-2): 15-32. doi:10.1016/j.enggeo.2008.01.016.

Willenberg, H., Loew, S., Eberhardt, E., Evans, K.F., Spillmann, T., Heincke, B., Maurer, H. & Green, A.G. (2008b). Internal structure and deformation of an unstable crystalline rock mass above Randa (Switzerland): Part I -- Internal structure from integrated geological and geophysical investigations. *Engineering Geology*, 101(1-2): 1-14. doi:10.1016/j.enggeo.2008.01.015.

Wolter, A., Stead, D. & Clague, J.J. (2014). A morphologic characterisation of the 1963 Vajont Slide, Italy, using long-range terrestrial photogrammetry. *Geomorphology*, 206(0): 147-164. doi:10.1016/j.geomorph.2013.10.006.

Wyllie, D.C. & Mah, C.W. (2004). Rock Slope Engineering. Civil and Mining. Spon Press, London.

Yugsi Molina, F.X., Oppikofer, T., Hermanns, R.L., Redfield, T.F., Bascuñan, I., Loew, S. & Sepúlveda, S.A. (2012). Mechanism and volume estimation of the 2007 Punta Cola rockslide-debris avalanche using terrestrial laser scanning and aerial photogrammetry. In: E. Eberhardt, C. Froese, K. Turner & S. Leroueil (Eds.), Landslides and Engineered Slopes: Protecting Society through Improved Understanding. Taylor & Francis Group, London, pp. 553-559.

Zischinsky, U. (1969a). Über Bergzerreißung und Talzuschub. *Geol Rdsch*, 58: 974 - 983.

Zischinsky, U. (1969b). Über Sackungen. *Rock Mechanics*, 1(1): 30-52. doi:10.1007/bf01247356.